# Developing Hole Selective Layers and Implementing Large-size Organic Cations for Perovskite Solar Cells

## **Department of Organic and Inorganic Chemistry**



# Meenakshi Pegu

A thesis submitted for the fulfilment of degree in Doctor of Philosophy

Supervisors:

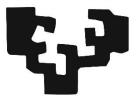
Shahzada Ahmad Samrana Kazim

*Tutor:* 

Luis Lezama

**June 2022** 

eman ta zabal zazu



Universidad del País Vasco

Euskal Herriko Unibertsitatea

This research work opts for the fulfilment degree of Doctor of Philosophy by the University of the Basque Country (UPV/EHU) that has been carried out in collaboration with the Foundation Basque Centre for Materials, Applications and Nanostructures (BC Materials) and the Department of Organic and Inorganic Chemistry, of the Faculty of Science and Technology of the UPV/EHU.



To my mother,

For her faith, her love and her strength....



# **ACKNOWLEDGEMENTS**

The completion of the thesis and earning a doctorate is long and arduous and today it has turned out into a reality. It has not been a ride through the magic carpet but yes, here we are, the journey has come to an end. This would not have been possible without those people who have provided constant assistance, encouragement and guidance. I offer my immense gratitude towards all those people who have provided so much of their time, support, love and strength in building up this thesis in order to attain the highest degree in academia. There are many people I would like to thank.

First and foremost, I would like to acknowledge my supervisor, Prof. Shahzada Ahmad, for the help and support during the three and a half years of doctoral period, for teaching me so much about writing research articles, for being available whenever I needed a discussion. I really appreciate the research freedom Prof. Shahzada gave to us so that we could develop our own ideas, implement them, make mistakes, to learn and correct them. This thesis took the shape because of his guidance, constant encouragement and support.

I am equally thankful to my co-supervisor, Dr. Samrana Kazim for guiding me during my PhD period. I appreciate all the discussions and am thankful for all the guidance.

I would like to thank Prof. Fernando Lopez Arbeloa and my tutor, Prof. Luis Lezama, for always extending their help regarding experimental and administrative purposes.

I am also thankful to our past and present group members for all their help.

I offer sincere gratitude to Prof. Angela Sastre, Prof. Dario M. Bassani and Dr. Thierry Buffetteo for our collaborations works.

I would like to thank Prof. Mohammed Khaja Nazeeruddin at EPFL, Sion, for being be my host supervisor during my short-term scientific visit of three months. I would also like to thank the group members and visitors of the GMF lab.

I would also like to thank the e-Cost Action- European Coopeartion in Science and Technology for the fellowship of Short-term Scientific Mission (STSM) for three months of research visit to EPFL.

Thanks to the Foundation Basque Centre for Materials, Applications and Nanostructures (BC Materials), which has been my research institute for all my experimental work during the doctoral programme. I would also offer my earnest gratitude to **ALL MY COLLEAGUES** here. Thank you all.

My gratitude toward the people of UPV, especially Maribel, Maria Belen, Aitor, Alex for the NMR, XPS, XRD and SEM measurements. Also, thanks to the general services of SGIker for conducting the measurements.

I would like to thank my previous supervisors from India, Prof. G. Krishnamoorthy and Prof. P. Thilagar who has passed their knowledge and the passion for research interest in me. Equally, I would like to thank my brother Dr. Samir Kumar Sarkar for always guiding me and teaching me the aspects of research whenever required.

This journey would not have been possible without thanking my best friends who were and are always a constant pillar of support since my masters' days, I will like to especially mention their names: Aritra, Sourav, Shreya, Ojaswini, Swagatam, Debasis, and Ranjan. Thank you so much, everyone.

My heartfelt gratitude to my Maa, thank you for this life, to raise us and for being the constant pillar of love and support. You are a blessing to us.

To my father for showering the blessings from the sky. Thank you so much Papa.

Baa, Dada you are the best sister and brother once can have, sharing joy every time with me and keeping me motivated.

To my grandparents and family in Kolkata.

Last but not least to the best person I have, Sunit Pal who is my best friend, my partner and my pillar of strength. You are such an amazing person; thank you for always providing a lot of positive energy in all the challenges of life.



Gracias todos, Thank you all, Eskerrik asko

# Meenakshi,

Leioa,

June 2022

# **ABSTRACT**

Organic-inorganic halide perovskite solar cells (PSCs) have emerged as one of the best candidates in next-generation photovoltaics since their introduction in 2009. The power conversion efficiency (PCE) has dramatically increased from 3.8% to 25.7% in a decade. However, due to their limited device stability, the path to commercialization has been hindered, despite excellent PCEs. The highest performing PSCs is composed of several layers such as electron transport layers, an n-type mesoporous TiO<sub>2</sub> layer, a perovskite layer, a hole transporting layer and a metal electrode. The high PCE can be achieved by effectively extracting and collecting the photogenerated holes and selectively reducing the charge recombination loss. The state-of-art Spiro-OMeTAD is the most commonly used hole transporting material in the literature, however, its high cost due to multistep synthesis process, complex purification and instability caused by adding of hygroscopic p-type dopants, hinders the large-scale industrialization of PSCs. Thus, the development of new designed HTMs is highly desired.

Additionally, the dimensionality of the perovskite influences the performance and stability of the PSCs. The reduction of dimensionality to produce lower-dimensional perovskites or an alternative approach to

implement an interfacial layer of the least amount of large organic cation to 3D perovskite surface to form bilayer or layered/3D mixed dimensional perovskites greatly enhance the photovoltaic performance and stability of PSCs.

Thus, the studies in this thesis aim to develop new hole-transporting materials that would be inexpensive and easily synthesizable and can be effectively implemented for PSC applications. A series of HTMs based on small molecules were designed and synthesized and investigated to understand the behaviour as a charge selective layer in PSCs, to further reduce the cost and improve the stability. Furthermore, the thesis discusses the work on the dimensionality of the perovskite and interface engineering of the perovskite absorber layer with large organic cations for improved performance and long-term stability purposes.

Thus, the thesis aims to discuss the studies and investigations on the molecularly designed hole-transporting materials (HTMs) and employ the large-size organic cation as an interface layer or doping to form reduced mixed-dimensional perovskite absorber for enhancing the overall performance and long-term stability of the PSCs.

*Keywords:* Perovskite solar cells, photovoltaics, hole transporting materials, interface engineering, doping, tetraindole, triazatruxene, phthalocyanines, 3-ammonium propionic acid iodide, *N*-Bromosuccinimide, bilayer perovskite.

# **RESUMEN**

Las células solares de perovskita de haluro orgánico-inorgánico (PSC) se han convertido en uno de los mejores candidatos para su uso en energía fotovoltaica de próxima generación, desde su introducción en 2009. La eficiencia de conversión energética (PCE) ha aumentado drásticamente del 3,8 % al 25,7 % en una década. Sin embargo, debido a la limitada estabilidad que tienen los dispositivos, su comercialización se ha visto obstaculizada a pesar de sus excelentes PCE. El PSC de mayor rendimiento se compone de varias capas, como una capa de transporte de electrones, una capa de TiO<sub>2</sub> mesoporoso de tipo n, una capa de perovskita, una capa de transporte de huecos (HTM) y un electrodo metálico. El alto PCE se puede lograr extrayendo y recolectando de manera efectiva los huecos foto-generados y reduciendo selectivamente la pérdida de recombinación de carga. El Spiro-OMeTAD de última generación es el material de transporte de huecos más comúnmente utilizado en la literatura, sin embargo, su alto costo debido al proceso de síntesis en múltiples pasos, su compleja purificación y su inestabilidad causada por la adición de dopantes higroscópicos de tipo p, dificulta la industrialización a gran escala de las PSC. Por lo tanto, es conveniente el desarrollo de nuevos HTM.

Además, la dimensionalidad de la perovskita influye en el rendimiento y la estabilidad de las PSC. Un enfoque alternativo para reducir la dimensionalidad de la perovskita es mediante intercaras con una menor cantidad de catión orgánico grande, formando perovskitas bicapa 2D/3D, o capas mixtas, lo cual mejora en gran medida el rendimiento fotovoltaico y la estabilidad de los PSC.

Por lo tanto, los estudios en esta tesis tienen como objetivo desarrollar nuevos materiales molecularmente de transporte de huecos que sean económicos, fácilmente sintetizables y que puedan implementarse de manera efectiva en PSC. Se diseñó, sintetizó e investigó una serie de HTM basados en moléculas pequeñas para comprender su comportamiento como capa selectiva de carga en las PSC, con el objetivo de reducir aún más el costo y mejorar la estabilidad. Además, en la tesis se analiza la dimensionalidad de la perovskita y se realiza ingeniería en la intercara de la capa absorbente de perovskita mediante grandes cationes orgánicos. Se emplean de cationes orgánicos de gran tamaño como capa de interfaz o dopaje para formar un absorbente de perovskita de dimensión mixta reducida, y así mejorar el rendimiento y la estabilidad a largo plazo de las PSC.

Palabras clave: Células solares de perovskita, energía fotovoltaica, materiales de transporte de huecos, ingeniería de interfaces, dopaje,

tetraindol, triazatruxeno, ftalocianinas, yoduro de ácido propiónico 3-amónico, N-bromosuccinimida, perovskita bicapa.

## **LABURPENA**

Haluro organiko-inorganikoko perovskitako eguzki-zelulak (PSC) hurrengo belaunaldiko energia fotovoltaikoan hautagai onenetako bat bihurtu dira 2009an sartu zirenetik. Energiaren konbertsioaren eraginkortasuna (PCE) izugarri handitu da hamarkada batean, % 3,8tik % 25,7ra. Hala ere, gailuaren egonkortasun mugatua dela eta, merkaturatzeko bidea oztopatu egin da, nahiz eta PCE bikainak izan.

Errendimendu handieneko PSCak hainbat geruza dituzte, hala nola elektroiak garraiatzeko geruza bat, n motako TiO2 geruza mesoporotsu bat, perovskita geruza bat, hutsuneak garraiatzeko geruza bat (HTM) eta metalezko elektrodo bat. PCE altua lortzeko, modu eraginkorrean atera eta bil daitezke sortutako foto-hutsuneak, eta selektiboki murriztuz kargabirkonbinazioaren galera. Azken belaunaldiko Spiro-OMeTAD-a da literaturan gehien erabiltzen den hutsuneen garraio-materiala. Hala ere, hainbat urratseko sintesi-prozesuaren ondorioz duen kostu handiak, haren arazketa konplexuak eta p motako dopatzaile higroskopikoak gehitzeak eragindako ezegonkortasunak zaildu egiten dute PSC-en eskala handiko industrializazioa. Beraz, komenigarria da HTM berriak garatzea.

Gainera, perovskitaren dimentsionaltasunak eragina du PSC-en errendimenduan eta egonkortasunean. Perovskitaren dimentsionaltasuna

murrizteko ikuspegi alternatibo bat katioi organiko handi gutxiago duten jeruza interfazialaren bidez da, 2D/3D perovskita bikapa edo geruza mistoak osatuz, eta horrek, neurri handi batean, errendimendu fotovoltaikoa eta PSC-en egonkortasuna hobetzen ditu.

Horrela, tesi honetako azterlanen helburua hutsuneak garraiatzeko material molekular berriak garatzea da, ekonomikoak, erraz sintetizatu daitezkeenak eta PSC-etan modu eraginkorrean inplementatu daitezkeenak. Molekula txikietan oinarritutako HTM batzuk diseinatu, sintetizatu eta ikertu dira, pertsona gorputzen karga-geruza selektibo gisa duten portaera ulertzeko, kostua are gehiago murrizteko eta egonkortasuna hobetzeko helburuarekin. Gainera, tesian perovskitaren dimentsionaltasunak daukan eragina aztertzen da eta perovskita geruza xurgatzailearen interfaze ingeniaritza egiten da katioi organiko handien bidez. Tamaina handiko katioi organikoak erabiltzen dira interfaze- edo dopin-geruza gisa, dimentsio misto txikiko perovskita-xurgatzaile bat osatzeko, eta, horrela, PSC-en epe luzerako errendimendua eta egonkortasuna hobetzeko.

*Hitz-gakoak*: Perovskita eguzki-zelulak, fotovoltaikoak, hutsune-garraiatzaile materialak, interfazearen ingeniaritza, dopina, tetraindola, triazatruxenoa, ftalozianinak, 3-amonio propionikoaren ioduroa, N-bromosuccinimida, geruza biko perovskita.

# ABBREVIATION AND SYMBOLS

Abs absorption

3-APAI ammonium propionic acid iodide

K Boltzmann's constant

 $V_{\rm bi}$  build-in potential

CdTe cadmium telluride

τ charge lifetime

Q charge of an electron

CBZ chlorobenzene

FK209 cobalt complex-based tris(2-(1H-pyrazol-1-

yl)-4-tert-

butylpyridine)cobalt(III)tri[bis(trifluoromet

hane) sulfonimide]

CB conduction band

CIGS copper indium gallium selenide/sulfide

CuS copper sulfide

CuI copper iodide

 $CuO_x$  copper oxide

CuSCN copper thiocyanate

*J-V* current density-voltage

CV cyclic voltammetry

DFT density functional theory

 $N_{\rm T}$  density of traps

W depletion width

DCM dichloromethane

DMSO dimethyl sulfoxide

DMF dimethylformamide

DSC differential scanning calorimetry

DSSCs dye-sensitized solar cells

 $\sigma$  electrical conductivity

ETL electron transport layer

EtOAc ethyl acetate

EQE external quantum efficiency

FF fill factor

FTO fluorine-doped tin oxide

FPEAI 2-(4-Fluorophenyl)ethylammonium iodide

FTIR Fourier transformation infrared

 $T_{\rm g}$  glass transition temperature

Au gold

HOMO highest occupied molecular orbital

M hole mobility

HTL hole transport layer

HTM hole transporting material

HBr hydrobromic acid

ITO indium doped tin oxide

IPCE incident photon-to-current conversion

efficiency

ICT intramolecular charge transfer

Cu2ZnSnS4 kesterite

LUMO lowest unoccupied molecular orbital

LiTFSI lithium bis(tri-fluoromethanesulfonyl)imide

MALDI-TOF matrix-assisted laser desorption/ionization-

time of flight

MPPT maximum power point tracking

 $J_{\text{max}}$  maximum photocurrent

 $P_{\text{max}}$  maximum power

mM millimolar

M molar

MO molecular orbital

MoO<sub>x</sub> molybdenum oxide

Nm nanometre

NBS N-Bromosuccinimide

NiO<sub>x</sub> nickel oxide

NMR nuclear magnetic resonance

 $\Omega \hspace{1cm} \text{ohm}$ 

 $V_{\rm oc}$  open-circuit voltage ( $V_{\rm oc}$ )

 $E_{\rm g}$  optical band gap

OLED organic light emitting diode

OPV organic photovoltaic

PSC perovskite solar cell

PCBM [6,6]-phenyl-C<sub>61</sub>-butyric acid methyl ester

PC<sub>71</sub>BM [6,6]-phenyl-C<sub>71</sub>-butyric acid methyl ester

PEAI phenethylammonium iodide

PV photovoltaic

PL photoluminescence

PMIRRAS polarization-modulated infrared reflection-

absorption spectroscopy

P3HT poly(3-hexylthiophene-2,5-diyl)

PTAA poly(triarylamine)

PEDOT: PSS poly(2,3-dihydrothieno-1,4-dioxin)-

poly(styrenesulfonate)

PCE,  $\eta$  power conversion efficiency

Jsc short circuit current density

Ag silver

AgTFSI silver(bis(tri- fluoromethanesulfonyl)imide

SCLC space charge limit current

T temperature

*t*-BP 4-tertbutylpyridine

F4TCNQ 2,3,5,6-tetra-fluoro-7,7,8,8-

tetracyanoquinodimethane

TTI tetraindole

THF tetrahydrofuran

Spiro-OMeTAD 2,2',7.7'-tetrakis(N,N-di-p-

 $methoxy phenylamine) \hbox{-9,9'-spirpbifluorene}$ 

TLC thin layer chromatography

3D three dimensional

TiO<sub>2</sub> titanium dioxide

TCO transparent conducting oxide

TAT triazatruxene

TMS trimethyl silyl

TPA triphenyl amine

 $WO_x$  tungsten oxide

2D two dimensional

UV ultraviolet

UPS ultraviolet photoemission spectroscopy

VB valence band

 $V_2O_5$  vanadium oxide

V volt

 $\lambda \hspace{1cm} wavelength$ 

XPS X-ray photoluminescence

XRD X-ray diffraction

ZnPc Zinc phthalocyanine

# **CONTENTS**

# Chapter 1. Perovskite Solar Cells.

1.1 Introduction to Perovskite Solar Cells	1-3
1.2 Organic-inorganic hybrid perovskite solar	3
1.2.1 Three-dimensional (3D) perovskite	3-4
1.2.2 Low-dimensional perovskite	4-8
1.2.3 Optical properties	8-9
1.2.4 Architecture	10-11
1.2.5 Components of perovskite solar cells	11-14
1.2.6 Charge transport in perovskite solar cells	14-16
1.2.7 Photovoltaic parameters	16-1
1.3 Interfacial engineering of perovskite solar cells	19-21
1.4 Organic semiconductors as hole transporting material	(HTM) for
perovskite solar cells	21-24
1.4.1 Characteristics of an ideal HTM	24-25
1.4.2 Classification of HTMs	25-27
1.4.3 Doping of HTMs in perovskite solar cells	27-30
1.5 Small-organic molecules as HTMs	30
1.5.1 Triarylamine-based HTMs	31-32
1.5.2 Carbazole-based HTMs	32-33
1.5.3 Triazatruxene-based HTMs	34-35
1.5.4 Thiophene- based HTMs	35-36
1.5.5 Organometallic compounds as HTMs	37-38
1.6 Motivation and outline of the thesis	39-42
1.7 References	43-49

Chapter 2. Tetra-indole Core as Hole Selective Layer that Passivate			
Defect in Perovskite Solar Cells.			
2.1 Introduction50-53			
2.2 Result and Discussion54			
2.2.1 Design and Synthesis54			
2.2.2 Optical, thermal and DFT studies55-56			
2.3 Electron paramagnetic resonance (EPR) spectroscopy56-59			
2.4 Spectroscopy, morphology and diffraction measurements60-63			
2.5 Photovoltaic properties of perovskite solar cells63-68			
2.6 Admittance spectroscopy measurements68-70			
2.7 Stability measurements of thin films and PSCs71-73			
2.8 Conclusions73-74			
2.9 References75-78			
Chapter 3. Implementing Fluorine Atoms in the Triazatruxene-based			
Hole-transporting Materials for Perovskite Solar Cells Application.			
3.1. Introduction79-81			
3.2 Results and discussion:82			
3.2.1 Synthesis of MP-TF HTMs82-83			
3.2.2 Optical, electrical and DFT studies83-87			
3.2.3 Ultraviolet photoelectron spectroscopy88			
3.2.4 Surface morphology88-89			
3.2.5 X-ray photoelectron spectroscopy89-90			

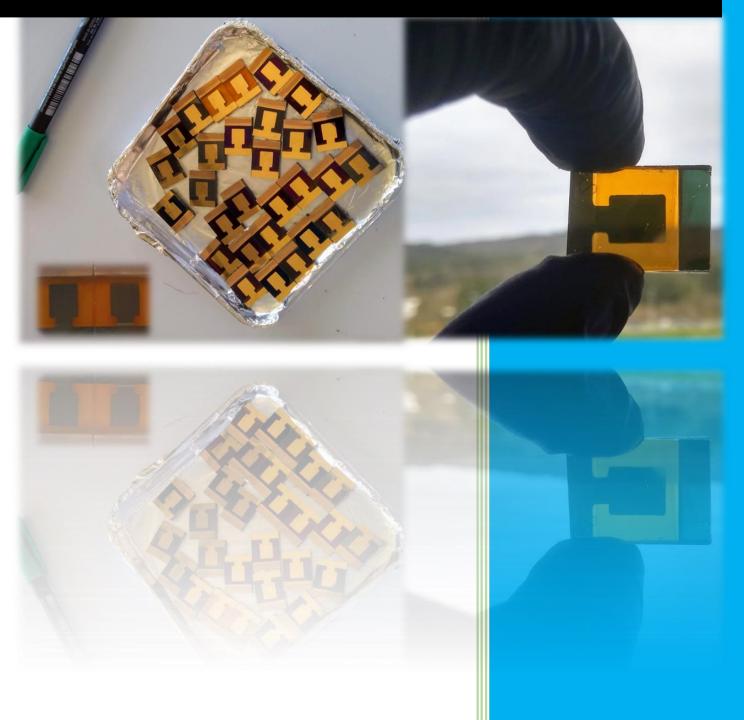
3.2.6 Optoelectrical and diffraction analysis91-92
3.2.7 Photovoltaic characterization and admittance
spectroscopy92-95
3.3 Conclusion95-96
3.4 References97-99
Chapter 4. Diethynyl-Conjugated Zinc-Phthalocyanine Dimers as Hole
Selective Layers for Perovskites solar cells Fabrication.
4.1 Introduction100-103
4.2 Result and Discussion104
4.2.1 Design and Synthesis104-105
4.2.2 Spectroscopic, diffractogram, electrochemistry, and surface
morphology studies105-110
4.3 Photovoltaic properties of the PSCs110-114
4.4 Stability and aadmittance spectroscopy measurements 115-117
4.5 Conclusions117-118
4.6 References119-123
Chapter 5. Understanding the Interaction of the Bifunctionalized
Cation 3-Amonium Propionic Acid Iodide with the Perovskite MAPbI $_3$
5.1 Introduction124-126
5.2 Result and Discussion126
5.2.1 Thin film analysis 126-131
5.3 Nuclear Magnetic Resonance Spectroscopy131-133

5.4 Surface morphology and contact angle measurements in thin	
films 134-1	35
5.5 Photovoltaic properties of PSCs135-1	38
5.6 Conclusion1	39
5.7 References140-1	44
Chapter 6. Deciphering the Orientation of the Aromatic Spacer Cati	on
in Bilayer Perovskite Solar Cells through Spectroscopic Techniques.	ı
6.1 Introduction 145-1	49
6.2 Result and Discussion1	49
6.2.1 PM-IRRAS study on bilayer perovskites 149-1	53
6.2.2 Thin film measurements153-1	59
6.3 Surface morphology and contact angle measurements 159-1	61
6.4 Photovoltaic properties of PSCs161-1	65
6.5 Admittance spectroscopy measurements165-1	68
6.5 Conclusion1	69
6.6 References170-1	73
Chapter 7. N-Bromosuccinimide as bromide contributor for hali	de
exchange in perovskite for solar cell fabrication.	
7.1 Introduction174-1	77
7.2 Result and Discussion177-1	79
7.2.1 Spectroscopic and X-ray diffraction (XRD) analysis of N	BS
treatment on MAPbI <sub>3</sub> 179-1	84

7.2.2 Spectroscopic and X-ray diffraction (XRD) analysis of NBS treatment
on (MAPbBr <sub>3</sub> ) <sub>0.15</sub> (FAPbI <sub>3</sub> ) <sub>0.85</sub> 184-187
7.2.2.1 PM-IRRAS measurement of the thin-films based on NBS
treatment on (MAPbBr <sub>3</sub> ) <sub>0.15</sub> (FAPbI <sub>3</sub> ) <sub>0.85</sub> 188-190
7.2.3 Surface morphology analysis of thin-films based
7.2.4 Contact-angle measurements192
7.2.5 Photovoltaic properties of PSCs193
7.2.5.1 Photovoltaic properties of PSCs based on NBS treatment
upon perovskite MAPbI <sub>3</sub> 193-196
7.2.5.2 Photovoltaic properties of PSCs based on NBS treatment
upon perovskite (MAPbBr <sub>3</sub> ) <sub>0.15</sub> (FAPbI <sub>3</sub> ) <sub>0.85</sub> 196-198
7.2.6 Admittance spectroscopy measurements of PSCs 198-203
7.3 Conclusion203-204
7.4 References
Chapter 8 Conclusion and Future Perspective.
8.1 Summary208-210
8.2 Future Outlook211
Experimental part212-230
<i>Appendix</i> 231-237
Curriculum Vitae238-242

# **Chapter 1**

# Perovskite Solar Cells



#### Chapter 1. Perovskite Solar Cells.

Hybrid organic-inorganic perovskite-based absorbers hold great promise for the emerging next-generation thin film photovoltaics, owing to their cost effectiveness and low amount of materials usage. In the current decade, three-dimensional perovskite analogs have shown outstanding potential in terms of power conversion efficiency. Additionally, the development and employment of the lower dimensional or the layered perovskite structures aspires scientists to achieve an excellent stable device with improved photovoltaic properties. Layered perovskite absorbers also provide a credible pathway of tuning the optoelectronic properties in order to achieve higher stability as well as efficiency. The use of organic small molecules as a hole transporting material has been studied extensively. Such molecules can be integrated in various type of device architecture such as mesoscopic and planar in perovskite solar cells. We discuss the selection criteria by taking into account, the cost competitiveness and simplistic synthesis process, stability of fabricated solar cells, power conversion efficiencies and its semiconducting behavior. Research efforts are being made to develop rational organic semiconductors which can work as a charge selective layers for performance enhancement in perovskite solar cells.

The parts of this chapter are based on published work:

M. Pegu et al. *Emergent Materials* 3, 751–778 (2020);

M. Pegu et al. https://doi.org/10.1002/9783527825790.ch10 (2021)

# Chapter 1. Perovskite Solar Cells.

# **Content:**

1.1 Introduction to Perovskite Solar Cells	1-3
1.2 Organic-inorganic hybrid perovskite solar	3
1.2.1 Three-dimensional (3D) perovskite	3-4
1.2.2 Low-dimensional perovskite	4-8
1.2.3 Optical properties	8-9
1.2.4 Architecture	10-11
1.2.5 Components of perovskite solar cells	11-14
1.2.6 Charge transport in perovskite solar cells	14-16
1.2.7 Photovoltaic parameters	16-19
1.3 Interfacial engineering of perovskite solar cells	19-21
1.4 Organic semiconductors as hole transporting materia	l (HTM) for
perovskite solar cells	21-24
1.4.1 Characteristics of an ideal HTM	24-25
1.4.2 Classification of HTMs	25-27
1.4.3 Doping of HTMs in perovskite solar cells	27-30
1.5 Small-organic molecules as HTMs	30
1.5.1 Triarylamine-based HTMs	31-32
1.5.2 Carbazole-based HTMs	32-33
1.5.3 Triazatruxene-based HTMs	34-35
1.5.4 Thiophene- based HTMs	35-36
1.5.5 Organometallic compounds as HTMs	37-38
1.6 Motivation and outline of the thesis	39-42
1.7 References	43-49

# Chapter 1. Perovskite Solar Cells

## 1.1 Intoduction to Perovskite solar cells

The world is advancing at the fastest pace towards technology. The industrial revolution in the 18th century empowered humans to go beyond all the odd limits and create new inventions. Electrification and related technologies emerged significantly in the last two centuries. With the rapidly rising economic growth, there is additional demand in the energy supply today. To meet the energy demand by mankind and limit greenhouse emissions, harvesting sunlight with cost-effective technology and converting it to electrical energy use is paramount. In the past, inorganic crystalline semiconductors, such as silicon, cadmium telluride (CdTe), and copper indium gallium selenide/sulfide (CIGS), were utilized as absorbers and are efficient and stable. However, it requires high energy input for manufacturing, involving high-temperature and high vacuum processes.<sup>[1-3]</sup> Among the potentially transformative technologies currently, perovskite solar cell (PSC) is seen as the front-runner, and is similar to organic and dyesensitized solar cells (DSSCs),<sup>[4]</sup> they can be made lightweight and flexible.

The perovskite solar cells are strong contenders in the third generation photovoltaic (PV) category and have earned significant interest (Figure 1.1a). <sup>[5, 6]</sup> Lead halide-based perovskites owing to their unique semiconducting properties have been intensively investigated since their first report by Miyasaka et al.<sup>[7]</sup> The power conversion efficiency (PCE) has seen a surge, and currently, 25.7% was reported for lab size cells (Figure 1.1b).<sup>[8]</sup> The first PSCs were reported with PCEs of 9.7% and 10.9% PCE, respectively.<sup>[9]</sup> The PCE stems from the exceptional optoelectrical properties of perovskites, such as the strong optical absorption coefficient, direct bandgap, long carrier lifetime and long diffusion length, and efficient charge

transport.<sup>[10-12]</sup> Hybrid perovskites generate loosely bound excitons under photo-irradiation, with small binding energy facilitating the generation of free charge carriers within the perovskite with a low driving force. Despite the competitive performance shown by PSCs, challenges remain that needs to be addressed to validate their commercial success. Research is being carried out to improve the operational stability of PSCs, and the search for environmentally benign perovskite composition is going on. The intrinsic degradation of perovskite under exposure to moisture, heat, and prolonged illumination under air, heat, and light needs to be addressed. <sup>[13-15]</sup>

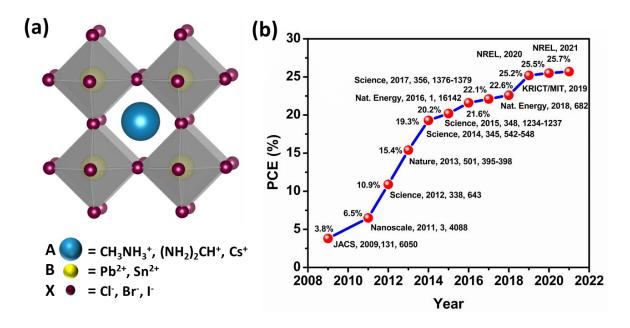


Figure 1.1: (a) Crystal structure of perovskite, and b) the rise in PCE of PSCs from 2009-2022.

To overcome the instability of the PSCs, various compositional engineering has been imposed on the three dimensional (3D) perovskite absorber, such as the use of ionic liquids, moisture impermeable layers, or use of electron transport layers (ETLs) or hole transport layers (HTLs) functionalised with distinct organic groups.<sup>[16, 17]</sup> Another phenomenal advancement involves reducing the dimensionality to produce lower-dimensional perovskites

(layered perovskites), quasi layered, quasi-3D perovskites that can enhance the stability of PSCs.[18-22] Research is being carried forward in this direction by incorporating a large bulky organic spacer cation that does not fit in the octahedral network of the perovskite structure (Figure 1.2). Incorporating the layered or mixed dimensional perovskite (referred to in the literature as two-dimensional or 2D perovskites) relaxes the limitations implied by the Goldschmidt tolerance factor and hinders the internal, ionic motion due to its robustness. Additionally, the hydrophobic character is induced by the larger organic cations that improves the stability by withstanding the surface water absorption.<sup>[23, 24]</sup> The most employed larger organic cation in layered/3D perovskite is demonstrated in Figure 1.3. However, their sizeable optical bandgap and lower charge carrier transport typically limit their choice as an ideal absorber for solar cell fabrication. An alternative approach of employing the least amount of layered perovskite to 3D perovskite absorber to form bilayer, layered or mixed dimensional perovskites or quasi 3D perovskites has been reported to boost the stability and performance of the PSCs.[25]

# 1.2 Organic-inorganic hybrid solar cells

# 1.2.1 Three-dimensional (3D) perovskite

Significant progress has been made during the current decade in using perovskites as a light harvester.  $^{[26]}$  The connectivity of metal halide octahedra constitutes the dimensionality of metal halide perovskites. The halide perovskites have a general formula of ABX<sub>3</sub>, where A is a monovalent cation (CH<sub>3</sub>NH<sub>3</sub><sup>+</sup>, CH (NH<sub>2</sub>)<sub>2</sub><sup>+</sup>, Cs<sup>+</sup>) and B is the divalent metal cation (Pb<sup>2+</sup>,

Sn<sup>2+</sup>, Ge<sup>2+</sup>), and X is a monovalent halide (Cl<sup>-</sup>, Br<sup>-</sup> and I<sup>-</sup>). 3D perovskites are characterized by the network of corner shared metal halide octahedra extended in all three directions. The A-type cations are occupied at the voids created by the interconnected octahedra where A, B and X can be one or multiple elements. The stability and distortion of 3D perovskite structures can be predicted employing some geometric calculations such as the Goldschmidt tolerance factor (t) and octahedral factor ( $\mu$ ).

$$t = \frac{r_A + r_X}{\sqrt{2}(r_B + r_X)}$$
$$\mu = \frac{r_B}{r_X}$$

where,  $r_A$ ,  $r_B$  and  $r_X$  indicate the ionic radii of A, B and X ions respectively.  $0.8 < t \le 1$  is the critical condition for obtaining a stable 3D octahedral network and any deviation from this scale will lead to an undesired octahedral distortion of perovskites. An octahedral factor can predict the possibility of octahedral coordination of B site cation and X site anions (generally between 0.4 and 0.9). The structural rigidity of 3D perovskites impedes its compositional tunability, and the reduced dimensionality has emerged as a promising solution.

# 1.2.2 Lower-dimensional perovskite

The lower-dimensional perovskites (Quasi-3D, Quasi-2D, 2D, 1D and 0D) are conceptually derived from cutting the 3D perovskites along their crystallographic planes to eliminate the tolerance factor curtailment. The choice of the crystallographic plane of slicing leads to the formation of three different layered perovskite families with orientation along <100>, <110>

and <111>. The thickness of the inorganic quantum well (QW, p = n, m, q for <100>, <110> and <111> oriented perovskites, respectively) and the choice of sizeable organic spacer cation plays a crucial role in determining the optoelectronic and structural properties of layered perovskites and thereby its PV compatibility. The inorganic QW thickness determines the dimensionality of layered perovskite; p=1 represents pure layered perovskites, whereas  $1 is commonly named quasi-layered. The layered perovskites with higher p values have mixed phases of layered, quasi-layered and 3D known as quasi-3D; moreover, the boundary condition of <math>p = \infty$  indicates the 3D perovskite structure.

The occurrence of <110> oriented layered perovskites is less common due to the availability of very few suitable spacer cations. They are known as layered corrugated structures due to the high degree of octahedral distortions. Mostly, perovskites with corrugation length (number of octahedra in each corrugation unit) of 2×2 are reported, and the extension of corrugation length to 3×3 and 4×4 could be possible by rational choice of spacer cations with site-specific hydrogen bonding and other secondary bonding interactions.<sup>[27]</sup> As of now, corrugated layered perovskites were synthesized mainly for m=1 (thickness of QW), and its octahedral distortions from self-trapped states to deliver white light emission at room temperature.<sup>[28]</sup> Slicing 3D perovskites along <111> plane creates a metal deficient structure; hence, the <111> oriented layered perovskites are rarely reported. The cutting along the body diagonal will eliminate the metal site. In contrast, neutral BX<sub>2</sub> fragments are wiped in the other two cases and the charge neutrality is only maintained for B<sup>3+</sup> (Bi, Sb or As) or a mixture of B<sup>2+</sup> and B<sup>3+</sup> metal cations. The p-type nature of <111> layered perovskites can be explored for future PV applications; provided its strong excitonic

character may limit the device performances.<sup>[29, 30]</sup> Unlike the <110> and <111> oriented perovskites, <100> family is the most explored layered perovskites for solar cell applications. The <100> oriented layered perovskites have been further classified into three groups depending on their structure such as Ruddlesden-Popper (RP), Dion-Jacobson (DJ) and Alternating Cation in the Interlayer space (ACI).

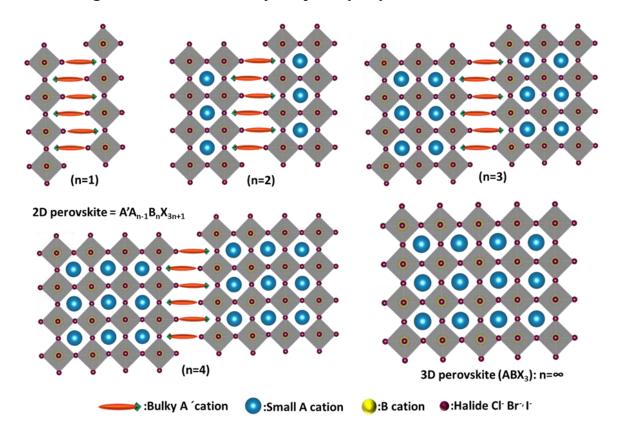


Figure 1.2: Schematic representation of 2D and 3D perovskite structures (2D n=1-4, 3D n= $\infty$ ).

The widely used RP perovskites have a structure of  $A'_2A_{n-1}B_nX_{3n+1}$ , where A' is a bulky alkyl or aryl ammonium cation spacer (Propylammonium-PA+, Butylammonium-BA+, Phenylethylammonium-PEA+). Conceptual slicing along the 100 plane and subsequent introductions of larger mono ammonium spacer cations generate the RP perovskites where inorganic sheets show a [1/2,1/2] displacement along the ab-plane. Thus, a staggered

formed structure with a bilayer of spacer cations between inorganic QWs creates a van der Waals gap.

Figure 1.3: Chemical structure of large-size organic cation used in reduced mixed dimensional perovskite.

On the other hand, the DJ perovskites (DJPs) replace the monovalent spacer cation with a divalent cation to reduce the interlayer distance. The DJPs are formed with  $A'A_{n-1}B_nX_{3n+1}$  general formula and show no shift along the abplane. The removal of the van der Waals gap by the divalent cations in DJPs is proposed to improve the charge carrier dynamics.

The mixed dimensional 2D/3D (Quasi 3D) perovskite absorbers are prepared by adding a layer of large organic cation over the 3D perovskite to partially replace the small amounts of organic cations with the bulky organic ones. Additionally, this thin layer of 2D perovskites overlaid on the top of the 3D perovskite absorber also forms an interfacial layer. More precisely, the

layered perovskites are categorized into pure 2D, quasi-2D and quasi-3D, where the n values vary between 1,  $1 < n \le 7$  and higher n values, respectively.

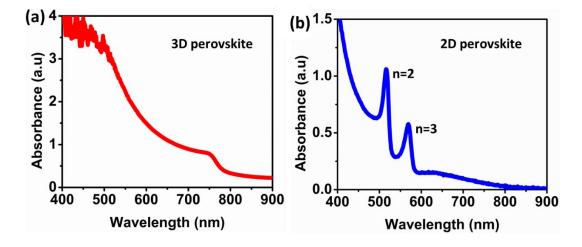


Figure 1.4: UV-visible absorption spectra of (a) 3D perovskite, (b) low dimensional 2D perovskite.

# 1.2.3 Optical Properties

In 3D halide perovskites, the organic cation has no significant role in determining the electronic structure, where the conduction band maximum (CBM) is donated by Pb, p-orbitals and the valence band maximum (VBM) derives from a combination of Pb, s and I p orbitals. The organic cations (methylammonium or MA, formamidinium or FA) are majorly employed to fulfill the stability and charge neutrality requirements. While the layered/quasi-layered perovskites composed of large organic cation interlayer between the inorganic sheets act as a barrier for charge carriers. The optical band gap ( $E_{\rm g}$ ) of layered/quasi-layered perovskites is much lower than corresponding 3D counterparts. The absorption spectra of the 3D halide perovskite and low dimensional perovskites are depicted in Figure 1.4. The bandgap of layered perovskites mainly depends upon the choice of

spacer cations. The structural distortions, primarily the I-Pb-I bond angle in the equatorial plane and the length of the organic spacer, strongly alter the optical bandgap. The high bandgap, originated from the quantum confinement, can be narrowed by manipulating the thickness of QW (n value); for example, the  $E_g$  values decrease from 2.24 eV (n=1) to 1.52 eV (n= $\infty$ ). The substitution of Pb with larger Sn ions can help lower the layered perovskite bandgap and avoid the toxicity burden. It is worth noting that, the absorption spectrum contains the exciton absorption peak and the absorption of layered materials are step-like near the bandgap,  $E_g$  can be determined from that step-like onset.

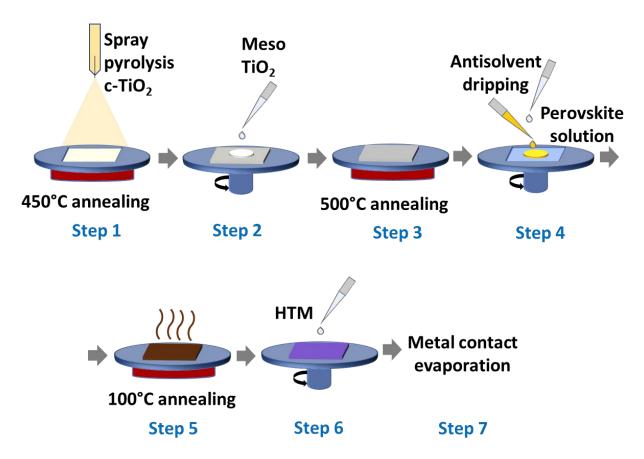


Figure 1.5: Schematic representation of stepwise fabrication process of perovskite solar cell in n-i-p configuration.

#### 1.2.4 Architecture

PSCs architecture is composed of various layers with combinations of materials such as transparent conducting electrodes (TCO), n-type semiconducting electron transporting layers (ETL), photoactive perovskite layer, p-type semiconducting hole transporting layers (HTL) and metallic electrode. The fabrication process of a complete perovskite solar cell is demonstrated in Figure 1.5. In typical PSCs, a perovskite layer is implemented between an ETL and an HTL. Depending on the structure of the n-type layer, PSCs can be classified into mesoscopic or planar heterojunction structures. Further, both can be subdivided into two categories, each depending on the selective contact of p-type and n-type materials. [31]

The PSCs can be fabricated into conventional (n-i-p) and inverted (p-i-n) devices, where the perovskite is a light-absorbing semiconductor and based on the overlaying ETLs and HTLs on the surface of the transparent electrode, the n-type or the p-type device structure is defined in Figure 1.6 (a-c). [32-35] The transparent glass electrode of fluorine-doped tin oxide (FTO) or indium doped tin oxide (ITO) is coated with a thin ETL or HTL depending on the device architecture used. Metallic electrodes are usually made of a high work function metal, such as gold, silver, aluminum or copper. The HTLs and ETLs used can be either inorganic or organic in nature. PSCs can yield high PCE depending on the charge carrier mobility of both doped and undoped inorganic and organic stacked layers. To date, the mesoscopic n-i-p device configuration shows the highest PCE of 25.7%.

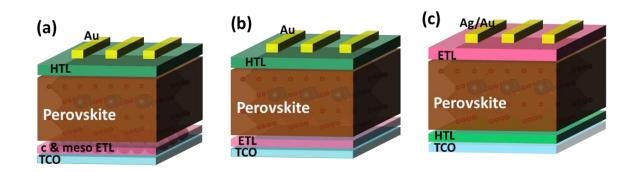


Figure 1.6: Perovskite device structure, a) mesoscopic *n-i-p*, b) planar regular *n-i-p*, c) inverted planar *p-i-n*.

# 1.2.5 Components of perovskite solar cells

PSCs generally consist of the transparent conducting oxide (TCO) as a working electrode, such as fluorine-doped tin oxide (FTO) or indium tin oxide (ITO) that is coated on glass or plastic substrates to provide electrical conductivity.

The ETL layer has the critical characteristic of preventing the photoinjected electrons in the conductive substrate from direct recombination with the holes. Hence the ETL acts as the hole blocking layer, directly deposited in the conducting substrate in the n-i-p configuration and atop the absorber layer in the p-i-n configuration. Another important property of the ETL layer is to satisfy the band alignment with the perovskite having a layer conduction band slightly higher than the ETL's CB for smooth transfer of electrons. The most common metal oxides such as  $TiO_2$ ,  $SnO_2$ , ZnO have been demonstrated as valuable ETMs in n-i-p configuration, and organic semiconductors such as [6,6]-phenyl- $C_{61}$ -butyric acid methyl ester (PCBM), [6,6]-phenyl- $C_{71}$ -butyric acid methyl ester (PC $_{71}$ BM), SF-PDI $_2$ , [36] dKM60s fullerene have been successfully employed as ETLs[37] in the p-i-n configuration (Figure 1.7).

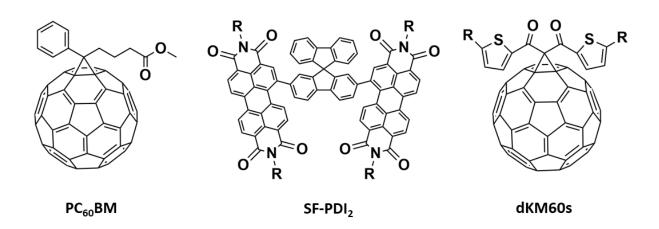


Figure 1.7: Chemical structure of electron-transporting materials.

Hybrid organic-inorganic halide perovskite is the main component in all the possible device configurations. It is the crucial component for light absorption and photogeneration of free carriers. The common perovskite used in PSCs is methylammonium lead halide perovskite, an ambipolar material that generates electron and hole pairs.[7] Methylammonium lead iodide (MAPbI<sub>3</sub>) perovskite has shown extraordinary performance due to its suitable optical and electronic properties. In the typical MAPbI<sub>3</sub>, MA+ (CH<sub>3</sub>NH<sub>3</sub>+) is a monovalent cation, Pb<sup>2+</sup> is a bivalent metal cation, and I- is a halogen anion, having a bandgap of 1.56 eV. Formamidinium cation (HC(NH<sub>2</sub>)<sub>2</sub><sup>+</sup>) has a relatively low bandgap (1.47 eV) which stems from its absorption onset at long-wavelength as compared to methylammonium cation (CH<sub>3</sub>NH<sub>3</sub>+). In comparison, the pure bromide-based anion shows a high bandgap (2.1 eV) due to shifting of absorption onset towards the short wavelength. The PSCs fabricated using mixed anion and cation-based  $Cs_{0.1}FAPbI_{3(0.81)}MAPbBr_{3(0.09)}$ perovskites such (CsFAMA), as or  $FAPbI_{3(0.85)}MAPbBr_{3(0.15)}$ or **FAMA** and  $Rb_{0.2}Cs_{0.2}(MA_{0.3}FA_{0.3})PbI_3$ RbCsFAMA gave high open-circuit voltage ( $V_{oc}$ ) and short circuit current density  $(I_{sc})$  measuring an unparalleled PCE through compositional

engineering.<sup>[38]</sup> This increase in performance comes at the cost of phase separation and compromise device reliability.

The p-type organic semiconductors as HTM, play a vital role in improving PSCs performance. [39, 40] The role of HTM is to extract and transfer the holes from the perovskite layer to the respective electrode. Some of the most employed HTMs in PSCs is represented in Figure 1.8. The optical merits of the HTMs contributes to the performance of the PSCs. [41] Various transitions such as  $n-\pi^*$ ,  $\pi-\pi^*$  or intramolecular charge transfer (ICT) influence the PV performance and PSCs' working life. On p-type doping of HTM, it converts into the oxidised form due to the formation of a radical cation, can be evidenced by a new absorption band in the visible region. The oxidised HTMs exhibit improved electrical conductivity and enhanced the charge transfer at the perovskite/HTM/Au interfaces. [42] The charge recombination and collection occur at the perovskite/HTM interface, and can be explained by build-in potential ( $V_{bi}$ ), interfacial defects or characterised by a lower photoluminescence (PL) intensity.

Figure 1.8: Chemical structure of hole-transporting materials.

The back contact, such as the counter electrode, is required to complete the solar circuit that functions as an electrode providing the current and voltage

for the external electrical work. The back contact of the PSC is formed by deposition of metals with high work function; required to achieve high open-circuit voltage ( $V_{\rm oc}$ ). The metals such as gold, silver, aluminium, and copper are used as back contacts with the choice of the configuration of the devices.

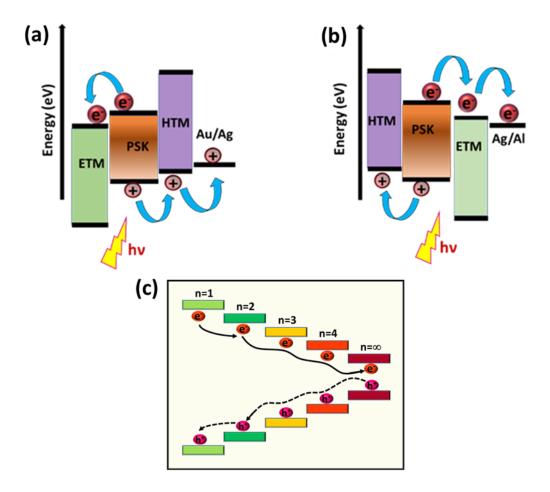


Figure 1.9: Corresponding charge transfer mechanism in PSCs, [40] (a) n-i-p configuration, (b) p-i-n configuration, [40] (c) illustrating the charge transport pathway through a multiphase layered perovskite. [43]

# 1.2.6 Charge transport in perovskite solar cells

The performance of PSCs is strictly dependent on the efficient transport of photogenerated excitons and their subsequent annihilation to free

carriers.[44] The instantaneous generation of free carriers occurs in 3D perovskites owing to their small exciton binding energy. Figure 1.9 (a, b) depicts that the perovskite layer absorbs light and generates exciton (electron and hole pairs) on photoexcitation. The electrons move towards the conduction band of ETM, and holes are transferred to the valence band of HTM, and they get collected to the respective front and back electrodes. [45-<sup>47]</sup> The undesirable charge transfer, i.e., the back transfer of electrons from the ETM to the perovskite and holes from HTM, can also occur, thus limiting of enhanced the device PCE bv means charge recombination phenomenon.[48]

On the other hand, the carrier transport of 2D perovskites is a complex phenomenon that relies on in-plane and out-of-plane distortions, Pb-I distance, I-Pb-I bond angle, exciton binding energy, trap sites etc. The carrier conductivity and mobility are highly favored in the out-of-plane orientation of crystallographic planes. The demonstration of the hot-casting method was significant for layered perovskite-based solar cells, which improved the PCE. Additionally, the use of additives, rational design of spacer cation and different salt-assisted anti-solvent treatments also further depicted the vertical aligned perovskite thin films with enhanced crystallinity, large grain size and reduced defect sites. Along with the vertically oriented crystal growth, the thickness of the inorganic cage (n value) contributes to the charge-transfer behavior (Figure 1.9 c). To date, most of the reports suggest that the crystallization of quasi-layered perovskites is followed by the formation of multiple <*n*> value species with a random distribution which delivers a desperate bandgap. It is reported that the transit time of photogenerated carriers across the electrodes is longer than the cascade energy transfer time, indicating that the carriers were relaxed to the band

edge of the smallest bandgap phase before the annihilation. This cascade energy transfer between different phases results in higher energy added to the additional cooling process in the charge transportation and the band tail states created by the high degree of energy disorder known to induce significant  $V_{oc}$  loss in the PSCs. To overcome this barrier, noticeable steps have been taken and a narrow phase distribution has been proposed to mitigate such issues.<sup>[49]</sup> Rational choice of spacer cations, additive engineering and manipulated fabrication processes have been employed to achieve the homogeneous phase distribution. However, these approaches still lack the understanding of crystallization kinetics, which further needs to be explored to overcome the tradeoff between device stability and efficiency.

The charge carrier dynamics in layered or mixed dimensional PSCs and their role in influencing device performance have been not been detailed. Investigations have been demonstrated that the small addition of large organic cations increases the crystallinity and reduces the trap mediated charge recombination, thereby increasing the adequate charge carrier mobility of the hybrid perovskite. The layered capping layer atop the 3D hybrid perovskite could also enhance the subtle excitonic effects and effectively passivate the trap states, thereby lowering the non-radiative charge recombination.

# 1.2.6 Photovoltaic parameters

The PSC performance is characterized by the current density-voltage (*J-V*) curve (Figure 1.10 a) comprising of the four fundamental parameters as the

open-circuit voltage ( $V_{oc}$ ), short circuit current ( $J_{sc}$ ), fill factor (FF), and power conversion efficiency (PCE,  $\eta$ ).

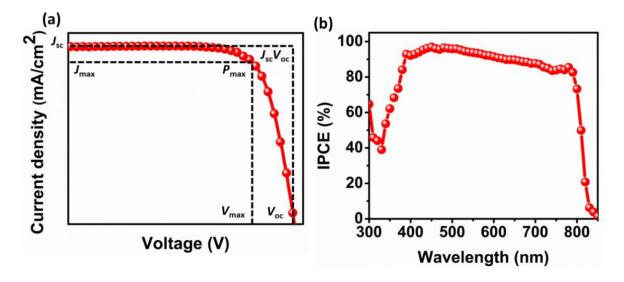


Figure 1.10: (a) Current-density (*J-V*) characteristics of a PSC under one sun illumination, (b) IPCE spectrum of a PSC as a function of wavelength.

The J-V measurements are conducted to evaluate the photovoltaic performance of the solar cell. The  $V_{\rm oc}$ ,  $J_{\rm sc}$ , FF combinedly yields the power conversion efficiency (PCE) of the PSCs. The measurement is performed at standard AM 1.5 G, 100 mW cm<sup>2</sup> illumination under one sun intensity from a 450 W AAA solar simulator (ORIEL, 94023 A).

Typically, the current density is recorded along with the linearly varying voltage from the  $V_{oc}$  to 0 V, which gives the J-V curve. The simplified equation to measure the current density of a solar cell is as follows:

$$J = J_{sc} - J_0 (e^{\frac{qV}{kT}} - 1)$$

 $J_0$  is the reverse saturation current, q is the charge of an electron, k is the Boltzmann's constant, and T is the temperature.  $J_{sc}$  is the photocurrent per unit area when the device is short-circuited.

The open-circuit voltage ( $V_{oc}$ ) is the difference in electrical potential between the two terminals of the cells. It is derived when a solar cell provides maximum voltage to an external circuit and is obtained from the dissociation of holes and electrons quasi-Fermi levels.  $V_{oc}$  is measured when the short circuit current is equal to zero and is given as the following equation:

$$V_{oc} = V_T \ln{(1 + \frac{J_{sc}}{J_0})}$$

Where  $V_T$  is the thermal voltage. During illumination of a solar cell, the maximum  $J_{\rm sc}$  is obtained when the cell is short-circuited; while no current flows under open-circuit conditions. If the voltage is zero, the value of the power at the short circuit is zero; likewise, if the current is zero, the value of the power at the open-circuit point s zero. Thus, there is a point where maximum of the power is generated by the solar cell in between, which is called the point of maximum power point ( $P_{\rm max}$ ), having points at X-axis with  $V_{\rm max}$  and Y-axis with  $J_{\rm max}$ .

The product of the maximum values of the photocurrent and voltage  $(J_{\text{max}}.V_{\text{max}})$  determines the maximum power point  $(P_{\text{max}})$ . Thus, the ratio of the maximum power point to the power of the light incidence  $(P_{\text{in}})$  defines the overall power conversion efficiency  $(\eta)$  and is given by the following equation:

$$\eta = \frac{P_{max}}{P_{in}} = \frac{J_{sc} \cdot V_{oc} \cdot FF}{P_{in}}$$

The fill factor (FF) of a PSC regulates the deviation of the measure solar cell efficiency from the theoretical maximum power output of the cell and is

given by the ratio of the full power ( $P_{max}$ ) to the external short circuit current and open-circuit voltage values as:

$$FF = \frac{J_{max}V_{max}}{J_{sc}V_{oc}}$$

The incident photon-to-current conversion efficiency (IPCE) determines how efficiently the incoming photons are transformed into the electrons by the PSC at a particular wavelength (Figure 1.10 b). The equation calculates the IPCE spectrum of a PSC:

$$IPCE(\lambda) = \frac{n_{electrons}(\lambda)}{n_{photons}(\lambda)} = \frac{J_{sc}(\lambda)}{eP_{in}(\lambda)}$$

 $J_{\rm sc}$  ( $\lambda$ ) is the short circuit photocurrent density, e is the elementary charge,  $P_{\rm in}$  ( $\lambda$ ) optical power input.

# 1.3 Interfacial engineering of perovskite solar cells

To enhance the performance of the perovskite solar cells, multiple approaches have been introduced such as reducing non-radiative recombination losses, ion compensation and interface engineering of the perovskite layer. Interfaces of the perovskite layer (ETL/perovskite; or perovskite/HTL) have always been the key factor in boosting the solar cell performance. Any fallibility in contact between each layer can lead to the formation of defects or trap sites producing non-radiative recombination losses that is detrimental to the performance of the PSCs. Thus, engineering of the interfaces by an interlayer ideally, lowers the surface defects and

encapsulate the perovskite layer from the ambient atmospheric conditions to improve the device stability.

During the solution process fabrication of the of the perovskite layer and annealing at low temperature, various types of defects are generated in the interfaces of the perovskite. These defects, also known as trap sites, favors the non-radiative recombination process and negatively impacting the  $V_{\rm oc}$  of the device (Figure 1.11). The types of defect associated with the ABX<sub>3</sub> perovskite crystal layer can generally be mentioned as: (a) B-site vacancy, (b) X-site vacancy, (c) insterstitial of A, (d) insterstitial of X, (e) grain boundaries or (f) B-X substitution. [50] Interface has a crucial role in charge dynamics of the PSCs. The defects at the interfaces could inherently affect the charge transfer processes leading to reduce in the PV performance and threats the stability of the PSCs. [51]

A recent progress on the interface engineering of the perovskite layer improved and highlights the efficiency and stability in PSCs. Passivating the perovskite layer could effectively reduce the surface recombination losses by mitigating the surface defects. Various passivating agents have been explored to target the specific defects at the interfaces such as (a) using excess PbI<sub>2</sub> that reduces trap charges at the grain boundaries and improves the crystallinity of the perovskite layer forming bigger grains, (b) implementing the large organic cation or alkylammonium halide salts that induces the lower dimensional perovskite formation; mitigating the cationic or anionic defects through hydrogen or ionic bonding at the trap-sites and thereby passivating the defects, (c) introducing hydrophobic cross-linking HTMs, (d) use of Lewis acids and bases to passivate the undercoordinate ions, that forms covalent bonds by sharing the electron lone pairs and reducing the trap states (e) passivation with wide band gap materials such

as amorphous silicon, SiN and  $SiO_2$  has been employed as an effective strategy to PSCs.

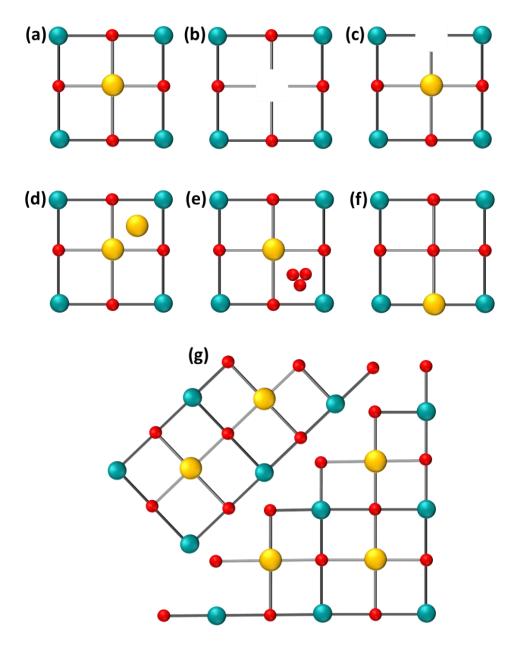


Figure 1.11: (a) a perfect crystal lattice, (b) B-site vacancy, (c) halide vacancy, (d) interstitial B cation, (e) interstitial halides, (f) B-cation/halide antisite substitution, (g) grain boundary.<sup>[50]</sup>

# 1.4 Organic molecules as hole transporting material (HTM) for perovskite solar cells

Organic semiconductors are largely explored due to their variation in synthesis and design that can easily tune the optoelectronic properties. Unlike the inorganic semiconductors, organic semiconductors are weakly bound through hydrogen bonding,  $\pi$ - $\pi$  interaction, van der Waals forces that allow a proper molecular packing in the structure. The intermolecular interaction between neighbouring functional groups of HTMs creates a supramolecular geometry with antiparallel molecular packing, which helps in charge transport.<sup>[52]</sup> In some cases, these molecular interactions can also enable amorphous HTM to transform to para-crystalline dimers at a certain temperature that increases hole mobility. [53] Organic semiconductors possess a conjugated  $\pi$ -electron system that helps in the conductivity of the charges.  $\pi$  -conjugation within the molecule improves the optical and conjugation leads to electrical properties. More more electron delocalisation, which increases the mobility of the charges through the  $\pi$ bonding system. A  $\pi$ -conjugated system possesses alternating double and single bonds linked to carbon atoms in the molecular structure. Hence, they are primarily employed as hole-transporting materials in PSC applications. The small electron cloud density over and below the molecular plane of the C-C  $\pi$ -bond has weak interaction that leads to semiconducting properties (Figure 1.12 a).<sup>[54]</sup> The weaker interaction of the *2p*-orbitals generated the weaker bonding  $(\pi)$  and antibonding  $(\pi^*)$  molecular orbital (MO) energy levels, leading to  $\pi$ - $\pi$ \* interaction possible within the conjugated molecular system. The  $\pi$ -bonding MO is the highest occupied molecular orbital (HOMO)

and the  $\pi^*$  antibonding orbital is the lowest unoccupied molecular orbital (LUMO).

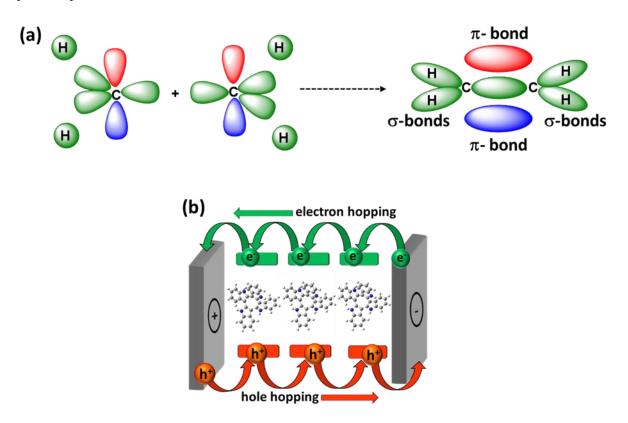


Figure 1.12: (a) Bonding orbitals in ethylene molecule (Source: chemtube3D), (b) electron and hole hopping in the organic semiconducting material.<sup>[54]</sup>

Organic semiconductors have the properties to conduct both the charge carriers (electrons and holes). The reorganisation of the Fermi level relative to the HOMO and LUMO energy level determines the nature of charge transport. The charge carriers are localised within the organic semiconductors, enabling the MO of each system to possess the HOMO and LUMO energies. [55,56] Thus, the charge transport in an organic semiconductor occurs via electron or hole hopping from the localised state by overcoming the energy barrier movement (Figure 1.12 b).

Developing of HTMs is paramount to fabricating stable PSCs. Currently, the maximum PCEs of 24.8% with HTM based devices have been reported using additives. By eliminating the use of dopants, device stability can be extended. Strategies are being developed to design efficient dopant-free HTMs based on different core structures to address the issues related to the intrinsic and extrinsic stability of the PSCs. Planar, rigid and fully conjugated molecules with suitable energy levels and larger  $\pi$ -conjugated systems are being developed in this direction.

HTMs, in some cases, demonstrate properties that supersede the use of Spiro-OMeTAD. A majority of HTMs reported are based on small organic molecules or polymers. Arguably, the molecular design of HTMs should be embodied with added  $\pi$  conjugated structures and specific functional groups having electron donating and accepting properties. These HTM can be synthesized using different cross-coupling reaction processes such as **Buchwald-Hartwig** Stille coupling, Suzuki-Miyuara, cross-coupling, Sonogashira coupling, Heck reactions, BuLi treatment or Schiff-base reactions. If the molecules display a planar and rigid geometry accompanied by a highly  $\pi$  conjugated molecular structure, exhibit  $\pi$ - $\pi$  stacking, deeplying HOMO energy level and donor – acceptor conjugated structure, it can facilitate the higher charge transport behaviour, thereby improving the hole mobility and conductivity. The alkoxy groups (-OR) in the HTM structure are responsible for adjusting the HOMO level of the material. Furthermore, they play a vital role in anchoring the material onto the underlying perovskite layer and improving material stability. The ease of synthesis, purification and their ability to form a highly crystalline layer favours their employment.

# 1.4.1 Characteristics of an ideal HTM

Ideally, an HTM for high-performance PSCs should fulfill essential characteristics. They should:

- have easy synthetic and purification process,
- solubility in orthogonal solvents,
- cost-competitive,
- thermally and photochemically stable,
- energy level alignment, i.e., the highest occupied molecular orbital HOMO should be slightly higher in energy level than the valence band of the perovskite layer for efficient hole extraction,
- the LUMO (lowest unoccupied molecular orbital) energy level should be significantly lower than that of the perovskite absorber,
- moisture tolerant, i.e., hydrophobic nature for device stability,
- high hole mobility (possibly >  $10^{-3}$  cm<sup>2</sup> V<sup>-1</sup> s<sup>-1</sup>) to facilitate hole conduction and prevent charge recombination,
- lower tendency towards crystallisation to avoid phase transition during device processing and operation and
- low light absorption in the visible spectrum. HTM should act as a barrier between the anode and perovskite layer to block electrons.

# 1.4.2 Classification of HTMs: Inorganic, Organometallic, Organic (small molecules, polymers)

Inorganic materials are expected to be stable in terms of high temperature and moisture tolerance, a variety of inorganic HTMs have been reported for PSCs such as vanadium oxide ( $V_2O_5$ ), molybdenum oxide ( $MoO_x$ ), tungsten oxide ( $WO_x$ ), cobalt oxide ( $CoO_x$ ), nickel oxide ( $NiO_x$ ), Kesterite ( $Cu_2ZnSnS_4$ ), copper sulfide ( $CuS_x$ ), copper iodide ( $CuI_x$ ), copper oxide ( $CuO_x$ ) and copper thiocyanate (CuSCN). The use of organometallic phthalocyanines as the HTM fabricates efficient and stable PSCs. These organic metal complexes with  $18\pi$ - electrons act as semiconductors by attaining high charge mobility and excellent thermal and chemical stability. The Cu(II), Ni(II) and Zn(II)-based phthalocyanines have recently attracted considerable attention in PSCs and gave an average PCE of >17%. The metal phthalocyanines are also used as organic semiconductors for organic transistors, solar cells, and electrocatalysts. However, most phthalocyanines have poor solubility in common organic solvents, and thus thermal evaporation methods are preferred.

Figure 1.13: Chemical structure of polymer-based HTMs.

Depending on the molecular weight, the organic HTMs can be divided into subclasses- small molecules and polymers. Organic *p*-type semiconducting polymers that have been used in optoelectronic devices are also suitable as HTM in PSCs (Figure 1.13). Among them, poly(3hexylthiophene-2,5-diyl) P3HT, poly(triarylamine) PTAA, poly(2,3dihydrothieno-1,4-dioxin)-poly(styrenesulfonate) PEDOT: PSS are more commonly reported. The important advantages of these polymers are scaleup synthesis, high thermo-mechanical stability, and intrinsic hole mobility. However, in some cases, there is a mismatch of band alignment with the perovskite layer that suppresses the efficient charge extraction and transfer, defects due to long-chain, which may lead to significant loss of open-circuit voltage and reproducibility in the device. The frequently used HTM employed in PSCs is Spiro-OMeTAD. However, it suffers from high costs due to challenging synthesis and purification steps. Moreover, it needs dopants and additives to improve its electrical properties for performance enhancement. Several dopants have been reported for Spiro-OMeTAD and other HTM.

# 1.4.3 Doping of hole-transporting materials in perovskite solar cells

To increase the carrier concentration of the organic HTMs, dopants and additives are being used (Figure 1.14 b) [57] to improve devices performance. The basic principle of doping is similar to inorganic materials, to generate several free charge carriers by adding electron acceptor or donor molecules and tuning the electronic properties. These external acceptor or electron

donor molecules are known as p-type (n-type) dopants to improve the electrical properties by removing or adding electrons from the matrix of the host organic semiconductor. Chemical p-type doping HTM can be defined as electron transfer from the highest occupied molecular orbital (HOMO) of a matrix of host HTM to the lowest unoccupied molecular orbital (LUMO) of a dopant molecule, thus leaving behind a mobile hole in the HOMO of the semiconductor.<sup>[58]</sup> Therefore, organic the *p*-doping in organic semiconductor-based HTM can occur only when the electron affinity of the dopant is equivalent or more significant than the ionisation potential of the host matrix, (Figure 1.14 a). [40, 59] As a result of p-type doping, electrical conductivity increases due to the further generation of free charge carrier concentration, shifting the Fermi level towards HOMO of the host HTM and minimizing the energy level mismatch [59] to reduce ohmic losses. [58, 60] Additionally, doping of organic semiconductors facilitates the charge carrier injection from electrodes to the doped molecules. It was noted that in PSCs, chemical doping of organic HTMs in a controlled amount tunes the energy level alignment at interfaces<sup>[61]</sup>, which facilitates improved charge carrier extraction and device voltage.

Various dopants have been developed and employed including 2,3,5,6-tetra-fluoro-7,7,8,8-tetracyanoquinodimethane (F4TCNQ), ionic liquids, silver(bis(tri- fluoromethanesulfonyl)imide) AgTFSI, benzoyl peroxide, copper(II) and cobalt(III) complexes. [62,63] Cobalt complex-based tris(2-(1H-pyrazol-1-yl)-4-tert-butylpyridine)cobalt(III) tri[bis(trifluoromethane) sulfonimide] (FK209), and lithium bis(tri-fluoromethanesulfonyl)imide (LiTFSI) with additivities of 4-tertbutylpyridine (t-BP) to improve the conductivity of Spiro-OMeTAD have been reported. LiTFSI favours the oxidation and t-BP molecules, prevents the aggregation of LiTFSI, and

improves its distribution, thus providing a better interface between the HTM and the perovskite layer. Recently, zinc bis(tri-fluoromethanesulfonyl)imide  $Zn(TFSI)_2$  has been used as a dopant that increases hole mobility and the long-term stability of the HTM. <sup>[64]</sup> The dopants used are hygroscopic and can cause instability to the devices through oxidation and ion migration that can accelerate the degradation of the perovskite layer.

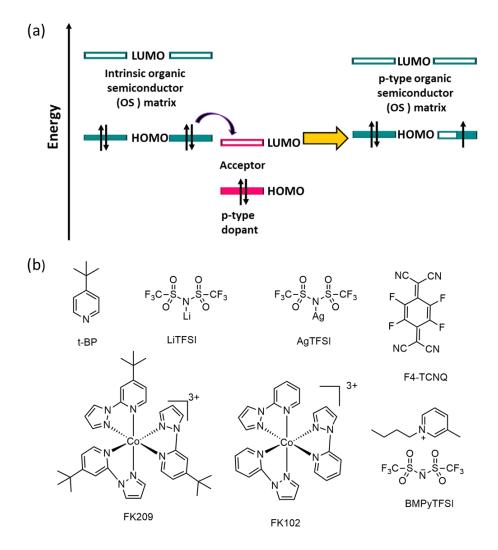


Figure 1.14: (a) Schematic energy-level diagram of an organic semiconductor's matrix: p-dopant molecule representing molecular p-doping in organic semiconductors.<sup>[40,59]</sup> Usually, electron transfer from the HOMO of the host matrix molecule to the LUMO of a dopant molecule assumes p-type doping (b) p-type dopants in HTMs.<sup>[58]</sup>

Furthermore, if the molecular dopants are not covalently linked to the organic HTMs, they may also diffuse. To overcome this, ionic liquid, 1-butyl-4-methylpyridiniumbis(trifluoromethanesulfonyl)imide [BMPyTFSI] was reported as hydrophobic dopants to substitute cobalt complex, LiTFSI and t-BP additive.[63] It increases the conductivity of Spiro-OMeTAD and reduces charge recombination at optimized concentration and demonstrated on par PCE, but with an extended lifetime.

# 1.5 Small-Organic molecules as HTMs

Small molecules have been the most explored p-type organic semiconductors used as hole conducting materials so far. Due to the aforementioned properties, various small molecules as HTMs are reported. Spiro-OMeTAD and PTAA represent the most used HTMs in PSCs. We divided them into parts depending on their molecular core and structure to provide an easy grasp of the properties.

# 1.5.1 Triarylamine-based HTMs

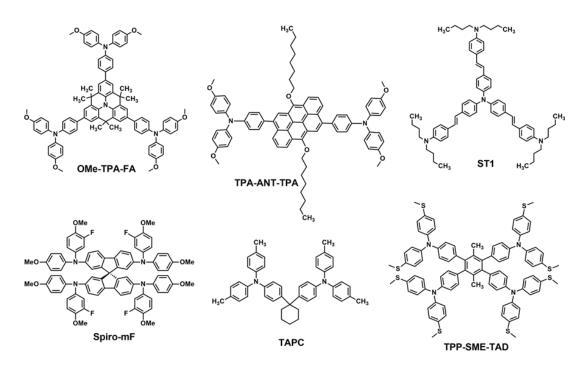


Figure 1.15: Chemical structure of triphenyl amine-based HTMs.

Triarylamine based HTMs have been extensively studied in different optoelectronic devices (OPV, DSSC, OLED) due to their efficient hole mobilities and conductivities. The facile synthesis and purification route and optoelectrical validate its application in PSCs. The central nitrogen atoms with three phenyl rings make it a propeller-like 3D structure with good electron donating and hole extraction ability. In addition, they possess a low-lying HOMO level that is appropriately aligned with the perovskite absorbers, along with effective hole extraction. Triarylamine-based compounds as building blocks or side groups in the HTMs have been reported in the past (Figure 1.15). Additionally, the non-planar geometry of the molecule in the solid-state influences the optoelectrical properties. In this section, only the most efficient TPA-based HTMs that have been primarily exploited in PSCs will be addressed. Ma et al. achieved a PCE of

10.4% with an open-circuit voltage ( $V_{oc}$ ) of 930 mV with a promising Spirothiophene (SCPDT-BiT) based molecule as an HTMs and was found to be promising due to the presence of the sulfur atoms as electron transfer group. [65] In another work, Choi et al. introduced TPA-MeOPh and FA-OMePh, two HTMs without the usage of any additive gave a PCEs of 7.45 and 9.18% respectively.[66] Later the same group developed OMeTPA-FA that showed an average PCE of 13.6% after adding the external dopants and dopants (LiTFSi, t-BP and FK209).<sup>[67]</sup> Star-shaped HTMs Z1011 and Z1013 were synthesised by Zhang et al. and their performance in PSCs with an average PCE of 12.4%, 15.4% and 16.3% was reported. [68, 69] These starshaped molecules have long branched arms and longer conjugated  $\pi$  bonds. Qin et al. have designed a low band gap HTM with triarylamine core, fused-F for PSC and reported a PCE of 12.8%.<sup>[70]</sup> Paek et al. developed FA-CN and TPA-CN using a star-shaped D- $\pi$ -A structure as stable (remarkable stability up to 500 hours) PSCs with a PCE of 18.9% and 17.55% respectively.[71] Yang et al. introduced another  $\pi$ -conjugated molecule, TAPC and achieved a PCE of 18.8%.<sup>[72]</sup> They explained that PCE increases due to thermal annealing, improving the surface crystallinity and enhancing the hole conductivity. The use of DFH was reported, and a remarkable PCE of 20.6% in an inverted (pi-n) PSCs was measured.[53] The authors noted that annealing the HTM at a specific temperature induces a preferential molecular organisation normal to the substrate and improved optical properties at 135°C. It was also explained that DFH could trigger the intermolecular C-H...O and C-H...π interactions between the neighbouring dioxane group, which helps transform amorphous DFH to polycrystalline dimers when heated above  $T_{\rm g}$ 120°C. Yip et al. reported TPE-S which showed excellent optoelectronic

properties and the HTM in all-inorganic based perovskite CsPbI<sub>2</sub>Br gave long term stability with a PCE of 15.4%.<sup>[73]</sup>

#### 1.5.2 Carbazole-based HTMs

Figure 1.16: Chemical structure of carbazole-based HTMs.

Carbazole based small molecules have been extensively exploited as the standard building blocks to synthesize HTMs so far. Carbazole is an electronrich heterocyclic aromatic compound with two phenyl rings fused on either side of the nitrogen-containing a five-membered ring. Their ease with synthetic variability, coupled with triphenylamine or other hetero-atombased conjugated moieties, explores their optoelectronic and electrical behavior that is favorable to be used as HTMs for PSCs (Figure 1.16). Carbazole has been extensively studied in organic solar cells as a donor unit coupled with different acceptor groups. (2-ethylhexyl)-9H-carbazole as core and N,N'-di-p-methylthiophenylamine, CMT as end groups with PCE of 13.05% ( $V_{\rm oc}$  of 1030 mV and  $J_{\rm sc}$  of 21.82%). They introduced methyl thiol groups in place of methoxy groups at the para position of the diphenylamine to lower the HOMO level of the molecule. Carbazole based HTM with suitable energy levels, high glass transition temperatures, high hole mobilities, PhCz-

4MeOTPA and BDT-4MeOTPA with PCE of 8.78% and 16.04% ( $V_{oc}$  of 1060 and 1080 mV;  $J_{sc}$  of 20.16 and 21.52 mA/cm<sup>2</sup> respectively) was reported.<sup>[75]</sup>

Figure 1.17: Chemical structure of triazatruxene-based HTMs.

#### 1.5.3 Triazatruxene-based HTMs

Triazatruxene (TAT) has been widely used as HTMs in PSCs, owing to its easy synthetic approach, delocalized  $\pi$ -system with reactive sites on the indole N atoms and benzene rings to tune the optoelectrical and morphological properties (Figure 1.17). TAT also has an electron-rich rigid planar molecular structure. The reactive sites allow more substitution to improve the material optoelectrical properties, as one benzene ring (delocalized electron) is connected to three indole rings. Ahmad and co-workers were the first to report TAT-based HTMs HMDI and HPDI, and their suitability were shown in PSCs. [76] The average PCEs measured to be 8.62% and 9.83%, respectively. However, when doped with the p-type dopants, the PCE of HPDI increased to 10.82%. Further modification of this molecule, by placing rational sidearms, a star-shaped planar triazatruxene based core with

thiophene based sidearms, KR321 has been reported and gave unparalleled PCE of over 19% with mixed perovskite composition.[77] The molecule possesses a face on the orientation that facilitates the charge transfer and thereby increasing the overall efficiency and stability of PSCs. Zhang et al. reported the use of pristine and doped TPDI as HTM, and a PCEs of 15.5% that showed high solubility, thermal stability and efficient hole mobility in PSCs.[65] Furthermore, vacuum-deposited TAT-based HTM named TBDI in p-in structured PSC was reported. A PCE of 7.3% was registered however by placing a thin layer of MoO<sub>3</sub> as a buffer layer, the PCE increases significantly to 14.83%.[78] Huang et al. reported Trux-OMe-TAD with C3h truxene core and planar and rigid geometry with a HOMO energy level of -5.28 eV that showed well-matched energetic levels with that of MAPbI<sub>3</sub> perovskite (-5.43eV).[79] It showed a high PCE of 18.6% and hole mobility of 10-3 cm<sup>2</sup>V-1s-<sup>1</sup> in a planar *p-i-n*-type PSCs. Recently, Grisorio and coworkers designed two new truxene based HTMs, Trux1 and Trux2, in typical and inverted structured PSCs.[80] The inverted structured PSCs showed a PCEs 13.4%. while the usual structure demonstrated 10.2%.

Figure 1.18: Chemical structure of thiophene-based HTMs.

# 1.5.4 Thiophene-based HTMs

Thiophene or polythiophene based small molecules organic semiconductors have been widely exploited in material chemistry (Figure 1.18). Thiophene embedded with sulfur as heteroatom is a five-membered aromatic ring representing the most investigated heterocyclic compounds with interesting electronic properties. The sulfur atom in thiophene is highly polarizable, facilitating electron donating properties and nonbonding interactions. Li et al. reported an electron-rich small molecule, H101, for PSCs.[81] They obtained an average PCE of 10.6% without using any dopant under AM1.5G solar simulation. Another molecule, KTM3, a novel 3,3'thiophene, was developed, which gave a PCE of 7.3%.[82] Various HTMs representing the acceptor-donor-acceptor type conjugated molecule such as M7-TFSI was reported, respectively.[83, 84] Such molecules shared benzodithiophene as the donor in their respective cores, and an average PCE of 17.4% was obtained. The HTM showed excellent higher hole mobility and conductivity without any additives, and the high PCE was attributed to a deep HOMO energy level. Star-shaped small molecules represent another notable building block used in optoelectrical devices. They have been widely used in organic light-emitting diodes (OLEDs). They possess the face on stacking on the surface, flat structure, extended delocalized  $\pi$ -system that allows further substitution to tune the optoelectrical properties. Recently, two donor-acceptor-donor based additive-free HTMs, MPA-BTI and MPA-BTTI, in an inverted planar system measured the highest PCE of 21.17% with reproducibility and long term stability.[85]

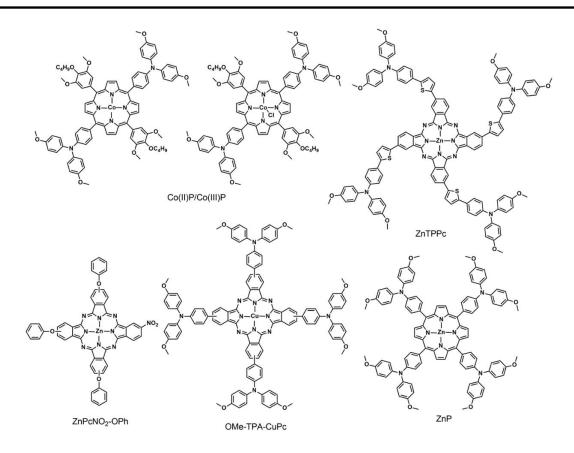


Figure 1.19: Chemical structure of metal-phthalocyanine based HTMs.

# 1.5.5 Organometallic compounds as HTMs

The organometallic compounds (Figure 1.19) with phthalocyanine or porphyrin cores are developed as dopant free HTMs. [86] The porphyrin cores are generally complexed with divalent metal cations such as Zn²+, Cu²+, Ni²+ and Co²+. Their optoelectronic properties can be tuned by modifying the metal centre and substituents on its periphery that could improve PV devices performances. A fully vacuum-processed planar PSCs with copper phthalocyanine (CuPc) as the HTM was reported. The champion device showed an overall PCE of 15.42%, and in addition, the encapsulated device maintained stability when stored in the dark under 20% humidity for 1000h.[87] Solution processable and cost-effective OMe-TPA-CuPc was reported by Feng et al. that showed the champion PCE of 19.67%. [88] A

nickel-based phthalocyanine derivative NiPc-(OBu)<sub>8</sub> with  $V_2O_5$  as the buffer layer was developed and delivered a PCE of 18.3%.<sup>[89]</sup> A Zn(II)-based ZnP as HTM in mesoscopic PSCs was reported with a PCE of 17.78%. <sup>[90]</sup> <sup>[91]</sup> Co(II)/Co(III) based mixed HTMs were introduced and afforded a PCE of 20.4% and high thermal stability at 85°C for 1000 h.<sup>[92]</sup>

Thus, one of the vital components of PSCs is the development of HTMs; among the organic molecules, the dopant free small molecules are being optimised to supersede the performance in terms of stability and efficiency. The main features of HTMs which need to be taken into account are high hole conductivity, low lying HOMO level located above the perovskite HOMO level, wide optical band gap ( $E_g$ ), LUMO with high enough energy level that blocks electron transfer at the interface of perovskite and HTM, uniform film-forming ability, effective molecular weight, solubility in orthogonal solvents and thermally and chemically stability, ease of functionalisation and  $\pi$ -conjugated bonds and low production cost. In some cases, the small molecules demand multi-step synthesis and low yield, influencing their price. It is beneficial to design planar molecules with a face-on orientation, which helps in better charge and exciton transport and allows more significant absorption strength when the transition dipole moment of the planar molecule (typically along its long axis) is aligned with the electric field of the incident light. A molecule that adopts face-on orientations enhances substrate-molecule and molecule-molecule interactions dominates interactions.

#### 1.6 Motivation and Outline of the Thesis

With the advancement of mankind towards technology, the demand for energy consumption is constantly increasing. The world needs another industrial revolution to easily access and afford sustainable energy sources. Research is mainly devoted to developing a potential means to implement renewable energy sources. Among all the renewable energy sources, solar energy is emerging as a forefront contender to generate electricity from environmentally friendly and sustainable energy technology. The current decade has witnessed landmark research progress in solar cells for solar energy conversion and various optoelectronics and is being discussed in the PV industries. Organic-inorganic halide perovskites have emerged as the competitive candidate for efficiently converting solar energy to electricity, with more than 25% power conversion efficiency. Perovskite solar cells (PSCs) emerged as the promising technology to meet the global energy need and is being widely explored. Research efforts have been delineated on optimising the different layers, including the perovskite absorber composition, hole transporting layer, electron transporting layer and selective contacts (Au, Ag, Cu) depending upon the architecture of the devices. Although PSCs have shown remarkable power conversion efficiency, the main challenge subsists in the solar cells' long-term stability, thus limiting its road towards industrialisation.

To endure the stability issue of the PSCs, various techniques have been imposed on the perovskite absorber by using multiple additives, moisture impermeable layers, molecularly engineered electron transport layers (ETLs) or hole transport layers (HTLs). Another phenomenal category involves the reduction of dimensionality to produce lower-dimensional

perovskites (layered perovskites), quasi layered, quasi-3D perovskites that can enhance the stability of PSCs.

To solve the challenges in PSCs, a bulk of work has been described in the thesis focussed on the design, synthesis and characterisation of small molecules as hole transporting material for perovskite solar cell application. Another essential part of the thesis comprises the work on the dimensionality reduction and interface engineering of the perovskite absorber layer for long-term stability purposes.

Thus, the general aim of the thesis is to study and investigate the molecularly designed hole-transporting materials (HTMs) and exploiting the large-size organic cation as an interface layer or doping to form reduced mixed-dimensional perovskite absorber for enhancing the overall performance and long-term stability of the PSCs.

Thus, the thesis work is divided into two parts, according to the aforementioned objective:

- (a) Developing small organic and organometallic compounds as molecularly engineered hole-transporting materials (HTMs) for perovskite solar cell application.
- (b) Implementing the large-size organic cation as an interfacial layer or doping to form dimensionality reduced mixed perovskite absorber for enhancing overall performance and the long-term stability of the perovskite solar cells.

The second chapter reports the synthesis of tetra-indole core (TTI) and a derivative of the TTI core. The tetra-indole core comprises an 8-annulene structure with four indole-moiety, which shows better charge transport properties. The TTI core is further derivatised containing fluorinated

methoxy engineered substituents that exhibited surface interaction with the perovskite layer resulting in efficient hole extraction and stability of the PSCs.

In the third chapter, a rapid and efficient synthesis of triazatruxene based HTMs is reported with fluorinated methoxy conjugated moieties. The HTMs are synthesised through a simple and inexpensive synthetic route with good yield compared to widely used spiro-OMeTAD. The devices based on the triazatruxene-based HTMs showed promising overall performance and improved stability of the PSCs.

In the fourth chapter, three different metal-phthalocyanines based dimers (ZnPc dimers) HTMs are discussed for the PSCs performance and stability. Phthalocyanines are known for their semi-conducting properties possessing excellent chemical and thermal stability. The molecular engineering of the ZnPc dimers can also form pinhole-free uniform films leading to good device performance. The improved efficiency of the PSC based on dimer ZnPc 3 of around 18.32% was obtained and showed long improved stability under ambient conditions such as moisture.

The fifth chapter discusses the formation of reduced mixed-dimensional perovskite by doping of 3-ammonium propionic acid iodide salt (3-APAI) and its interaction with the 3D perovskite layer. An array of measurements such as NMR, FTIR, XPS and XRD were conducted to study bonding interaction with the absorber layer. The overall PV performance was also recorded with stability.

The sixth chapter shows that polarization-modulated infrared reflectionabsorption spectroscopy (PM-IRRAS) can rapidly provide the necessary information on the interfacial layers formed by PEAI and FPEAI, which form

parallel and perpendicularly oriented monolayers and noted substantial differences in the orientation due to the presence of fluorine substitution. We hypothesise that the more robust van der Waals interactions due to the higher electronegativity in FPEAI govern the orientation.

The seventh chapter reported the halide (I/Br) exchange behaviour upon surface treatment of *N*-Bromosuccinimide (*NBS*) on the perovskite layer. Halide exchange occurs after deposition and during the thermal annealing process through oxidation of the solvent (isopropyl alcohol) by *NBS*. *NBS* induces oxidation of secondary alcohols is expected to release HBr, which assists in the crystallisation process of the perovskite to offer large size grain, lowers the grain boundaries, and further decreases the trap density through passivating the defects.

#### 1.7 References

- 1. A. P. Alivisatos, *Science*, **1996**, *271*, 933-937.
- 2. C. Eberspacher, J. Ermer, C. Fredric, C. Jensen, R. Gay, D. Pier, D. Willett and F. Karg, 1991.
- 3. I. Repins, M. A. Contreras, B. Egaas, C. DeHart, J. Scharf, C. L. Perkins, B. To and R. Noufi, *Prog Photovolt.*, **2008**, *16*, 235-239.
- 4. M. Grätzel, *J. Photochem. Photobiol. C: Photochem. Rev.*, **2003**, *4*, 145-153.
- 5. M. Green, K. Emery, Y. Hishikawa, W. Warta and E. Dunlop, *Prog. Photovolt: Res. Appl. 20, 12 (2012)*.
- 6. S. Kazim, M. K. Nazeeruddin, M. Grätzel and S. Ahmad, *Angew. Chem. Int. Ed.*, **2014**, *53*, 2812-2824.
- 7. A. Kojima, K. Teshima, Y. Shirai and T. Miyasaka, *J. Am. Chem. Soc*, **2009**, *131*, 6050-6051.
- 8. NREL, Research Cell Efficiency Record, 2022).
- 9. H.-S. Kim, C.-R. Lee, J.-H. Im, K.-B. Lee, T. Moehl, A. Marchioro, S.-J. Moon, R. Humphry-Baker, J.-H. Yum and J. E. Moser, *Sci. Rep.*, **2012**, *2*, 591.
- 10. T. Zhao, W. Shi, J. Xi, D. Wang and Z. Shuai, Sci. Rep., 2016, 6, 1-9.
- 11. Q. Dong, Y. Fang, Y. Shao, P. Mulligan, J. Qiu, L. Cao and J. Huang, *Science*, **2015**, *347*, 967-970.
- 12. T. J. Savenije, C. S. Ponseca Jr, L. Kunneman, M. Abdellah, K. Zheng, Y. Tian, Q. Zhu, S. E. Canton, I. G. Scheblykin and T. Pullerits, *J. Phys. Chem. Lett.*, **2014**, *5*, 2189-2194.
- 13. G. Niu, W. Li, F. Meng, L. Wang, H. Dong and Y. Qiu, *J. Mater. Chem. A*, **2014**, *2*, 705-710.

- 14. G. Divitini, S. Cacovich, F. Matteocci, L. Cinà, A. Di Carlo and C. Ducati, *Nat. Energy*, **2016**, *1*, 1-6.
- 15. T. Leijtens, G. E. Eperon, S. Pathak, A. Abate, M. M. Lee and H. J. Snaith, *Nat. Commun.*, **2013**, *4*, 1-8.
- D. Yang, R. Yang, X. Ren, X. Zhu, Z. Yang, C. Li and S. Liu, *Adv. Mater.*,
   2016, 28, 5206-5213.
- 17. L. Calio, M. Salado, S. Kazim and S. Ahmad, *Joule*, **2018**, *2*, 1800-1815.
- 18. P. Huang, S. Kazim, M. Wang and S. Ahmad, *ACS Energy Lett.*, **2019**, *4*, 2960-2974.
- 19. A. Krishna, S. Gottis, M. K. Nazeeruddin and F. Sauvage, *Adv. Funct. Mater.*, **2019**, *29*, 1806482.
- 20. F. Zhang, H. Lu, J. Tong, J. J. Berry, M. C. Beard and K. Zhu, *Energy Environ. Sci.*, **2020**, *13*, 1154-1186.
- 21. L. Mao, C. C. Stoumpos and M. G. Kanatzidis, *J. Am. Chem. Soc*, **2018**, *141*, 1171-1190.
- 22. M. Pegu, M. P. Haris, S. Kazim and S. Ahmad, *Emergent Mate.*, **2020**, *3*, 751-778.
- 23. G. Grancini and M. K. Nazeeruddin, Nat. Rev. Mater., 2019, 4, 4-22.
- 24. A. R. b. M. Yusoff and M. K. Nazeeruddin, *Adv. Energy Mater.*, **2018**, *8*, 1702073.
- 25. F. Zhang, D. H. Kim and K. Zhu, *Curr Opin Electrochem*, **2018**, *11*, 105-113.
- 26. N.-G. Park, *Mater. Today*, **2015**, *18*, 65-72.
- 27. M. Szafrański and A. Katrusiak, *Phys. Rev. B*, **2000**, *61*, 1026.
- 28. T. Hu, M. D. Smith, E. R. Dohner, M.-J. Sher, X. Wu, M. T. Trinh, A. Fisher, J. Corbett, X.-Y. Zhu and H. I. Karunadasa, *J. Phys. Chem. Lett.*, **2016**, *7*, 2258-2263.

- 29. B. Saparov and D. B. Mitzi, *Chem. Rev.*, **2016**, *116*, 4558-4596.
- 30. D. B. Mitzi, *Inorg. Chem.*, **2000**, *39*, 6107-6113.
- 31. G. Xing, N. Mathews, S. Sun, S. S. Lim, Y. M. Lam, M. Grätzel, S. Mhaisalkar and T. C. Sum, *Science*, **2013**, *342*, 344-347.
- 32. J. M. Ball, M. M. Lee, A. Hey and H. J. Snaith, *Energy Environ. Sci.*, **2013**, 6, 1739-1743.
- 33. J.-M. Cha, J.-W. Lee, D.-Y. Son, H.-S. Kim, I.-H. Jang and N.-G. Park, *Nanoscale*, **2016**, *8*, 6341-6351.
- 34. Q. Chen, H. Zhou, Z. Hong, S. Luo, H.-S. Duan, H.-H. Wang, Y. Liu, G. Li and Y. Yang, *J. Am. Chem. Soc.*, **2014**, *136*, 622-625.
- 35. M.-c. Kim, B. J. Kim, D.-Y. Son, N.-G. Park, H. S. Jung and M. Choi, *Nano Lett.*, **2016**, *16*, 5756-5763.
- 36. J. Zhao, Y. Li, H. Lin, Y. Liu, K. Jiang, C. Mu, T. Ma, J. Y. L. Lai, H. Hu and D. Yu, *Energy Environ. Sci.*, **2015**, *8*, 520-525.
- 37. G. Yang, H. Tao, P. Qin, W. Ke and G. Fang, *J. Mater. Chem. A* **2016**, *4*, 3970-3990.
- 38. H. Lu, A. Krishna, S. M. Zakeeruddin, M. Grätzel and A. Hagfeldt, *Iscience*, **2020**, *23*, 101359.
- 39. L. Calió, S. Kazim, M. Grätzel and S. Ahmad, *Angew. Chem. Int. Ed.*, **2016**, *55*, 14522-14545.
- 40. M. Pegu, S. Ahmad and S. Kazim, in *Perovskite Solar Cells*, 2021, DOI: https://doi.org/10.1002/9783527825790.ch10, pp. 331-367.
- 41. Y. Liu, H. Zhang, Y. Zhang, B. Xu, L. Liu, G. Chen, C. Im and W. Tian, *J. Mater. Chem. A*, **2018**, *6*, 7922-7932.
- 42. S. Wang, W. Yuan and Y. S. Meng, *ACS Appl. Mater. Interfaces.*, **2015**, *7*, 24791-24798.

- 43. W. Zhao, Q. Dong, J. Zhang, S. Wang, M. Chen, C. Zhao, M. Hu, S. Jin, N. P. Padture and Y. Shi, *J. Mater. Chem. A*, **2020**, *8*, 9919-9926.
- S. V. N. Pammi, V. D. Tran, R. Maddaka, J. H. Eom, J. S. Jung, H. M. Jeong,
   M. D. Kim, V. Pecunia and S. G. Yoon, *Adv. Opt. Mater.*, 2020, 8, 2000845.
- 45. A. Marchioro, J. Teuscher, D. Friedrich, M. Kunst, R. Van De Krol, T. Moehl, M. Grätzel and J.-E. Moser, *Nat. Photonics*, **2014**, *8*, 250.
- 46. A. Guerrero, G. Garcia-Belmonte, I. Mora-Sero, J. Bisquert, Y. S. Kang, T. J. Jacobsson, J.-P. Correa-Baena and A. Hagfeldt, *J. Phys. Chem. C*, **2016**, *120*, 8023-8032.
- 47. S. Shao and M. A. Loi, *Adv. Mate. Interfaces*, **2020**, *7*, 1901469.
- 48. W. Ke, G. Fang, J. Wan, H. Tao, Q. Liu, L. Xiong, P. Qin, J. Wang, H. Lei and G. Yang, *Nat. Commun.*, **2015**, *6*, 1-7.
- 49. T. He, S. Li, Y. Jiang, C. Qin, M. Cui, L. Qiao, H. Xu, J. Yang, R. Long and H. Wang, *Nat. Commun.*, **2020**, *11*, 1-11.
- 50. F. Gao, Y. Zhao, X. Zhang and J. You, *Adv. Energy Mater.*, **2020**, *10*, 1902650.
- 51. J. Y. Kim, J.-W. Lee, H. S. Jung, H. Shin and N.-G. Park, *Chem. Rev.*, **2020**, *120*, 7867-7918.
- 52. Z. a. Li, Z. Zhu, C.-C. Chueh, S. B. Jo, J. Luo, S.-H. Jang and A. K.-Y. Jen, *J. Am. Chem. Soc*, **2016**, *138*, 11833-11839.
- 53. Y. Cao, Y. Li, T. Morrissey, B. Lam, B. O. Patrick, D. J. Dvorak, Z. Xia, T. L. Kelly and C. P. Berlinguette, *Energy Environ. Sci.*, **2019**, *12*, 3502-3507.
- 54. J. Pople and D. Santry, *Mol. Phys.*, **1965**, *9*, 301-310.
- 55. V. Coropceanu, J. Cornil, D. A. da Silva Filho, Y. Olivier, R. Silbey and J.-L. Brédas, *Chem. Rev.*, **2007**, *107*, 926-952.
- 56. W. Dai, B. Zhang, Y. Kang, H. Chen, G. Zhong and Y. Li, *J. Phys. D: Appl. Phys*, **2013**, *46*, 385103.

- 57. I. Salzmann, G. Heimel, M. Oehzelt, S. Winkler and N. Koch, *Acc. Chem. Res.*, **2016**, *49*, 370-378.
- 58. A. Abate, T. Leijtens, S. Pathak, J. Teuscher, R. Avolio, M. E. Errico, J. Kirkpatrik, J. M. Ball, P. Docampo and I. McPherson, *Phys. Chem. Chem. Phys.*, **2013**, *15*, 2572-2579.
- 59. K. Walzer, B. Maennig, M. Pfeiffer and K. Leo, *Chem. Rev.*, **2007**, *107*, 1233-1271.
- 60. L. K. Ono, P. Schulz, J. J. Endres, G. O. Nikiforov, Y. Kato, A. Kahn and Y. Qi, *J. Phys. Chem. Lett.*, **2014**, *5*, 1374-1379.
- 61. X. Liu and X. Liu, *RSC Adv.*, **2019**, *9*, 24733-24741.
- 62. G. Gong, N. Zhao, J. Li, F. Li, J. Chen, Y. Shen, M. Wang and G. Tu, *Org. Electron.*, **2016**, *35*, 171-175.
- 63. B. Xu, J. Huang, H. Ågren, L. Kloo, A. Hagfeldt and L. Sun, *ChemSusChem*, **2014**, *7*, 3252-3256.
- 64. J.-Y. Seo, H.-S. Kim, S. Akin, M. Stojanovic, E. Simon, M. Fleischer, A. Hagfeldt, S. M. Zakeeruddin and M. Grätzel, *Energy Environ. Sci.*, **2018**, *11*, 2985-2992.
- 65. S. Ma, H. Zhang, N. Zhao, Y. Cheng, M. Wang, Y. Shen and G. Tu, *J. Mater. Chem. A* **2015**, *3*, 12139-12144.
- 66. H. Choi, S. Park, S. Paek, P. Ekanayake, M. K. Nazeeruddin and J. Ko, *J. Mater. Chem. A* **2014**, *2*, 19136-19140.
- 67. H. Choi, S. Paek, N. Lim, Y. H. Lee, M. K. Nazeeruddin and J. Ko, *Chem. Eur. J.*, **2014**, *20*, 10894-10899.
- 68. F. Zhang, C. Yi, P. Wei, X. Bi, J. Luo, G. Jacopin, S. Wang, X. Li, Y. Xiao and S. M. Zakeeruddin, *Adv. Energy Mater.*, **2016**, *6*, 1600401.
- 69. F. Zhang, X. Zhao, C. Yi, D. Bi, X. Bi, P. Wei, X. Liu, S. Wang, X. Li and S. M. Zakeeruddin, *Dyes Pigm.*, **2017**, *136*, 273-277.

- 70. P. Qin, S. Paek, M. I. Dar, N. Pellet, J. Ko, M. Grätzel and M. K. Nazeeruddin, *J. Am. Chem. Soc*, **2014**, *136*, 8516-8519.
- 71. S. Paek, P. Qin, Y. Lee, K. T. Cho, P. Gao, G. Grancini, E. Oveisi, P. Gratia, K. Rakstys and S. A. Al-Muhtaseb, *Adv. Mater.*, **2017**, *29*, 1606555.
- 72. L. Yang, F. Cai, Y. Yan, J. Li, D. Liu, A. J. Pearson and T. Wang, *Adv. Funct. Mater.*, **2017**, *27*, 1702613.
- 73. K. Jiang, J. Wang, F. Wu, Q. Xue, Q. Yao, J. Zhang, Y. Chen, G. Zhang, Z. Zhu and H. Yan, *Adv. Mater.*, **2020**, *32*, 1908011.
- 74. L. Xu, P. Huang, J. Zhang, X. Jia, Z. Ma, Y. Sun, Y. Zhou, N.-Y. Yuan and J.-N. Ding, *J. Phys. Chem. C*, **2017**, *121*, 21821-21826.
- 75. J. Qiu, H. Liu, X. Li, S. Wang and F. Zhang, *Sol. RRL*, **2019**, *3*, 1900202.
- 76. F. J. Ramos, K. Rakstys, S. Kazim, M. Grätzel, M. K. Nazeeruddin and S. Ahmad, *RSC Adv.*, **2015**, *5*, 53426-53432.
- 77. K. Rakstys, S. Paek, P. Gao, P. Gratia, T. Marszalek, G. Grancini, K. T. Cho, K. Genevicius, V. Jankauskas and W. Pisula, *J. Mater. Chem. A*, **2017**, *5*, 7811-7815.
- 78. L. Calió, C. Momblona, L. Gil-Escrig, S. Kazim, M. Sessolo, Á. Sastre-Santos, H. J. Bolink and S. Ahmad, *SoSol. Energy Mater Sol. Cells*, **2017**, *163*, 237-241.
- 79. C. Huang, W. Fu, C.-Z. Li, Z. Zhang, W. Qiu, M. Shi, P. Heremans, A. K.-Y. Jen and H. Chen, *J. Am. Chem. Soc*, **2016**, *138*, 2528-2531.
- 80. R. Grisorio, R. Iacobellis, A. Listorti, L. De Marco, M. P. Cipolla, M. Manca, A. Rizzo, A. Abate, G. Gigli and G. P. Suranna, *ACS Appl. Mater. Interfaces*, **2017**, *9*, 24778-24787.
- 81. H. Li, K. Fu, A. Hagfeldt, M. Grätzel, S. G. Mhaisalkar and A. C. Grimsdale, *Angew. Chem. Int. Ed.*, **2014**, *53*, 4085-4088.

- 82. T. Krishnamoorthy, F. Kunwu, P. P. Boix, H. Li, T. M. Koh, W. L. Leong, S. Powar, A. Grimsdale, M. Grätzel and N. Mathews, *J. Mater. Chem. A*, **2014**, *2*, 6305-6309.
- 83. M. Cheng, K. Aitola, C. Chen, F. Zhang, P. Liu, K. Sveinbjörnsson, Y. Hua, L. Kloo, G. Boschloo and L. Sun, *Nano Energy*, **2016**, *30*, 387-397.
- 84. M. Cheng, B. Xu, C. Chen, X. Yang, F. Zhang, Q. Tan, Y. Hua, L. Kloo and L. Sun, *Adv. Energy Mater.*, **2015**, *5*, 1401720.
- 85. Y. Wang, W. Chen, L. Wang, B. Tu, T. Chen, B. Liu, K. Yang, C. W. Koh, X. Zhang and H. Sun, *Adv. Mater.*, **2019**, *31*, 1902781.
- 86. T. Duong, J. Peng, D. Walter, J. Xiang, H. Shen, D. Chugh, M. Lockrey, D. Zhong, J. Li and K. Weber, *ACS Energy Lett.*, **2018**, *3*, 2441-2448.
- 87. W. Ke, D. Zhao, C. R. Grice, A. J. Cimaroli, G. Fang and Y. Yan, *J. Mater. Chem. A*, **2015**, *3*, 23888-23894.
- 88. Y. Feng, Q. Hu, E. Rezaee, M. Li, Z. X. Xu, A. Lorenzoni, F. Mercuri and M. Muccini, *Adv. Energy Mater.*, **2019**, *9*, 1901019.
- 89. M. Cheng, Y. Li, M. Safdari, C. Chen, P. Liu, L. Kloo and L. Sun, *Adv. Energy Mater.*, **2017**, *7*, 1602556.
- 90. S. Chen, P. Liu, Y. Hua, Y. Li, L. Kloo, X. Wang, B. Ong, W.-K. Wong and X. Zhu, *ACS Appl. Mater. Interfaces*, **2017**, *9*, 13231-13239.
- 91. P. Huang, A. Hernández, S. Kazim, J. Ortiz, Á. Sastre-Santos and S. Ahmad, *Sustain. Energy Fuels.*, **2020**, *4*, 6188-6195.
- 92. J. Cao, X. Lv, P. Zhang, T. T. Chuong, B. Wu, X. Feng, C. Shan, J. Liu and Y. Tang, *Adv. Mater.*, **2018**, *30*, 1800568.

### Chapter 2

Tetra-indole Core as Hole Selective Layer that Passivate Defect in Perovskite Solar Cells





We synthesized small molecules composed on tetra-indole core and introduced as hole selective layer in perovskite solar cells (PSCs) fabrication. 5,10,15,20-tetrahydrotriindole[2',3':4:2',3':5,6:2',3':7,8]cycloocta[1,2-(5aE,10aE,15aE,20aE)-N<sup>2</sup>,N<sup>7</sup>,N<sup>12</sup>,N<sup>18</sup>blindole (TTI) and a derivative tetrakis(2-fluoro-4-methoxyphenyl)-5,10,15,20-tetrahexyl-N<sup>2</sup>,N<sup>7</sup>,N<sup>12</sup>,N<sup>18</sup>tetrakis(4-methoxyphenyl)-5,10,15,20-tetrahydrocycloocta[1,2-b:3,4b':5,6-b":7,8-b"']tetraindole-2,7,12,18-tetraamine  $(MP-TTIF^{o})$ were integrated in PSCs. TTI showed passivation of the defects in perovskite by the non-radiative recombination suppressing photoluminescence and electrochemical impedance (EIS) measurements and gave improve photovoltaic performances. The PSCs based on TTI and MP-TTIF<sup>o</sup> showed a power conversion efficiency of 15.83% and 16.62 respectively, when employed as an hole transporting materials (HTMs). However, on passivating the interface of perovskite/HTL, the PCE largely improved to 19.23%. Additionally, the TTI treated device showed improved charge transfer behaviour and long-term stability when store in dark under ambient atmosphere.

A part of this chapter is based on published work: *M. Pegu et al. J. Mater. Chem. C,* **2021**, 9, 7074

**DOI**: https://doi.org/10.1039/D1TC01258D

#### **Content:**

2.1 Introduction50-53
2.2 Result and Discussion
2.2.1 Design and Synthesis54
2.2.2 Optical, thermal and DFT studies55-56
2.3 Electron paramagnetic resonance (EPR) spectroscopy56-59
2.4 Spectroscopy, morphology and diffraction measurements60-63
2.5 Photovoltaic properties of perovskite solar cells
2.6 Admittance spectroscopy measurements68-70
2.7 Stability measurements of thin films and PSCs71-73
2.8 Conclusions
2.9 References

#### 2.1 Introduction

Halide perovskite solar cells (PSCs) have attracted a surge in attention due to their outstanding performances in photovoltaics. Its low-cost solution fabrication technique, exciting photophysical properties, long carrier diffusion length, small exciton binding energy, and high power conversion efficiencies (PCE) through the device engineering.[1-5] So far, the certified PCE has reached over 25.5% has put PSCs on par with well-established photovoltaic technologies. These semiconducting materials could be viable alternatives to silicon-based counterparts and as competitive nextgeneration solar technology. [6] The impressive photovoltaic performances of PSCs benefit from the well-established device architecture engineering, modulating the perovskite composition, methods to grow high-quality perovskite, and choice of charge extraction materials led to the rapid development in PSCs.<sup>[7]</sup> To further boost the performances and reliability of PSCs, not only the development in the active layer is required but also the effective interfacial layers such as the hole transport layers and the electron transport lavers.[8, 9]

The device architecture of PSCs is divided mainly into three classes: mesoporous, or planar (n-i-p), and inverted planar (p-i-n) structure. Currently, the most efficient PSCs are mainly based on n-i-p architect, where n-type layer of mesoporous  $TiO_2/SnO_2$  and p-type layer of Spiro-OMeTAD (or PTAA) are used, together with mixed halide perovskite as light absorbers. The hole transport materials (HTM) play a critical role in PSCs as they not only enhance the device performances but also control the stability of the device by preventing moisture permeability into the perovskite layer. HTMs should possesses higher hole conductivity and

electron blocking properties.<sup>[14, 15]</sup> To date many HTMs have been developed for PSC applications based on small molecules, polymers, and inorganic materials.[16] Inorganic HTMs are promising candidates due to its robust nature and high stability, however, the PCE performance is limited by their surface defects, low intrinsic conductivity, poor solubility in common organic solvents, and particle size reproducibility.[17] Whereas, the polymers-based HTM display upright morphological properties but low stability and reproducibility, especially when the dopants are used.[18] Compared to the inorganic and polymeric counterparts, small molecules have been incredibly exploited due to several benefits, including high purity and solubility, promising yield, choice of molecular structure, and reproducibility. In addition, the interface properties between the perovskite and HTM play a trivial role in achieving high reliability in PSCs.[19-22] The interfacial property is dependent on the HTM layer, mainly due to the appropriate energy levels of their highest occupied molecular orbitals (HOMO) for band alignment.[23] So far, Spiro-OMeTAD has been considered a standard and widely used HTM in PSCs. The highly investigated Spiro-OMeTAD induce instability in the PSCs on addition of the hygroscopic dopants, which is a prerequisite, as pristine Spiro-OMeTAD does not possess the intrinsic charge carrier mobility and the post-oxidation of the HTM has an adverse effect on the perovskite layer.<sup>[24]</sup> Besides, the high material cost, from multi-step synthesis process escalate the future commercialization of PSCs.[25]

The aromatic hydrocarbon has become an important class of materials that are extensively studied owing to their unique optical and electronic behaviour.<sup>[26-28]</sup> These molecules are known to have wide applications in organic electronic devices such as organic field-effect transistors (OFETS),

organic light-emitting diodes (OLEDs), and photovoltaics organic development of new (OPVs). ENREF 10 The heterocyclic aromatic hydrocarbons with large  $\pi$ -extended systems has been extensively exploited as functional materials in organic electronics. Amidst the heterocycles, the indole based motifs are an important class of heteroatomic molecules<sup>[29-31]</sup> that was investigated as HTM, light harvesters, or emitters in the optoelectronic field, owing to their electrical and thermal merits.[32, 33] Among the various indole motifs, 10,15-dihydro-5H-diindolo[3,2-a:3',2'-c] carbazole (triindole or triazatruxene or TAT) was largely explored in solar cell applications. The first reports on the synthetic methodology of triazatruxene reported in 1980s.[34] The TAT based derivatives are widely utilized as organic semiconductors in various optoelectronic fields. Owing to easy modification of its photophysical and electrochemical properties with strong  $\pi$ - $\pi$  stacking and charge transport ability, these indole motifs have been extensively studied.[35] Additionally, the nitrogen atoms of indole moiety provide stability against oxidative doping from the atmospheric oxygen. Wang and co-workers showed the synthesis of triazatruxene compound, constituting of two or more indole units, fused with six membered benzene rings with an extended delocalized  $\pi$ -system with  $C_3$ symmetric conjugated structure.[36] It is composed of three indole rings linked to the central phenyl ring with extended  $\pi$ -system.

Cyclo-octatraene (COT) is another class of polycyclic aromatic compounds with a nonplanar saddle-shaped geometry consisting of  $8-\pi$  annulene as the structure. [37, 38]

Scheme 2.1: Synthesis of TTI and MP-TTIF<sup>o</sup>.

The advantageous property of COT-based system includes the structural coalescing with various several aromatics systems such as phenyl, thiophene, furan, pyrimidine, and thiazole.<sup>[36]</sup> To date the cyclic tetramer COT fused indole motif 5,10,15,20-tetrahydrotriindole[2',3':4:2',3':5,6:2',3':7,8]cycloocta[1,2-b]indole (TTI) have been known in literature,<sup>[39,40]</sup> however rarely studied. Plausibly, the synthesis route toil may be the cause behind the infrequent research.

#### 2.2 Result and Discussion

#### 2.2.1 Design and Synthesis

The structure and synthesis route of TTI is shown in Scheme 2.1 (a). The onepot synthesis of the tetra-indole moiety was carried out in POCl3 under a dry environment. However, the reaction of 2-oxindole in POCl<sub>3</sub> provides both triindole and tetra-indole as the products.<sup>[36]</sup> The tetra-indole compound was further derivatized with ortho-fluorinated methoxy-based substituents as  $(5aE,10aE,15aE,20aE)-N^2,N^7,N^{12},N^{18}-tetrakis(2-fluoro-4-methoxyphenyl)-$ 5,10,15,20-tetrahexyl-N<sup>2</sup>,N<sup>7</sup>,N<sup>12</sup>,N<sup>18</sup>-tetrakis(4-methoxyphenyl)-5,10,15,20tetrahydrocycloocta[1,2-b:3,4-b':5,6-b":7,8-b""]tetraindole-2,7,12,18tetraamine (MP-TTIF<sup>o</sup>) (Scheme 2.1 b, c). The intermolecular condensation of 2-oxindole in the presence of phosphorous oxychloride yielded TTI, followed by alkylation with an n-hexyl chain to yield 1. The alkylated TTI core 2 was brominated using N-bromo succinimide (NBS). Subsequently, Buchwald-Hartwig coupling reaction of **2** with ortho-substituted methoxy engineered diphenylamine moieties yielded the final HTMs MP-TTIF<sup>o</sup>. Both the product mixtures were purified and characterized by NMR ( $^{1}$ H and  $^{13}$ C) spectrometric analysis. The <sup>1</sup>H and <sup>13</sup>C spectral patterns and relative integrated values are consistent with the structure of TTI and MP-TTIFo. Both TTI and MP-TTIF<sup>o</sup> were readily soluble in dichloromethane (DCM), tetrahydrofuran (THF), and toluene.

#### 2.2.2 Optical, thermal and DFT studies.

Absorption of TTI and MP-TTIF° was recorded in solvents such as chlorobenzene, ethyl acetate, and a mixture of chlorobenzene and ethyl acetate (Figure 2.1 a). The absorption spectra in the solvents show a clear  $\pi$ -  $\pi$ \* transition peak at 312.8 nm and 327 nm for TTI and MP-TTIF° respectively.

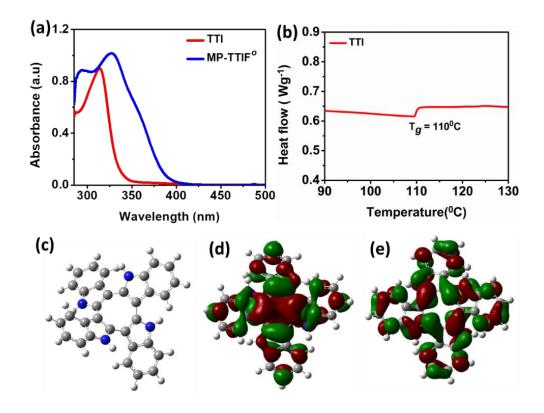


Figure 2.1: (a) UV-Visible absorption spectra of TTI in various solvents (b) DSC curve of TTI under  $N_2$  at a scanning rate of  $10^{\circ}$ C. (c) Optimized molecular conformation (d) HOMO and (e) LUMO of TTI calculated using Gaussian (B3LYP/631G (d)).

The differential scanning calorimetry (DSC) curve was recorded for TTI to measure the thermal stability. The DSC studies revealed a glass transition temperature ( $T_g$ ) at and a peak at 110°C (Figure 2.1 b). Thus, we can expect

that the tetra-indole moiety would offer thermal and morphological stability during the PSCs fabrication and operation. No distinctive transitions for crystallization and melting behaviour during the DSC scan from room temperature to 350°C were observed, suggesting TTI amorphous nature.

We performed the density functional theory (DFT) calculation to ascertain the electronic transition in TTI.<sup>[36]</sup> The highest occupied molecular orbital (HOMO) of -4.6 eV and the lowest unoccupied molecular orbital (LUMO) of -1.06 eV were obtained. The saddle shaped core of the tetra-indole derivative showed a twisted molecular structure (Figure 2.1 c), with a non-planarity because of strong steric hindrance. The HOMO as well as LUMO of TTI was found to be delocalized and loaded over the backbone of TTI (Figure 2.1 d, e). Overlap of the partial wave function between the two orbitals was noted, which indicates that the delocalization occurs at the tetra-indole core and this can be beneficial for the neutral exciton generation and hole transfer transitions. The HOMO and LUMO value suggest that TTI are suited as HTM for PSCs and further derivatization or doping of TTI could allow for improvement in the energy levels.

# 2.3 Electron paramagnetic resonance (EPR) spectroscopy

We performed electron paramagnetic resonance (EPR) spectroscopy experiments to compare the charge formation by doping and the mobility of the free radical cations on TTI with respect to that observed in Spiro-OMeTAD. The EPR measurements were carried out under similar conditions

with a concentration of 30 mM solutions of doped and undoped Spiro-OMeTAD and TTI (Figure 2.2 a).

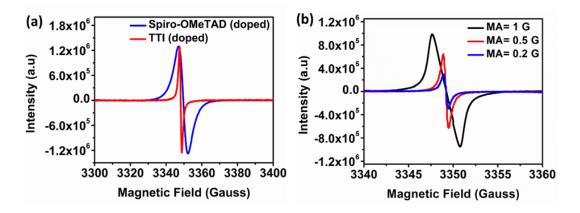


Figure 2.2: (a) EPR spectra registered on 30mM chlorobenzene solutions of doped Spiro-OMeTAD and TTI (b) Influence of the modulation amplitude of the applied field on the EPR signal of doped TTI.

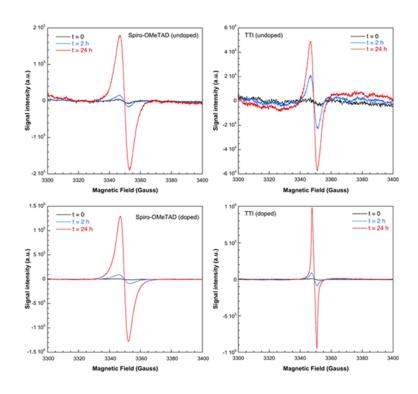


Figure 2.3. EPR spectra registered at room temperature on 30mM chlorobenzene solutions.

The undoped Spiro-OMeTAD solution shows a weak signal due to Spiro-OMeTAD+ species generated by natural oxidation.<sup>[41-43]</sup> In all cases, the intensity of the signals initially increases with time under illumination (Figure 2.3). However, the intensity of the signal starts to decrease after 24 hrs. With light exposure, a remarkable enhancement of the EPR signal was noted for the doped materials as compared to the undoped ones.

**Table 2.1** EPR spectral parameters for 30mM chlorobenzene solutions of doped and undoped spiro-OMeTAD and TTI

	g- factor	∆Bpp (Gauss)	Spin/mol	% Lorentz
Spiro-OMeTAD (undoped)	2.0034	6.1	9.8 x10 <sup>16</sup>	50 %
Spiro-OMeTAD (doped)	2.0033	4.7	1.3 x10 <sup>18</sup>	87 %
TTI (undoped)	2.0039	5.1	4.6 x10 <sup>16</sup>	92 %
TTI (doped)	2.0037	0.55	3.5 x10 <sup>17</sup>	100 %

The spectral parameters were deduced by a computer simulation program working at the second order of the perturbation theory (Table 2.1). For all the samples good fits were obtained considering the presence of only a type of free radicals. Therefore, the photo-generated radicals appear to be similar to those derived from exposure to oxygen or oxidation by the dopants, however, the photo-generation of radicals with a very short lifetime ( $<10^{-6}$  s) cannot be disregarded.[44] The values of the g-factor are not affected by the doping and are slightly higher for TTI samples indicating a higher orbital contribution which implies that the unpaired electron resides longer on the nitrogen atoms. But the most significant differences between both types of compounds are observed in the peak-to-peak linewidths. The signals

observed for the doped TTI is narrower than of an undoped sample or for the Spiro-OMeTAD solutions (c.a. 0.5 vs 5 Gauss). To detect the signal without distorting it, it was necessary to reduce the modulation amplitude of the EPR experiment to 0.2 G (Figure 2.2 b).

In this type of solution with free radicals, the linewidth of the EPR signal is mainly related to the density of the solvent (molecular movements), the concentration of the paramagnetic effects (exchange/dipolar intermolecular interactions), and the mobility of the spins. The peak-to-peak linewidth of the undoped Spiro-OMeTAD is 6.1 G, being 4.7 G than that of the doped sample. Similar peak narrowing in other Spiro-OMeTAD doped samples after light irradiation was reported. Lamberti et al attribute this behavior to the exchange narrowing derived from the increase of radical concentrations caused by both the irradiation and the dopants.[45] However, radical peak narrowing similar to doped TTI was only observed for a Spiro:LiTFSi:t-BP after 40 days of light exposure. This narrowing of peak accompanied by a change from Lorentzian to Gaussian profile of the EPR lines in Perovskite-Spiro-OMeTAD films was attributed to the formation of mobile holes by the light irradiation.<sup>[46]</sup> In the present case, the concentration of spins is higher in the doped Spiro-OMeTAD than in the doped TTI solution, therefore the narrowing of the signal cannot be attributed only to a fast intermolecular exchange. In addition, the fit of the doped TTI EPR signal has been achieved with a 100% Lorentzian line shape. Arguably, the doping of TTI favors the formation of mobile holes under light exposure.

# 2.4 Spectroscopy, morphology and diffraction measurements (UV-visisble, photoluminecence, surface and cross sectional SEM, XRD, XPS)

The photon absorption of the perovskite with HTMs profile shows similar behaviour (Figure 2.4 a). To investigate the charge extraction behaviour at the perovskite/HTM interface, we recorded the steady-state PL spectra of the perovskites (Figure 2.4 b). The PL peak of the perovskite (on the quartz) at 770 nm was significantly reformed after coating of TTI and quenching displayed a similar profile as of Spiro-OMeTAD. The small discrepancy, we ascribed to the higher valence band ( $E_{\rm HOMO}$ ) of TTI compared to Spiro-OMeTAD. The cross-sectional SEM image of the TTI- based PSC (Figure 2.4 c), shows the perovskite thickness between 450-500 nm, and that of 30 mM TTI had a thickness of 73 nm.

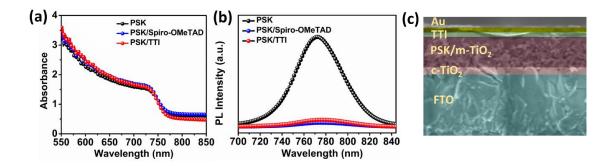


Figure 2.4: (a) UV-Visible absorption spectra, (b) Steady-state PL spectra of perovskite and perovskite/HTM treated films, (c) Cross-sectional SEM-image of the TTI based HTM fabricated device.

Arguably, the four -NH group with the electron pairs in the tetra-indole core of TTI can also act as Lewis bases and expectedly passivate the positively charged defects and trap states of the perovskite layer.<sup>[47]</sup> The strong

electron-donating ability of the -NH group in TTI can help in coordinating with the Pb<sup>2+</sup>, leading to Lewis-adduct formation, which can deactivate the charged defects on the surface of the perovskite layer.

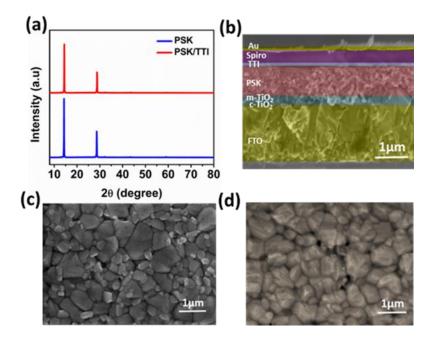


Figure 2.5: (a) X-ray diffraction patterns of the pure PSK and TTI treated thin films (b) Cross-sectional SEM-image of the 3 mg/mL TTI treated device; surface SEM images of (c) pure PSK (d) TTI treated thin films.

The passivation of the interfacial layer can also be advantageous in improving the charge extraction by the interface and readily lowering the non-radiative recombination in the PSCs.<sup>[48]</sup> The crystallinity of the perovskite upon the passivation by TTI was analysed by X-ray diffraction (XRD) measurement. We noted the diffraction peaks at 14.28°, 28.65° that is related to the (110) and (220) planes of the perovskite crystal (Figure 2.5 a). The XRD peaks after TTI treatment tends to slightly decrease; it could plausibly be due to the amorphous nature of the TTI passivated layer atop of the perovskite that supress the peak signal and its intensity. The cross-sectional SEM image of the TTI passivated device, along with the surface

images of the perovskites layer with and without TTI treated films are presented (Figure 2.5 b-d).

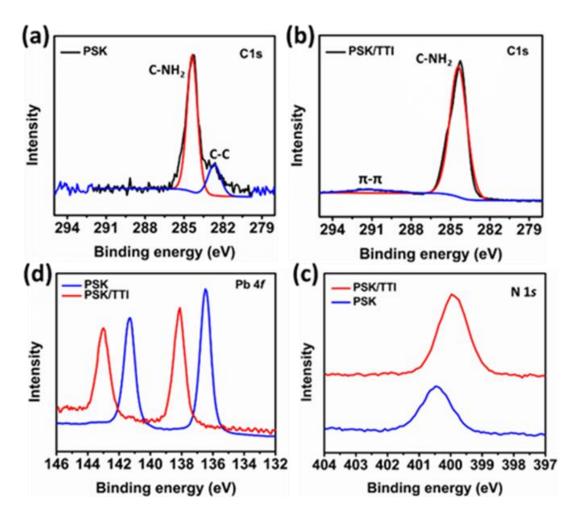


Figure 2.6: X-ray photoelectron spectroscopy (XPS), (a, b) high resolution deconvoluted spectra of C1s, (c) Pb 4f and d) N 1s, peaks of the PSK and TTI passivated perovskite films

To understand the coordination between TTI and perovskite, we performed X-ray photoelectron spectroscopy (XPS). The core-level peak of C1s spectra shows the presence of TTI on the surface of the perovskite layer (Figure 2.6 a, b).<sup>[49]</sup> The binding energy of Pb core electrons in Pb  $4f_{7/2}$  and Pb  $4f_{5/2}$  was shifted by 1.7 eV towards higher ionization potentials (Figure 2.6 c), which experimentally ascribes the formation of a covalent bond between TTI and

Pb atoms in the perovskite. Moreover, N 1s peak shifting and increase in the number of N atoms in the TTI treated perovskites, indicates the increment in electron cloud density of the lone pairs of N-atoms interacting with the Pb<sup>2+</sup> ions of the perovskite (Figure 2.6 d). The I 3d peak of the TTI treated thin film as well as the perovskite, shows the different binding energies of the organic structure on the surface of the perovskite.

## 2.5 Photovoltaic properties of perovskite solar cells

We measured the Hole mobility by fabricating a hole only device with the structure of FTO/PEDOT:PSS/HTM/Au. The hole mobility of TTI was measured using the space charge limit current model. By fitting the current density-voltage (J-V) curve, the mobility value was derived according to the Mott-Gurney equation (Figure 2.7 a). The undoped TTI showed higher mobility ( $4.4\times10^{-5}$  cm $^2$ V $^{-1}$ s $^{-1}$ ) than the undoped Spiro-OMeTAD ( $5.1\times10^{-5}$  cm $^2$ V $^{-1}$ s $^{-1}$ ) in our case. While we found the mobility of doped Spiro-OMeTAD ( $1.4\times10^{-4}$  cm $^2$ V $^{-1}$ s $^{-1}$ ) was higher than that of doped TTI ( $1.0\times10^{-5}$  cm $^2$ V $^{-1}$ s $^{-1}$ ). We also measured the conductivity in a sandwich configuration in FTO/HTM/Au. The conductivity of the undoped TTI was found to be 1.214 (uScm $^{-1}$ ) and the Spiro was 0.318 (uScm $^{-1}$ ) (Figure 2.7 b).

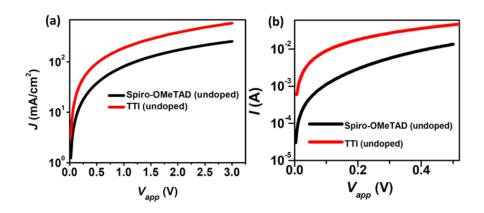


Figure 2.7: (a) Hole mobility measurements (device structure: FTO/PEDOT: PSS/HTM/Au.) (b) Conductivity measurements (device structure: FTO/HTM/Au); of the undoped TTI and Spiro-OMeTAD devices.

To evaluate TTI and MP-TTIF<sup>o</sup> as potential HTMs in PSCs, the MAPbI<sub>3</sub> based devices fabricated n-i-p configuration of FTO/blwere in mesoTiO<sub>2</sub>/CH<sub>3</sub>NH<sub>3</sub>PbI<sub>3</sub>/HTM. The current density-voltage curves for the *ni-p* based PSCs under the illumination of 100 mWcm<sup>-2</sup> AM 1.5G are shown in (Figure 2.8 a), while the corresponding photovoltaic parameters namely the short circuit current ( $I_{sc}$ ), open-circuit voltage ( $V_{oc}$ ), fill factor, and PCE are listed in Table 2.2. The PSCs fabricated with TTI exhibited a PCE of 15.8%.  $(J_{sc} = 20.82 \text{ mAcm}^{-2}, V_{oc} = 1003 \text{ mV}, FF = 75.72\%)$  with minimum hysteresis, while under similar condition, the Spiro-OMeTAD based device yielded a PCE of 17.22% ( $I_{sc}$ = 22.53 mAcm<sup>-2</sup>,  $V_{oc}$ = 1.014V, FF=75.37%). The device with TTI possessed similar  $V_{oc}$  and comparable FF values but lower  $I_{sc}$  values as compared to the standard Spiro-OMeTAD. We ascribe the marginally lower performance due to the mismatched energy levels and slow rate of charge extraction arising from lower hole mobility. The HOMO energy level (as calculated from DFT) of TTI is lower compared to the Spiro-OMeTAD, resulting in lower open circuit voltage, while the lower short circuit current is ascribed to the low hole mobility of doped TTI.

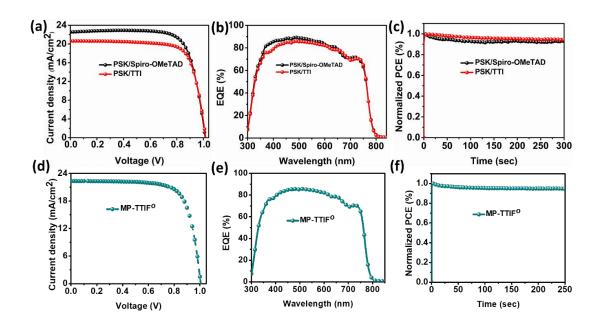


Figure 2.8: (a) Current density-voltage (*J-V*) characteristics of PSCs based on TTI and Spiro-OMeTAD, under Air-Mass (AM) 1.5G illumination on PSCs, (b) Corresponding EQE spectra of PSCs based on TTI and Spiro-OMeTAD, (c) The stabilized power output of the TTI and Spiro-OMeTAD based devices, (e) Current density-voltage (*J-V*) characteristics of PSCs based on MP-TTIF<sup>o</sup> under Air-Mass (AM) 1.5G illumination on PSCs, (f) Corresponding EQE spectra of PSCs based on MP-TTIF<sup>o</sup>, (g) The stabilized power output of MP-TTIF<sup>o</sup> based devices.

**Table 2.2:** PV properties

PSK/HTM	V <sub>oc</sub> (mV)	J <sub>sc</sub> (mA/cm <sup>2</sup> )	FF (%)	PCE (%)
PSK/Spiro	1014	22.53	75.37	17.22
PSK/TTI	1003	20.83	75.72	15.83
PSK/MP-TTIF <sup>o</sup>	1006	22.34	73.55	16.62
PSK/TTI/Spiro	1070	23.55	76.29	19.23

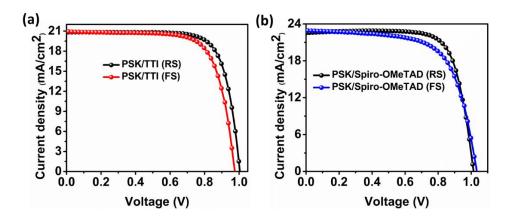


Figure 2.9: Current density-voltage curves characteristics of forward and reverse scans of PSCs based on (a) TTI, (b) with Spiro-OMeTAD, under Air-Mass (AM) 1.5G illumination.

The series resistance and shunt resistance for TTI based PSC showed a value of 42.28  $\Omega$  and 43.53 k $\Omega$  whereas for the Spiro-OMeTAD the value was 54.14  $\Omega$  and 85.22 k $\Omega$ . The overall device fabricated with TTI exhibited a PCE of 15.13%, which is slightly lower than that of the PSC with a state-of-art spiro-OMeTAD under the same conditions. The corresponding external quantum efficiency (EQE) was recorded (Figure 2.8 b) and illustrates photon to current response covering the broad spectrum from 300 – 800 nm. An onset of photocurrent generation is displayed in the EQE spectra, which is in agreement with the band gap of the perovskite. Expectedly, the device with TTI exhibits an EQE of around 80% which is slightly lower than that of Spiro-OMeTAD (around 85%), due to the lower  $I_{sc}$  value obtained. The steady-state output of TTI and Spiro-based PSCs for a short time (300 s) was evaluated and the TTI based PSCs were observed to be fairly stable as compared to the Spiro-OMeTAD (Figure 2.8 c). Notably, only 30 mM of TTI was employed as compared to 70 mM of Spiro-OMeTAD, which will further cut down the materials consumption and reduce the cost. The PV performance of the PSCs based on MP-TTIFo was also recorded (Figure 2.8 d). MP-TTIFo based PSC

exhibited a PCE of 16.62%. ( $J_{sc}$ = 22.34 mAcm<sup>-2</sup>,  $V_{oc}$ = 1006 mV, FF=73.55%). The corresponding EQE and steady-state output graphs are shown in Figure 2.8 e,f.

The hysteresis index (HI) was calculated by measuring the devices in both the forward scan (FS) and reverse scan (RS) direction (Figure 2.9 a, b). TTI based devices showed a low HI of 0.060 compared to Spiro-OMeTAD which is 0.084 due to its uniform surface morphology. The HI of the devices was calculated according to the equation:

$$HI = [J_{RS}(0.8 V_{oc}) - J_{FS}(0.8 V_{oc})] / J_{RS}(0.8 V_{oc})$$

The performance of the PSCs improved on treatment with TTI at the interface between perovskite and the hole selective layer. We fabricated the PSCs in *n-i-p* configuration: FTO/bl-mesoTiO<sub>2</sub>/PSK/TTI/Spiro-OMeTAD. The device architecture affords the effective transport of charges (Figure 2.10 a). The *J-V* curves with passivation (Figure 2.10 b) show improvement in the PCE. A superior PCE of 19.23% ( $V_{oc}$  = 1070 mV,  $J_{sc}$  = 23.55 mA/cm<sup>2</sup>, FF = 76.29%) was obtained upon TTI treatment (Table 2.2) as an interfacial layer. From the PSCs statistics, it is evident that the average values of the PV parameters improved upon TTI passivation (Figure 2.10 d-g). The increase in average  $V_{\rm oc}$  increases is attributed to the decreased non-radiative recombination and enhanced charge carrier lifetime. The average FF was improved from 75±4.26 to 76±1.58 due to better hole extraction and reduced density of traps. This, the overall PCE was improved from 17.64±1.12 to 19.23±0.42 with TTI treatment. In the EQE for the TTI treated and pristine PSCs (Figure 2.10 c), an onset of photocurrent generation was noted, and in the measured spectrum region, the PSCs with TTI passivation exhibits an improved EQE value.

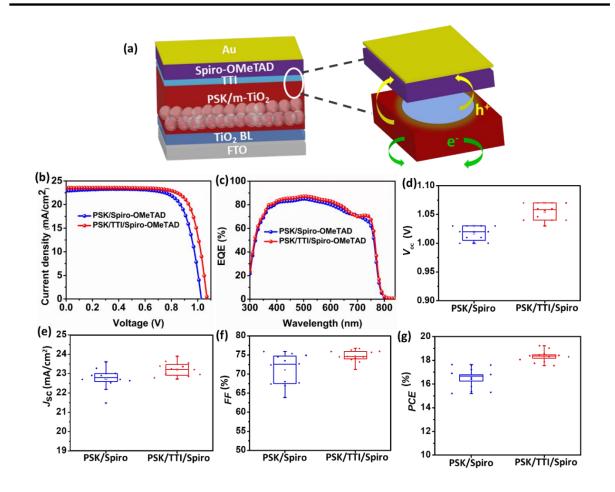


Figure 2.10: (a) Device architecture of TTI treated PSCs, (b) Current density-voltage curves of PSCs, under Air-Mass (AM) 1.5G illumination, (c) Corresponding EQE spectra. Statistics of devices (d)  $V_{oc}$  (e)  $I_{sc}$  (f) FF (g) PCE.

#### 2.6 Admittance spectroscopy measurements

The photo-carrier density increases in the photoactive layer in case of reduced non-radiative charge recombination. The quasi-Fermi-level splitting, in this case, is enhanced, which thereby increases the build-in-potential ( $V_{\rm bi}$ ) of the PSCs and subsequently, gives improved PCE. The Mott Schottky analysis made under dark conditions (Figure 2.11 a) of the TTI treated and pristine PSCs describing the build-in potential ( $V_{\rm bi}$ ) and

depletion layer width (W) was derived from C-2-V plot.<sup>[50, 51]</sup> An improved build-in potential of 740 mV for the TTI treated PSC was extracted at 10 kHz, while the pristine PSC gave a value of 734 mV. The calculated  $V_{\rm bi}$  value for TTI treated device is slightly higher as compared to the untreated one, which ascribes better charge extraction and high photocurrent. Additionally, with the increase in the build-in potential  $V_{\rm bi}$ , we calculated the depletion width (W) for pristine PSC and the TTI treated PSC ( $W = \sqrt{((2\mathcal{E}EoV_{bi})/qN)}$ ) where,  $\mathcal{E}$  is the dielectric constant,  $\mathcal{E}_0$  is the permittivity of the vacuum,  $V_{\rm bi}$  is the build-in potential, N is the density of fully ionized defects). The depletion layer width (W) was observed to be 168.51 nm for the pristine PSC, which increased to 198.55 nm for TTI treated device.

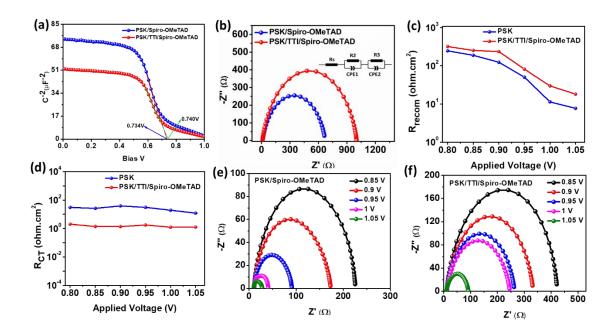


Figure 2.11: (a) Mott Schottky plot and (b) Nyquist plots for PSCs with and without TTI passivation, (c) charge transfer resistance at applied voltage for PSK and PSK/TTI passivation, (d) recombination resistance at applied voltage PSK and PSK/TTI passivated device. Nyquist plots for PSCs (e) pristine PSC (f) with TTI passivation at different voltages.

To further substantiate the passivation effects, the electrochemical impedance spectroscopic (EIS) analysis was performed (Figure 2.11 b), and the spectral analysis provide insight into the charge transfer and recombination behavior.<sup>[52, 53]</sup> We measured the Nyquist plots under dark conditions at 0.8V. We noted that the recombination resistance in the TTI treated PSC (larger semicircle) is higher as compared to the untreated one, The TTI passivation leads to larger recombination resistance and decipher its role in passivating the defects and is in accordance with the PL and spectroscopic measurements. The charge transfer resistance and recombination resistance as function of voltage (Figure 2.11 c, d) was derived from Nyquist plots (Figure 2.11 e, f), which display a single arc and the equivalent circuit model used is shown. The profile of the recombination resistance follows a similar trend and at voltage close to  $V_{\rm oc}$ , they display lower recombination, suggesting the key contribution of recombination processes are in the bulk of the perovskite material and does not arise at the interface. With the passivation of TTI, lower recombination resistance was noted, suggesting its use to suppress non-radiative recombination losses. Recombination resistance, near the  $V_{\rm oc}$ , is higher for TTI treated PSCs, pointing to a reduction in the non-radiative recombination defects. Furthermore, the charge transfer resistance was lower for TTI treated PSCs, which we ascribed to the filling of grain boundaries as well as defects passivation.

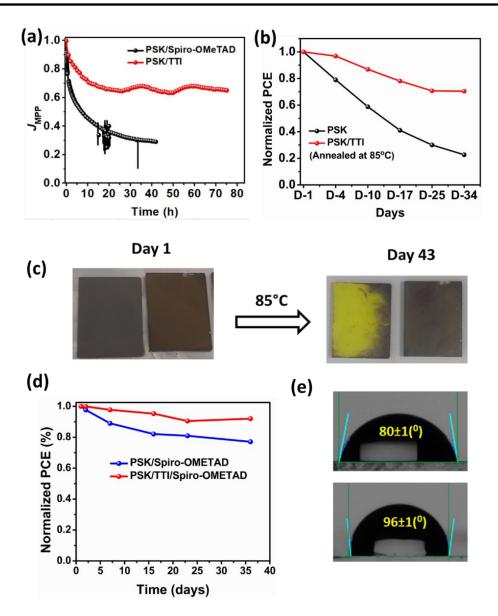


Figure 2.12: (a) Maximum power point tracking for the PSK and PSK/TTI HTM without encapsulation for around 80 h under illumination at ambient condition, (b) normalized efficiencies of the pristine and PSK/TTI HTM based PSCs under continuous annealing at 85°C at ambient atmospheric condition, (c)Thin films of PSK (top left; both sides) and PSK/TTI (top right; both sides) under thermal annealing and aging at 85°C at ambient atmospheric conditions, (d) comparison of device stability with and without TTI treatment and (e) contact angle measurements pure perovskites (top) and TTI treated (bottom) films.

### 2.7 Stability measurements of thin films and PSCs

The passivation of the perovskite layer by TTI is expected to enhance the stability of the PSCs. We evaluated the long-term moisture and thermal stability of the PSCs (Figure 2.12 a, b). It can be deduced from the figure, 70% of its initial PCE was retained for the TTI-based un-encapsulated device, kept under continuous illumination at 1 sun at room temperature with a relative humidity of 50-60% under 0.8V. Moreover, about 80% of its initial PCE value was retained for TTI based device upon thermal annealing at 85°C, demonstrating its superior thermal stability. We further investigated the impact of thermal and atmospheric stability of the pure perovskite and TTI treated perovskite (Figure 2.12c). We studied the long-term stability and measured the PCE with and without TTI treatment, periodically (stored in a dry box with 30-40% relative humidity at RT) for 36 days. The PCE values of the devices with TTI maintained about 90% of initial values whereas the device without TTI treatment retained only 77% of its initial values after 36 days (Figure 2.12d). The hydrophobicity induced by TTI can also be deduced by the contact angle measurement (Figure 2.12e), which showed a higher angle of 96° for TTI treated as compared to the pristine surface (80°), this will induce device stability. The optical absorbance spectra were recorded for the freshly prepared films with and without TTI treatment (Figure 2.13). The films were left for aging under continuous heating at 85°C (ambient atmosphere) and the absorbance spectra were recorded accordingly. The results indicate that the absorption onset of the TTI treated perovskite was retained and the dark color of the perovskite was also maintained, while the pure perovskite was noted to be degraded (yellow colored) upon continuous

annealing and exposure to the ambient atmospheric conditions. We can suggest, the TTI treated perovskite film showed excellent stability upon continuous exposure to relative humidity and heat.

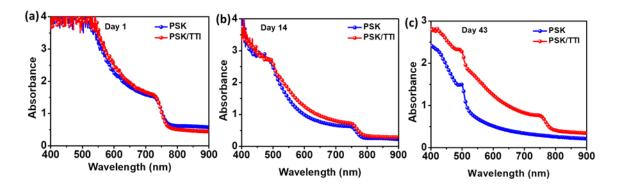


Figure 2.13: Stability measurement by absorption spectra pristine PSK and PSK/TTI passivated films under thermal annealing at 85°C (a) Day1 (b) Day 14 (c) Day 43

#### 2.8 Conclusions

We design a tetra-indole-based core as a small molecule (TTI and MP-TTIF<sup>o</sup>) and studied their hole transporting ability. TTI gave competitive performance when used as hole selective layers in perovskite solar cells, however, the photovoltaic performance further improved when used as passivating agent. A PCE of 19.23% was obtained when TTI was placed as an interfacial layer between perovskites and hole selective layers. Admittance spectroscopy suggests that TTI helped in reducing the defects, and noted a reduction in the non-radiative recombination. Furthermore. hydrophobic nature of TTI helped in enhancing the stability of the devices. We believe that further derivatization of the TTI core will accelerate its investigation as an effective hole transporting materials to rival the use of

Spiro-OMeTAD. Our approach suggests its dual functionality as hole transporting materials and complementing to improve the defects in the perovskite layer.

#### 2.9 References

- 1. A. Kojima, K. Teshima, Y. Shirai and T. Miyasaka, *J. Am. Chem. Soc*, **2009**, *131*, 6050-6051.
- J. M. Ball, M. M. Lee, A. Hey and H. J. Snaith, *Energy Environ. Sci.*, **2013**, 6, 1739-1743.
- 3. N. J. Jeon, J. H. Noh, W. S. Yang, Y. C. Kim, S. Ryu, J. Seo and S. I. Seok, *Nature*, **2015**, *517*, 476-480.
- 4. M. Grätzel, *Acc. Chem. Res.*, **2017**, *50*, 487-491.
- 5. T. Zhou, M. Wang, Z. Zang, X. Tang and L. Fang, *Sol. Energy Mater. Sol. Cells*, **2019**, *191*, 33-38.
- 6. N. NREL, Journal, 2020.
- 7. J. Y. Kim, J.-W. Lee, H. S. Jung, H. Shin and N.-G. Park, *Chem. Rev.*, **2020**, *120*, 7867-7918.
- 8. A. K. Jena, A. Kulkarni and T. Miyasaka, *Chem. Rev.*, **2019**, *119*, 3036-3103.
- 9. G. Xing, N. Mathews, S. Sun, S. S. Lim, Y. M. Lam, M. Grätzel, S. Mhaisalkar and T. C. Sum, *Science*, **2013**, *342*, 344-347.
- 10. Y. Zhao and K. Zhu, *Chem. Soc. Rev.*, **2016**, *45*, 655-689.
- 11. Z. Liu, A. Zhu, F. Cai, L. Tao, Y. Zhou, Z. Zhao, Q. Chen, Y.-B. Cheng and H. Zhou, *J. Mater. Chem. A* . **2017**, *5*, 6597-6605.
- 12. L. Calió, S. Kazim, M. Grätzel and S. Ahmad, *Angew. Chem. Int. Ed.*, **2016**, *55*, 14522-14545.
- 13. P. Huang, Manju, S. Kazim, G. Sivakumar, M. Salado, R. Misra and S. Ahmad, *ACS Appl. Mater. Interfaces*, **2020**, *12*, 22881-22890.
- 14. K. Rakstys, C. Igci and M. K. Nazeeruddin, *Chem. Sci.*, **2019**, *10*, 6748-6769.

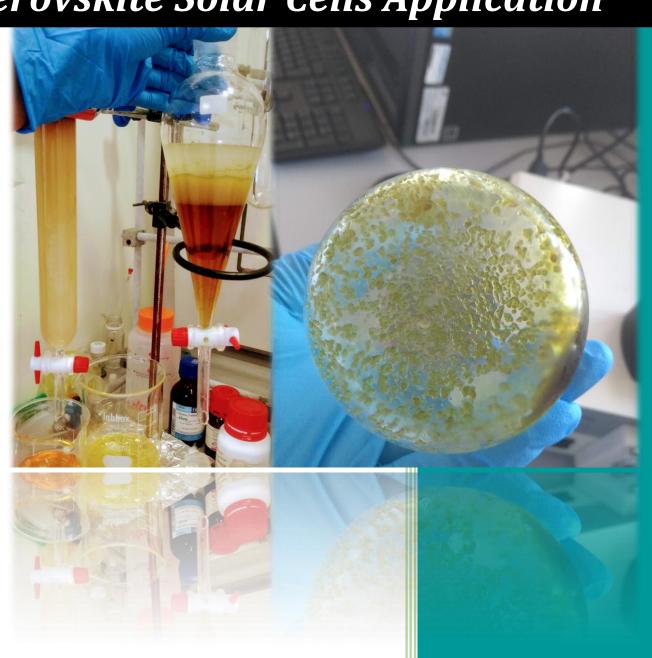
- 15. N. J. Jeon, H. Na, E. H. Jung, T.-Y. Yang, Y. G. Lee, G. Kim, H.-W. Shin, S. I. Seok, J. Lee and J. Seo, *Nat. Energy*, **2018**, *3*, 682-689.
- 16. J. Urieta-Mora, I. García-Benito, A. Molina-Ontoria and N. Martín, *Chem. Soc. Rev.*, **2018**, *47*, 8541-8571.
- 17. S. S. Mali, J. V. Patil, J. A. Steele, S. R. Rondiya, N. Y. Dzade and C. K. Hong, *ACS Energy Lett.*, **2021**, *6*, 778-788.
- 18. Q. Zhao, R. Wu, Z. Zhang, J. Xiong, Z. He, B. Fan, Z. Dai, B. Yang, X. Xue and P. Cai, *Org. Electron.*, **2019**, *71*, 106-112.
- 19. P. Huang, S. Kazim, M. Wang and S. Ahmad, *ACS Energy Lett.*, **2019**, *4*, 2960-2974.
- 20. W. Zhao, Q. Dong, J. Zhang, S. Wang, M. Chen, C. Zhao, M. Hu, S. Jin, N. P. Padture and Y. Shi, *J. Mater. Chem. A*, **2020**, *8*, 9919-9926.
- 21. Z. Zhou, S. Pang, Z. Liu, H. Xu and G. Cui, *J. Mater. Chem. A* **2015**, *3*, 19205-19217.
- 22. T. Zhou, M. Wang, Z. Zang and L. Fang, *Adv. Energy Mater.*, **2019**, *9*, 1900664.
- 23. M. Hao, W. Chi and Z. Li, *Nanoscale*, **2021**.
- 24. X. Yin, Z. Song, Z. Li and W. Tang, *Energy Environ. Sci.*, **2020**, *13*, 4057-4086.
- 25. N. Li, X. Niu, Q. Chen and H. Zhou, *Chem. Soc. Rev.*, **2020**.
- 26. P. T. Herwig and K. Müllen, *Adv. Mater.*, **1999**, *11*, 480-483.
- 27. Y.-J. Cheng, S.-H. Yang and C.-S. Hsu, *Chem. Rev.*, **2009**, *109*, 5868-5923.
- 28. S. Hashimoto, T. Ikuta, K. Shiren, S. Nakatsuka, J. Ni, M. Nakamura and T. Hatakeyama, *Chem. Mater.*, **2014**, *26*, 6265-6271.
- 29. S. Wakim, J. Bouchard, M. Simard, N. Drolet, Y. Tao and M. Leclerc, *Chem. Mater.*, **2004**, *16*, 4386-4388.

- 30. E. Wang, W. Mammo and M. R. Andersson, *Adv. Mater.*, **2014**, *26*, 1801-1826.
- 31. N. Wahlström, J. Slätt, B. Stensland, A. Ertan, J. Bergman and T. Janosik, *J. Org. Chem.*, **2007**, *72*, 5886-5889.
- 32. E. Wang, W. Mammo and M. R. Andersson, *Adv. Mater.*, **2014**, *26*, 1801-1826.
- 33. L. Gao, T. H. Schloemer, F. Zhang, X. Chen, C. Xiao, K. Zhu and A. Sellinger, *ACS Appl. Energy Mater.*, **2020**, *3*, 4492-4498.
- 34. J. Bergman and N. Eklund, *Tetrahedron*, **1980**, *36*, 1445-1450.
- 35. F. Wang, X.-C. Li, W.-Y. Lai, Y. Chen, W. Huang and F. Wudl, *Org. Lett.*, **2014**, *16*, 2942-2945.
- 36. F. Wang, X.-C. Li, W.-Y. Lai, Y. Chen, W. Huang and F. Wudl, *Org. Lett.*, **2014**, *16*, 2942-2945.
- 37. A. Matsuura and K. Komatsu, *J. Am. Chem. Soc.*, **2001**, *123*, 1768-1769.
- 38. H. Hiyoshi, T. Sonoda and S. Mataka, *Heterocycles*, **2006**, *68*, 763-769.
- 39. O. Talaz and N. Saracoglu, *Tetrahedron*, **2010**, *66*, 1902-1910.
- 40. M. Yurtsever and E. Yurtsever, *Polymer*, **2002**, *43*, 6019-6025.
- 41. A. Abate, D. J. Hollman, J. l. Teuscher, S. Pathak, R. Avolio, G. D'Errico, G. Vitiello, S. Fantacci and H. J. Snaith, *J. Am. Chem. Soc*, **2013**, *135*, 13538-13548.
- 42. G. Sathiyan, A. A. Syed, C. Chen, C. Wu, L. Tao, X. Ding, Y. Miao, G. Li, M. Cheng and L. Ding, *Nano Energy*, **2020**, *72*, 104673.
- 43. L.-L. Jiang, Z.-K. Wang, M. Li, C.-H. Li, P.-F. Fang and L.-S. Liao, *J. Mater. Chem. A* **2019**, *7*, 3655-3663.
- 44. T. Nagamori and K. Marumoto, *Adv. Mater.*, **2013**, *25*, 2362-2367.

- 45. F. Lamberti, T. Gatti, E. Cescon, R. Sorrentino, A. Rizzo, E. Menna, G. Meneghesso, M. Meneghetti, A. Petrozza and L. Franco, *Chem*, **2019**, *5*, 1806-1817.
- 46. M. Namatame, M. Yabusaki, T. Watanabe, Y. Ogomi, S. Hayase and K. Marumoto, *Appl. Phys. Lett.*, **2017**, *110*, 123904.
- 47. X. Liu, J. He, P. Wang, Y. Liu, J. Xiao, Z. Ku, Y. Peng, F. Huang, Y. B. Cheng and J. Zhong, *ChemSusChem*, **2019**, *12*, 2385-2392.
- 48. M. Salado, M. Andresini, P. Huang, M. T. Khan, F. Ciriaco, S. Kazim and S. Ahmad, *Adv. Funct. Mater.*, **2020**, *30*, 1910561.
- 49. Q. Zhou, L. Liang, J. Hu, B. Cao, L. Yang, T. Wu, X. Li, B. Zhang and P. Gao, *Adv. Energy Mater.*, **2019**, *9*, 1802595.
- 50. K. Jiang, J. Wang, F. Wu, Q. Xue, Q. Yao, J. Zhang, Y. Chen, G. Zhang, Z. Zhu and H. Yan, *Adv. Mater.*, **2020**, *32*, 1908011.
- 51. M. Pegu, S. Kazim, T. Buffeteau, D. M. Bassani and S. Ahmad, *ACS Appl. Energy Mater.*, **2021**.
- 52. M. T. Khan, P. Huang, A. Almohammedi, S. Kazim and S. Ahmad, *iScience*, **2021**, *24*, 102024.
- 53. S.-Y. Wang, C.-P. Chen, C.-L. Chung, C.-W. Hsu, H.-L. Hsu, T.-H. Wu, J.-Y. Zhuang, C.-J. Chang, H. M. Chen and Y. J. Chang, *ACS Appl. Mater. Interfaces*, **2019**, *11*, 40050-40061.

### Chapter 3

Implementing Fluorine Atoms in the Triazatruxene-based Holetransporting Materials for Perovskite Solar Cells Application



Triazatruxene based hole-transporting materials (HTMs) with fluorine substituted methoxydiphenylamine based small molecules are synthesized applied on perovskite solar cells (PSCs). The fluorineand methoxydiphenylamine in MP-TF<sup>m</sup> and MP-TF<sup>o</sup> are found to align the band energy level, hole extraction, and smooth film morphology that enables the subsequent growth of the perovskite layer. In addition, the MP-TF based HTMs showed higher glass transition temperature (~130 °C) that would enhance the shelf-life stability of the PSCs. The fluorination of HTMs leads to a strong interaction between the HTMs and the A and B site cations of the perovskite layer. The devices using meta-substituted fluorinemethoxydiphenylamine ( $MP-TF^m$ ) showed improved power conversion efficiency (PCE) of 18.72% than the ortho-substituted fluorinemethoxydiphenylamine based HTM (MP-TFo). Furthermore, the device with **MP-TF** gave improved stability and charge transport properties.

#### **Content:**

3.1. Introduction79-8
3.2 Results and discussion:
3.2.1 Synthesis of MP-TF HTMs82-83
3.2.2 Optical, electrical and DFT studies83-8
3.2.3 Ultraviolet photoelectron spectroscopy8
3.2.4 Surface morphology88-89
3.2.5 X-ray photoelectron spectroscopy89-9
3.2.6 Optoelectrical and diffraction analysis91-92
3.2.7 Photovoltaic characterization and admittance
spectroscopy92-9
3.3 Conclusion95-9
3.4 References

#### 3.1 Introduction

Hybrid perovskite solar cells (PSCs) have gained extensive research interest owing to their unique optoelectronic properties such as higher charge coefficient, higher charge mobility. absorption carrier processability, and low manufacturing cost.[1-4] ENREF 1 The power conversion efficiency (PCE) has reached >25%, a remarkable achievement in the last ten years.<sup>[5]</sup> Various architectures of PSCs have been developed. including mesoporous n-i-p, planar n-i-p and planar p-i-n structures. [6,7] The perovskite layer is sandwiched between the hole and electron transport layers in all these cases. The regularly used device architecture is the mesoporous n-i-p configuration. [8-10] The organic hole transport layer (HTL) 2,2',7.7'-tetrakis(N,N-di-p-methoxyphenylamine)-9,9'such as spirpbifluorene or Spiro-OMeTAD, poly(3-hexylthiophene-2,5-diyl) or P3HT and poly(triarylamine) or PTAA is layered on the perovskite top to extract holes and block electrons selectively.[11-13] Spiro-OMeTAD is the most influential and widely employed HTL, yielding a PCE of up to 25.17%.[14] However, the challenge remains to address Spiro-OMeTAD as the best choice of the hole transporting material (HTM); due to its high cost and low hole mobility in the undoped state.[15] Owing to their low hole mobility in the undoped state, incorporation of the hygroscopic dopants such LiTFSi and t-BP is highly required for Spiro-OMeTAD, which is detrimental to PSCs' durability.[16] As a result, developing a new strategy to improve device stability and cost-efficient processability is indispensable.

Fluorine atoms in organic semiconductors are widely employed as hydrophobic moieties to provide moisture resistance in PSCs.[17, 18] ENREF 17

Fluorine substitution in molecular design is also an effective strategy to tune the optoelectronic properties and film morphology, improving the photovoltaic performance of the PSCs.[18] Park et al. reported the fluorinated indolo[3,2]-indole derivative as HTL, which had a tightly stacked molecular arrangement and was employed in PSCs, demonstrating a satisfactory PCE of 19%.[19] Jeong et al. developed two fluorinated isomeric analogues of Spiro-OMeTAD that was beneficial for PSCs and featured a high PCE up to 24.82%.[20] Fluorination of small molecules possibly lowers the energy levels, enhances the PSCs' durability, and improves the molecular packing through the induced dipole moment along with the C-F bond.[20] Additionally, fluoride ion effectively passivates both the halide anion and organic cation vacancies by forming a strong ionic bond, chelating with Pb<sup>2+</sup> cations and strong hydrogen bonds (N-H...F) with the organic cations (MA/FA) of the perovskite layer. [21-23] Indolo-carbazole moiety termed as triazatruxene (TAT), is a versatile candidate used as HTM for PSCs.[24-26] The three nitrogen atoms as reactive sites in each indole ring and the fused benzene ring enable tuning the optical, electronic and morphological properties with wide synthetic variations. Furthermore, TAT possesses a planar molecular structure core which helps in inducing  $\pi$ - $\pi$  stacking for vertical hole transport and strong intermolecular interaction, showing higher charge carrier mobility.<sup>[27]</sup> In addition, the nitrogen atoms in the molecular core of TAT assist in stabilising the radical cation of the oxidised HTM formed during device operation.<sup>[28]</sup> Recently reported TAT-based dopant free HTMs - KR321 and CI-B reflected strong intermolecular charge transfer (ICT) with superior photovoltaic performance and long-term

stability of the PSCs.<sup>[27, 29]</sup> The existence of the Lewis base blocks effectively passivated the perovskite surface, thus reducing the defect states.

Considering the advantages of fluorinated atoms and TAT-based small molecules reported in the literature,[30-33] we opted to combine both and design a fluorinated diphenylamine-triazatruxene based HTM for PSC application. We developed two isomeric analogues N2,N7,N12-tris(3-fluoro-4-methoxyphenyl)-5,10,15-trihexyl-N2,N7,N12-tris(4-methoxyphenyl)-10,15-dihydro-5H-diindolo[3,2-a:3',2'-c]carbazole-2,7,12-triamine and N2,N7,N12-tris(2-fluoro-4-methoxyphenyl)-5,10,15-trihexyl-N2,N7,N12tris(4-methoxyphenyl)-10,15-dihydro-5H-diindolo[3,2-a:3',2'-c]carbazole-2,7,12-triamine (coded as  $MP-TF^m$  and  $MP-TF^o$ ) and measured the optoelectronic and photovoltaic performance. Notably, the fabricated devices showed improved photovoltaic performance and long-term device stability, outperforming Spiro-OMeTAD when measured under similar environmental conditions. We also investigated the charge transport properties through admittance spectroscopy measurements and noted improved electrical properties for TAT-based HTMs.

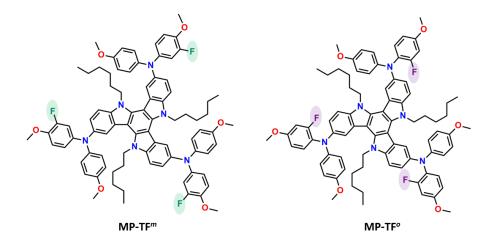


Figure 3.1: Molecular structure of MP-TF<sup>m</sup> and MP-TF<sup>o</sup>.

#### 3.2 Results and discussion:

#### 3.2.1 Synthesis of MP-TF HTMs

The molecular structure of the MP-TF<sup>m</sup> and MP-TF<sup>o</sup>, are depicted in Figure 3.1. The general synthetic route to prepare N<sup>2</sup>,N<sup>7</sup>,N<sup>12</sup>-tris(3-fluoro-4methoxyphenyl)-5,10,15-trihexyl-N<sup>2</sup>,N<sup>7</sup>,N<sup>12</sup>-tris(4-methoxyphenyl)-10,15dihydro-5H-diindolo[3,2-a:3',2'-c]carbazole-2,7,12-triamine (MP-TFm) and N<sup>2</sup>,N<sup>7</sup>,N<sup>12</sup>-tris(2-fluoro-4-methoxyphenyl)-5,10,15-trihexyl-N<sup>2</sup>,N<sup>7</sup>,N<sup>12</sup>-tris(4methoxyphenyl)-10,15-dihydro-5H-diindolo[3,2-a:3',2'-c]carbazole-2,7,12triamine (MP-TFo) is shown in Scheme 3.1 and detailed synthetic procedure provided in the supporting information. The intermolecular condensation of 2-oxindole in the presence of phosphorous oxychloride yielded triazatruxene (1), followed by alkylation with an n-hexyl chain to yield **2.** The alkylated planar TAT core **2** was brominated using *N*bromosuccinimide (NBS). Subsequently, Buchwald-Hartwig coupling reaction of 3 with meta-fluoro and ortho-fluoro substituted methoxy engineered diphenylamine moieties yielded the final HTMs MP-TF<sup>m</sup> and **MP-TF**<sup>o</sup>. The chemical structures of the synthesised precursors are verified by nuclear magnetic resonance (NMR) spectroscopy such as <sup>1</sup>H NMR. The final HTMs MP-TFm and MP-TFo are characterised with <sup>1</sup>H/<sup>13</sup>C NMR and matrix-assisted laser desorption/ionization-time of flight (MALDI-TOF) measurements. The characterised spectra (NMR, MALDI-TOF) of the synthesised precursors and final HTMs. All the final compounds are checked for solubility in common organic solvents and found soluble in DCM, THF, chloroform, chlorobenzene and toluene. The n-hexyl chain attached to the TAT-core contributes to its solubility in common organic solvents.

Scheme 3.1: Synthetic route for **MP-TF**<sup>m</sup> and **MP-TF**<sup>o</sup>, (i) Pd<sub>2</sub>dba<sub>3</sub>, P(t-bu)<sub>3</sub>HBF<sub>4</sub>, NaO<sup>t</sup>Bu, toluene (reflux) and (ii) Pd<sub>2</sub>dba<sub>3</sub>, P(t-bu)<sub>3</sub>HBF<sub>4</sub>, NaO<sup>t</sup>Bu, toluene (reflux).

#### 3.2.2 Optical, electrical and DFT studies

The normalised UV-visible absorption spectra of **MP-TF**<sup>m</sup> and **MP-TF**<sup>o</sup> in both solution and thin films are characterised and shown (Table1, Figure 2a-b). **MP-TF**<sup>m</sup> and **MP-TF**<sup>o</sup> exhibit characteristic absorption peaks in the spectral region between 280 nm-400 nm. The distinct absorption peaks at 339 nm for **MP-TF**<sup>m</sup> and 337 nm for **MP-TF**<sup>o</sup> are assigned to the  $\pi$ - $\pi$ \* electronic transitions of the conjugated system (Figure 3.2 a) and originate from the TAT-core to the outer methoxy-substituted phenyl; moieties. Notably, broad absorption bands in the visible region for the HTMs are assigned to the molecules' intermolecular charge transfer (ICT) transitions. Additionally, shoulder peaks at around 360 nm to 380 nm are observed that reflect the planar TAT-core's conjugated system and different conformations such system may undergo. In the thin films (Figure 3.2 b), the absorption

profile of **MP-TF**<sup>m</sup> and **MP-TF**<sup>o</sup> seems slightly red-shifted likely due to the formation of J-aggregation that is observed in many  $\pi$ -conjugated systems. The two HTMs exhibit almost identical curves (both in solution and solid-state), indicating the positions of F-atom substitution have a negligible effect on the conjugated backbone. The optical band gap ( $E_g^{\text{opt}}$ ) deduced from the edges of the solution state absorption spectra are found to be 3.19 eV and 3.18 eV for **MP-TF**<sup>m</sup> and **MP-TF**o.

To probe the thermal stability of the two HTMs, differential scanning calorimetry analysis (DSC) was performed. As shown in Table 3.1 and Figure 3.2 c-d, the DSC analysis reveals distinct thermal properties of the two HTMs. For  $MP-TF^o$ , a glass transition temperature (Tg) of 129°C is observed (Figure 2c), while for  $MP-TF^m$ , a Tg of 133°C is higher than that of the ortho-F counterpart is detected (Figure 2d). Higher thermal stability of  $MP-TF^m$  is essential during the fabrication and for the shelf-life stability of the PSCs.

**Table 3.1** Optical and electrochemical parameters of MP-TF<sup>m</sup> and MP-TF<sup>o</sup>

нтм	λ <sub>abs/so</sub>	$\lambda_{abs/}$	$E_{\text{ox}1}$	$E_{\mathrm{g}}$	НОМОс	LUM	Tg	μ	σ
	lution	solid	(eV)	EC <sup>b</sup>	CV/DFT	Od	(°C	(10-4	(µScm-
	(nm)	(nm				CV/D	)	cm <sup>2</sup> V <sup>-1</sup> s <sup>-1</sup> )	1)
	a	<b>)</b> b				FT			
MP-TF <sup>m</sup>	339/	342	0.11	3.19	-5.11/-	-	13	1.18	0.65
	362	/36			4.43	1.92/	3		
		4				-0.64			
MP-TFo	337/	339	0.08	3.18	-5.08/-	-	12	1.13	0.73
	360	/36			4.30	1.90/	9		
		3				-0.45			

a,bAbsorption spectra were measured in DCM solution and quartz thin films.  $E_a^{\text{opt}}$  was calculated frm the absorbtion onset.

 $<sup>^{</sup>d}E_{LUMO, CV} = E_{HOMO} + E_{g}^{opt}$ 

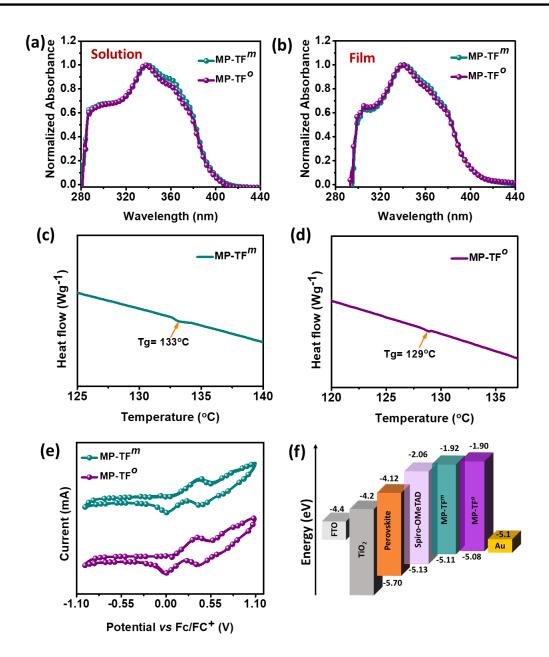


Figure 3.2: UV-Visible normalised spectra of **MP-TF** (a) DCM solution, 10<sup>-5</sup> M concentration, (b) thin films, 30 mM concentration, (c) CV spectra of MP-TF in DCM solution (d) energy level alignment in n-i-p configuration in PSC.

The electrochemical properties of MP-TF<sup>m</sup> and MP-TF<sup>o</sup> were estimated using cyclic voltammetry (CV) measurements with a standard three-electrode configuration and Fc/Fc<sup>+</sup> as an external reference in DCM solutions. The CV curves are represented in Figure 3.2e, and the related

experimental details are summarised in Table 3.1. The highest occupied molecular orbital (HOMO) level from the oxidation onset potentials ( $E^{\text{ox}}_{\text{onset}}$ ) is 5.11eV and -5.08 eV for **MP-TF**<sup>m</sup> and **MP-TF**<sup>o</sup>, respectively. The corresponding lowest unoccupied molecular orbital (LUMO) energy levels -1.92 eV and -1.90 eV are estimated according to their HOMO energy level and  $E_g^{\text{opt}}$ . The calculated HOMO/LUMO levels evidence that **MP-TF**<sup>m</sup> and **MP-TF**o can extract holes from the perovskite layer and block electrons. The band alignment diagram concerning the perovskite and hole transport layer is depicted in Figure 3.2f.

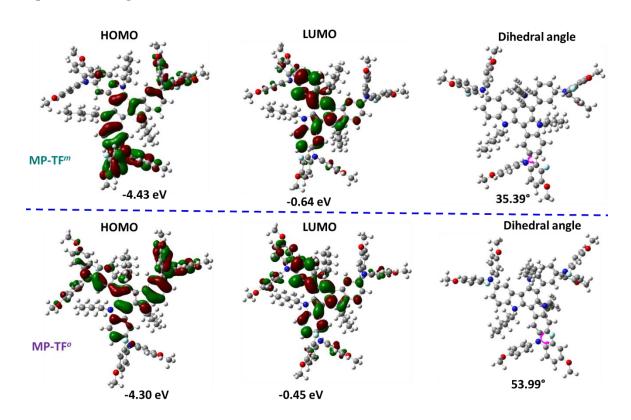


Figure 3.3: Density functional theory (DFT) calculation of HOMO, LUMO and dihedral angle for **MP-TF**<sup>m</sup> and **MP-TF**<sup>o</sup>.

We investigated the molecular geometries of the HTMs, the frontier molecular orbital distribution and the optimised geometry through the

density functional theory (DFT) using gaussian software at B3LYP/6-31G (p) as the basis set. Figure 3.3 shows the highest occupied molecular orbital (HOMO), lowest unoccupied molecular orbital (LUMO) and the dihedral angle of the optimised structures of HTMs **MP-TF**<sup>m</sup> and **MP-TF**<sup>o</sup>. The electron densities of the HOMO level for both the HTMs have mainly been localised on the triazatruxene core, and the two of the fluoro-substituted methoxy engineered diphenylamine moieties, while the LUMO is slightly spread over similarly as the HOMO electron densities. The HOMO and LUMO are well separated, and the calculated HOMO and LUMO energy levels are 4.43 eV and -0.64 eV for **MP-TF**<sup>m</sup> and -4.30 eV and -0.45 eV for **MP-TF**<sup>o</sup>. Furthermore, the dihedral angle calculated for **MP-TF**<sup>m</sup> (35.39°) shows more planarity than MP-**TF**<sup>o</sup> (53.99°), promoting better charge transport at the interface of perovskite and hole transporting layer.

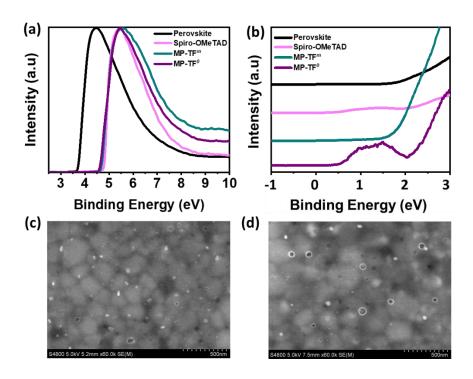


Figure 3.4: (a, b) UPS spectra of PSK, PSK/Spiro, PSK/**MP-TF**<sup>m</sup>, PSK/**MP-TF**<sup>o</sup>. Surface SEM image (c) PSK/**MP-TF**<sup>m</sup>, (d) PSK/**MP-TF**<sup>o</sup>.

#### 3.2.3 Ultraviolet photoelectron spectroscopy

To probe the band alignment between the absorbing material and the **MP-TF** based HTMs, we performed ultraviolet photoelectron spectroscopy (**UPS**) measurements of the perovskite and perovskite/HTL films. The work function and the valence band spectra of the perovskite and perovskite/HTL samples are depicted in Figure 3.4 a,b. The  $E_{\text{HOMO}}$  values of the doped Spiro-OMeTAD, **MP-TF**<sup>m</sup> and **MP-TF** $^{o}$  were measured and as displayed (Table 3.2), were to be 5.29 eV, 5.20 eV and 5.18 eV. The results of the doped Spiro-OMeTAD match with other reports. As compared to the valence band maxima of the perovskite (5.70 eV), the energy offset at the interface between perovskite/MP-TF is slightly higher compared to the interface between the perovskite/Spiro-OMeTAD layer.

Table 3.2 UPS measurements of MP-TFm and MP-TFo

Sample Name	WF	VB	IP
Perovskite	3.94	1.76	5.70
Spiro-OMeTAD	4.69	0.60	5.29
MP-TF <sup>m</sup>	4.65	0.55	5.20
MP-TFo	4.57	0.61	5.18

#### 3.2.4 Surface morphology

The surface morphology was investigated using scanning electron microscopy (SEM) measurements (Figure 3.4 c,d). Nevertheless, it is known that a uniform film formation of the perovskite/HTL influences the charge transfer and recombination phenomenon at the interface. In the figure, **MP-TF**<sup>m</sup> and **MP-TF**<sup>o</sup> display the formation of a homogeneous layer, while **MP-**

**TF**<sup>0</sup> shows blurred grain boundaries and **MP-TF**<sup>m</sup> showed a textured and better film coverage than **MP-TF**<sup>0</sup> on the surface of the perovskite layer, which could influence the photovoltaic performance of the PSCs.

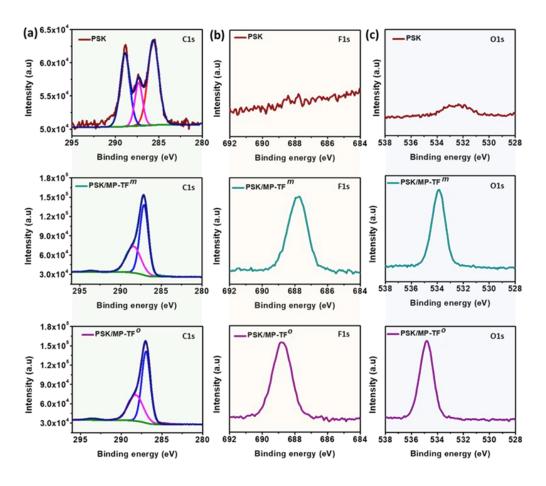


Figure 3.5: XPS spectra of PSK, PSK/MP-TFm, PSK/MP-TFo (a) C1s (b) F1s (c) O1s.

#### 3.2.5 X-ray photoelectron (XPS) spectroscopy

To characterise the elemental distribution and chemical environments in the perovskite films with **MP-TF**<sup>m</sup> and **MP-TF**<sup>o</sup> on the surface, we performed the X-ray photoelectron spectroscopy (XPS) measurements. The binding energies of the surface elements are shown in Figure 3.5. The C1s spectra of the perovskite layer have strong binding energy peaks at 288.86 and 287.32

eV, attributed to the FA and MA components of the perovskite (Figure 3.5a). The peak at 293.4 eV confirms the presence of conjugated **MP-TF** moiety on the surface of the perovskite layer. The strong intensity peak of F-atom presents in the **MP-TF**<sup>m</sup> and **MP-TF**<sup>o</sup> confirms the existence of the HTMs on the perovskite surface (Figure 3.5b). We noted a gradual peak shift iof 0.98 eV (687.82 eV to 688.80 eV) towards higher energy in the case of **MP-TF**<sup>o</sup>, which is influenced by the position of the fluorine atoms (meta and ortho) that lies in the vicinity of the nitrogen atoms. Furthermore, the presence of oxygen atoms from the methoxy groups of the **MP-TF** moieties is reflected by the binding energy peaks of O1s spectra for **MP-TF**<sup>m</sup> and **MP-TF**<sup>o</sup> 533.17 eV and 534.82 eV respectively, as depicted in Figure 3.5c.

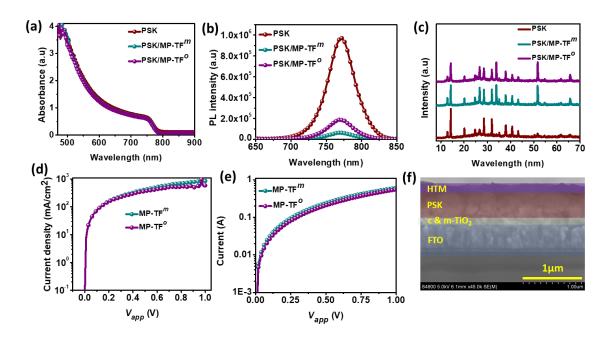


Figure 3.6: (a) UV-visible absorption spectra of PSK, PSK/MP-TF<sup>m</sup>, PSK/MP-TF<sup>o</sup>, (b) photoluminescence PL, spectra of PSK, PSK/MP-TF<sup>m</sup>, PSK/MP-TF<sup>o</sup>, (c) XRD spectra of PSK, PSK/MP-TF<sup>m</sup>, PSK/MP-TF<sup>o</sup>, (d) SCLC hole mobility measurements of MP-TF<sup>m</sup> and MP-TF<sup>o</sup> based devices, (e) conductivity measurements of MP-TF<sup>m</sup> and MP-TF<sup>o</sup> based devices, (f) cross-sectional SEM image of MP-TF<sup>m</sup>.

#### 3.2.6 Optoelectrical and diffraction analysis

The effects of  $MP-TF^m$  and  $MP-TF^o$  on the optical and charge transfer properties of the perovskite thin films are carefully investigated by an array of measurements. The UV-Visible spectroscopy was conducted to examine the light-harvesting changes among the perovskite and perovskite/HTL films (Figure 3.6a). The photon absorption of the perovskite with **MP-TF**<sup>m</sup> and MP-TF<sup>o</sup> shows a similar profile and remains unchanged. The charge extraction obtained from transfer and were the steady-state photoluminescence (PL) spectra (Figure 3.6b). The perovskite films with **MP-TF** exhibit higher PL quenching behaviour and is more pronounced for  $\mathbf{MP}$ - $\mathbf{TF}^m$  perovskite film. This indicates that  $\mathbf{MP}$ - $\mathbf{TF}^m$  has a more efficient hole extraction ability between the perovskite/HTL interface than MP-TFo. The results are concurrent with the steady-state PL measurements. The Xray diffraction (XRD) analysis shows the lower perovskite peak intensity at 14.5° of the perovskite/HTL films, stipulating the presence of top **MP-TF** small molecules as HTM layers. (Figure 3.6c).

The hole mobilities of the doped **MP-TF**<sup>m</sup> **and MP-TF**<sup>o</sup> are investigated based on the space charge-limited current (SCLC) with the device configuration FTO/PEDOT: PSS/HTM/Au (Figure 3.6d). The hole mobilities of are **MP-TF**<sup>o</sup> **and MP-TF**<sup>o</sup> found to be 1.18 x 10<sup>-4</sup> cm<sup>2</sup>V<sup>-1</sup>s<sup>-1</sup> and be 1.13 x 10<sup>-4</sup> cm<sup>2</sup>V<sup>-1</sup>s<sup>-1</sup>, respectively. The conductivity measurements were carried out with the device configuration FTO/HTM/Au (Figure 3.7e). The conductivity values obtained are 0.65 and 0.73  $\mu$ Scm<sup>-1</sup>, which are comparable. The cross-sectional SEM image of the film based on **MP-TF**<sup>o</sup> is depicted in Figure 3.6f,

and the corresponding values obtained for the ETM, perovskite and HTM layers are 143, 403 nm, and 119.6 nm, respectively.

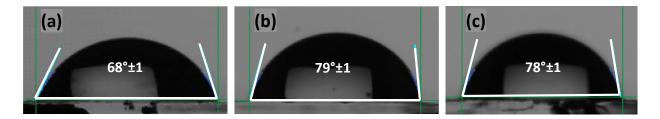


Figure 3.8: Contact angle measurement of (a) PSK, (b) PSK/**MP-TF**<sup>m</sup>, (c) PSK/**MP-TF**<sup>o</sup>.

The contact angle measurement was performed to evaluate the hydrophobicity induced by F-atoms. The contact angle measurement reveals that the perovskite layer has an angle of 68°, while for **MP-TF**<sup>m</sup> **and MP-TF**<sup>o</sup>, the contact angle values were 79° and 78° respectively° (Figure 3.8). The higher values for the fluorine substituted HTMs could further assist in the long-term stability of the PSCs.

### 3.2.7 Photovoltaic characterization and admittance spectroscopy

We fabricated PSCs in the n-i-p configuration of FTO/b&mp-TiO<sub>2</sub>/3D-/perovskite/HTM/Au architecture (Figure 3.9 a). The J-V curves of PSCs based on **MP-TF**<sup>m</sup> and **MP-TF**<sup>o</sup> as HTLs and the derived PV values are tabulated in Figure 3.9b and Table 3.2. The PSCs fabricated with **MP-TF**<sup>m</sup> and **MP-TF**<sup>o</sup> as HTLs yielded a PCE of 18.72% ( $V_{oc}$  of 1040 mV,  $J_{sc}$  of 23.04 mA cm<sup>-2</sup>, FF of 77.2%) and 17.13% ( $V_{oc}$  of 1021 mV,  $J_{sc}$  of 22.65 mA cm<sup>-2</sup>, FF of 72.6%) respectively. The more planar orientation of **MP-TF**<sup>m</sup> than **MP-TF**<sup>o</sup>

(as calculated by the dihedral angle from DFT) is fundamental to the device's performance.  $\mathbf{MP}$ - $\mathbf{TF}^m$  displays higher planarity than of the perovskite layer, promoting more effective extraction and transport of charge carriers to yield higher *FF*. The *FF* in **MP-TF**<sup>m</sup> based PSC was found significantly higher than MP-TFo based PSC, suggesting the planar orientation of the HTL is decisive to transport charge effectively. The IPCE graph of PSCs based on HTLs MP- $\mathbf{T}\mathbf{F}^m$  and  $\mathbf{MP}\mathbf{T}\mathbf{F}^o$  are depicted in Figure 3.9c. the photon-to-electron conversion was noted at over 80% in the wavelength region of 350 – 750 nm, MP-TF<sup>m</sup> based PSC showed a higher response compared to the MP-TF<sup>o</sup> HTL. The integrated current calculated from IPCE spectra was found to be 21.13 mAcm<sup>-2</sup> and 21.04 mAcm<sup>-2</sup> respectively for MP-TF<sup>m</sup> and MP-TF<sup>o</sup> based PSCs. The molecular  $\pi$ - $\pi$  stacking of the small molecules attached to the perovskite layer may promote interlayer electronic coupling, allowing better charge transfer in the PSCs. The improved charge mobility and electrical conductivity with the HTL treatment were reported as high current density in the fabricated PSCs.

**Table 3.3** Photovoltaic parameters of PSCs based on HTLs MP-TF<sup>m</sup> and MP-TF<sup>o</sup>.

HTMs	$\mathbf{V}_{oc}$	Jsc	FF	PCE	
	(mV)	(mA/cm <sup>2</sup> )	(%)	(%)	
	1055	23.04	77.2	18.72	
$MP-TF^m$	$1030 \pm 15$	22.63 ± 0.6	75.5 ± 1.35	$17.6 \pm 0.48$	
	1032	22.92	72.6	17.13	
MP-TFº	1021 ± 21	$22.65 \pm 0.36$	71.3 ± 2.13	16.48 ± 0.65	

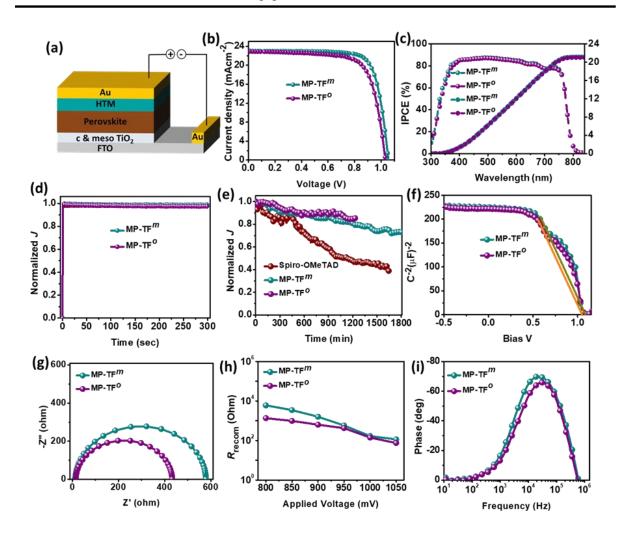


Figure 3.9: (a) Device architecture in the n-i-p configuration of PSCs, (b) *J-V* curves of PSCs based on **MP-TF**<sup>m</sup> and **MP-TF**<sup>o</sup> (c) IPCE graphs of PSCs based on **MP-TF**<sup>m</sup> and **MP-TF**<sup>o</sup>, (d) stabilized power output of PSCs based on **MP-TF**<sup>m</sup> and **MP-TF**<sup>o</sup> (e) long-term stability at 800 mV, (f) Mott-Schottky analysis of PSCs based on **MP-TF**<sup>m</sup> and **MP-TF**<sup>o</sup>, (g) Nyquist plots of PSCs based on **MP-TF**<sup>m</sup> and **MP-TF**<sup>o</sup> (h) charge recombination resistance extracted from the Nyquist plots in the dark, (i) Bode plot of PSCs based on **MP-TF**<sup>m</sup> and **MP-TF**<sup>o</sup> measured in the dark.

The Mott-Schottky plot for the fabricated PSCs of both the HTMs  $\mathbf{MP}$ - $\mathbf{TF}^m$  and  $\mathbf{MP}$ - $\mathbf{TF}^o$  were conducted to decipher the built-in-potential  $(V_{bi})$ , that was derived from the intercept on the bias axis (Figure 7f).  $V_{bi}$  for the  $\mathbf{MP}$ - $\mathbf{TF}^m$  and  $\mathbf{MP}$ - $\mathbf{TF}^o$  based PSCs were 1062 and 1045 mV, respectively. The Nyquist

plots through electrical impedance spectroscopy (EIS) were recorded to probe the charge accumulation behavior and the device kinetics of PSCs (Figure 7g). The recombination resistance was higher for the PSC based on HTL MP-TF<sup>m</sup> than MP-TF<sup>o</sup>, signaling lower recombination processes at the perovskite/HTL interface. The recombination resistance near the open-circuit voltage was conducted and found higher for PSC based on MP-TF<sup>m</sup> than MP-TF<sup>o</sup> based PSC, signalling a reduction in the non-radiative recombination losses (Figure 7h).

#### 3.3 Conclusion

We designed and synthesized two TAT based fluorinemethoxydiphenylamine substituted HTMs (MP-TFm than MP-TFo) for perovskite solar cell application. The fluorination of the methoxy engineered moieties showed higher T<sub>q</sub> and improved energy level alignment with respect to the perovskite layer. The band alignment with the perovskite layer was evidenced with the spectroscopic techniques (CV, UPS) and DFT calculations. Both the HTMs exhibit the charge extraction and faster decay characteristics and non-radiative recombination losses as obtained from the PL and TRPL studies. The meta-substituted fluorine-methoxydiphenylamine based HTM (MP-TFm) showed better film morphology than the orthosubstituted fluorine-methoxydiphenylamine based HTM (MP-TFo) and hence, MP-TF<sup>m</sup> exhibited an improved PCE of 18.72 % than MP-TF<sup>o</sup>. Furthermore, both the fluorinated MP-TF as HTMs showed enhanced stability without any encapsulation. Further, the EIS spectra suggest lesser recombination for the meta-substituted fluorine-methoxydiphenylamine

based HTM. These findings provide a favourable way to imply fluorine-methoxydiphenylamine substituents in designing efficient hole-transporting materials.

#### 3.4 References

- 1. A. Kojima, K. Teshima, Y. Shirai and T. Miyasaka, *J. Am. Chem. Soc*, **2009**, *131*, 6050-6051.
- 2. J.-P. Correa-Baena, A. Abate, M. Saliba, W. Tress, T. J. Jacobsson, M. Grätzel and A. Hagfeldt, *Energy Environ. Sci.*, **2017**, *10*, 710-727.
- 3. H.-S. Kim, C.-R. Lee, J.-H. Im, K.-B. Lee, T. Moehl, A. Marchioro, S.-J. Moon, R. Humphry-Baker, J.-H. Yum and J. E. Moser, *Sci. Rep.*, **2012**, *2*, 1-7.
- 4. H. J. Snaith, *J. Phys. Chem. Lett.*, **2013**, *4*, 3623-3630.
- 5. B. Xu, J. Huang, H. Ågren, L. Kloo, A. Hagfeldt and L. Sun, *ChemSusChem*, **2014**, *7*, 3252-3256.
- 6. S. Kazim, M. K. Nazeeruddin, M. Grätzel and S. Ahmad, *Angew. Chem. Int. Ed.*, **2014**, *53*, 2812-2824.
- 7. L. Calió, S. Kazim, M. Grätzel and S. Ahmad, *Angew. Chem. Int. Ed.*, **2016**, *55*, 14522-14545.
- 8. M. Jeong, I. W. Choi, K. Yim, S. Jeong, M. Kim, S. J. Choi, Y. Cho, J.-H. An, H.-B. Kim and Y. Jo, *Nat. Photonics*, **2022**, 1-7.
- 9. M. Pegu, S. Kazim, T. Buffeteau, D. M. Bassani and S. Ahmad, *ACS Appl. Mater. Interfaces* **2021**, *13*, 48219-48227.
- A. A. Sutanto, P. Caprioglio, N. Drigo, Y. J. Hofstetter, I. Garcia-Benito, V. I. Queloz, D. Neher, M. K. Nazeeruddin, M. Stolterfoht and Y. Vaynzof, *Chem*, 2021, 7, 1903-1916.
- 11. J. Y. Seo, S. Akin, M. Zalibera, M. A. R. Preciado, H. S. Kim, S. M. Zakeeruddin, J. V. Milić and M. Grätzel, *Adv. Funct. Mater.*, **2021**, *31*, 2102124.

- 12. M. J. Jeong, K. M. Yeom, S. J. Kim, E. H. Jung and J. H. Noh, *Energy Environ. Sci.*, **2021**, *14*, 2419-2428.
- 13. K. Chen, W. Kong, N. Ali, W. Song, Z. Wang, A. Wang, Z. Yu, J. Tao, S. Yang and G. Fu, *Sol. RRL*, **2020**, *4*, 2000365.
- 14. G. Ren, W. Han, Y. Deng, W. Wu, Z. Li, J. Guo, H. Bao, C. Liu and W. Guo, *J. Mater. Chem. A*, **2021**, *9*, 4589-4625.
- 15. W. Zhou, Z. Wen and P. Gao, *Adv. Energy Mater.*, **2018**, *8*, 1702512.
- 16. A. K. Jena, Y. Numata, M. Ikegami and T. Miyasaka, *J. Mater. Chem. A*, **2018**, *6*, 2219-2230.
- 17. T. Fuchigami and S. Inagi, *Acc. Chem. Res.*, **2020**, *53*, 322-334.
- 18. G. Sathiya, H. Wang, C. Chen, Y. Miao, M. Zhai and M. Cheng, *Dyes Pigm.*, **2022**, *198*, 110029.
- 19. I. Cho, N. J. Jeon, O. K. Kwon, D. W. Kim, E. H. Jung, J. H. Noh, J. Seo, S. I. Seok and S. Y. Park, *Chem. Sci.*, **2017**, *8*, 734-741.
- 20. N. J. Jeon, H. Na, E. H. Jung, T.-Y. Yang, Y. G. Lee, G. Kim, H.-W. Shin, S. Il Seok, J. Lee and J. Seo, *Nat. Energy*, **2018**, *3*, 682-689.
- 21. S. Wang, A. Wang, X. Deng, L. Xie, A. Xiao, C. Li, Y. Xiang, T. Li, L. Ding and F. Hao, *J. Mater. Chem. A* **2020**, *8*, 12201-12225.
- 22. L. Tao, B. Wang, H. Wang, C. Chen, X. Ding, Y. Tian, H. Lu, X. Yang and M. Cheng, *ACS Appl. Mater. Interfaces*, **2021**, *13*, 13470-13477.
- 23. J. Yang, W. Tang, R. Yuan, Y. Chen, J. Wang, Y. Wu, W.-J. Yin, N. Yuan, J. Ding and W.-H. Zhang, *Chem. Sci.*, **2021**, *12*, 2050-2059.
- 24. K. Rakstys, A. Abate, M. I. Dar, P. Gao, V. Jankauskas, G. n. Jacopin, E. Kamarauskas, S. Kazim, S. Ahmad and M. Grätzel, *J. Am. Chem. Soc*, **2015**, *137*, 16172-16178.

- 25. F. J. Ramos, K. Rakstys, S. Kazim, M. Grätzel, M. K. Nazeeruddin and S. Ahmad, *RSC Adv.*, **2015**, *5*, 53426-53432.
- 26. M. Pegu, S. Kazim, P. Huang, L. Lezama and S. Ahmad, *J. Mater. Chem. C*, **2021**, *9*, 7074-7082.
- K. Rakstys, S. Paek, P. Gao, P. Gratia, T. Marszalek, G. Grancini, K. T. Cho,
   K. Genevicius, V. Jankauskas and W. Pisula, *J. Mater. Chem. A*, 2017, 5,
   7811-7815.
- 28. A. Connell, Z. Wang, Y.-H. Lin, P. C. Greenwood, A. A. Wiles, E. W. Jones, L. Furnell, R. Anthony, C. P. Kershaw and G. Cooke, *J. Mater. Chem. C*, **2019**, *7*, 5235-5243.
- 29. C. Igci, S. Paek, K. Rakstys, H. Kanda, N. Shibayama, V. Jankauskas, C. Roldán-Carmona, H. Kim, A. M. Asiri and M. K. Nazeeruddin, *Sol. RRL*, **2020**, *4*, 2000173.
- 30. L. Calió, C. Momblona, L. Gil-Escrig, S. Kazim, M. Sessolo, Á. Sastre-Santos, H. J. Bolink and S. Ahmad, *Sol. Energy Mater Sol. Cells*, **2017**, *163*, 237-241.
- 31. P.-Y. Su, L.-B. Huang, J.-M. Liu, Y.-F. Chen, L.-M. Xiao, D.-B. Kuang, M. Mayor and C.-Y. Su, *J. Mater. Chem. A*, **2017**, *5*, 1913-1918.
- 32. I. Petrikyte, I. Zimmermann, K. Rakstys, M. Daskeviciene, T. Malinauskas, V. Jankauskas, V. Getautis and M. K. Nazeeruddin, *Nanoscale*, **2016**, *8*, 8530-8535.
- 33. X.-C. Li, Y.-G. Tu, C. Meng, W. Song, T. Cheng, Y.-T. Gong, J. Min, R. Zhu, W.-Y. Lai and W. Huang, *ACS Appl. Mater. Interfaces*, **2019**, *11*, 45717-45725.

### Chapter 4

Diethynyl-Conjugated Zinc-Phthalocyanine Dimers as Hole Selective Layers for Perovskites solar cells Fabrication



#### Chapter 4. Diethynyl-Conjugated Zinc-Phthalocyanine Dimers as Hole Selective Layers for Perovskites solar cells Fabrication.

The developed triple bonded  $\pi$ -conjugated zinc-phthalocyanine dimers (ZnPc-t-DPP-t-ZnPc 1, ZnPc-t-t-ZnPc 2, ZnPc-t-Spiro-t-ZnPc 3) synthesized by molecular engineering have been employed as hole-transporting materials (HTMs) in perovskite solar cells (PSCs). It showed band alignment with mixed cation perovskite, as well as improved charge extraction capability, allowing improvement in the photocurrent density and, consequently, the performance of PSCs. Designed dimers can form uniform films with no pinholes leading to high-performance devices. The fabricated PSC with dimer ZnPc-t-Spiro-t-ZnPc 3 measured a power conversion efficiency of 18.32%, which surpasses the PSC based on the state-of-the-art Sprio-OMeTAD (17.42%). ZnPc dimers displayed improved long-term stability under stress conditions such as moisture and thermal.

#### Chapter 4. Diethynyl-Conjugated Zinc-Phthalocyanine Dimers as Hole Selective Layers for Perovskites solar cells Fabrication.

#### **Content**

4.1 Introduction 100-103
4.2 Result and Discussion104
4.2.1 Design and Synthesis104-105
4.2.2 Spectroscopic, diffractogram, electrochemistry, and
surface mor phology studies105-110
4.3 Photovoltaic properties of the PSCs110-114
4.4 Stability and admittance spectroscopy measurements 115-117
4.5 Conclusions
4.6 References119-122

#### Chapter 4. Diethynyl-Conjugated Zinc-Phthalocyanine Dimers as Hole Selective Layers for Perovskites solar cells Fabrication.

#### 4.1 Introduction

Halide-based perovskite solar cells (PSCs) are being considered as a new paradigm for sustainable energy harvesting owing to their potentially attractive optoelectronic properties, such as high absorption coefficients and long carrier diffusion lengths, high tolerance to defects, and the possibility of processing them from solutions at low temperatures.<sup>1-3</sup> Their application in photovoltaic (PV) further promises flexibility, lightweight, and efficient device performances. The PSCs comparably match the performance of mature silicon-based cells (26.7%), measuring power conversion efficiencies (PCEs) up to 25.5%.4 Nevertheless, the vital challenge for PSCs to be commercially exploited is the lack of long-term stability against heat, and prolonged light soaking results in ion migration and segregation. Another detrimental factor affecting the PSCs is the moisture stability due to the ionic nature of organic cations which makes them vulnerable to hydrolysis.<sup>5</sup> The charge-carrying layers play an effective role in achieving the high performance of PSCs. The photoactive perovskite layer is sandwiched between the hole transporting material (HTM) and the electron transporting material (ETM).6-8 Depending on the stacking of each layer, the standard PSCs architecture is integrated into various configurations such as mesoscopic (n-i-p) and inverted planar (p-i-n). Focusing on standard devices, HTM stands between the active layer and the metal electrode.9 The HTMs are critical in promoting charge extraction and transport, including the inhibition of the photoinduced carrier recombination as well. Thus, HTMs play a vital role in the stability of

PSCs to isolate and protect the active layer from moisture. Various families of HTMs have been developed and they can be polymers or single molecules. The reference is the single-molecule 2,2',7,-7'-tetrakis(N,N-di-p-methoxyphenylamine)-9,9'-spirobifluorene (Spiro-OMeTAD) and the polymer poly-(triarylamine) (PTAA), that provide high PCEs but are cost-uncompetitive and induce instability over time.<sup>10</sup>

Phthalocyanines (Pc) are known to be robust semiconductor materials with remarkable optoelectronic properties, such as an intense absorption in the visible and near-infrared region, excellent thermal and chemical stability, and chemical versatility. 11-14 Such merits led to the Pcs application in multiple technologies, including photosensitizers for photodynamic therapy against cancer, as active materials in organic solar cells, in gas sensors, etc. 15, 16 Pcs have been employed as HTMs layer in PSCs 12, 17, 18 and a nickel phthalocyanine based dopant-free HTM gave an efficient performance in the PSCs. 19 While, zinc phthalocyanines as HTM in PSCs, yielded a PCE of 17.5%. Notably, PSCs with Pcs as HTM are usually more stable against deterioration than those of reference devices. 21-23 Pc dimers are known to be used in the application of controllable molecular switches, and their large delocalization and high charge mobility favors them to be the new class of semiconductor materials. 24,25

Zinc-phthalocyanine (ZnPc) dimers <sup>26</sup> shown to be an excellent material as HTMs, providing both good performance and stability to PSCs. <sup>27</sup> ZnPc-DPP-ZnPc resulted in the best PCE when applied as dopant-free HTM in n-i-p type PSCs, reaching 16.8% PCE, and also showed improved

stability as compared to the Spiro-OMeTAD based devices. It is worth highlighting the planar molecular structures, that can favor the mobility of charges in the solid state.<sup>27</sup> Rather, such structures can aggregate forming extensive crystalline domains that result in incomplete coverage as well as overly thick layers. Three-dimensional (3D) structures can solve this issue since less intense intermolecular interactions lead to more uniform layers. A well-designed 3D molecule will result in a layer of controlled thickness with adequate charge mobility. Here, the study of three diethynyl conjugated ZnPc dimers as HTMs is presented (ZnPc-t-DPP-t-ZnPc 1, ZnPc-t-t-ZnPc 2, and ZnPc-t-Spiro-t-ZnPc 3, Figure 4.1). For the ease of reading here on, we have referred to the ZnPc dimers ZnPc-t-DPP-t-ZnPc 1, ZnPc-t-t-ZnPc 2, and ZnPc-t-Spiro-t-ZnPc 3 as ZnPc 1, ZnPc 2, and ZnPc 3 respectively. Diketopyrolopyrole (DPP) is a well-known electron-deficient building block and their potentials have been discussed as active materials due to their higher carrier mobility and surface morphology.<sup>28</sup> A strong  $\pi$ - $\pi$ stacking is well induced in the solid-state due to the planar molecular core and strong supramolecular interaction is favored. Additionally, the alkyl substituents also help in fine-tuning intermolecular packing structures and therefore render different charge transport properties. Moreover, the larger polarizability of the sulfur atoms of the thiophene heterocycle stabilizes the molecular system and valence band of the frontier molecular orbitals and the two oxygen atoms in the fused ring enhance the molecular dipole, constructing an internal electrical field to facilitate the charge transport.19 Additionally, the more polarizable sulfur atoms can induce effective mobility that is desirable to achieve

higher current density. ZnPc 1 represents a simple modification of ZnPc-DPP-ZnPc that involves binding the DPP to the ZnPc rings through triple bonds to distinguish the impact of a higher degree of self-organization  $(\pi-\pi)$  aggregation) for device application. The inclusion of the triple bonds along the  $\pi$ -linker in the ZnPc dimers allows co-planarity in the molecular core structure of the HTMs.<sup>29</sup> ZnPc 2 is a simplify structure with two contiguous triple bonds as linkers of both ZnPc macrocycles. In this context, to obtain a 3D structure, we designed a new dimer containing 2',7'-diethynylfluorene as the linker element (ZnPc 3). Spirobifluorene based building blocks have been extensively investigated in organic semiconductors for organic electronics, owing to the existence of the sp<sup>3</sup> hybrid atoms at the junction of the  $\pi$ -conjugated system, the fluorene-based molecule offers advantages such as the high glass transition temperature  $(T_g)$ , morphological stability and excellent solubility.

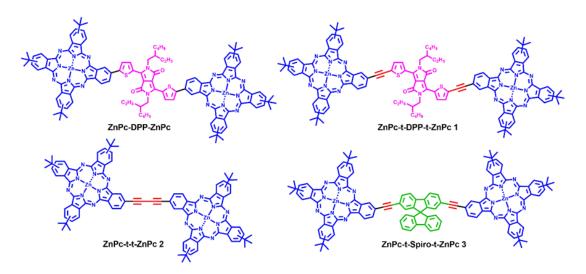


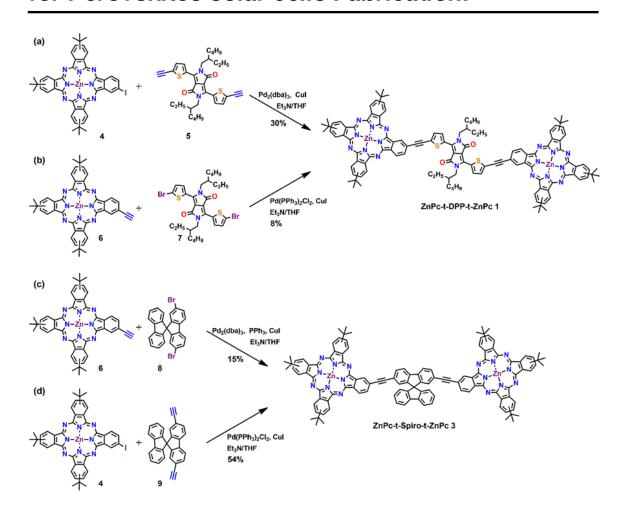
Figure 4.1. Structure of ZnPc ZnPc-DPP-ZnPc and the three ZnPc dimers ZnPc-t-DPP-t-ZnPc 1, ZnPc-t-t-ZnPc 2, and ZnPc-t-Spiro-t-ZnPc 3 under study.

#### 4.2 Results and discussion

#### 4.2.1 Design and Synthesis

The three ZnPc dimers were the products of Sonogashira couplings. Dimer ZnPc 1 was synthesized as our previous report<sup>28</sup> from iodophthalocyanine 4 with diethinyl-DPP 5 with 30% yield (Scheme 4.1a) and also with 8% yield from ethinylphthalocyanine 6 and dibrominated DPP 7 (Scheme 4.1b). ZnPc 2 was synthesized according to the literature.<sup>30</sup> ZnPc 3 was also initially synthesized from ethinylphthalocyanine 6 and the corresponding dibromo derivative 8 in 15% yield (Scheme 4.1c), although the performance was improved up to 54% by coupling iodophthalocyanine 4 and diethinylspirofluorene 9 (Scheme 4.1d). ZnPc-t-Spiro-t-ZnPc 3 was fully characterized by 1H NMR, UV-Vis and FTIR spectrophotometry, and MALDI-ToF mass spectrometry.

The three dimers are readily soluble in THF, although ZnPc 1 and ZnPc 3 are less soluble in common organic solvents, however, ZnPc 2 is nearly soluble in solvents such as chloroform, chlorobenzene, and dichloromethane at room temperature.



Scheme 4.1. Figure 1. Structure of Pc dimers ZnPc-DPP-ZnPc, ZnPc-t-DPP-t-ZnPc 1, ZnPc-t-t-ZnPc 2, and ZnPc-t-Spiro-t-ZnPc 3.

# 4.2.2 Spectroscopic, diffractogram, electrochemistry, and surface morphology studies

The UV-Vis absorption properties of the ZnPc dimers ZnPc 1, ZnPc 2, and ZnPc 3 were studied in THF solution as well as in their thin films, as shown in (Figure 4.2a, Table 4.1). The absorption spectra of Pcs exhibit two typical characteristic bands, which are usually the B bands located around 250-350 nm in the ultraviolet region, and the Q band that

appears at a higher wavelength region around 500-750 nm. Notably, the Pcs are highly conjugated molecules, thus the absorption maxima corresponding to the Q bands appear at longer wavelengths, 709 nm, 703 nm, and 690 nm for ZnPc 1, ZnPc 2, and ZnPc 3, respectively. The bathochromic shifts of the phthalocyanines can be ascribed to the intramolecular charge transfer (ICT) transitions. It can be deduced from the absorption spectra, the Q bands of the dimers appear to split into two by the existence of several regioisomers with a non-symmetric character that induces  $\pi$ - $\pi$ \* excitation between the bonding and the antibonding molecular orbitals. ZnPc 1 has a lower molar extinction coefficient, probably it tends to stack more than the other dimers even in dilute solutions. The absorption spectra of the thin films display a large broadening for the Q bands which reflects the strong molecular interactions.

To investigate the potential application of ZnPc 1, ZnPc 2, and ZnPc 3 as HTMs in PSCs energy alignment was determined via the cyclic voltammetry (CV) measurement. The solution of phthalocyanines was prepared in THF and measured to deduce the highest occupied molecular orbital (HOMO) and lowest unoccupied molecular orbital (LUMO) (Figure 4.2c. Table 4.1). The redox couple ferrocene/ferricenium ion (Fc/Fc+) was used as the external standard, and 4.8 eV below the vacuum was noted as reference level. HOMO values were favorable to extract holes from the active layer and similar for the three derivatives (-4.89 eV, -5.00 eV, and -4.87 eV for ZnPc 1, ZnPc 2, and ZnPc 3, respectively). The hole extraction ability of the developed HTMs was noted to be worthy for device integration. According to the

calculated LUMO values, while ZnPc 1, ZnPc 2, and ZnPc 3 (-3.16 eV, -3.67 eV, and -3.64 eV, respectively) could effectively block electrons. The energy level band diagram of ZnPc 1, ZnPc 2, and ZnPc 3 is in alignment with the perovskite used (Figure 4.2d).

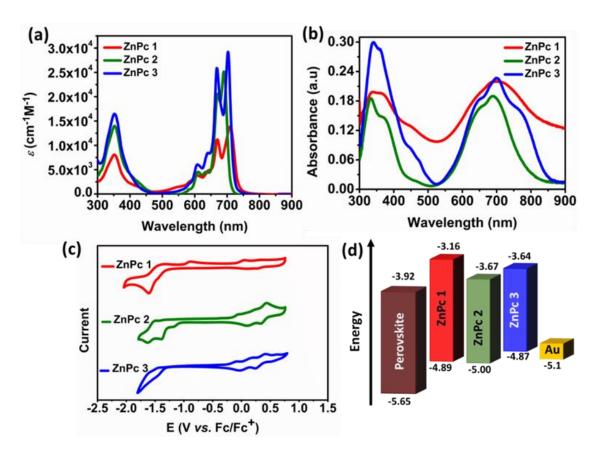


Figure 4.2. . UV-Visible spectra of Pc dimers ZnPc 1, ZnPc 2, and ZnPc 3, (a) in THF solution, (b) in thin films, (c) cyclic voltammetry of Pc dimers ZnPc 1, ZnPc 2, and ZnPc 3 in THF solutions, and (d) energy level band diagram of ZnPc dimers ZnPc 1, ZnPc 2, and ZnPc 3.

Table 4.1. Optical and electrochemical parameters of ZnPc 1, ZnPc 2 and ZnPc 3.

Chapter 4. Diethynyl-Conjugated Zinc-Phthalocyanine Dimers as Hole Selective Layers for Perovskites solar cells Fabrication.

HTM	$\lambda_{ m abs}$	$E_{ m red1}$	$E_{ m ox1}$	$E_{ m g\;EC}^{ m b}$	$HOMO^c$	LUMOd	μ	σ
	(nm)a	(eV)	(eV	Ü			$(10^{-5} \mathrm{cm}^2\mathrm{V}^{-1}\mathrm{s}^{-1})$	(µScm <sup>-1</sup> )
	( )	( )	)				,	(proving
ZnPc 1	670/70	-	0.0	1.73	-4.89	-3.16	2.83	1.05
	9	1.64	9					
ZnPc 2	671/70	-	0.2	1.33	-5.00	-3.67	1.5	0.51
	3	1.13	0					
ZnPc 3	671/69	-	0.0	1.23	-4.87	-3.64	4.08	1.23
	0	1.16	7					

<sup>&</sup>lt;sup>a</sup>Absorption spectra were measured in THF solution. <sup>b</sup> $E_{g EC}$  (eV) was calculated by  $E_{g EC}$  =  $E_{red1}$  -  $E_{ox1}$ . <sup>c</sup>HOMO (eV) was calculated by HOMO = LUMO -  $E_{g EC}$  (eV). <sup>d</sup>LUMO (eV) was calculated by LUMO = -|E<sub>red1</sub> (vs. Fc/Fc<sup>+</sup>) + 4.8 (CV).

To evaluate the influence of the ZnPc dimers as HTMs on the perovskite layer, the light absorption properties of the perovskite and with ZnPc dimers as HTM layers were performed (Figure 4.3a). We noted higher absorption intensity peaks with the Pcs as over layer as compared to the perovskite. Metal phthalocyanines are known to show excellent light absorption properties in the near-infrared (NIR) region. The higher absorption for ZnPc dimers in the range of 550-800 nm could be assumed due to the Q-band transition and hence its addition as an HTL layer on the top of perovskite influenced the optical wavelength of the perovskite/HTL thin films in the region 550-780 nm.

We performed the steady-state photoluminescence (PL) measurement for the perovskite and with ZnPc dimers as HTMs, Pcs coated perovskite shows quenching, indicating the effectiveness of HTMs in hole extraction (Figure 4.3b). The  $\pi$ - $\pi$  stacking present in the Pcs with the peripheral groups allows the favorable interface with the perovskite layer that favors PL quenching. ZnPc 3 showed the maximum PL quenching behavior, followed by ZnPc 1 and ZnPc 2. Suggesting, the ZnPc 3 suitability as HTM to yield better PV parameters.

Lower surface roughness and uniform film coverage of an HTM play a role in enhancing PV performances in PSCs, we recorded surface microstructure of the perovskite with Pcs under doped and undoped conditions, by scanning electron microscopy (SEM) experiments (Figure 4.4a-c). The microstructure of the perovskite with Pcs exhibits a uniform capping layer deposition with fewer pinholes in the undoped state. Under doped state the microstructure of ZnPc 1 was observed to be aggregated on the top surface of the perovskite layer with less uniformity, resulting in incomplete coverage as well as overly thick layers. While ZnPc 2 and ZnPc 3 showed a similar pattern in morphology and uniformity in the surface coverage, owing to the molecular self-assembly nature of Pcs.

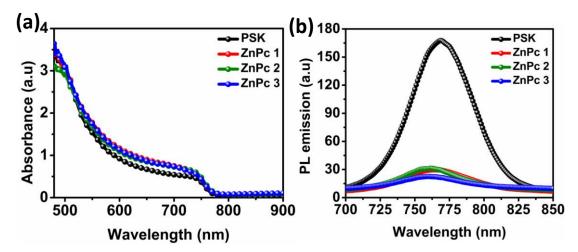


Figure 4.3: (a) Absorbance spectra of PSK and with ZnPc dimers (ZnPc 1, ZnPc 2, ZnPc 3) thin films, and (b) photoluminescence (PL) spectra of PSK and with ZnPc dimers (ZnPc 1, ZnPc 2, ZnPc 3) thin films.

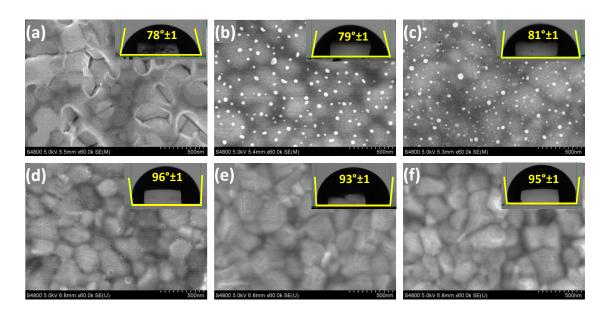


Figure 4.4: Surface SEM images and contact angle measurements of Pc dimers. Doped ZnPcs (a) ZnPc 1, (b) ZnPc 2, and (c) ZnPc 3; undoped ZnPcs (d) ZnPc 1, (e) ZnPc 2, and (f) ZnPc 3, as HTLs on the surface of perovskite layer thin films.

The role of surface properties induced by Pcs is studied by goniometry measurements (Figure 4.4a-f). The contact angle value for the perovskite film and with undoped ZnPc 1, ZnPc 2, and ZnPc 3 was found to be 75°, and 96°, 93°, 95°; while under the doping conditions, we observed that the contact angle values accordingly reduced to 78°, 79°, 81° for ZnPc 1, ZnPc 2, ZnPc 3 respectively. The higher contact angle values for the perovskite/ZnPc films in the undoped state, would impart higher tolerance to environmental moisture penetration and potentially induce long-term stability in PSCs.

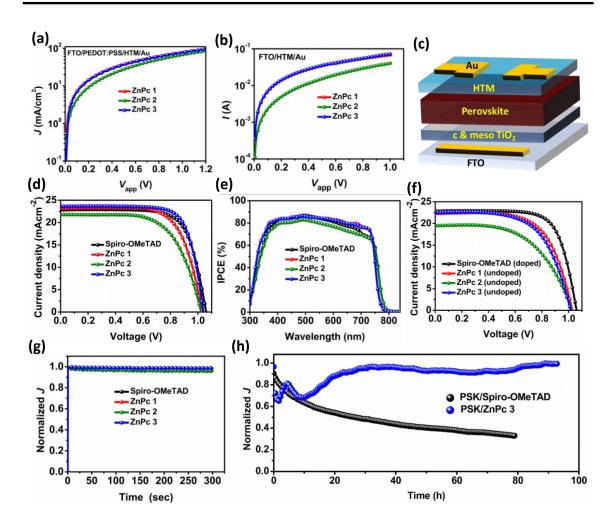


Figure 4.5: (a) Hole mobility curves, (b) conductivity measurement curves; of the devices based on Spiro-OMeTAD and Pc dimers ZnPc 1, ZnPc 2, ZnPc 3, (c) adopted architect of ZnPcs in PSC, (d) *J-V* curves of the PSCs, (e) IPCE graph of PSCs with Spiro-OMeTAD and Pc dimers ZnPc 1, ZnPc 2, ZnPc 3, (f) *J-V* curves of the PSCs based on undoped and Pc dimers ZnPc 1, ZnPc 2, ZnPc 3, (g) steady-state MPPT measurement for 300s of the based on Spiro-OMeTAD and Pc dimers ZnPc 1, ZnPc 2, ZnPc 3, and (h) MPP tracking of the PSCs based on Spiro-OMeTAD and ZnPc 3 under light for at 0.8 V around 1 sun illumination.

#### 4.3 Photovoltaic properties of the PSCs

We perform the space-charge-limit-current (SCLC) measurement to hole mobility  $(\mu)$ with the device architecture measure FTO/PEDOT:PSS/HTM/Au. The hole mobility (Figure 4.5a) was calculated from the I-V curves by fitting to the Mott-Gurney law (I =  $9EE_0\mu Vapp^2/8L^3$ ). The doped ZnPc 1, ZnPc 2, and ZnPc 3 showed hole mobilities of 2.83×10<sup>-5</sup>, 1.5×10<sup>-5</sup>, and 4.08×10<sup>-5</sup> cm<sup>2</sup>V<sup>-1</sup>s<sup>-1</sup>, while doped Spiro-OMeTAD was found to be 1.19×10-4. hole extracting and transporting behavior, corresponding, corresponding to molecular conjugation and  $\pi$ - $\pi$  stacking. The trend of hole mobility is following the HOMO level of the Pcs.

We probed the charge transport properties of ZnPc 1, ZnPc 2, and ZnPc 3 by measuring the linear current vs voltage (I-V) profile (Figure 4.5b) of the device (FTO/HTL/Au) under dark conditions. The calculated conductivities were found to be 1.05, 0.51, and 1.23  $\mu$ Scm-1 for ZnPc 1, ZnPc 2, and ZnPc 3 respectively. To evaluate the Pcs as HTMs in PSCs we fabricated n-i-p devices as FTO/bl-meso TiO2/ (MAPbBr3)0.15(FAPbI3)0.85/HTM/Au (Figure 4.5c).

The short circuit current ( $J_{sc}$ ), open-circuit voltage ( $V_{oc}$ ), and fill factor (FF), under simulated AM 1.5G solar illumination at 100 mW cm<sup>2</sup>, of the PSCs with ZnPc dimers ZnPc 1, ZnPc 2, ZnPc 3, and Spiro-OMeTAD as HTMs are presented (Figure 4.5d), and tabulated (Table 4.2). We noted the optimized concentration is 15 mM, for ZnPc 1, ZnPc 2, and ZnPc 3 as HTMs for PSCs. The Pcs were doped with tert-butyl pyridine (t-BP) and lithium bis(trifluoromethane)sulfonimide (Li-TFSi) as dopants. The PSC

based on ZnPc 3 as HTM demonstrated a PCE of 18.32%, ( $V_{oc}$  of 1039 mV, J<sub>sc</sub> of 23.63 mAcm<sup>-2</sup>, and FF of 74.62%), outperformed the performance of Spiro-OMeTAD based PSC with a PCE of 17.42% ( $V_{\rm oc}$ 1059 mV,  $J_{sc}$  22.84 mAcm<sup>-2</sup>, FF 71.97%). The competitive performance of ZnPc 3 is in agreement with our electro-optical characterization. ZnPc 1 yielded a relatively lower performance (PCE 16.49%, Voc 1030 mV, Jsc 23.21 mAcm-2, FF 68.93%) and ZnPc 2 (PCE 12.82% Voc 1041 mV, Jsc 22.25 mAcm-2, FF 55.30%). The plausible reason for the lower performance could be the lower solubility in the preferred solvent or the molecular aggregation that hinders the effective energetic coupling of the layers, resulting in lower device PCE. The improved current density (Isc) observed for ZnPc 1 and ZnPc 3 would be acribed to the effective hole extraction at the interfaces, as noted from PL spectra. In addition, the presence of DPP as a linker in the dimer ZnPc 1 and fluorene mediated linker in dimer ZnPc 3 contributes to the charge extraction and carrier mobility and enhancement in  $J_{\rm sc}$ . PSCs statistics with ZnPcs including  $V_{oc}$ ,  $J_{sc}$ , FF, and PCE are presented (Figure 4.6a-d).

The incident photon-to-current conversion efficiency (IPCE) spectra of PSCs with the Spiro-OMeTAD and dimers ZnPc 1, ZnPc 2, and ZnPc 3 were measured (Figure 4.5e). The IPCE spectra display a panchromatic response from 300-800 nm, showing a broad plateau (400-700nm) with >80% for Spiro-OMeTAD and with developed dimers ZnPc 1 and ZnPc 3, however, dimer ZnPc 2 showed a lower IPCE response, correlating with J-V measurements. The integrated J<sub>sc</sub> values obtained from the IPCE curves are found to be lower than that of the J<sub>sc</sub> from the J-V

measurements which we ascribe to the differences in intensities of the light sources used.

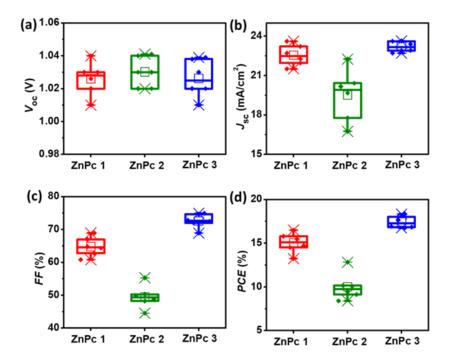


Figure 4.6: Device statistics of doped ZnPc dimers as HTMs (a)  $V_{oc}$  (b)  $J_{sc}$  (c) *FF* (d) *PCE*.

We further fabricated *n-i-p* type PSCs to evaluate the performances of ZnPc dimers (ZnPc 1, ZnPc 2, and ZnPc 3) as dopant-free HTM and doped Spiro-OMeTAD as a control. The PV parameters for undoped ZnPc dimers are illustrated in Table 4.2 and the statistical device performance is depicted in Figure 4.7. Arguably, doped Spiro-OMeTAD showed higher performance than the undoped ZnPc dimers (Figure 4.5f), notably, the undoped ZnPc dimers with ZnPc 1 and ZnPc 3 yielded a PCE of 14.71% and 14.03%, respectively; and ZnPc 2 of 11.17%. The ZnPC dimers also showed a competitive performance in their pristine form i.e., as dopant-free HTMs, and by further optimization and design principle rule, it can outperform doped Spiro-OMeTAD in PSCs.

Table 4.2: PSCs parameters with various HTM in pristine and doped form.

НТМ	V <sub>oc</sub> (mV)	$J_{\rm sc}({\rm mAcm}^{-2})$	FF (%)	PCE (%)
Spiro-OMeTAD	1059	22.84	71.97	17.42
ZnPc 1	1030	23.21	68.93	16.49
Avg.	1026 ±0.014	22.53 ±1.06	63.58 ±5.3	14.83 ±1.65
Undoped	1026	22.27	64.34	14.71
Avg.	1020 ±0.0075	21.33 ±0.938	62.50 ±7.37	13.68 ±1.023
ZnPc 2	1041	22.25	55.30	12.82
Avg.	1030 ±0.01	19.5 ±2.75	49.49 ±5.8	$9.88 \pm 2.82$
Undoped	1021	19.48	56.12	11.17
Avg.	1000 ±0.115	19.14 ±0.421	53.06 ±3.02	10.28 ±0.89
ZnPc 3	1039	23.63	74.62	18.32
Avg.	1020 ±0.012	$23.18 \pm 0.44$	72.46 ±2.44	17.41±0.91
Undoped	1014	22.49	61.47	14.03
Avg.	1010 ±0.016	21.74 ±0.738	60.83 ±1.13	13.45 ±0.571

### 4.4 Stability and admittance spectroscopy measurements

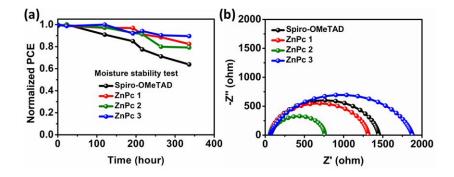


Figure 4.7: (a) Device stability (without encapsulation) of PSCs with Spiro-OMeTAD and Pc dimers ZnPc 1, ZnPc 2, and ZnPc 3 under moisture, the devices were stored in dark condition, (b) Nyquist plots for the Spiro-OMeTAD and Pc dimers ZnPc 1, ZnPc 2, and ZnPc 3 measured with an applied voltage of 950 mV under dark conditions.

The steady-state power output of PSCs based on Spiro-OMeTAD and Pcs dimers ZnPc 1, ZnPc 2, and ZnPc 3 are investigated to verify the J at the maximum power point. We noted the Pcs gave stabilized current during the 300 s exposure (Figure 4.5g). We evaluated, the storage stability of the PSCs, and the Pcs dimers showed improved stability when the PCE was measured periodically (devices stored in a dry box under vacuum condition) for a month. Additionally, we probed PSCs with Spiro-OMeTAD and ZnPc 3 for operational stability through the maximum power point tracking (MPPT) of the un-encapsulated PSCs under ambient conditions and nearly sun illumination for nearly 95 h, under a relative humidity of 50-60% at 800 mV (Figure 4.5h). The Spiro-OMeTAD based PSC showed lower stability and retained nearly 32% of its initial I value, while the devices based on ZnPc 3 displayed liner response, retaining around >80% of its initial *J* value for nearly >90 h. We conducted moisture stability tests for the PSCs fabricated with the different ZnPc dimers as HTMs under ambient conditions. The normalized PCE of the unencapsulated PSCs with the ZnPc dimers in comparison to Spiro-OMeTAD is displayed (Figure 6a).

We conducted stability tests for the PSCs fabricated with the different HTMs under ambient conditions. The moisture stability tests were conducted for the PSCs with Spiro-OMeTAD and ZnPc dimers. The normalized PCE of the unencapsulated PSCs with the ZnPc dimers in comparison to Spiro-OMeTAD is displayed (Figure 4.7a). Noticeably, both ZnPc 1 and ZnPc 3 showed higher stability, remaining almost 90% of the initial PCE after >300 h. ZnPc 2 also showed comparable performance as ZnPc 1 and ZnPc 3, remaining almost 80% of the initial

PCE. On the contrary, the Spiro-OMeTAD based PSC showed a decrease in its initial PCE to about 70% and degrades rapidly compared to the ZnPc dimers. We ascribed this to the hydrophobic properties of ZnPc dimers which showed higher hydrophobicity angles, favoring an effective shielding of the perovskite layer towards moisture.

We noted increased recombination resistance for ZnPc 3 based PSC as compared to the ZnPc 1, ZnPc 2, and Spiro-OMeTAD by electrical impedance spectroscopy (EIS) measurement<sup>32</sup> made under dark conditions (Figure 4.7b). The values for Rrecom for Spiro-OMeTAD, ZnPc 1, ZnPc 2, and ZnPc 3 treated PSCs were calculated to be 1306  $\Omega$ , 981.1  $\Omega$ , 634.2  $\Omega$  and 1679  $\Omega$  respectively. The EIS studies suggest the improved interfacial charge extraction, maximum obtained for ZnPc 3, that subsequently impacts the performance of the PSCs resulting in lower charge recombination at the perovskite/hole selective layer interfaces. We made Mott-Schottky analysis of the PSCs based on Spiro-OMeTAD and ZnPc dimers ZnPc 1, ZnPc 2, and ZnPc 3 (Figure 4.8). The extracted build-in-potential ( $V_{bi}$ ) for Spiro-OMeTAD and ZnPc dimers ZnPc 1, ZnPc 2, and ZnPc 3 are 1031 mV, 833 mV, 1014 mV, and 914 mV respectively,2 thus follow the  $V_{oc}$  trend.

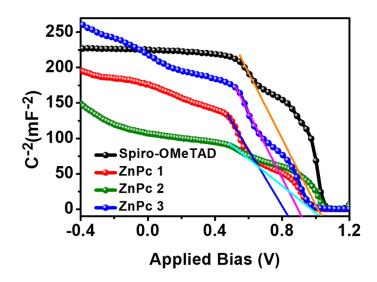


Figure 4.8 Mott- Schottky plots for PSCs based on Spiro-OMeTAD and ZnPc dimers ZnPc 1, ZnPc 2, and ZnPc 3.

#### 4.5 Conclusions

The position of the diethynyl  $\pi$ -conjugated linkers on the phthalocyanine rings was tuned to synthesize different ZnPc dimers (ZnPc 1, ZnPc 2, and ZnPc 3). Amendment of the phthalocyanine dimers with the triple bonds and the  $\pi$ -linkers in ZnPc dimers leads to coplanarity in the molecular structure of the core, resulting in competing enhancements of charge extraction and carrier mobility at the perovskite/phthalocyanine interface. Suggested by the investigation of the impact of the substituents' groups in the ZnPc dimers on the hole transport capability and microstructure in thin films. The fabricated perovskite solar cells with the dimer ZnPc 3 showed a PCE of 18.32%, which surpasses that of the Spiro-OMeTAD (17.42%). The reported performance supersedes previous reports for both ZnPc-based and

phthalocyanine-dimers-based hole selective layers, in PSCs. Notably, a very thin layer is used which in turn will consume low materials and reduce the cost. Using admittance spectroscopy, we quantified the performance of the dimers and noted reduced non-radiative recombination at the interface and improved charge transfer kinetics. The ZnPc dimers are shown to be hydrophobic and protect the perovskite layer, thereby will contribute to enhancing the PSC stability.

#### 4.6 References

- [1] L. Chouhan, S. Ghimire, C. Subrahmanyam, T. Miyasaka and V. Biju, *Chem. Soc. Rev.*, 2020, 49, 2869-2885.
- [2] M. Pegu, S. Kazim, T. Buffeteau, D. M. Bassani and S. Ahmad, *ACS Appl. Mater. Interfaces*, 2021, 13, 48219-48227.
- [3] T. Baikie, Y. Fang, J. M. Kadro, M. Schreyer, F. Wei, S. G. Mhaisalkar, M. Graetzel and T. J. White, *J. Mater. Chem. A*, 2013, 1, 5628-5641.
- [4] J. Jeong, M. Kim, J. Seo, H. Lu, P. Ahlawat, A. Mishra, Y. Yang, M. A. Hope, F. T. Eickemeyer and M. Kim, *Nature*, 2021, 592, 381-385.
- [5] R. Wang, M. Mujahid, Y. Duan, Z. K. Wang, J. Xue and Y. Yang, *Adv. Funct. Mater.*, 2019, 29, 1808843.
- [6] L. Calió, S. Kazim, M. Grätzel and S. Ahmad, *Angew. Chem. Int. Ed.*, 2016, 55, 14522-14545.
- [7] M. Pegu, S. Kazim, P. Huang, L. Lezama and S. Ahmad, *J. Mater. Chem. C*, 2021, 9, 7074-7082.
- [8] K. T. Cho, K. Rakstys, M. Cavazzini, S. Orlandi, G. Pozzi and M. K. Nazeeruddin, N*ano Energy*, 2016, 30, 853-857.
- [9] M. Saliba, J.-P. Correa-Baena, C. M. Wolff, M. Stolterfoht, N. Phung, S. Albrecht, D. Neher and A. Abate, *Chem. Mater.*, 2018, 30, 4193-4201.
- [10] W. Zhou, Z. Wen and P. Gao, Adv. Energy Mater., 2018, 8, 1702512.
- [11] S. Kong, X. Wang, L. Bai, Y. Song and F. Meng, *J. Mol. Liq.*, 2019, 288, 111012.

- [12] M. Urbani, G. de la Torre, M. K. Nazeeruddin and T. Torres, *Chem. Soc. Rev.*, 2019, 48, 2738-2766.
- [13] K. Kadish, R. Guilard and K. M. Smith, The porphyrin handbook: phthalocyanines: spectroscopic and electrochemical characterization, *Academic Press*, 2012.
- [14] L. Caliò, J. Follana-Berná, S. Kazim, M. Madsen, H.-G. Rubahn, Á. Sastre-Santos and S. Ahmad, *Sustain. Energy Fuels.*, 2017, 1, 2071-2077.
- [15] X. Tang, Q. Liu, C. Wei, X. Lv, Z. Jin, Y. Chen and J. Jiang, *J. Rare Earths.*, 2021, 39, 113-120.
- [16] L. Martín-Gomis, F. Fernández-Lázaro and Á. Sastre-Santos, *J. Mater. Chem. A* . 2014, 2, 15672-15682.
- [17] H.-H. Chou, Y.-H. Chiang, M.-H. Li, P.-S. Shen, H.-J. Wei, C.-L. Mai, P. Chen and C.-Y. Yeh, *ACS Energy Lett.*, 2016, 1, 956-962.
- [18] S. Kazim, F. J. Ramos, P. Gao, M. K. Nazeeruddin, M. Grätzel and S. Ahmad, *Energy Environ. Sci.*, 2015, 8, 1816-1823.
- [19] Z. Yu, L. Wang, X. Mu, C. C. Chen, Y. Wu, J. Cao and Y. Tang, *Angew. Chem. Int. Ed.*, 2021, 133, 6364-6369.
- [20] K. T. Cho, O. Trukhina, C. Roldán-Carmona, M. Ince, P. Gratia, G. Grancini, P. Gao, T. Marszalek, W. Pisula and P. Y. Reddy, *Adv. Energy Mater.*, 2017, 7, 1601733.
- [21] P. Huang, A. Hernández, S. Kazim, J. Follana-Berná, J. Ortiz, L. Lezama, A. n. Sastre-Santos and S. Ahmad, *ACS Appl. Energy Mater.*, 2021, 4, 10124-10135.

- [22] Y. Matsuo, K. Ogumi, I. Jeon, H. Wang and T. Nakagawa, *RSC Adv.*, 2020, 10, 32678-32689.
- [23] Q. Hu, E. Rezaee, L. Dong, Q. Dong, H. Shan, Q. Chen, M. Li, S. Cai, L. Wang and Z.-X. Xu, *Sol. RRL*, 2019, 3, 1900182.
- [24] C. L. Mai, Y. L. Huang, G. H. Lee, S. M. Peng and C. Y. Yeh, *Chem. Eur. J.*, 2008, 14, 5120-5124.
- [25] K. Susumu, P. R. Frail, P. J. Angiolillo and M. J. Therien, *J. Am. Chem. Soc.*, 2006, 128, 8380-8381.
- [26] Y.-H. Chiang, H.-H. Chou, W.-T. Cheng, Y.-R. Li, C.-Y. Yeh and P. Chen, *ACS Energy Lett.*, 2018, 3, 1620-1626.
- [27] D. Molina, M. A. Ruiz-Preciado, B. Carlsen, F. T. Eickemeyer, B. Yang, N. Flores-Díaz, M. J. Álvaro-Martins, K. Nonomura, A. Hagfeldt and Á. Sastre-Santos, *ChemPhotoChem*, 2020, 4, 307-314.
- [28] D. Molina, M. E. El-Khouly, M. El-Kemary, S. Fukuzumi, F. Fernández-Lázaro and Á. Sastre-Santos, *Chem. Eur. J.*, 2016, 22, 17800-17807.
- [29] L. A. Illicachi, J. Urieta-Mora, C. Momblona, A. Molina-Ontoria, J. Calbo, J. Aragó, B. Insuasty, A. Ortiz, E. Ortí and N. Martín, *ChemPlusChem*, 2021, 86, 1006-1013.
- [30] H. Yoshiyama, N. Shibata, T. Sato, S. Nakamura and T. Toru, *ChemComm.*, 2008, 1977-1979.
- [31] H. Ali and J. E. van Lier, Tetrahedron Lett., 2014, 55, 4163-4167.

[32] J. Bisquert, L. Bertoluzzi, I. Mora-Sero and G. Garcia-Belmonte, *J. Phys. Chem. C*, 2014, 118, 18983-18991.





Understanding the interaction of the bifunctionalized cation 3-amino propionic acid iodide with the perovskite MAPI



Reduced dimensional perovskite solar cells have gained remarkable attention due to their optoelectronic properties. Two-dimensional (2D) perovskites are incredibly stable; however, it shows limited charge transport properties due to lower absorption in the visible region. Combining the 2D perovskite with the three-dimensional (3D) perovskite to form a mixed dimensional hybrid maintains the stability and high performance of perovskite solar cells (PSCs). In this chapter, we introduced a biofunctionalized organic cation 3-aminopropanoic acid iodide (3-APAI), doped with pure methylammonium lead iodidebased (MAPbI<sub>3</sub>) for better stability and performance of the PSCs. The biofunctionalized cation is known to coordinate with MAPbI<sub>3</sub> perovskite and is evidenced via XPS, NMR and FTIR spectroscopic method. The PL measurement analysed the carrier recombination dynamics, which showed peak enhancement for the 3-APAI treated perovskite thin film compared to MAPbI<sub>3</sub> film. The admittance spectroscopy justifies the trap density and surface defects mitigation due to the strong interaction of the biofunctionalized cation with the perovskite.

#### **Content**

5.1 Introduction	124-126			
5.2 Result and Discussion	126			
5.2.1 Thin film analysis	126-131			
5.3 Nuclear Magnetic Resonance Spectroscopy	131-133			
5.4 Surface morphology and contact angle measurements in thin				
films	134-135			
5.5 Photovoltaic properties of PSCs	135-138			
5.6 Conclusion	139			
5.7 References	140-144			

#### 5.1 Introduction

Organic-inorganic hybrid perovskite solar cells (PSCs) have gained considerable attention for their implementation to fabricate solar cells, 1-<sup>3</sup> tremendous progress has been made, and power conversion efficiency of 25.5% has been measured in the lab.4 The long charge carrier diffusion length, higher light-absorbing properties, higher hole and electron generating properties, high carrier mobility and tunable bandgap has allowed it to be an attractive next-generation photovoltaic (PV) material.<sup>5-7</sup> Such properties together with wet chemistry processing, attribute easy device fabrication process with low manufacturing cost. Among the lead halide perovskites, the most widely and extensively studied methylammonium lead iodide perovskite (MAPbI<sub>3</sub>) has unique properties of favorable bandgap (1.56 eV), longer charge diffusion lengths, small exciton binding energy as well as higher extinction coefficient.8,9 According to the Shockley-Quessier limit, the optical bandgap of a perovskite-based material of around 1.4 eV are expected to have the optimum light-harvesting ability for the solar cell's applications. In this context, MAPbI<sub>3</sub> favors the nearest band gap value to the theoretical one. Despite the achievement of MAPbI<sub>3</sub> in PSCs, their instability towards heat, moisture, and oxygen has led to an obstacle in the large-scale deployment.<sup>10</sup> If such an intrinsic issue can be overcome, demands for sustainable energy production can be pushed by addressing the insufficient long-term stability of the devices. Various strategies have been employed to enhance the strength of MAPbI<sub>3</sub>, including interface encapsulation technique, engineering,

dimensionality tuning and compositional or additive engineering. 11-14 Another approach to overcoming the instability issue includes employing the reduced dimension engineering, layered perovskite (2D) or 2D/3D hybrids) by incorporating or replacing the A-site cation with another bulkier organic moieties to form bilayer of mixed dimension perovskite with MAPbI<sub>3</sub> to stabilize the PSCs.<sup>15-18</sup> Reduced dimensional perovskite incorporating a wide range of longer chain alkyl ammonium or carboxylic functionalized organic cations has been implemented to develop efficient PSCs with improved stability. 19,20 Intercalation of the large-sized cations enhances the stability of the perovskite structure against environmental stress such as humidity and provides resistance to moisture penetration. Therefore, compositional engineering of largesize organic cations with MAPbI<sub>3</sub> has improved on par with the stability of PSCs.<sup>21</sup> Alternatively, the strong hydrogen bonding favored by the large-size cations when used as an additive arguably improve escalated the PSCs crystallinity and charge extraction properties, forming a crosslink with the 3D and low dimensional perovskite interfaces.<sup>22</sup> The most widely studied large-size cation includes aliphatic and aromatic alkylammonium cations such as butyl ammonium iodide (BAI), cyclopropyl ammonium iodide (CAI), phenyl ethyl ammonium iodide (PEAI), benzyl ethyl amine iodide (BEAI), 4-fluoro phenylmethyl ammonium iodide (FPEAI) into the crystal lattice for on the surface of the 3D based perovskites to form mixed dimensional hybrid perovskite.<sup>23-29</sup> 5-aminovaleric acid iodide (AVAI) was the large-size the reduced-dimensional perovskite with cation reported as bifunctional groups that significantly improved the crystallinity and

stability of the 3D perovskite. <sup>12,19,30</sup> In recent work, hydrogen bonding interaction of AVAI to FAPbI<sub>3</sub> was revealed at the atomic level through solid-state NMR studies, stabilizing it against phase transition ( $\alpha$ -to- $\delta$  phase) of the perovskite. <sup>31</sup>

Substantially, the large-size organic cation aids the long-term stability of the PSCs.<sup>29,32-34</sup> In this work, we employed a sizeable size-organic cation 3-Ammonium propionic acid iodide (3-APAI) having a bifunctional group into MAPbI<sub>3</sub> perovskite. 3-APAI owing to its strong steric effect due to the presence of the bifunctional groups will slow down the crystallization rate and favors large grain formation with good grain connectivity. The introduction of 3-APAI to the perovskite precursor solution led to the formation of highly crystalline perovskites and improved charge carrier properties. Furthermore, the fabricated PSCs with optimized APAI concentration (APAI-PSK, thereafter) showed a photovoltaic performance with a PCE of 16.16% in a mesoscopic heterojunction along with the PSC stability under ambient condition.

#### 5.2 Result and discussion:

### 5.2.1 Thin film analysis (XRD and spectroscopic analysis)

To evaluate the changes in the structural features that regulate the optoelectronic properties, the UV-visible absorption measurements were performed for APAI-MAPbI<sub>3</sub> films coated on the quartz substrates

(Figure 5.1 a). Notably, the optimised 3-APAI content in the perovskite is 0.3 and 0.5 %, based on the methylammonium iodide (MAI) total weight in the precursor solution. We observed that the band edges of the 3-APAI treated perovskite films overlap at the region 755 nm concerning the absorption edge of MAPbI<sub>3</sub> and a similar absorption profile for all the perovskite films is observed. A slight increment in the intensity of the absorption peak can be attributed to the large-grained perovskite and a reduction in the light scattering of the grains.<sup>[1]</sup> The absorption spectra suggest that the presence of 3-APAI at this quantity does not compromise the optical properties of MAPbI<sub>3</sub>.

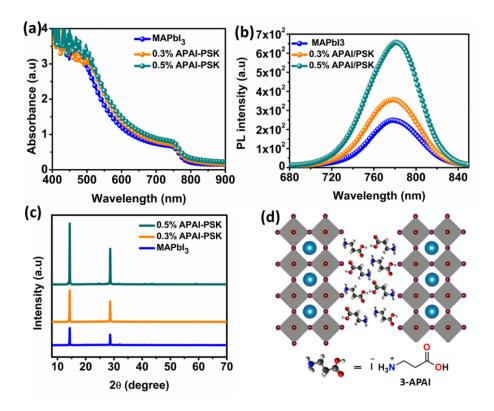


Figure 5.1: (a) UV-Visible absorption (b) photoluminescence spectra (c)X-ray diffraction analysis of MAPbl<sub>3</sub>, 0.3% and 0.5% APAI-PSK films (d) structural model of the 3-APAI-modified-MAPbI<sub>3</sub> reduced mixed dimensional perovskite.

A slight increment in the intensity of the absorption peak could attribute to the formation of a smooth and crystalline layer followed by a reduction in the light scattering of the grains.

To further assess the impact of the 0.5% APAI/PSK perovskite on the emission behaviour we performed the steady-state photoluminescence (PL) measurements (Figure 5.1 b). The peak emission grows in intensity with the added amount of 3-APAI and also display a slight red-shift.<sup>[1]</sup> Notably, the intensified peaks could ascribe to the higher crystallinity induced in the 0.5% APAI/PSK perovskite. The enhanced crystallinity of the films is following UV-Visible measurements and stems from the APAI to lower the surface defects.

X-ray diffraction (XRD) analysis was conducted to investigate the impact of the 3-APAI doping in the perovskite crystallinity and phase change. The XRD pattern shows clear and sharp characteristics of perovskite peaks at 14.41°, 28.80° correspond to (110) and (220) planes of the 0.5% APAI/PSK perovskite film. The prominent peak at 14.41° corresponds to the perovskite peak, which was observed to slightly redshift to a higher angle for APAI-PSK films. Improved crystallinity behaviour of the APAI-PSK layer could be observed from the enhanced intensity of the XRD spectra upon adding the salt at different concentrations (Figure 5.1c).² the interaction of 3APAI salt with the perovskite is depicted in Figure 5.1d.

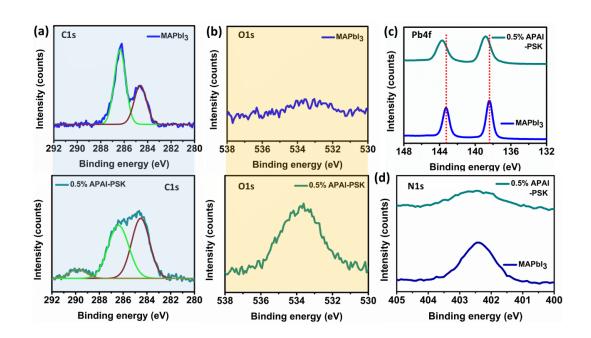


Figure: 5.2 XPS patterns of (a) C 1s spectra MAPbl<sub>3</sub> (top) and 0.5% APAI-PSK (below) films; (b) O 1s spectra MAPbl<sub>3</sub> (top) and 0.5% APAI-PSK (below) films (c) Pb 4f spectra MAPbl<sub>3</sub> and 0.5% APAI-PSK films (d) N 1s spectra MAPbl<sub>3</sub> and 0.5% APAI-PSK films.

The 0.5% APAI/PSK perovskite (APAI-PSK) was further investigated using the X-ray photoelectron spectroscopy (XPS) method. [2] The corelevel spectra pf C 1s, O 1s, Pb 4f and N 1s, are represented in Figure 5.2, a new peak at 289.8 eV appears (Figure 5.2a) for the C1s after adding the optimal concentration of 3-APAI (0.5%) to the MAPbI<sub>3</sub> precursor. This corresponding C 1s peak at 289.8 eV is associated with the oxidised carbon species such as C=O, and O-C=O detected in the films. [3] We noted higher intensity and binding energy for O 1s core-level spectrum peak at 533.72 eV for APAI-PSK, attributed to the binding energy peaks from the carboxylic (-COOH) functional group of 3-APAI moieties (Figure 5.2b). The weaker O 1s signal in the MAPbI<sub>3</sub> film can be ascribed to the chemisorbed oxygen species formed during the preparation of the

samples. The shifting of the Pb 4f spectrum to the higher binding energy ( $\sim 0.4 \text{ eV}$ ) and broadening the N 1s core-level spectra of 0.5% APAI-PSK film suggests that 3-APAI cations have interacted the perovskite MAPbI<sub>3</sub> to form APAI-MAPbI<sub>3</sub>. Similarly, the I 3d core level spectrum (620.3 eV, 631.8 eV) shows a shift ( $\sim 1 \text{ eV}$ ) towards higher binding energy points towards the formation of the APAI-MAPbI<sub>3</sub> (Figure 5.3a). The XPS spectra of 0.3% APAI-PSK (Figure 5.3 b-d), display similar behaviour as of 0.5% APAI-PSK.

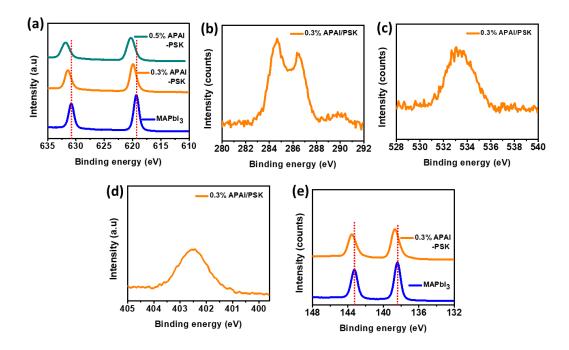


Figure 5.3: XPS spectra (a) I3d peaks MAPbI<sub>3</sub>, 0.3% APAI/PSK and 0.5% APAI/PSK. XPS spectra 0.3% APAI/PSK- (b) C1s (c) O1s (d) N1s (d) Pb4f.

To monitor the extent of interaction of the bifunctional organic cation (3-APAI) with the perovskite (MAPbI<sub>3</sub>), we conducted the Fourier-transform infrared (FTIR) analysis (Figure 5.4a, b). The perovskite solution comprising of 3-APAI and MAPbI<sub>3</sub> were prepared on the quartz substrates and measured.<sup>[3]</sup> The vibrational fingerprints of the

functional group of the organic cation present agree with other spectroscopic investigations. These results suggest that 3-APAI reacts with MAPbI<sub>3</sub> to form (APA)<sub>x</sub>(MA)<sub>1-x</sub>PbI<sub>3</sub>. We noted the characteristic vibrational peak of C=O ( $\upsilon_{C=0}$ ) from -CH<sub>2</sub>COO- at 1701 cm<sup>-1</sup> of APAI-PSK film, slightly shifted to a lower wavenumber as compared to the  $\upsilon_{C=0}$  peak (1707 cm<sup>-1</sup>) in the 3-APAI film (Figure 5.4a). This shift to lower wavenumber suggests that the -C=O from the carboxylic group interacts strongly with perovskite, illustrated by the covalent bond or electron delocalisation formed between the carboxylate functionality and Pb<sup>2+</sup> ions to form an intermediate adduct.

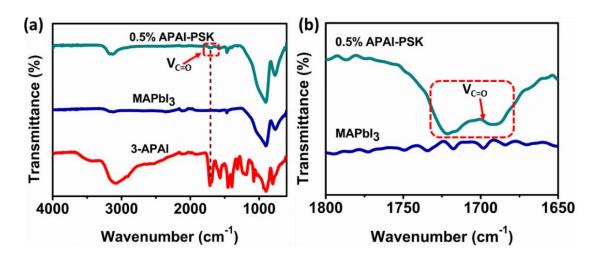


Figure 5.4: FTIR spectra of (a) 3-APAI, MAPbI<sub>3</sub> and 0.5% APAI-PSK (b) magnified FTIR spectra of MAPbI<sub>3</sub> and 0.5% APAI-PSK.

#### **5.3 Nuclear Magnetic Resonance Spectroscopy**

We decipher the effects of the biofunctionalized 3-APAI on the interaction strength with the perovskite precursor, such interactions determine the intermediate state and influence the crystallisation

process of the perovskite layer. [4\_ENREF 4, 5] For, this we probed the interaction between 3-APAI and MAPbI<sub>3</sub> by using <sup>1</sup>H-NMR experiments. The <sup>1</sup>H-NMR of biofunctionalized 3-APAI salt, MAPbI<sub>3</sub> and 0.5% APAI-PSK is illustrated in Figure 5.5a. The peaks at  $\delta$ 2.56,  $\delta$ 2.98 and  $\delta$ 7.66 parts per million (ppm) are assigned to  $-CH_2$  (b),  $-CH_2$  (c) and  $-NH_3^+$  (a) of the 3-APAI moieties. Similarly, peaks at  $\delta$ 2.36 and  $\delta$ 7.47 are assigned to -CH<sub>3</sub> (b') and -NH<sub>3</sub>+ (a) groups of MA+ in MAPbI<sub>3</sub>. Notably, in the 0.5%APAI-PSK, we can observe all the pronounced peaks that indicate the formation of the adduct. The -NH<sub>3</sub>+ peak of 0.5% APAI-PSK significantly broadens, and the -NH<sub>3</sub>+ peaks ( $\delta$ 7.47 and  $\delta$ 7.65 ppm) of MAPbI<sub>3</sub> and 3-APAI cation is noted. This broadening of the peak further confirms the existence of the hydrogen bonding effect in the 0.5% APAI-PSK. Due to the de-shielding effect, hydrogen bonding causes chemical field shifts to a lower field (high ppm). Thus, -OH in the carboxylic group can form hydrogen bonding interaction with the ammonium functionality of the MA+ in MAPbI<sub>3</sub>, thereby explaining the peak broadening at the NH<sub>3</sub>+ region of 0.5% APAI-PSK. [ref] Moreover, the lone pairs of oxygen atom in C=O is expected to form a coordinative bonding with the Pb<sup>2+</sup> of the perovskite and C-O- can also act as a proton acceptor.

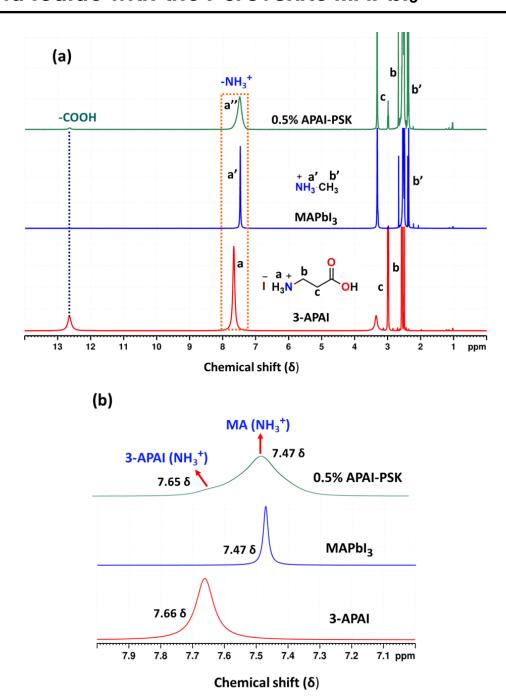


Figure 5.5: (a)  $^1$ H NMR spectra of the bifunctional organic cation 3-APAI, MAPbI $_3$  and 0.5% APAI-PSK recorded in DMSO-d6 (b) magnified  $^1$ H NMR peak from  $\delta6.00$  ppm to  $\delta8.00$  ppm. The solvent residual peak of DMSO-d6 is at  $\delta2.50$  ppm and the corresponding  $H_2O$  peak at  $\delta3.3$  ppm.

#### 5.4 Surface morphology and contact angle measurements in thin films

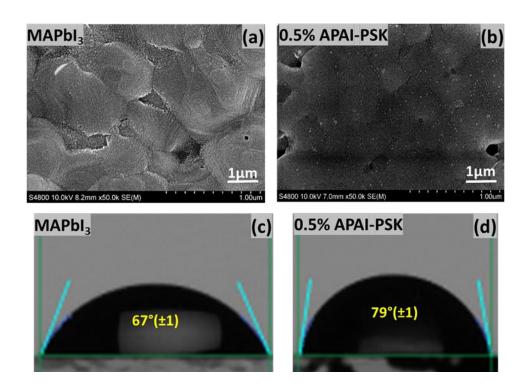


Figure 5.6: Surface SEM images (a) MAPbI<sub>3</sub> (b) 0.5% APAI/PSK. Contact angle measurement (c) MAPbI<sub>3</sub> (d) 0.5% APAI/PSK.

Device performance is impacted by the microstructure and its potential to form a favourable interface. Slow crystallisation favours a larger grain size and better grain connectivity. The coordination phenomenon induced by the carboxylic group of 3-APAI moiety enhances the slow crystallisation process resulting in a compact and even surface of the doped film. To unravel the microstructure, we performed scanning electron microscopy (SEM) measurements for MAPbI<sub>3</sub> and with 3-APAI film (Figure 5.6 a-b). MAPbI<sub>3</sub> film displays large grain size but with less regularity, while 0.5% APAI-PSK shows a more uniformity in grain size

distribution, well-oriented grains with a reduction in grain boundaries. To study the surface properties, we performed goniometry experiments to know the hydrophobic behaviour by drop-casting water on the perovskite film surface (Figure 5.6 c-d). MAPbI $_3$  exhibited a contact angle of 67° (±1) while the 0.5% APAI-PSK film exhibited 79° (±1), which showed higher hydrophobicity that can tolerate more atmospheric attack and contribute to the stability of the PSCs

#### 5.5 Photovoltaic properties of Perovskite solar cells

To evaluate the effect of the 3-APAI on the photovoltaic performances, we fabricated PSCs with the n-i-p structure of FTO/c- & Meso TiO<sub>2</sub>/PSK/Spiro-OMeTAD/Au (Figure 5.7a). The estimated thicknesses of each layer are measured by the cross-sectional SEM image (Figure 5.7b), the thickness of the meso-TiO<sub>2</sub> electron transport layer, perovskite overlayer, and the Spiro-OMeTAD hole transport layer is found to be approximately 191 nm, 405 nm and 162 nm, respectively. The J-V characteristics of MAPbI<sub>3</sub> and APAI-PSK (0.3%, 0.5%) are illustrated (Figure 5.7c), and the corresponding PV parameters are listed in Table 5.1. The PSCs with 0.5% 3-APAI measured a PCE of 16.16% (V<sub>oc</sub> of 997 mV, J<sub>sc</sub> of 20.81 mA/cm<sup>2</sup> and FF of 77.67 %). The PSC based on MAPbI<sub>3</sub> outperformed which yielded a 17.17% PCE (V<sub>oc</sub> of 1013 mV, J<sub>sc</sub> of 22.65 mA/cm<sup>2</sup> and FF of 74.79%). The improved fill factor and open-circuit voltage with the use of 0.5% APAI are ascribed

to the progressive reduction in the surface defects and device resistance. The 0.5% APAI addition into the PSCs is noted to give optimized performance as of 0.3% APAI-PSK. However, the fill factor remains unchanged for both the concentrations of the 3-APAI treated PSCs. The enhancement in the FF appears to be the main factor for the increment in the PCE of the PSCs, additionally, the wettability of the perovskite formed with 3-APAI remains uniform and favours the coverage for the subsequent Spiro-OMeTAD as HTL layer. The statistical of PSCs performances based on MAPbI<sub>3</sub> and 3-APAI treatment is depicted in Figure 5.8. The external quantum efficiency (EQE) (Figure 5.7d), which covers the range from 300-800 nm with greater than > 80 %, is in agreement with the slight increase in absorption achieved in the APAIadded perovskites. The integrated Isc current derived from the EQE spectra is by and large in accordance with the  $I_{\rm sc}$  values derived from the *I-V* curve, with a slight difference which can be explained due to the intensity of light used in both measurements. The PSCs steady-state power output (SPO) for 300 seconds by measuring the photocurrent density under continuous one sun illumination under ambient conditions with a relative humidity of 50-60 % (Figure 5.7 e) suggest the stable SPO. We noted that the 3-APAI treated PSCs showed induce stability than of pristine MAPbI<sub>3</sub> (Figure 5.7 f), and this was also replicated when stored in a dry box (relative humidity < 15 %) and measured periodically over time up to 250 hours. The higher degree of binding between 3-APAI and MAPbI<sub>3</sub> through the biofunctionalized groups (-COO- and -NH<sub>3</sub>+ in 3-APAI) can be the critical factor in

improving the stability and performances of the PSCs as compared to the MAPbI3 one.

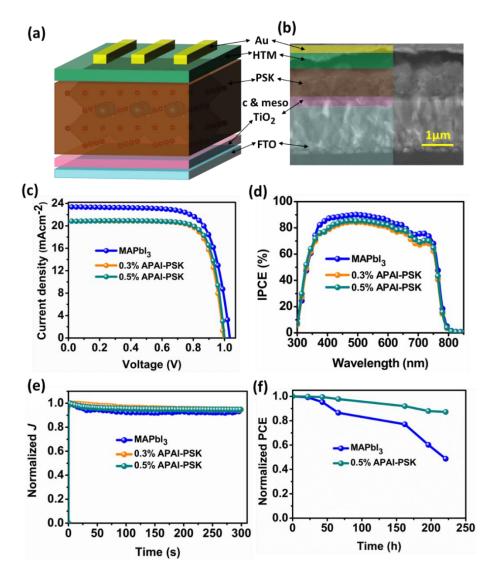


Figure: 5.7 (a) Device architecture in *n-i-p* configuration (b) cross-sectional SEM image of 0.5% APAI-PSK PSC (c) current-voltage spectral characteristics of PSCs based on MAPbl<sub>3</sub>, 0.3% APAI-PSK and 0.5% APAI-PSK under Air-Mass (AM) 1.5G illumination (d) EQE graphs of pristine and different passivated devices (d) steady state output for 300 s for PSCs based on MAPbl<sub>3</sub>, 0.3% APAI-PSK and 0.5% APAI-PSK (f) Device stability over time for PSCs based on MAPbl<sub>3</sub>, and 0.5% APAI-PSK.

**Table:5.1** Photovoltaic parameters

Sample	V <sub>oc</sub> [mV]	Jsc [mA/cm <sup>2</sup> ]	FF [%]	PCE [%]
MAPbI <sub>3</sub>	1013	22.64	74.79	17.17
Average	1022 ± 09	21.92 ± 0.78	74.79 ± 2.13	16.62± 0.54
0.3%	993	20.82	76.87	15.90
APAI-PSK	950 ± 43	20.70± 0.12	$76.04 \pm 0.82$	15.08± 0.82
0.5%	997	20.81	77.67	16.16
APAI-PSK	991 ± 08	20.77± 0.038	77.51 ± 0.15	16.04± 0.12

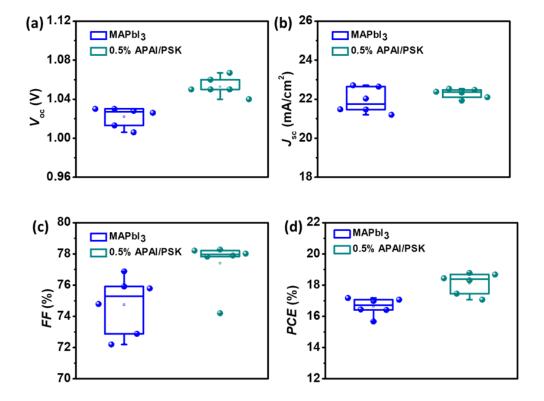


Figure 5.8: Device statistics (a)  $V_{oc}$  (b)  $J_{sc}$  (c) FF (d) PCE.

#### 5.7 Conclusion

To summarize, we achieved the mixed-cation perovskite after treating 3-APAI salt into the MAPbI<sub>3</sub> precursor solution. The biofunctionalized cation is found to be coordinated with MAPbI<sub>3</sub> through H-bonding and is unravelled via an array of spectroscopic techniques. The PL measurement showed enhancement in the peak intensity with 3-APAI treated perovskite as compared to the MAPbI<sub>3</sub> film and red shifting. We noted 3-APAI-treatment on the PV performances induce H-bonding to give higher voltage and FF in the PSCs, and subsequently an enhancement in the PCE that also showed stability upon prolonged storage. We envisage that introducing 3-APAI in the perovskite precursor solution could improve the photovoltaic performances, lowering the trap states, and pave the way for reliable solar cells.

#### **5.8 References**

- 1. T. Zhou, H. Lai, T. Liu, D. Lu, X. Wan, X. Zhang, Y. Liu and Y. Chen, Adv. Mater., 2019, 31, 1901242.
- 2. A. Q. Alanazi, D. J. Kubicki, D. Prochowicz, E. A. Alharbi, M. E. Bouduban, F. Jahanbakhshi, M. Mladenović, J. V. Milić, F. Giordano and D. Ren, J. Am. Chem. Soc, 2019, 141, 17659-17669.
- 3. Q. Yao, Q. Xue, Z. Li, K. Zhang, T. Zhang, N. Li, S. Yang, C. J. Brabec, H. L. Yip and Y. Cao, Adv. Mater., 2020, 32, 2000571.
- 4. N. Wei, Y. Chen, Y. Miao, T. Zhang, X. Wang, H. Wei and Y. Zhao, J. Phys. Chem. Lett., 2020, 11, 8170-8176.
- 5. G. Han, T. M. Koh, J. Li, B. Febriansyah, Y. Fang, N. F. Jamaludin, Y. F. Ng, P. J. S. Rana, S. Mhaisalkar and N. Mathews, ACS Appl. Energy Mater., 2021, 4, 2716-2723.
- 6. R. A. Kerner, T. H. Schloemer, P. Schulz, J. J. Berry, J. Schwartz, A. Sellinger and B. P. Rand, J. Mater. Chem. C, 2019, 7, 5251-5259.
- 7. P. Li, Y. Zhang, C. Liang, G. Xing, X. Liu, F. Li, X. Liu, X. Hu, G. Shao and Y. Song, Adv. Mater., 2018, 30, 1805323.
- 8. J. Li, T. Jiu, C. Duan, Y. Wang, H. Zhang, H. Jian, Y. Zhao, N. Wang, C. Huang and Y. Li, Nano Energy, 2018, 46, 331-337.
- 9. C. Lermer, S. T. Birkhold, I. L. Moudrakovski, P. Mayer, L. M. Schoop, L. Schmidt-Mende and B. V. Lotsch, Chem. Mater., 2016, 28, 6560-6566.

- 10. Y.-B. Lu, W.-Y. Cong, C. Guan, H. Sun, Y. Xin, K. Wang and S. Song, J. Mater. Chem. A 2019, 7, 27469-27474.
- 11. Y. Wu, F. Xie, H. Chen, X. Yang, H. Su, M. Cai, Z. Zhou, T. Noda and L. Han, Adv. Mater., 2017, 29, 1701073.
- 12. T. Ye, A. Bruno, G. Han, T. M. Koh, J. Li, N. F. Jamaludin, C. Soci, S. G. Mhaisalkar and W. L. Leong, Adv. Funct. Mater., 2018, 28, 1801654.
- 13. N. J. Jeon, J. H. Noh, W. S. Yang, Y. C. Kim, S. Ryu, J. Seo and S. I. Seok, Nature, 2015, 517, 476-480.
- 14. M. Pegu, S. Kazim, P. Huang, L. Lezama and S. Ahmad, J. Mater. Chem. C, 2021.
- 15. S. Jeong, S. Seo, H. Yang, H. Park, S. Shin, H. Ahn, D. Lee, J. H. Park, N. G. Park and H. Shin, Adv. Energy Mater., 2021, 11, 2102236.
- 16. M. Pegu, M. P. Haris, S. Kazim and S. Ahmad, Emergent Mater., 2020, 1-28.
- 17. G. Grancini and M. K. Nazeeruddin, Nat. Rev. Mater., 2019, 4, 4-22.
- 18. F. Zhang, H. Lu, J. Tong, J. J. Berry, M. C. Beard and K. Zhu, Energy Environ. Sci., 2020, 13, 1154-1186.
- 19. G. Grancini, C. Roldán-Carmona, I. Zimmermann, E. Mosconi, X. Lee, D. Martineau, S. Narbey, F. Oswald, F. De Angelis and M. Graetzel, Nat. Commun., 2017, 8, 1-8.

- 20. P. Huang, S. Kazim, M. Wang and S. Ahmad, ACS Energy Lett., 2019, 4, 2960-2974.
- 21. M. H. Li, H. H. Yeh, Y. H. Chiang, U. S. Jeng, C. J. Su, H. W. Shiu, Y. J. Hsu, N. Kosugi, T. Ohigashi and Y. A. Chen, Adv, Mater., 2018, 30, 1801401.
- 22. Q. Yao, Q. Xue, Z. Li, K. Zhang, T. Zhang, N. Li, S. Yang, C. J. Brabec, H. L. Yip and Y. Cao, Adv. Mater., 2020, 32, 2000571.
- 23. A. Krishna, S. Gottis, M. K. Nazeeruddin and F. Sauvage, Adv. Funct. Mater., 2019, 29, 1806482.
- 24. C. Ran, J. Xi, W. Gao, F. Yuan, T. Lei, B. Jiao, X. Hou and Z. Wu, ACS Energy Lett., 2018, 3, 713-721.
- 25. A. H. Proppe, A. Johnston, S. Teale, A. Mahata, R. Quintero-Bermudez, E. H. Jung, L. Grater, T. Cui, T. Filleter and C.-Y. Kim, Nat. Commun., 2021, 12, 1-9.
- 26. A. A. Sutanto, P. Caprioglio, N. Drigo, Y. J. Hofstetter, I. Garcia-Benito, V. I. Queloz, D. Neher, M. K. Nazeeruddin, M. Stolterfoht and Y. Vaynzof, Chem. 2021, 7, 1903-1916.
- 27. M. Pegu, S. Kazim, T. Buffeteau, D. M. Bassani and S. Ahmad, ACS Appl. Mater. Interfaces 2021, 13, 48219-48227.
- 28. D. Prochowicz, P. Yadav, M. Saliba, M. Saski, S. M. Zakeeruddin, J. Lewinski and M. Gratzel, ACS Appl. Mater. Interfaces, 2017, 9, 28418-28425.

- 29. T. Niu, Y. M. Xie, Q. Xue, S. Xun, Q. Yao, F. Zhen, W. Yan, H. Li, J. L. Brédas and H. L. Yip, Adv. Energy Mater., 2022, 12, 2102973.
- 30. E. V. Péan, C. S. De Castro, S. Dimitrov, F. De Rossi, S. Meroni, J. Baker, T. Watson and M. L. Davies, Adv. Funct. Mater., 2020, 30, 1909839.
- 31. A. Q. Alanazi, D. J. Kubicki, D. Prochowicz, E. A. Alharbi, M. E. Bouduban, F. Jahanbakhshi, M. Mladenović, J. V. Milić, F. Giordano and D. Ren, J. Am. Chem. Soc, 2019, 141, 17659-17669.
- 32. M. A. Mahmud, T. Duong, J. Peng, Y. Wu, H. Shen, D. Walter, H. T. Nguyen, N. Mozaffari, G. D. Tabi and K. R. Catchpole, Adv. Funct. Mater., 2021, 2009164.
- 33. Y. Zhang, F. Li, K.-J. Jiang, J.-H. Huang, H. Wang, H. Fan, P. Wang, C.-M. Liu, L.-P. Zhang and Y. Song, J. Mater. Chem. A 2018, 6, 17867-17873.
- 34. J. M. Hoffman, I. Hadar, X. Li, W. Ke, E. S. Vasileiadou, J. Strzalka, L. X. Chen and M. G. Kanatzidis, Chem, 2022.
- 35. T. Zhou, H. Lai, T. Liu, D. Lu, X. Wan, X. Zhang, Y. Liu and Y. Chen, Adv. Mater., 2019, 31, 1901242.
- 36. N. Wei, Y. Chen, Y. Miao, T. Zhang, X. Wang, H. Wei and Y. Zhao, J. Phys. Chem. Lett., 2020, 11, 8170-8176.
- 37. G. Han, T. M. Koh, J. Li, B. Febriansyah, Y. Fang, N. F. Jamaludin, Y. F. Ng, P. J. S. Rana, S. Mhaisalkar and N. Mathews, ACS Appl. Energy Mater., 2021, 4, 2716-2723.

- 38. R. A. Kerner, T. H. Schloemer, P. Schulz, J. J. Berry, J. Schwartz, A. Sellinger and B. P. Rand, J. Mater. Chem. C, 2019, 7, 5251-5259.
- 39. P. Li, Y. Zhang, C. Liang, G. Xing, X. Liu, F. Li, X. Liu, X. Hu, G. Shao and Y. Song, Adv. Mater., 2018, 30, 1805323.
- 40. L. Yang, X. Ma, X. Shang, D. Gao, C. Wang, M. Li, C. Chen, B. Zhang, S. Xu and S. Zheng, Sol. RRL, 2021, 5, 2100352.

#### Chapter 6

Deciphering the Orientation of the Aromatic Spacer Cation in Bilayer Perovskite Solar Cells through Spectroscopic Techniques



Slowing the degradation of perovskite-based solar cells (PSCs) is of substantial interest. We engineered the surface by introducing a hydrophobic overlayer on a 3-dimensional perovskite using fluorinated or nonfluorinated aryl ammonium cation spacers. The placement of a fluoroarene cation allows the formation of a bilayer structure i.e., layered/3dimensional perovskites. By doing so, the surface hydrophobic character increases notably by the virtue of perfluorinated benzene moiety. The fabricated devices thereof gave higher performance and longevity than control devices, in addition to mitigating reliability. The fluorophenethylammonium iodide (FPEAI) based devices showed lower nonradiative carrier recombination. To decipher the orientation of the spacer cation in this bilayer structure, we probed the surface by polarizationreflection-absorption spectroscopy infrared modulated and substantial differences in the orientation due to the presence of fluorine substitution. We hypothesize that the stronger van der Waals interactions due to the higher electronegativity in FPEAI govern the orientation, performance enhancement, and acts as a barrier to moisture decomposition.

This chapter is published as *Pegu* et al. *ACS Appl. Mater. Interfaces* 2021, 13, 40, 48219–48227

DOI: https://doi.org/10.1021/acsami.1c13166

#### **Content:**

6.1 Introduction
6.2 Result and Discussion
6.2.1 PM-IRRAS study on bilayer perovskites 149-15
6.2.2 Thin film measurements 153-15
6.3 Surface morphology and contact angle measurements 159-16
6.4 Photovoltaic properties of PSCs
6.5 Admittance spectroscopy measurements
6.5 Conclusion
6.6 References

#### 6.1 Introduction

Hybrid perovskite-based solar cells (PSCs) have witnessed tremendous progress and a rise in performance and reliability.<sup>[1, 2]</sup> It is known that the photovoltaic (PV) power conversion efficiency (PCE) and reliability are influenced by the quality of the microcrystalline grain, boundary size, and surface properties.[3] The use of layered perovskites has shown improvement, and efforts have focussed on the employment of interfacial materials to increase reliability.<sup>[4-6]</sup> In the case of bilayer perovskites, the crystalline growth condition and orientation of these materials are of paramount importance as they impact interfacial losses and thus PCE. Allinorganic based PSCs display improved stability but also demand higher annealing temperatures, possess relatively lower PCE, and show phase transformation.<sup>[7]</sup> Annealing at high temperatures (>250 °C) is not compatible with the inert atmosphere fabrication process such as glove box. Dimensionally reduced perovskites display higher moisture resistance and lower thermal diffusion compared to 3-dimensional (bulk) perovskites.[8-10] However, the high quantum well, lower quantum and dielectric confinement, and anisotropic charge transport properties<sup>[11, 12]</sup> make free carriers difficult to generate in pristine layered perovskites, and the high density of acceptor type trap states at the surface limits PCE values.[13] One approach is to use bilayer formation to increase the light-harvesting properties of the active layers.[14] Nevertheless, achieving PCE similar to bulk perovskites along with high operational stability remains challenging.[15] Controlled deposition of a hydrophobic, uniform, and conformal layer on top of a bulk perovskite has been used to mitigate dispersion forces. Arguably, fluorinated compounds

with carbon-fluorine (C-F) bonds having low polarizability are a contributing factor to the stability of the material and are deterrence towards moisture.<sup>[16, 17]</sup> Fluorinated compounds contribute to the formation of hydrogen-bonding interactions between electronegative fluorine atoms and the surface of perovskites.<sup>[18]</sup>

The use of partially fluorinated aliphatic amines for the passivation of interfacial defects and fluorous aliphatic spacer groups within layered (fashionably termed 2D) perovskites gave PCE close to 20%, without hysteresis correction and scan speed-independent maximum power point (MPP) data reported.<sup>[19]</sup> Similarly, fluorinated tin perovskites were also reported.<sup>[20]</sup> Additionally, employing fluoro-halogenated layers as molecular moisture barriers for stability purposes can increase reliability by forming halogen bonding with the bulk perovskites.<sup>[21, 22]</sup> We reported the use of a perfluoroalkyl-substituted imidazolium derivative as a doping agent compared to iodopentafluorophenol, and the hydrophobic nature of the dopant allows the formation of a protective layer.<sup>[23]</sup> With the surge in the reports dealing with the use of bilayers/passivation/doping agents to improve PCE and moisture resistance, a rapid and effective approach to deduce the molecular orientation of the layer is paramount in deciphering its action.<sup>[24]</sup>

In addition to <u>ENREF 20</u> imparting moisture stability, the perfluorinated benzene unit possesses electronic properties conducive towards hole extraction while constraining ion migration. Both ion migration and moisture-induced degradation negatively affect the reliability of PSCs,<sup>[25]</sup> and an overlayer can intrinsically mitigate such issues. Ion migration, axial rotation, and moisture-induced degradation are interwoven as surface-

bound water and ions can diffuse into the absorber layer through grain boundaries to accelerate degradation.<sup>[26]</sup>

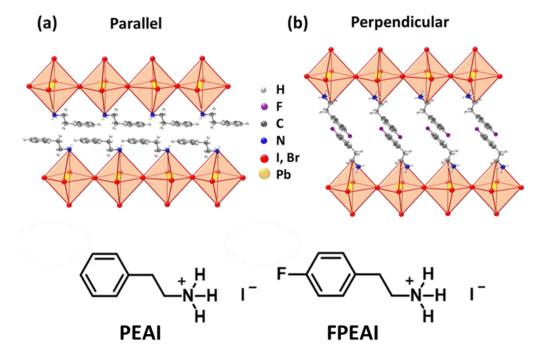


Figure 6.1. Proposed molecular orientation of (a) PEAI, flat (parallel) orientation, and (b) FPEAI, vertical (perpendicular) orientation.

For layered perovskites, *in situ* growth using bulky organic cations derived from organic salts and the corresponding halides is widely adopted. These react with excess PbI<sub>2</sub> present on the surface to form a layered structure post-annealing through the interaction of the Pb-I framework of the bulk perovskite. Placement of a low dimensional perovskite facilitates the nucleation at the interfaces, resulting in minimal structural disorder and higher charge carrier lifetimes.<sup>[27]</sup> While fluoroarene bilayer-based PSCs display higher operational stability under humid conditions.<sup>[17]</sup> In our efforts to probe interfacial layers that passivate surface defects or add functionality, we focus on the role played by surface mitigation and its impact on stability. Particularly, the non-random orientation of the interfacial layers is decisive

in controlling the electronic effects. However, elucidation of a single or molecular layer's organizational order can be extremely challenging, especially when they are placed on hybrid materials due to the inherent complexity of underlying layers. Recently, techniques such as grazing incidence wide-angle X-rays diffraction (GIWAXD), combined nuclear magnetic resonance (NMR), X-ray crystallography, and ab-initio calculations have been used to glean information concerning nature, thickness, and orientation, e.g. PEA spacers in directing the formation of bilayer hybrid perovskites.<sup>[28, 29]</sup> ENREF 26 Considering the plethora of possible interfacial layer compositions, a straightforward technique to probe the composition and organization of such materials would be extremely valuable. Herein, we polarization-modulated infrared show that reflection-absorption spectroscopy (PM-IRRAS) is capable of rapidly providing the necessary information, without using sophisticated techniques and time investment. PM-IRRAS is a surface-specific IR technique that combines the electric field enhancement induced by IRRAS and the surface selection rules for the study of self-assembled monolayers.[30, 31] The shifting in the energy of the IR transitions can be assigned to the interaction of the various functional groups present with the surface and, similarly to IR spectroscopy, it provides information on a material's composition and organization. It is a nondestructive technique in which band intensities can be used to obtain information on the relative proportion and orientation of different functional groups to the surface. The latter is of significant interest, as it allows one to specifically assign certain orientations to portions of a molecule that may be partially organized on a surface whereas another part of the same molecule is more randomly oriented. To demonstrate the utility

of this approach, we have re-examined interfacial layers formed by PEAI and FPEAI, which form parallel and perpendicularly oriented monolayers, respectively (Figure 6.1).

Our results confirm that both PEAI and FPEAI are non-randomly ordered on the surface and display different orientations. PEAI lies flat (long axis parallel) on the surface whereas FPEAI is found to be vertically oriented. Moreover, the surface concentration/density of PEAI is constant and is independent of the concentration used for deposition (0.3 or 0.7%), whereas in the case of the FPEAI the surface concentration is higher at 0.7% than at 0.3%. From this, we may rationalize the advantage of the FPEAI over the non-fluorinated or aliphatic counterpart even though both PEAI and FPEAI improve the crystallinity and moisture tolerance significantly.<sup>[32]</sup> We measured a PCE of 20.63% along with a significant increase in stability than of control and PEAI based PSCs, corroborating that a single F atom in PEA improves the material's moisture resistance.<sup>[5]</sup>

#### 6.2. Result and Discussions

#### 6.2.1 PM-IRRAS study on bilayer perovskites

The PM-IRRAS spectra of the pristine perovskites and samples treated with 0.3% and 0.7% FPEAI are shown in Figure 6.2 a, along with the isotropic (non-oriented) spectra of FPEAI and the assignment of the principal vibrations. From this we can deduce that the spectral signature of FPEAI is visible in the bilayer perovskites and the intensity of the FPEAI bands

increases by a factor of 2.15 which is close to the ratio of concentrations used for deposition (0.7% and 0.3%).

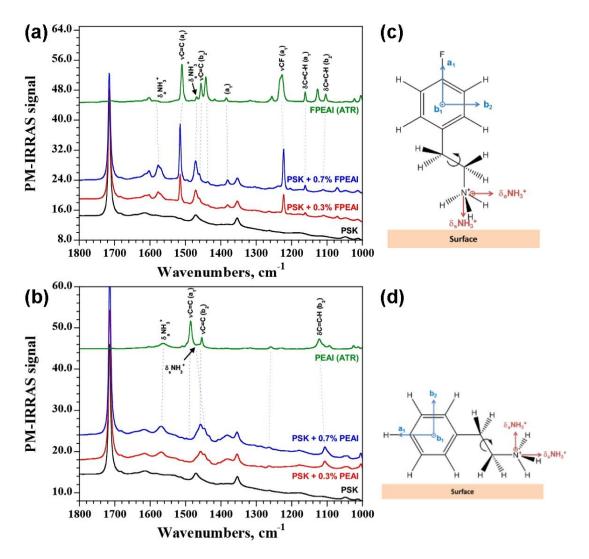


Figure 6.2. PM-IRRAS spectra of pristine PSK (black), PSK + 0.3% (red) and 0.7% (blue) of (a): FPEAI and (b): PEAI. The assignment of the vibrations is from the ATR spectrum (green) of an isotropic sample of the ammonium iodide salt. Proposed orientation of FPEAI (c) and PEAI (d) on the PSK surface in agreement with the enhancement of those transitions that are perpendicular to the surface and suppression of the transitions parallel to the surface. The NH<sub>3</sub> fragment is disordered and shows no orientational preference.

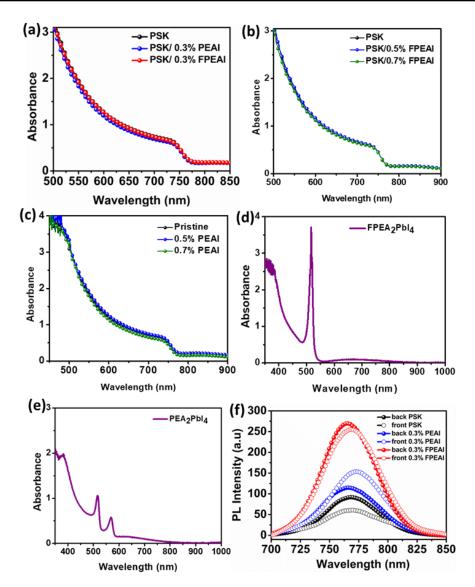


Figure 6.3. UV-Visible absorption spectra of (a) PSK and PSK with 0.3% PEAI/FEAI and (b) PSK and PSK with 0.5% and 0.7% PEAI (c) PSK and PSK with 0.5% and 0.7% FPEAI (d) FPEA<sub>2</sub>PbI<sub>4</sub> (e) PEA<sub>2</sub>PbI<sub>4</sub> (f) photoluminescence emission spectra of front-side and back-side of the thin films.

Concerning the orientation of the molecules on the surface, we note that the bands possessing  $a_1$  symmetry (aligned with the C–F bond) are enhanced, whereas the phenyl ring vibrations possessing  $b_1$  or  $b_2$  symmetry (perpendicular to the C–F bond) are strongly reduced. From this, we can conclude that the molecule is preferentially oriented with the C–F bond

perpendicular to the surface (Figure 6.2 c). There is no difference in the intensities of the  $\delta_a NH_3^+$  vibrations to the  $\delta_s NH_3^+$ , suggesting no preferential orientation of the  $NH_3^+$  group. From this information, we conclude that the FPEAI molecules are oriented vertically. The structure is shown with the  $NH_3$  oriented towards the surface, but this is arbitrary although in agreement with previous studies. [33, 34] A small shift in the C–F vibration is observed, which would be in agreement with the possibility that the fluorine atom may be interacting with the surface.

A similar situation is seen in the PM-IRRAS spectra of PSK treated with 0.3% and 0.7% PEAI solutions (Figure 6.2 b). Despite the absence of the easily identifiable C-F bond, the spectral signature of PEAI is nonetheless evident in the treated samples, albeit less intense and somewhat broader than for FPEAI. In the case of PEAI, we note that the band intensities for samples prepared using 0.7% and 0.3% solutions are similar (ratio = 1.44 vs. expected 2.33). In the absence of the C–F bond, determining the orientation of the molecule is more challenging. Here, the vibrations of the phenyl ring can be used to provide orientational information. We can see that the bands possessing  $a_1$  symmetry (aligned with the long axis of the molecule) are decreased in intensity when the molecule is on the surface. This indicates that the molecule is preferentially lying with the long axis parallel to the surface. Additionally, if we compare the intensity of the vibrations with b symmetry, we can deduce that the phenyl ring is not flat on the surface, but it is lying edge-on or at an angle since vibrations possessing  $b_2$  symmetry are visible. Furthermore, no difference in the intensities of the  $\delta_a NH_3^+$  vibrations to the  $\delta_s NH_3^+$  was noted, signifying no preferential orientation of the  $NH_3^+$ group. These observations suggest that the PEAI molecule is oriented

horizontally with the phenyl ring perpendicular to the surface (Figure 6.2 d). Remarkably, two bands from the  $\delta_s NH_{3^+}$  vibration (1446 and 1433 cm<sup>-1</sup>) are present, implying two different environments for the  $NH_3$  group. The two different orientations of the molecule may explain the reduced surface coverage observed for PEAI as compared to FPEAI. The vertical orientation of FPEAI occupies a smaller surface area than PEAI which on the contrary lies flat on the surface. Upon increasing the concentration from 0.3% to 0.7%, the FPEAI molecules can pack vertically on the surface whereas the horizontal surface packing of PEAI is already close to the maximum at 0.3% concentration.

#### 6.2.2 Thin film measurements (Spectroscopy and XRD)

The UV-visible absorbance spectra of the pristine and of bilayer perovskites (Figure 6.3 a-c) suggest that varying the percentage of either FPEAI or PEAI has a negligible effect on the perovskite's absorption. The absorbance profile remains unchanged after three weeks of exposure to the ambient atmosphere. The absorbance spectra of pure-phase layered perovskites (FPEA<sub>2</sub>PbI<sub>4</sub>, PEA<sub>2</sub>PbI<sub>4</sub>) were also measured to identify their optical behavior (Figure 6.3 d, e).

Steady-state photoluminescence (PL) experiments were made in which the samples were excited either through the glass substrate or directly on the thin film side (Figure 6.3 f). Quartz substrate without and with 0.3 % PEAI or 0.3 % FPEAI treatment on perovskites was used with an excitation wavelength of 450 nm having a penetration depth of less than 100 nm.<sup>[35]</sup>

When the thin film sample was excited from the front side (Figure 6.3 f), this will excite sites that are close to the PEAI or FPEAI/PSK interface, while in case of excitation from the back (glass) side, the beam will strike firstly to the perovskite layer. We noted substantial differences in both side and front illumination shows red shifting in the case of PEAI treated films while backside illumination evidences a blue shift in the case of PEAI and FPEAI treated perovskite films. The small amount of PEAI on the perovskite surface causes a redshift of the emission of the perovskite. [36] The PL emission peak of the bulk PSK is c.a. 768 nm and 770 nm when excited from the quartz (back) and front side respectively, which is consistent with the absorption results. The small shift in the peak position of bulk PSK might be due to the variation in crystal size and microstructure on the top and bottom of the surface.[37] Upon formation of low-dimensional perovskite layers due to PEAI/FPEAI treatment, the PL intensity increases irrespective of the illumination side. We also noted a stronger PL intensity that is blue-shifted (2-3 nm) for FPEAI treated films (irrespective of excitation side). The observation of strong PL intensity in the case of FPEAI treated perovskite regardless of the illumination side can be ascribed to the filling of traps when less concentrated FPEAI was used which diffuses inside the grain along with the grain boundaries and the surface during the annealing process.

Chapter 6. Deciphering the Orientation of the Aromatic Spacer Cation in Bilayer Perovskite Solar Cells through Spectroscopic Techniques.

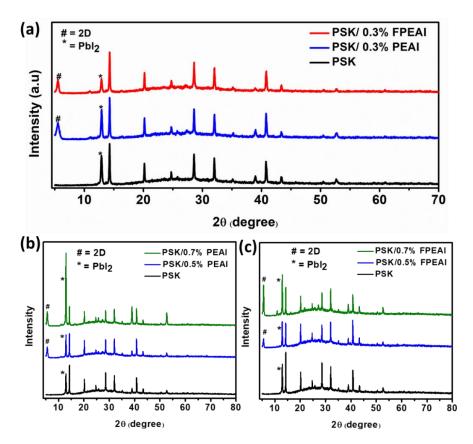


Figure 6.4. X-ray diffraction patterns for (a) pristine PSK and 0.3% (PEAI, FPEAI) bilayer perovskite, (b) PEAI (0.5%, 0.7%), and (c) FPEAI (0.5%, 0.7%) respectively.

X-ray diffraction analyses were performed to elucidate changes in the structural properties (Figure 6.4 a) for pristine and 0.3% treated bilayer perovskites. The PEAI and FPEAI dissolved in isopropanol (IPA) were coated on the bulk (3D) perovskite layer and annealed at  $100^{\circ}$ C to allow *in situ* growth for the formation of a bilayer perovskite. The diffractograms are unchanged and this suggests that the over layers of the organic spacer group on top of bulk perovskites do not substantially alter the structure. The peak at  $12.8^{\circ}$  is ascribed to the excess PbI<sub>2</sub> phase present in the films. The presence of well-defined layered perovskite is reflected from the characteristic peak patterns at lower angle  $2\theta$  region (<10°), which are

associated with the formation of a bilayer perovskite. The increase in signal of the perovskite peak at 14.33° indicates higher crystallinity and large grain size of the films. The X-ray diffraction pattern with 0.5% and 0.7% treated bilayer perovskite (Figure 6.4 b, c), reflects the high-intensity peaks of layered perovskite with increment in the concentration of the bulk layer.

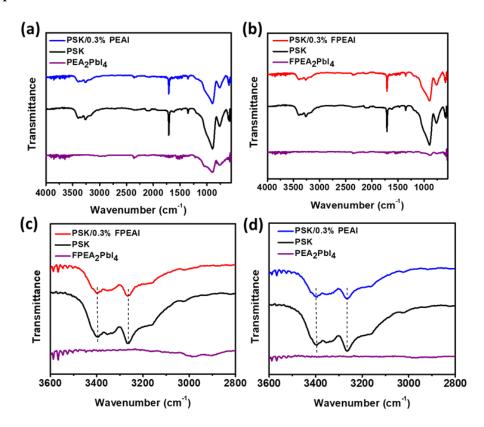


Figure 6.5: FTIR spectra of a) 2D FPEA2PbI4, pristine PSK, 0.3% FPEAI treated PSK thin films (b) 2D PEA2PbI4, pristine PSK, 0.3% PEAI treated PSK thin films (c) Enlarged region showing N-H stretching region of 2D FPEA2PbI4, pristine PSK, 0.3% FPEAI treated PSK thin films (d) Enlarged region showing N-H stretching region of 2D FPEA2PbI4, pristine PSK, 0.3% FPEAI treated PSK thin films

To probe the molecular interactions between the bulk perovskite and the bulky organic cations, we collected FTIR spectra for the corresponding pure phase layered perovskite, bulk, and the bilayer perovskite layers (Figure

6.5).<sup>[19]</sup> A similar profile was noted in all the samples (pristine and 0.3% PEAI, FPEAI treated) in the higher wavenumber region (3000–3500 cm<sup>-1</sup>), which corresponds to the N-H stretching frequency of the formamidinium cation (FA) cations.

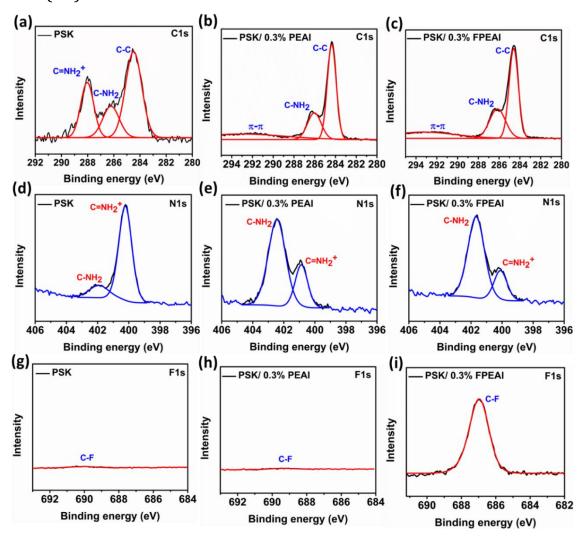


Figure 6.6. X-ray photoelectron spectroscopy (XPS), (a-c) high-resolution deconvoluted spectra of C1s, (d-f) N 1s peaks, and (g-i) F 1s peaks of the pristine and bilayer perovskite.

To investigate the elemental distribution on the surface, we performed X-ray photoelectron spectroscopy (XPS) of thin films. The core-level peaks of C, N, and F (Figure 6.6) suggest the formation of bilayer perovskite, while the

strong C1s spectra in the profile are attributed to the *ex-situ* measurements condition (Figure 6.6 a-c). In the case of bulk perovskite, the presence of MA and FA components from the C1s and N1s spectra is supported by the presence of peaks at 286.21 eV and 288.03 eV. While the N1s peaks of MA and FA with 400.24 eV and 401.9 eV positions are per report. Layered perovskites with PEAI and FPEAI display a characteristic peak at the binding energy of 292.03 eV due to the presence of the aromatic (phenyl) group in the PEA+ or FPEA+ cations. The peaks at 402.44 eV and 401.68 eV of the N1s spectra (Figure 6.6 d-f) are assigned to the C-N of the amino groups in the cations (PEAI, FPEAI). The fluoro substitution at the phenyl group (FPEA+) was confirmed by the appearance of a 686.97 eV peak in the F1s spectrum (Figure 6.6 g-i). The Pb 4f and I 3d peaks of the bulk as well as the layered perovskite (Figure 6.7) shows the different binding energies of the organic moieties on the surface of the bulk perovskite.

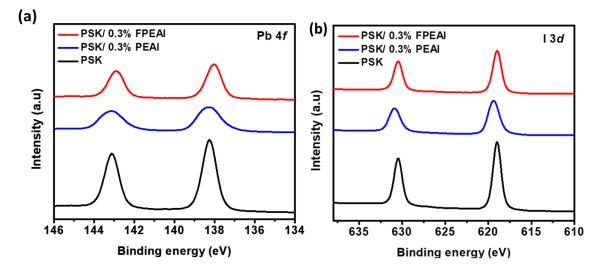


Figure 6.7: X-ray photoelectron spectroscopy (XPS), a) high resolution deconvoluted spectra of (a) Pb 4*f*, (b) I 3*d*, peaks of the pristine and bilayer perovskites

Chapter 6. Deciphering the Orientation of the Aromatic Spacer Cation in Bilayer Perovskite Solar Cells through Spectroscopic Techniques.

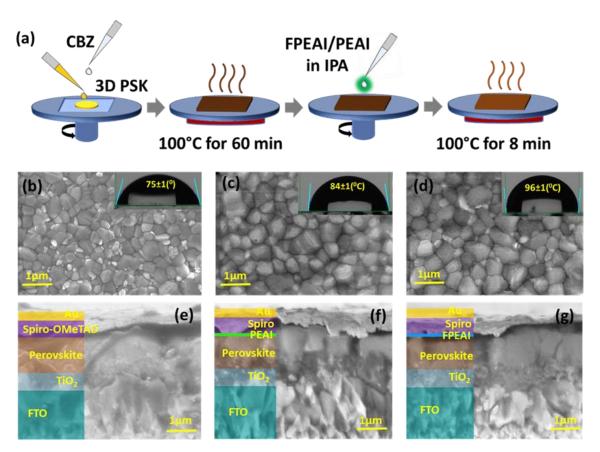


Figure 6.8. (a) Schematic illustration of bilayer perovskite formation; microstructures and contact angle measurements for (b) pristine perovskite, (c) with 0.3% PEAI, d) with 0.3% FPEAI; Cross sectional SEM images of PSCs with (e) pristine perovskite, (f) with 0.3% PEAI and (g) with 0.3% FPEAI.

#### 6.3 Surface morphology and contact angle measurements

The microstructure of the bulk and bilayer perovskites was studied with the help of scanning electron microscopy (Figure 6.8 b-d). The images suggest films composed of a uniform distribution of crystals without any voids. A significant difference for the bilayer perovskites was the presence of larger-sized crystals, which in turn minimizes the number of grain boundaries. We

note from the images that increasing the thickness (concentration) of PEAI or FPEAI has a small impact on the shape of the microstructure, while orderly crystal size with the coarser surface was also noted (Figure 6.9). The average grain size of pristine perovskites was 300 nm, while for PEAI or FPEAI we find it to be around 550 nm.

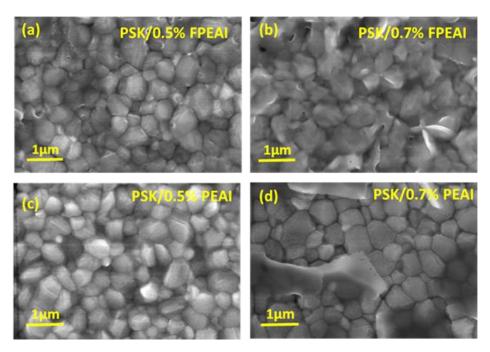


Figure 6.9: Surface SEM images (a) 0.5% FPEAI, (b) 0.7% FPEAI (c) 0.5% FPEAI (d) 0.7% FPEAI, perovskite thin films.

We undertook goniometer contact angle measurements to probe the hydrophobicity induced by the deposition of the PEAI or FPEAI layers. Pristine perovskites showed an average value of 74°, while the bilayer perovskites layered with PEAI gave an average value of 84°. This value increased significantly with FPEAI coated perovskites to give a contact angle value of 96°. This signals the hydrophobic character induced on the surface (Figure 6.8 b-d) owing to the presence of fluorinated molecules. The layer thickness was approximated by performing cross-sectional SEM imaging

experiments (Figure 6.8 e-g) according to our experimental protocol. The cross-section SEM images represent a defined layer-by-layer structure with intimate interfaces, reflecting the architect adopted. The mixed perovskite ( $FA_{0.15}MA_{0.85}PbI_{3-x}Br_x$ ) layer represents the thickness of (t = 453 nm), while PEAI and FPEAI showed a thickness which we speculate to be <20 nm, could be hardly measured as it lies as a thin sandwich layer between the 3D perovskite and the hole transport layer (Figure 6.8 e-g).

#### 6.4 Photovoltaic properties of PSCs

Though the performance was not the main aim of the current investigation, we fabricated PSCs to report figures of merit with an objective for added optimization. PSC with an FTO/b&mp-TiO<sub>2</sub>/3D-/layered perovskites/Spiro-OMeTAD/Au architecture (Figure 6.10 a) were fabricated and the corresponding band diagram (Figure 6.10 b) suggests proper alignment for the transport of charges. The device *J-V* curves (Figure 6.10 c) and the derived PV values are tabulated in Table 6.1. Pristine perovskites-based PSCs yielded a PCE of 17.55%, with a  $V_{\rm oc}$  of 1072 mV,  $J_{\rm sc}$  of 22.96 mA cm<sup>-2</sup>, and FF of 71.27 %, while the device fabricated with bilayer perovskites showed improved performance. The PSC fabricated with PEAI showed significantly boosted  $V_{\rm oc}$  of 1087 mV,  $J_{\rm sc}$  of 25.01 mA cm<sup>-2</sup>, and FF of 71.85%, with an overall PCE of 19.12 %, while in the case of FPEAI based bilayer perovskites a PCE of 20.63% was measured, with a  $V_{\rm oc}$  of 1107 mV, improved  $I_{\rm sc}$  and FF value of 25.06 mA cm<sup>-2</sup>, 74.37% respectively. The use of PEAI/FPEAI also passivate the surface defects and lower the non-radiative charge recombination and boosted the photovoltage by 40mV.

The orientation of molecules (PEAI/FPEAI) is fundamental to the device performance and FPEAI displays preferred orientation which promotes an interlayer formation that can more effectively extract and transport charge carriers to yield higher FF. The FF in FPEAI based bilayer perovskite was significantly higher than bulk and PEAI based bilayer perovskites, suggesting the perpendicular orientation of the overlayer is decisive to transport charge effectively. The statistical data of fifteen devices for the pristine as well as the bilayer perovskite-based PSCs are summarized (Figure 6.11). The integrated current density values derived from the incident photon-to-current conversion efficiency (IPCE) follow the values obtained from *J-V* curves (Figure 6.10 d). In the wavelength region of 400 – 600 nm, over 85% photon-to-electron conversion was noted and FPEAIbased PSC showed higher response with a shoulder shift to the red part of the spectrum (extended absorption). The molecular stacking of the organic cations attached to the perovskite layer may promote interlayer electronic coupling that in turn allows better charge transfer in the PSCs. The out-ofplane conductivity in FPEA to the molecular stacking with both the organic and inorganic phases was deduced to be higher and can influence the current density of the PSCs. High charge carrier conduction and improved electrical conductivity with the FPEAI treatment were reported and high current density in the fabricated PSCs stems from this. Further, higher light absorption by the PEAI/FPEAI treated perovskite, as reflected by the PL spectra, also supports photocurrent value.

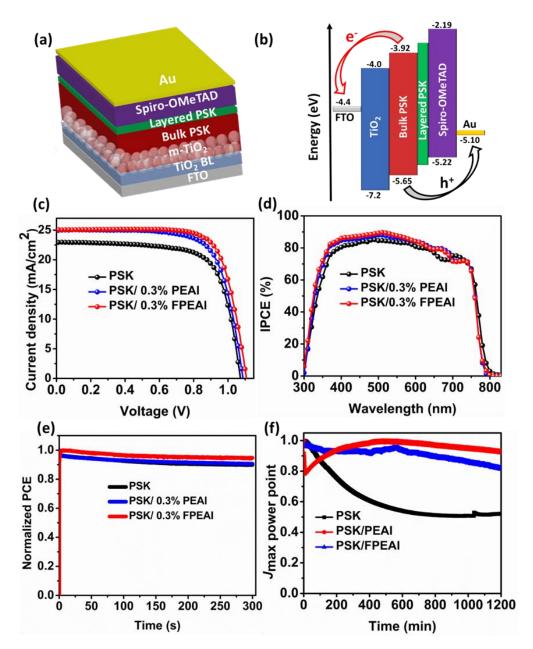


Figure 6.10. (a) Device architecture of the fabricated PSCs, (b) band diagram of the fabricated PSC, (c) current-voltage characteristics of PSCs based on pristine and bilayer perovskites with 0.3% PEAI and 0.3% FPEAI under Air-Mass (AM) 1.5G illumination, (d) corresponding EQE, (e) steady-state output for 300 s at 0.8V, and (f) maximum power point tracking for the pristine and bilayer perovskite with 0.3% PEAI and 0.3% FPEAI at 0.8V without encapsulation for 1200 mins under 1 sun illumination at ambient condition.

The hysteresis index (HI) was calculated for the PSCs by measuring *J-V* curves under the forward and reverse scan directions (Table 6.1). The bilayer perovskites-based PSCs showed a lower HI value of 0.058 for PEAI and 0.061 for FPEAI treated PSCs as compared to pristine perovskites which were 0.144 (Figure 6.12).

**Table 6.1**: Photovoltaic parameters for bulk and bilayer fabricated perovskites solar cells.

Samples	$V_{ m oc}$	$J_{\rm sc}$ (mA/cm <sup>2</sup> )	FF (%)	PCE (%)	Avg. PCE	HI
	(mV)					
PSK	1072	22.96	71.27	17.55	16.87	0.144
PSK/0.3%	1087	25.01	71.85	19.54	18.85	0.058
PEAI						
PSK/0.3%	1107	25.06	74.37	20.63	19.25	0.061
FPEAI						

Bilayer perovskites based on FPEAI, therefore, gave higher PCE than PEAI based PSCs. To determine the influence of layered structure on the operational stability of PSCs, we performed maximum power point tracking (MPPT) of the un-encapsulated devices under ambient conditions and at 1 sun illumination (Figure 6.10 e,f). The pristine perovskite showed lower performance as compared to PEAI based layered PSCs, while the PSCs based on FPEAI showed a linear response and negligible loss in performance. Apart from improving the PCE, steady output performance is fundamental to evaluate the performance of bilayer PSCs. The bilayer PSCs was also probed for long-term stability to acquire the self-life period, where the unencapsulated devices were kept in a dry box and measured on a regular interval.

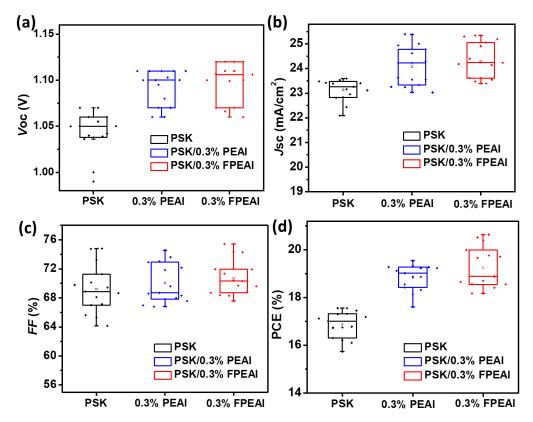


Figure 6.11: Devices statistics (15 cells each) (a)  $V_{oc}$ , (b)  $J_{SC}$ , (c) FF, (d) PCE, for pristine PSK, 0.3% PEAI, 0.3% FPEAI PSCs.

#### **6.4 Admittance spectroscopy measurements**

The electrical parameters such as built-in-potential ( $V_{bi}$ ), and depletion layer width (W) were deciphered by using Mott-Schottky analysis (Figure 6.13 a) under dark conditions. The Mott-Schottky plot for the fabricated PSCs yields a straight region from which  $V_{bi}$  was derived from the intercept on the bias axis. [38]  $V_{bi}$  for the bilayer perovskites-based PSC increases to 1003 mV (0.3% PEAI treatment) and 1050mV (0.3% FPEAI treatment) as compared to 950 mV for the pristine PSCs without the interfacial layer. Subsequently,

the depletion width  $(W = \sqrt{\frac{2\varepsilon\varepsilon_0 V_{bi}}{qN}})$  increases from 99.98 nm (pristine) to 106.13 nm (0.3% FPEAI) for the bilayer PSCs.

To elucidate the device kinetics that led to the increment in PCE with bilayer PSCs, we probed the charge accumulation behavior by examining the Nyquist plots through electrical impedance spectroscopy (EIS). The recombination resistance (Figure 6.13 c), and charge transfer resistance (Figure 6.13 d) as function of voltage was were derived from Nyquist plots (Figure 6.13 b). A single arc was displayed, a characteristic of mixed perovskites and the equivalent circuit used is shown in Figure 6.14.[39, 40] We can deduce from the curves that the recombination resistance follows a similar trend and at voltage close to  $V_{oc}$ , they display lower recombination, signaling the main contribution of recombination processes are in the bulk of the perovskite material not at the interface. Further, the use of bilayer perovskites irrespective of PEAI or FPEAI shows lower recombination resistance, suggesting its role in suppressing non-radiative recombination losses. Recombination resistance, near to the open-circuit voltage, is higher for bilayer perovskite-based PSCs, signaling a reduction in the non-radiative recombination defects. Bulk perovskites-based PSCs showed a trap-state recombination, while a change in the slope was noted for bilayer perovskites. Similarly, the charge transfer resistance was lower for bilayer perovskites based PSCs, illustrating its advantageous properties stemmed from filling of grain boundaries as well as defects passivation.

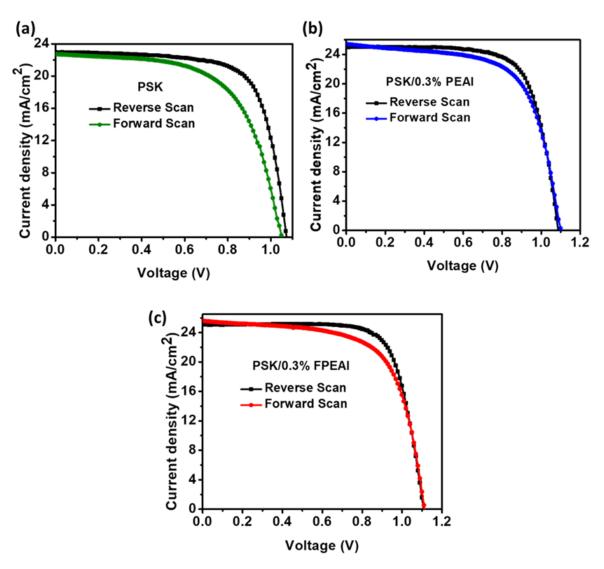


Figure 6.12: Current-voltage (J-V curves) characteristics of forward and reverse scans of PSCs based on (a) pristine PSK, (b) PSK/0.3% PEAI (c) PSK/0.3% FPEAI, under Air-Mass (AM) 1.5G illumination.

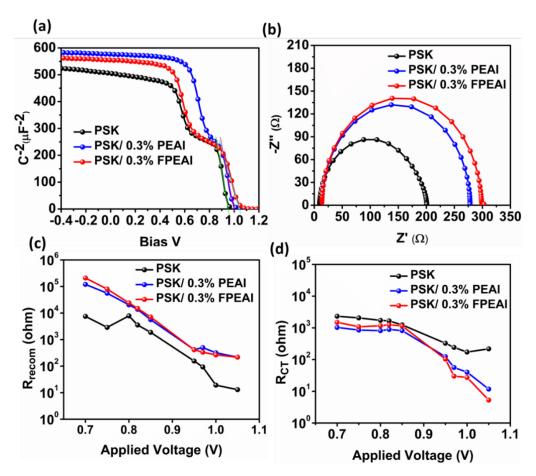


Figure 6.13. (a) Mott-Schottky plot for the pristine and bilayer perovskites with 0.3% PEAI and 0.3% FPEAI, (b) Nyquist plot for the pristine and bilayer perovskites 0.3% PEAI and 0.3% FPEAI, (c) recombination resistance at the applied voltage for pristine and bilayer perovskites 0.3% PEAI and 0.3% FPEAI, and (d) charge transfer resistance at the applied voltage for pristine and bilayer perovskites 0.3% PEAI and 0.3% FPEAI.

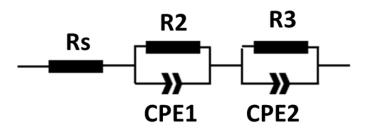


Figure 6.14: Electrical equivalent circuit model used for impedance spectra

#### 6.5. Conclusion

We report inclusive methodology to fabricate a bilayer (layered/bulk) perovskite-based solar cells which combine the panchromatic absorption characteristics of bulk perovskites with the stability of the layered structure. This in turn increases the stability of the perovskite structure while reducing the non-radiative charge recombination through suppression of defects. By employing PM-IRRAS studies we decipher the orientation of PEAI and FPEAI, which are located with the phenyl groups parallel and perpendicular to the interface, respectively. Due to its high electro-negativity, strong van der Waals interactions, and surface tension, FPEAI layers perpendicular to the surface while PEAI lies parallel to the bulk surface. We further evidence the decisive role of perpendicular orientation for effective charge transport and extraction. Bilayer formation may also stabilize the surface through hydrogen bonding contributions. Such synergistic approaches gave improve PV performance and the device's efficiencies by over 20%.

#### **6.6 References**

- 1. H. S. Jung and N. G. Park, *Small*, **2015**, *11*, 10-25.
- 2. M. Grätzel, *Nat. Mater.*, **2014**, *13*, 838-842.
- 3. C. Bi, Q. Wang, Y. Shao, Y. Yuan, Z. Xiao and J. Huang, *Nat. Commun.*, **2015**, *6*, 1-7.
- 4. L. Mao, C. C. Stoumpos and M. G. Kanatzidis, *J. Am. Chem. Soc*, **2018**, *141*, 1171-1190.
- 5. I. C. Smith, E. T. Hoke, D. Solis-Ibarra, M. D. McGehee and H. I. Karunadasa, *Angew. Chem. Int. Ed.*, **2014**, *126*, 11414-11417.
- A. Q. Alanazi, D. J. Kubicki, D. Prochowicz, E. A. Alharbi, M. E. Bouduban,
   F. Jahanbakhshi, M. Mladenović, J. V. Milić, F. Giordano and D. Ren, J. Am. Chem. Soc, 2019, 141, 17659-17669.
- 7. J. Liang, P. Zhao, C. Wang, Y. Wang, Y. Hu, G. Zhu, L. Ma, J. Liu and Z. Jin, *J. Am. Chem. Soc*, **2017**, *139*, 14009-14012.
- 8. G. Grancini, C. Roldán-Carmona, I. Zimmermann, E. Mosconi, X. Lee, D. Martineau, S. Narbey, F. Oswald, F. De Angelis and M. Graetzel, *Nat. Commun.*, **2017**, *8*, 1-8.
- 9. H. Tsai, W. Nie, J.-C. Blancon, C. C. Stoumpos, R. Asadpour, B. Harutyunyan, A. J. Neukirch, R. Verduzco, J. J. Crochet and S. Tretiak, *Nature*, **2016**, *536*, 312-316.
- 10. M. Pegu, M. P. Haris, S. Kazim and S. Ahmad, *Emergent Materials*, **2020**, 1-28.
- 11. C. Katan, N. Mercier and J. Even, *Chem. Rev.*, **2019**, *119*, 3140-3192.
- 12. S. Liu, S. Sun, C. K. Gan, A. G. Del Águila, Y. Fang, J. Xing, T. T. H. Do, T. J. White, H. Li and W. Huang, *Sci. Adv.*, **2019**, *5*, eaav9445.

- 13. H. Li, X. Wang, T. Zhang, X. Gong, Q. Sun, H. Pan, Y. Shen, S. Ahmad and M. Wang, *Adv. Funct. Mater.*, **2019**, *29*, 1903293.
- 14. Z. Wang, Q. Lin, F. P. Chmiel, N. Sakai, L. M. Herz and H. J. Snaith, *Nat. Energy*, **2017**, *2*, 1-10.
- 15. G. Grancini and M. K. Nazeeruddin, Nat. Rev. Mater., 2019, 4, 4-22.
- I. García-Benito, C. Quarti, V. I. Queloz, S. Orlandi, I. Zimmermann, M. Cavazzini, A. Lesch, S. Marras, D. Beljonne and G. Pozzi, *Chem. Mater.*,
   2018, 30, 8211-8220.
- 17. Q. Zhou, L. Liang, J. Hu, B. Cao, L. Yang, T. Wu, X. Li, B. Zhang and P. Gao, *Adv. Energy Mater.*, **2019**, *9*, 1802595.
- 18. S. Sadhu, K. Aqueche, T. Buffeteau, J.-M. Vincent, L. Hirsch and D. M. Bassani, *Mater Horiz.*, **2019**, *6*, 192-197.
- 19. Q. Zhou, Q. Xiong, Z. Zhang, J. Hu, F. Lin, L. Liang, T. Wu, X. Wang, J. Wu and B. Zhang, *Solar RRL*, **2020**, *4*, 2000107.
- 20. P. Li, H. Dong, J. Xu, J. Chen, B. Jiao, X. Hou, J. Li and Z. Wu, *ACS Energy Lett.*, **2020**, *5*, 2327-2334.
- K. T. Cho, Y. Zhang, S. Orlandi, M. Cavazzini, I. Zimmermann, A. Lesch,
   N. Tabet, G. Pozzi, G. Grancini and M. K. Nazeeruddin, *Nano Lett.*, 2018,
   18, 5467-5474.
- 22. A. Abate, M. Saliba, D. J. Hollman, S. D. Stranks, K. Wojciechowski, R. Avolio, G. Grancini, A. Petrozza and H. J. Snaith, *Nano Lett.*, **2014**, *14*, 3247-3254.
- M. Salado, F. J. Ramos, V. M. Manzanares, P. Gao, M. K. Nazeeruddin, P. J. Dyson and S. Ahmad, *ChemSusChem*, 2016, 9, 2708-2714.
- 24. J. W. Lee and N. G. Park, *Adv. Energy Mater.*, **2020**, *10*, 1903249.

- 25. Y. Jiang, S.-C. Yang, Q. Jeangros, S. Pisoni, T. Moser, S. Buecheler, A. N. Tiwari and F. Fu, *Joule*, **2020**, *4*, 1087-1103.
- 26. J. Ning, Y. Zhu, Z. Hu, Y. Shi, M. U. Ali, J. He, Y. He, F. Yan, S. Yang and J. Miao, *Adv Funct Mater.*, **2020**, *30*, 2000837.
- 27. S. Song, S. J. Yang, W. Choi, H. Lee, W. Sung, C. Park and K. Cho, *Adv. Energy Mater.*, **2020**, *10*, 2001759.
- 28. M. E. Bouduban, V. I. Queloz, V. M. Caselli, K. T. Cho, A. R. Kirmani, S. Paek, C. Roldan-Carmona, L. J. Richter, J. E. Moser and T. J. Savenije, *J. Phys. Chem. Lett.*, **2019**, *10*, 5713-5720.
- 29. M. A. Hope, T. Nakamura, P. Ahlawat, A. Mishra, M. Cordova, F. Jahanbakhshi, M. Mladenović, R. Runjhun, L. Merten and A. Hinderhofer, *J. Am. Chem. Soc.*
- 30. E. A. Monyoncho, V. Zamlynny, T. K. Woo and E. A. Baranova, *Analyst*, **2018**, *143*, 2563-2573.
- 31. S. Sadhu, T. Buffeteau, S. Sandrez, L. Hirsch and D. M. Bassani, *J. Am. Chem. Soc*, **2020**, *142*, 10431-10437.
- 32. V. E. Madhavan, I. Zimmermann, A. A. Baloch, A. Manekkathodi, A. Belaidi, N. Tabet and M. K. Nazeeruddin, *ACS Appl. Energy Mater.*, **2019**, *3*, 114-121.
- 33. K.-z. Du, Q. Tu, X. Zhang, Q. Han, J. Liu, S. Zauscher and D. B. Mitzi, *Inorg.*, **2017**, *56*, 9291-9302.
- 34. J. Hu, I. W. Oswald, S. J. Stuard, M. M. Nahid, N. Zhou, O. F. Williams, Z. Guo, L. Yan, H. Hu and Z. Chen, *Nat. Commun.*, **2019**, *10*, 1-11.
- 35. J. J. van Franeker, K. H. Hendriks, B. J. Bruijnaers, M. W. Verhoeven, M. M. Wienk and R. A. Janssen, *Adv. Energy Mater.*, **2017**, *7*, 1601822.

- 36. N. Li, Z. Zhu, C. C. Chueh, H. Liu, B. Peng, A. Petrone, X. Li, L. Wang and A. K. Y. Jen, *Adv. Energy Mater.*, **2017**, *7*, 1601307.
- 37. G. Grancini, S. Marras, M. Prato, C. Giannini, C. Quarti, F. De Angelis, M. De Bastiani, G. E. Eperon, H. J. Snaith and L. Manna, *J. Phys. Chem. Lett.*, **2014**, *5*, 3836-3842.
- 38. M. T. Khan, M. Salado, A. Almohammedi, S. Kazim and S. Ahmad, *Adv. Mater. Interfaces*, **2019**, *6*, 1901193.
- 39. S. M. Abdulrahim, Z. Ahmad, J. Bahadra and N. J. Al-Thani, *Nanomaterials*, **2020**, *10*, 1635.
- 40. J. Wang, H. Shi, N. Xu, J. Zhang, Y. Yuan, M. Lei, L. Wang and P. Wang, *Adv Funct Mater.*, **2020**, *30*, 2002114.

#### **Chapter 7**

N-Bromosuccinimide as Bromide Contributor for Halide Exchange in Perovskite for Solar Cell Fabrication



The past decade has witnessed tremendous advancement in the field of halide perovskite (PSK) as a choice of material for high-performing solar cells fabrication. Here, we investigate the impact of the halide exchange N-Bromosuccinimide (NBS) treatment in MAPbI<sub>3</sub> through and (MAPbBr<sub>3</sub>)<sub>0.15</sub>(FAPbI<sub>3</sub>)<sub>0.85</sub> based solar cells to improve stability. We observed the partial halide exchange (I- to Br-) or the filling of halide (X-) vacancy upon treatment of different NBS concentrations experimentally by spectroscopic and diffractograms studies. The NBS treatment promotes enhanced charge extraction and improved photovoltaic performance. Thus, formed perovskite layers exhibit grain size increment and lowered trap density. Improved device performance was noted with an optimized concentration of 0.5% NBS as compared to pristine perovskites due to the increment in open-circuit voltage and short circuit current density. The coordination of bromide influences the crystal lattice as shown by polarization modulatedinfrared reflection-absorption spectroscopy in the case of mixed perovskite, which in turn may influence charge transport and interfacial properties.

The parts of this chapter are based on published works-

**DOI**: doi.org/10.1021/acsaem.0c02920, doi.org/10.1002/cplu.202200021

#### **Content**

7.1 Introduction174-177
7.2 Result and Discussion177-179
7.2.1 Spectroscopic and X-ray diffraction (XRD) analysis of NBS
treatment on MAPbI <sub>3</sub> 179-184
7.2.2 Spectroscopic and X-ray diffraction (XRD) analysis of NBS
treatment on (MAPbBr <sub>3</sub> ) <sub>0.15</sub> (FAPbI <sub>3</sub> ) <sub>0.85</sub> 184-187
7.2.2.1 PM-IRRAS measurement of the thin-films based on NBS
treatment on (MAPbBr <sub>3</sub> ) <sub>0.15</sub> (FAPbI <sub>3</sub> ) <sub>0.85</sub> 188-190
7.2.3 Surface morphology analysis of thin-films based . 191-192
7.2.4 Contact-angle measurements192
7.2.5 Photovoltaic properties of PSCs193
7.2.5.1 Photovoltaic properties of PSCs based on NBS treatment
upon perovskite MAPbI <sub>3</sub> 193-196
7.2.5.2 Photovoltaic properties of PSCs based on NBS treatment
upon perovskite (MAPbBr <sub>3</sub> ) <sub>0.15</sub> (FAPbI <sub>3</sub> ) <sub>0.85</sub> 196-198
7.2.6 Admittance spectroscopy measurements of PSCs. 198-203
7.3 Conclusion203-204
7.4 References205-207

#### 7.1 Introduction

Organic-inorganic hybrid perovskites are the subject of intense investigations for the fabrication of solar cells. Owing to their high absorption coefficient, tunable bandgap and unparalleled semiconducting properties, promising results for photovoltaics (PV) and optoelectronics applications have been documented.[1] The reported power conversion efficiency (PCE) in perovskite solar cells (PSCs) has shown an exceptional boost from a mere 3.8% to 25.7%  $^{[2,\ 3]}\text{,}$  and are adaptable to solutionprocessable manufacturing routes.[4-6] Reports suggest, that the electronhole pair can travel far and wider than exciting thin-film-based solar cells, and efforts have been laid to discover new architects to push the lightharvesting properties. Sincere efforts have been laid to boost the PCE, however, quantifying the materials which are less sensitive to moisture is foremost. Halide perovskites display attractive properties for their use in thin-film based PV, such as a high absorption coefficient, high charge carrier mobilities, and long diffusion lengths, which led to a remarkable increase in their PCE through the use of innovative charge selective (electron and hole transport) layers (ETLs, HTLs), interface engineering, energy level engineering. ENREF 22To improve the device performance, it is of importance to optimize the surface through defect passivation, which minimizes the charge recombination, trap states and grain size increment to reduce the surface grain boundaries.<sup>[7,8]</sup> A plethora of reports on PSCs deal with the use of hybrid organic lead halide perovskite, an ambipolar material that generates electron and hole pairs.[9] However, rapid degradation of perovskite in ambient air and moisture has resulted in poor long-term stability. To surmount the stability issue, several approaches have been

adopted, including device encapsulation with the hydrophobic organic moieties, inorganic oxides or engineering the charge selective layers to be moisture resistant. Controllable substitution of bromide (Br-) ions put forward an effective route to improve the moisture resistance and thus, stability of the PSCs. The improved stability is attributed to the smaller size Br- ions to I- ions that transforms the tetragonal phase to the cubic phase.<sup>[10]</sup> The substitution of bromide also enables tuneable of optical band gaps with a minimal impact on the light absorption of the perovskite.

Bromide-based perovskites exhibit a wider bandgap of 2.3 eV, which yields higher open-circuit voltage as compared to the iodide counterpart. Such properties make them applicable to tandem solar cell applications. The report suggests that bromide ions promote the separation of electrons and holes at grain boundaries. Br- anions had a strong passivation effect on Pb interstitial and halide vacancies by forming robust ionic bonds with Pb<sup>2+</sup> and hydrogen bonds (N-H···Br) with MA+/FA+ cations. Surface passivation is another effective protocol to reduce defects present at the surface of perovskites and suppress undesirable ion movement. The defects present on the perovskite surface accelerate the decomposition pathways and promote nonradiative recombination that limits performance and reliability. Surface defects can be interstitial, created through vacancy, or stem from grain boundaries, and impacts carrier concentration, transport, and its recombination.

Additionally, bromide incorporation influences the open-circuit voltage ( $V_{\rm oc}$ ) of the PSCs. The use of hydrobromic acid as an additive provides a stable phase, a quality film that exhibits low hysteresis and high  $V_{\rm oc}$ .<sup>[11]</sup> Furthermore, the addition of the bromide ion in the perovskites can allow

structural transition from the metastable tetragonal phase to the more stable cubic phase.<sup>[12]</sup>

Through ENREF 35 the use of hydrophobic materials, prolonged device stability was investigated using polarization modulated-infrared reflectionabsorption spectroscopy (PM-IRRAS).[13] ENREF 39. ENREF 40 ENREF 44 Several pre-treatment of the perovskite solution with halide precursors is being discussed in the literature for the successful solution-phase halide exchange reaction using suitable additives or acids.[12, 14] Several methods of addition of acids (HX; X=halides) to the formation of an intermediate phase that allows the formation of well-defined pre-crystallized domains before annealing have been reported.[15] The use of the hydrogen halides (HBr) acts as a strong donor that interacts strongly with Pb2+ and as a result forms bromide-plumbate complexes that are beneficial for the growth of highquality films. The oxidation of HBr generates Br2 that is converted to bromide ions; which gets coordinated to the Pb<sup>2+</sup> centers and then partially substitute the iodide-based perovskite.[16-18] However, despite Brsubstitution observed by the doping effect of HBr, occasionally the existence of a substantial amount of H<sub>2</sub>O in the aqueous HBr acid reduces the crystallinity of the perovskite film.

We demonstrate the N-haloimides such as N-Bromo succinimide (NBS) as a source of bromide ions that can be used as an alleviator atop of the MAPbI<sub>3</sub> and (MAPbBr<sub>3</sub>)<sub>0.15</sub>(FAPbI<sub>3</sub>)<sub>0.85</sub> to optimize the crystal, microstructure and photovoltaic performance. NBS is a common chemical reagent, readily used as a source of bromine and routinely employed in organic chemistry for a various substitution or brominating reactions.<sup>[19]</sup> NBS was reported as a bromide precursor for stable and highly luminescent perovskite

nanocrystals.<sup>[20]</sup> Our results suggest that NBS is potentially active for halide exchange, grain growth and device stability. The NBS treatment and its role was probed using an array of spectroscopic techniques, including PM-IRRAS measurements. We employed NBS as an interfacial layer in the device architecture FTO/bl-TiO<sub>2</sub>/meso-TiO<sub>2</sub>/PSK/NBS/Spiro-OMeTAD/Au or Ag. The oxidation of NBS with isopropyl alcohol released HBr<sup>[21]</sup> which further assist to the improvement in stability and charge transport properties by reducing the carrier recombination rates.  $V_{\rm oc}$  is seen to improve at an optimized concentration that is attributed to Br-/I-exchange in the perovskite layer. Our methodology simultaneously provides an approach to overcome defects at the interfaces, while having the beneficial effect of bromide substitution without having halide phase segregation.

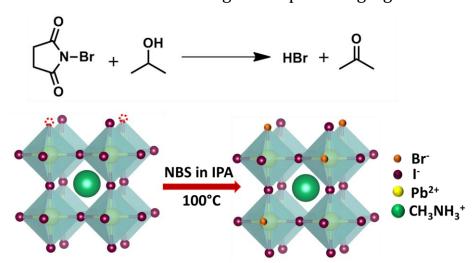


Figure 7.1. (a) NBS reaction with isopropyl alcohol generating HBr, and (b) three-dimensional perovskite with NBS treatment.

#### 7.2 Results and Discussion

The device architecture and possible reaction between the NBS and perovskite are depicted in Figure 1. Different concentrations of NBS in

isopropanol (IPA) (3 mg/mL, 5 mg/mL and 10 mg/mL) was investigated for treatment of the perovskite layer. For the ease of terminology, they are defined as 0.3%, 0.5%, 1% NBS, methylammonium lead iodide as MAPbI<sub>3</sub> and mixed perovskite as pristine PSK respectively.

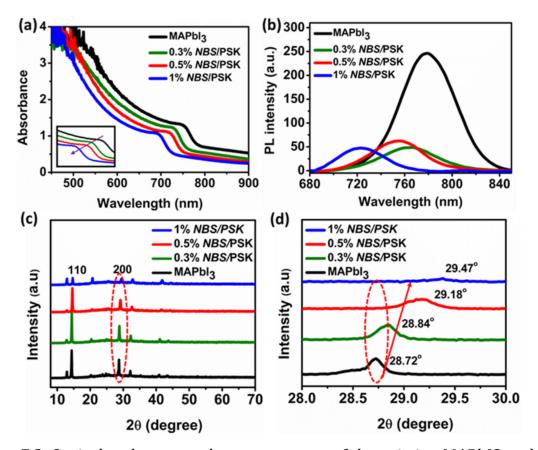


Figure 7.2. Optical and structural measurements of the pristine MAPbI3 and NBS treated MAPbI3 / perovskite (PSK) films at varying concentration, (a) UV-Visible absorption of pristine, (b) Tauc plot of the pristine PSK and NBS/PSK at different concentrations (c) photoluminescence spectra, (d) normalized photoluminescence spectra, (e) X-ray diffraction patterns, and (f) magnified area of the diffractograms in the 2θ range (28°-30°).

PM-IRRAS experiments on mixed perovskite interface with NBS treatment suggest release of bromide anions by NBS treatments and the latter can be

formed thermally during the deposition process through oxidation of the solvent (isopropyl alcohol) by NBS. NBS oxidation of secondary alcohols is expected to release HBr,<sup>[21, 22]</sup> which assists in the crystallization process of the perovskite to offer large size grain, and lowering the grain boundaries and further lowering the trap density through passivating the defects.

In this chapter we will first discuss the halide exchange results based on NBS treatment on MAPbI<sub>3</sub>, then we will illustrate our results obtained from the interfacial treatment of NBS upon mixed perovskite  $(MAPbBr_3)_{0.15}(FAPbI_3)_{0.85}$ .

#### 7.2.1 Spectroscopic and X-ray diffraction (XRD) analysis of NBS treatment on MAPbI<sub>3</sub>

To determine the effect of NBS treatment on the light absorption properties of the pristine MAPbI $_3$  and NBS treated PSK films after annealing (100°C), we performed the UV-vis absorption measurement. The varying concentration of NBS incorporated (0.3 – 4%) perovskites were studied for their optoelectronic properties. The absorption spectra for the pristine MAPbI $_3$  and NBS treated perovskite are represented (Figure 1a) and we noted a blue shift in the band edge of the perovskite film upon NBS treatment. It was observed that higher bromide content upon NBS treatment resulted in a higher bandgap, owing to the blue shift of the band edge upon the I/Br exchange. The absorption peak at concentrations >1% NBS treatment (1.5 – 4%), significantly blue shifts to a lower wavelength (Figure 7.2 b) suggesting Br contribution as the partial replacement of I- in MAPbI $_3$  and tuning of the optical properties. Compared to the pristine perovskite, the

blue shifting of the band edge of the NBS treated MAPbI<sub>3</sub> (inset, Figure 7.2 a), signaling the incorporation of Br<sup>-</sup> after annealing and Br<sup>-</sup> entered the MAPbI<sub>3</sub> lattice by replacing I<sup>-</sup> site or filling a vacancy under temperature treatment. The bandgap ( $E_g$ ) was calculated from the Tauc's plot (Figure 7.3) and a gradual increase of band gap value was observed from 1.56 eV (MAPbI<sub>3</sub>) to 1.79 eV (4% NBS treatment).[12] The corresponding  $E_g$  of MAPbI<sub>3</sub> and different concentrations of NBS/PSK films are presented (Table 7.1). This absorption behaviour is consistent with the higher excitonic binding energy reported for bromide-based perovskites.

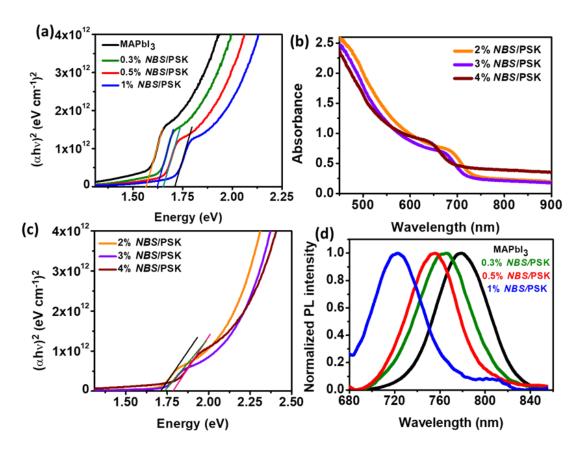


Figure 7.3: (a) Tauc plots for MAPbI<sub>3</sub> and varying NBS/PSK concentrations, (b) UV-Visible absorption of NBS/PSK at higher concentrations, (c) Tauc plots for

NBS/PSK at higher concentrations, (d) Normalized photoluminescence emission spectra.

**Table 7.1**: Band gap derived from the Tauc's plots for MAPbI<sub>3</sub> and varying NBS-PSK films.

Thin films	Band gap, E <sub>g</sub> (eV)		
MAPbI <sub>3</sub>	1.56		
0.3% NBS/PSK	1.62		
0.5% NBS/PSK	1.64		
1% NBS/PSK	1.70		
2% NBS/PSK	1.72		
3% NBS/PSK	1.74		
4% NBS/PSK	1.79		

Further, we performed photoluminescence (PL) studies to glean charge transfer behavior at the interface with NBS treatment (Figure 7.2 b). Similar to optical absorption, the addition of NBS also influenced the emission of the perovskite layer and notably, the band gap tuning was also reflected in the PL spectra that showed a progressive shift (blue) towards the higher energy from the 778 nm (pristine perovskite) to 722 nm for the 1% NBS treated perovskite (Figure 7.3 d). The systematic shift observed in the PL spectra towards the shorter wavelength suggests tuning of the energy bandgap (Eg) from lower to higher bandgap perovskite. The emission from the NBS treated perovskite showed a significantly weaker signal than the iodide-rich

pristine perovskite, pointing that the charge carrier is quickly transported.<sup>[23-25]</sup> It is well-known that perovskites with higher bromide concentrations are known to undergo phase segregation. However, in this case, we employed an optimal range of NBS concentration of 0.3–1% for fabricating PSCs, that replace a small proportion of iodide with bromide ions without showing the halide segregation as noted from the PL spectra. Usually, the PL emission from a halide segregated region typically displays a strong bathochromic shift (red-shift) and increased intensity, which was not observed in our case.

The X-ray diffraction (XRD) patterns of the pristine perovskite and NBS (0.3%, 0.5%, and 1%) treated perovskite typically display similar diffraction peaks. However, the expanded area of each peak showed varied 2θ values. The diffraction peak at 14.38°, 20.28°, 28.72°, and 32.26° can be indexed to (110), (112), (200), and (211) crystal planes of the pure tetragonal phase of MAPbI<sub>3</sub>. The peak at 12.8° is associated with the (100) crystal plane of PbI<sub>2</sub>. In pure MAPbI<sub>3</sub>, the dominant diffraction peak (110) appears at 14.38°; however, in case of 1% NBS treatment, Br- progressively replaced I- in pristine perovskite and the diffraction peak shifted to 14.72° (diffraction peak; 14.41° for 0.3% NBS, 14.61° for 0.5% NBS treated PSK films). We ascribed this peak shifting towards a higher 2θ value to the decrease in lattice spacing upon replacement of larger I- (ionic radius 2.2Å) with smaller Br (ionic radius 1.96 Å). Further, Figure 7.2 c, exhibits the diffraction patterns monitored in the 20 range of 28.5-30° for NBS/PSK varied concentration. This peak at 28.72° corresponds to the (200) plane, shifting monotonically (represented by an arrow, Figure 7.2 d) to a higher 2θ region, suggesting the existence of mixed halide (iodine-bromine) phase in the 3D

domain. A prominent peak of PbI<sub>2</sub> was observed for 1% NBS/PSK, signifying the NBS treatment induces the coordination of under-coordinated Pb<sup>2+</sup> during the exchange of halides (I, Br).

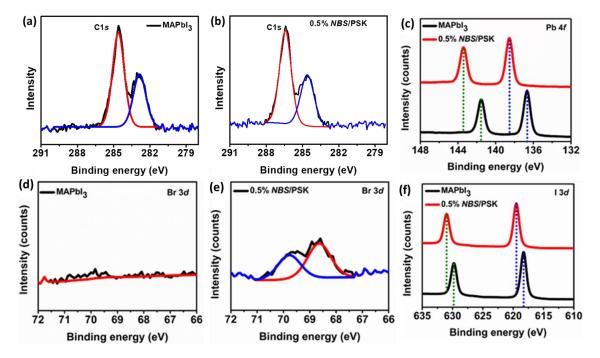


Figure 7.4: XPS spectra (a) C1s peak of MAPbI<sub>3</sub> (b) C1s peak of 0.5% NBS, (c) Pb 4f peak of MAPbI<sub>3</sub>, (d) I 3d peak of 0.5% NBS/PSK, (e) Br 3d peak of MAPbI<sub>3</sub>, and (f) Br 3d peak of 0.5% NBS/PSK.

To quantify the chemical composition on the perovskite layer upon NBS treatment, X-ray photoelectron spectroscopy (XPS) measurements were conducted for pristine PSK and 0.5% NBS/PSK. The C1s spectra of the MAPbI3 and with 0.5% NBS treatment remain unaltered. (Figure 7.4 a, b). In the Pb 4f spectra of MAPbI3, two characteristic peaks at 136.67 eV and 141.55 eV were observed and can be associated with the Pb<sup>2+</sup> (Pb 4f 5/2 and Pb 4f 7/2). Upon treatment of 0.5% NBS (Figure 7.4 c), it exhibited a shift of around 2 eV, which demonstrates that NBS is chemically anchored on the surface of the MAPbI3 crystal. The decrease in iodine peaks (I 3d) ratio and

shift in binding energy (Figure 7.3 d) is ascribed to the partial replacement of iodide with bromide ions in the pristine MAPbI<sub>3</sub>. Nevertheless, we can simultaneously detect the presence of Br from Br 3d peaks at 68.3 eV and 69.8 eV for 0.5% NBS treated in situ films, which were not apparent in MAPbI<sub>3</sub> (Figure 7.4 e, f).

## 7.2.2 Spectroscopic and X-ray diffraction (XRD) analysis of NBS treatment on $(MAPbBr_3)_{0.15}$ $(FAPbI_3)_{0.85}$

The absorption spectra of pure perovskite and NBS treated films exhibiting an excitonic peak at 750 nm is demonstrated in Figure 7.5 a. It can be deduced from spectra that the NBS treated perovskite layer exhibits the highest absorption in the range of 550-800 nm up to a certain concentration (0.3% and 0.5% NBS). The 0.5% NBS treated film shows the highest absorbance intensity due to improved crystallinity. 1% NBS treated films exhibit relatively lower absorbance in the range of 550-800 nm because of relatively higher amount of PbI<sub>2</sub> as reflected by X-ray diffractograms.

To evaluate the effect of NBS on the interfacial properties with the mixed perovskite, we performed steady state PL measurements on quartz substrates using 450 nm excitation from the back side (Figure 7.5 b). With the increase in NBS concentration (1%), the PL curves shift slightly to longer wavelengths and attain maximum PL intensity similar to that of pristine PSK. As stated earlier, the PL emission from a halide segregated region typically displays a strong bathochromic shift (red-shift) and increased intensity, hence 1% NBS treatment on the surface of mixed perovskite layer may undergo phase segregation.

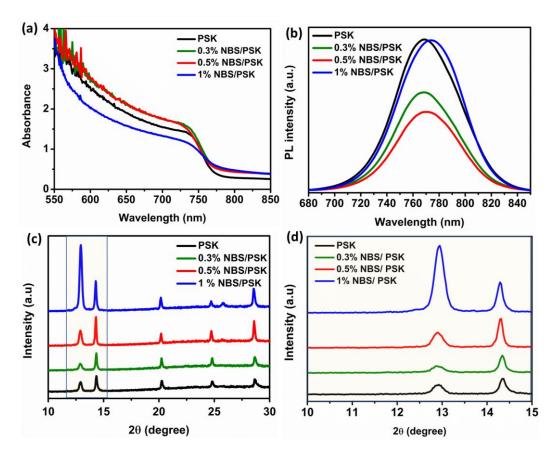


Figure 7.5: Structural, diffraction, absorption and emission spectroscopy of the pristine PSK and NBS/PSK layers at varying concentration, (a) UV-Visible absorption, (b) Photoluminescence spectra, (c) X-ray diffraction patterns of the pristine PSK and with 0.3%, 0.5% and 1% NBS/PSK and (d) Magnified area of the diffractograms in the low  $2\theta$  range ( $12^{\circ}$ - $15^{\circ}$ ).

A passivated perovskites shows gradual reduction in the PL intensity for 0.3% and 0.5% NBS, attributed to the passivated trap states on the surface or to the grain boundaries.<sup>[26]</sup> The reduction in the PL intensity indicates that the charge carrier extractions at interfaces were enhanced by the certain amount of NBS and NBS assists in photo generated holes extraction from the perovskite to the hole transporting layer. The reduced PL intensity

favours the good PV properties and exhibits the same tendency as the PV performance for 0.3% and 0.5% NBS treated device.

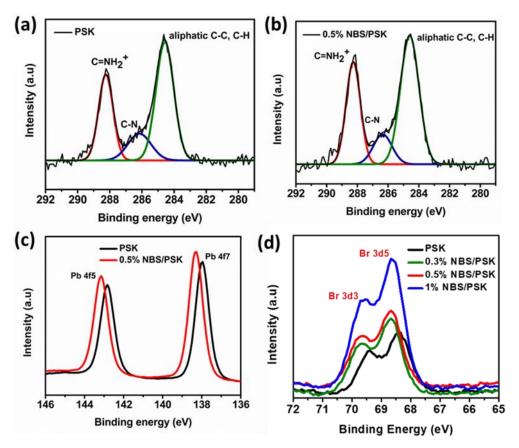


Figure 7.6: X-ray photoelectron spectroscopy (XPS); high resolution deconvoluted spectra of (a) C1s peak of PSK layer, (b) C1s peak of 0.5%/PSK bromine (c) Pb 4f peak (d) Br 3d peaks spectra for different samples.

We recorded the diffraction patterns in a thin film geometry (Figure 7.5 c, d) upon NBS treatment. The peak at  $12.92^{\circ}$  represents the (001) PbI<sub>2</sub> while  $14.34^{\circ}$  represents the characteristic peak (110) of the perovskite. On increasing the concentration up to 0.5% NBS, the intensity of the perovskite peak (110) increases, attributed to the higher crystallinity. In case of 1% NBS the intensity of the PbI<sub>2</sub> (001) peak gradually increases, as compared to the pristine PSK, 0.3% and 0.5% NBS treated PSK. Higher NBS treatment can

induce the coordination of under coordinated  $Pb^{2+}$  with the iodide ions released during bromide exchange with iodide ions. This coordination behaviour with  $Pb^{2+}$  is studied by the XPS spectra of Pb. High intensity peak of perovskite (14.34°) in the 1 % NBS treated films was noted, suggesting it retainment of the perovskite cubic structure.

We probed the role of NBS by means of XPS measurements and the comparison of the core level peaks of C, Br, Pb attributing the surface elemental properties of the pristine PSK as well as the NBS treated ones are shown in the Figure 7.6. We compared the core level peaks of C, Br, Pb of the mixed perovskite PSK and optimized 0.5% NBS treated perovskite film. The C1s spectra were compared and the peak at the lower binding energy (284.6 eV) (Figure 7.6 a, b) is related to C-C and C-H bonds. The C-N peak of FA and MA components have their binding energy at around 286.4 eV.51 The peak at higher binding energy 288.3 eV is related to C=NH<sub>2</sub>+ of the organic cations. On treatment with NBS, the enhancement of the peak area at 288.3 eV at higher concentration signals overall chemical transformation or the crystallinity achieved due to the annealing step after NBS deposition. We also note an increase in the area of corresponding C1s peak with the higher concentration of NBS treatment. In the Pb 4f spectra (Figure 7.6 c), 0.5% NBS shows peak shifting to higher binding energy with 0.2 eV as compared to pristine PSK. This we ascribed to the formation of  $PbX_2$  (X = Br-, I-), as a result of exchange of some of the I- by the excess Br- ions from the NBS. In the Br 3d spectra (Figure 7.6 d), the binding energies of Br 3d3 and Br 3d5 peaks are 69.4 eV and 68.4 eV, respectively. The increase in the intensity of the Br 3d peak, suggests the role of NBS and in NBS treated PSK, a shift of 0.4

eV (Br 3d) occurs with respect to pristine PSK, attributed to the exchange of bromide with the iodide ions.

# 7.2.2.1 PM-IRRAS measurement of the thin-films based on NBS treatment on $(MAPbBr_3)_{0.15}$ $(FAPbI_3)_{0.85}$

The NBS treatment induces modifications in the crystallinity of the material which are evidenced by the changes in the vibrational spectra, grain size, and ultimately, in the electronic characteristics and overall performance of the devices. We follow the change in the vibrational signature of the material upon NBS treatment through PM-IRRAS spectroscopy. PM-IRRAS has been previously shown to be well adapted to collecting the vibrational spectrum of hybrid perovskite materials and possess sufficient sensitivity to detect the presence of even single molecular layers.[13, 27] The samples deposited by spin coating the precursor solution onto gold-coated glass substrates for PM-IRRAS. The PM-IRRAS spectrum of the pristine PSK is shown in (Figure 7.7 a) along with the assignment of the most important bands.<sup>[28, 29]</sup> The NBS treatment results in significant changes in the spectrum, even for the low NBS concentrations, 0.02% and 0.2% NBS samples {(Figure 7.7 b), black and orange curves, respectively. Notably, regardless of the concentration of the NBS used (0.02 - 1%), no signals corresponding to the presence of NBS appeared. Indeed, the most significant IR absorption bands of NBS (shown in Figure 7.7 b for clarity), are absent in the differential PM-IRRAS spectra of the NBS-treated perovskite. Instead, we observed an enhancement in the

formamidinium (FA) bands that is indicative of an overall modification of the material's crystallinity.

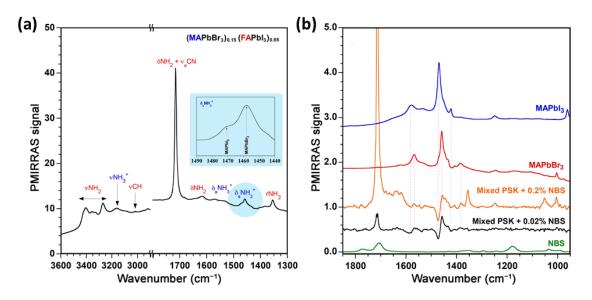


Figure 7.7. Differential PM-IRRAS spectra of (a) the pristine PSK before NBS treatment (b) and differential PM-IRRAS spectra following treatment with 0.02 (black spectrum) and 0.2% (orange spectrum) NBS. The ATR spectrum of NBS is shown in green for comparison, along with the reference spectra of MAPbBr<sub>3</sub> (red spectrum) and MAPbI<sub>3</sub> (blue spectrum).

The absence of clear signals attributable to the presence of NBS on the material's surface evidence that it underwent a chemical transformation during the deposition or subsequent annealing step. We observe a decrease in the  $\delta_s(NH_3^+)$  signal assigned to perovskite containing methyl ammonium (MA) iodide, and an increase of the  $\delta_s(NH_3^+)$  signal assigned to perovskite containing MA bromide. The two signals are close in energy (1470 and 1458 cm<sup>-1</sup>, respectively), but distinguishable when compared to the pristine PSK. Based on these observations, we conclude that the deposition of NBS results in the incorporation of additional bromide ions into the material. In the case of the 0.2 and 1% samples, the increase in the intensity of the FA bands is

significant (+15% and + 82%, respectively) and suggests a more substantial modification of the material's crystallinity or, to a change in the polarizability of the material. Furthermore, we note that the 1% (highest concentration) treated NBS sample also evidences a slow chemical alteration leading to the appearance of bromomethane (CH<sub>3</sub>Br) signals (antisymmetric stretching vibration at 2964 cm<sup>-1</sup> and symmetric bending vibration at 1264 cm<sup>-1</sup>) over the course of several days (Figure 7.8). These signals are accompanied by the associated grow-in of signals which can be attributed to ammonia at ca. 1100 cm<sup>-1</sup>, thereby indicating that the excess bromide ions introduced by the NBS treatment may be involved in an SN<sub>2</sub> reaction with the MA+ cations of the material to form CH<sub>3</sub>Br and NH<sub>3</sub>.

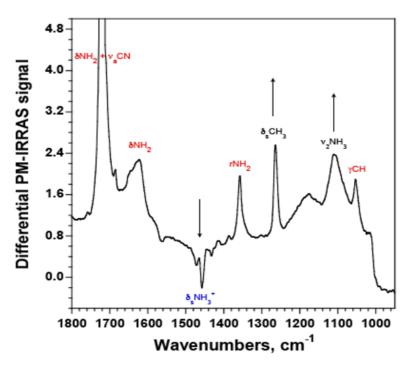


Figure 7.8: Differential PM-IRRAS spectrum of a sample 3 days after treatment with 1% NBS showing the decrease of the & of the NH $_3$  + fragment and grow-in of the signals attributed to the methyl group of CH $_3$ Br and to the v2 of ammonia.

# 7.2.3 Surface morphology analysis of thin-films based on of NBS treatment on perovskites MAPbI<sub>3</sub> and (MAPbBr<sub>3</sub>) $_{0.15}$ (FAPbI<sub>3</sub>) $_{0.85}$

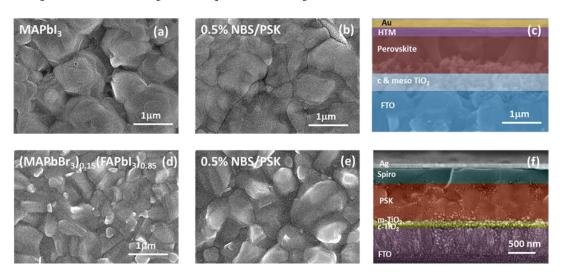


Figure 7.9: Surface SEM images of the (a) MAPbI<sub>3</sub>, (b) 0.5% NBS/PSK. Crossectional SEM image of PSC based on (c) 0.5% NBS/PSK (MAPbI<sub>3</sub>). Surface SEM images of the (d) (MAPbBr<sub>3</sub>)<sub>0.15</sub> (FAPbI<sub>3</sub>)<sub>0.85</sub>, (e) 0.5% NBS/PSK. Crossectional SEM image of PSC based on (f) 0.5% NBS/PSK ((MAPbBr<sub>3</sub>)<sub>0.15</sub> (FAPbI<sub>3</sub>)<sub>0.85</sub>).

The microstructure of the MAPbI<sub>3</sub> and 0.5% NBS/PSK were recorded with the help of a scanning electron microscope (SEM), the microstructure of 0.5% NBS /PSK exhibits complete coverage with large grains without pinholes and lesser grain boundaries (Figure 7.9 a-b; d-e). We noted that with an increase in the concentration of NBS the grain size increased progressively on both MAPbI<sub>3</sub> and (MAPbBr<sub>3</sub>)<sub>0.15</sub> (FAPbI<sub>3</sub>)<sub>0.85</sub> surfaces. This could be aided by the fact that as soon as Br- is incorporated in the perovskite crystal, the initial heterogeneous nucleation rate was induced and slowed down the crystal growth of the newly formed mixed halide

perovskite.[35] The cross-sectional SEM images of the PSCs based on 0.5% NBS/PSK (MAPbI<sub>3</sub> and (MAPbBr<sub>3</sub>)<sub>0.15</sub> (FAPbI<sub>3</sub>)<sub>0.85</sub>) are demonstrated in Figure 7.9 c, f. The perovskite layer thickness of MAPbI<sub>3</sub> was found to be  $\sim$ 409 nm and that of (MAPbBr<sub>3</sub>)<sub>0.15</sub> (FAPbI<sub>3</sub>)<sub>0.85</sub> was found to be  $\sim$  570 nm.

# 7.2.4 Contact-angle measurements of thin-films based on of NBS treatment on perovskites MAPbI<sub>3</sub> and (MAPbBr<sub>3</sub>)<sub>0.15</sub> (FAPbI<sub>3</sub>)<sub>0.85</sub>

We studied the role of NBS for surface properties and stabilization on bromide addition by the goniometry measurements. The contact angle value for MAPbI<sub>3</sub> was 69° and this value increases to 80° upon treatment of 0.5% NBS (Figure 7.10 a, b). Similarly, of the contact angle values for the (MAPbBr<sub>3</sub>)<sub>0.15</sub>(FAPbI<sub>3</sub>)<sub>0.85</sub> was 77° that increased to 94±1° for 0.5% NBS/PSK respectively (Figure 7.10 c,d), evidencing the role of NBS in modifying the surface properties and induced hydrophobicity.

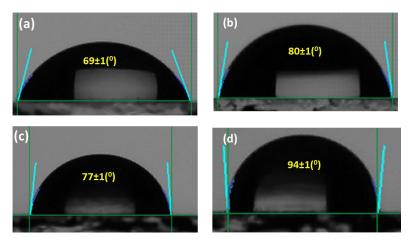


Figure 7.10: Contact angle measurements for (a) MAPbI<sub>3</sub>, (b) 0.5% NBS/PSK (MAPbI<sub>3</sub>), (c) (MAPbBr<sub>3</sub>)<sub>0.15</sub> (FAPbI<sub>3</sub>)<sub>0.85</sub> (c) 0.3% NBS/PSK (d) 0.5% NBS/PSK ((MAPbBr<sub>3</sub>)<sub>0.15</sub> (FAPbI<sub>3</sub>)<sub>0.85</sub>).

#### 7.2.5 Photovoltaic properties of PSCs

To appraise the role of *NBS* as the bromide contributor, we fabricated PSCs, in the mesoscopic n-i-p configuration with the structure of FTO/bl-Meso-TiO<sub>2</sub>/PSK/*NBS*/Spiro-OMeTAD/Au or Ag. For the ease of discussion, we have divided the device performances into two different sections of PSCs based on NBS treatment on MAPbI<sub>3</sub> and (MAPbBr<sub>3</sub>)<sub>0.15</sub> (FAPbI<sub>3</sub>)<sub>0.85</sub>.

#### 7.2.5.1 Photovoltaic properties of PSCs based on NBS treatment upon perovskite MAPbI<sub>3</sub>

The current density-voltage (J-V) curves for the PSCs with NBS under the AM 1.5G illumination (100 mWcm<sup>-2</sup>) are shown (Figure 7.11 a), and the corresponding PV parameters, the short-circuit current ( $J_{sc}$ ), open-circuit voltage ( $V_{oc}$ ), fill factor (FF), and PCE are listed in Table 7.2. The PSCs fabricated with pristine MAPbI<sub>3</sub> exhibited a PCE of 16.54 %. ( $J_{sc}$ = 21.41 mAcm<sup>-2</sup>,  $V_{oc}$ = 1035 mV, FF = 74.56%), while under similar condition, the 0.5%NBS/PSK (optimised concentration) based PSCs yielded a PCE of 17.87% ( $J_{sc}$ = 22.72 mAcm<sup>-2</sup>,  $V_{oc}$  = 1074 mV, FF = 73.17 %). The addition of NBS as a bromide precursor on the perovskite layer influenced the energy gap and thus the PV parameters  $V_{oc}$ ,  $J_{sc}$ , and finally PCE. The performance enhancement is due to the improvement in charge separation and carrier diffusion, arising from lower charge recombination. The voltage deficit was minimized by 34 mV. The incident photon-to-current conversion efficiency (Figure 7.11 b) measurement demonstrates a broad absorption range, with an absorption onset at around 780 – 790 nm.

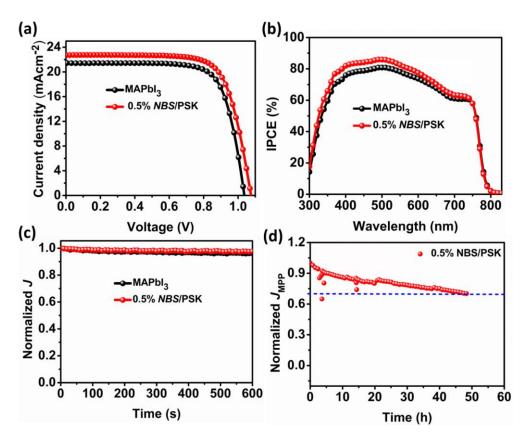


Figure 7.11: (a) *J-V* graph of pristine and 0.5% *NBS*/PSK treated PSCs, (b) corresponding incident-photon-to-current-efficiency graphs, (c) steady-state output for 600 s at 850 mV, (d) maximum power point tracking for the 0.5% *NBS*/PSK treated PSC at 850 mV without encapsulation for 50h under nearly 1 sun illumination at ambient condition.

**Table 7.2**: PSCs photovoltaics parameters for MAPbI<sub>3</sub> and NBS treated perovskites.

	Voc		FF	PCE	R <sub>s</sub>	R <sub>shunt</sub>
PSC	(mV)	Jsc (mA/cm <sup>2</sup> )	(%)	(%)	$(\Omega)$	$(k\Omega)$
MAPbI <sub>3</sub>	1035	21.41	74.56	16.54		
Average	±0.012	±0.379	±4.13	±0.77	56.65	27.67
0.5% NBS/PSK	1074	22.72	73.17	17.87		
Average	±0.013	±0.561	±2.29	±0.94	53.11	40.37

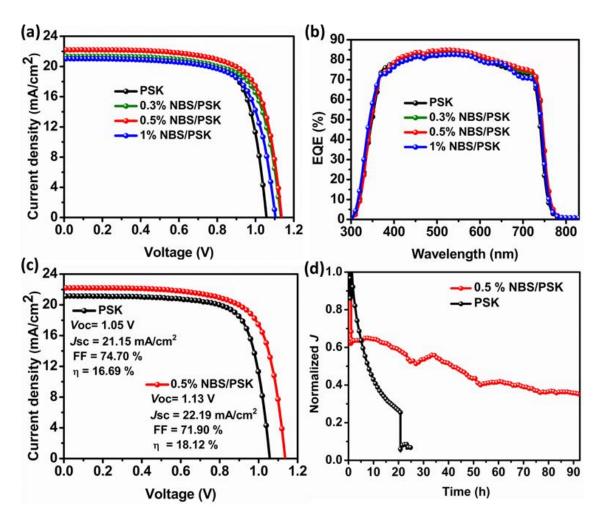


Figure 7.12: (a) Current-voltage characteristics of PSCs with and without NBS treatment under Air-Mass (AM) 1.5G illumination, (b) corresponding EQE, (c) comparative J-V curves of the pristine PSK and with 0.5% NBS/PSK, and (d) maximum power point tracking for the pristine PSK and 0.5% NBS/PSK devices without encapsulation for 92 h under 1 sun illumination at ambient condition.

The stabilized power output at maximum power point for 600 seconds is tracked for the MAPbI<sub>3</sub>, as well as 0.5% *NBS*/PSK treated PSCs were measured (Figure 7.11 c) with no apparent changes. Furthermore, the long-term operational stability of the MAPbI<sub>3</sub> and optimized concentration of 0.5% *NBS*/PSK unencapsulated PSC were examined at the maximum power

point voltage under continuous light illumination at nearly 1 sun for  $\sim 50$  hours at ambient atmospheric conditions (25–27°C,  $\sim 60\%$  RH environment). Notably, the *NBS* treated PSCs maintained almost 70% of their initial performance as compared to MAPbI<sub>3</sub><sup>[30]</sup> based PSC in our previous report, which retained only 29% of its initial device performance. (Figure 7.11 d).<sup>[30, 31]</sup>

#### 7.2.5.2 Photovoltaic properties of PSCs based on NBS upon treatment of (MAPbBr<sub>3</sub>) $_{0.15}$ (FAPbI<sub>3</sub>) $_{0.85}$

The *I-V* curves of fabricated PSCs with pristine or NBS treated perovskites are shown (Figure 7.12 a) and results are summarized in Table 7.3. Pristing PSK gave a PCE of 16.69% ( $V_{oc} = 1050 \text{ mV}$ ,  $J_{sc} = 21.15 \text{ mA/cm}^2$ , FF = 74.69%), while device fabricated with 0.5% NBS outperformed and yielded a PCE of 18.12% (Figure 7.12 c). With the increase in NBS concentration up to 0.5% we note an increment in  $V_{\text{oc}}$  by 80 mV, ascribed to a reduction in defectinduced recombination. For 0.3% and 0.5% NBS based devices a  $V_{oc}$  of 1130 mV was measured, with a minute decrement in FF. Our results show an increase in PCE by 8.6% with respect to control devices and the process can be adopted for fabrication of high-performance devices. For 1% NBS, the device performance is reduced. The enhancement with 0.5% NBS is attributed to the increased  $V_{\text{oc}}$  and reduced recombination of photogenerated charges at the interface of the perovskite layer, which is reflected also by the large value of the shunt resistance (90.19 k $\Omega$ .cm<sup>2</sup>). The hysteresis index (HI) was calculated for the PSCs with and without NBS treatment (Figure 7.13). NBS treated device gave lower HI (0.031) as compared to

pristine perovskite (0.11), which we ascribe to improved microstructure. The external quantum efficiencies (EQE) of the PSCs show (Figure 7.12 b) increment with 0.5% NBS treatment. The improved light harvesting and charge extraction are attributed to the increased absorbance and reduced emission intensity of NBS treated PSK.

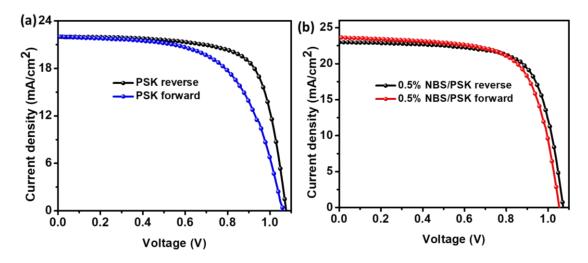


Figure 7.13: Current-voltage (J-V curves) characteristics of forward and reverse scans of PSCs based on (a) pristine PSK, (b) 0.5% NBS/PSK (AM) 1.5G illumination.

To correlate the PV performances with the device stability, we measured *J* at maximum power point tracking (MPPT) for the pristine and 0.5% NBS treated PSCs (Figure 7.12 d). The improved power output was observed for 0.5% NBS treated PSCs and to test their long-term stability, un-encapsulated devices were kept under continuous illumination at 1 sun at room temperature with a relative humidity of 50-60% under 0.8V. The pristine PSK device lost its initial photo-current value and retained only around <10% after 20 h of continuous illumination, while the 0.5% NBS treated devices showed an initial drop followed by a much slower decline in the photocurrent value.

**Table 7.3.** PSCs photovoltaics parameters for (MAPbBr<sub>3</sub>)<sub>0.15</sub> (FAPbI<sub>3</sub>)<sub>0.85</sub> and NBS treated perovskites.

PSC	V <sub>oc</sub> (mV)	J <sub>sc</sub> (mA/cm <sup>2</sup> )	FF (%)	PCE (%)	R <sub>s</sub> (Ω.cm <sup>2</sup> )	R <sub>sh</sub> (kΩ.cm <sup>2</sup> )
PSK	1056	21.15	74.69	16.69	4.24	4.47
0.3% NBS/PSK	1132	21.33	71.99	17.39	4.63	40.97
0.5% NBS/PSK	1136	22.18	71.90	18.12	4.19	90.19
1% NBS/PSK	1104	21.02	71.76	16.65	4.97	7.87

#### 7.2.6 Admittance spectroscopy measurements of PSCs

To unravel the role of NBS on the defect state and high value of shunt resistance achieved, thermal admittance spectroscopy (TAS) was performed.

#### 7.2.6.1 Admittance spectroscopy measurements of PSCs with NBS treatment of MAPbI<sub>3</sub>

To access the impact of *NBS* treatment on the density of defects grown in the perovskite layer, the hole only devices with the structure FTO/PEDOT:PSS/MAPbI<sub>3</sub>/*NBS*/Au are fabricated. [33, 34] The *I-V* curves of the devices with and without *NBS* treatment are represented (Figure 7.14 a, b). The trap-state density is determined by the trap-filled limit voltage ( $V_{TFL}$ ) following the equation:

$$N_{defects} = \frac{2\mathcal{E}_r \mathcal{E}_0 V_{TFL}}{eL^2} \tag{1}$$

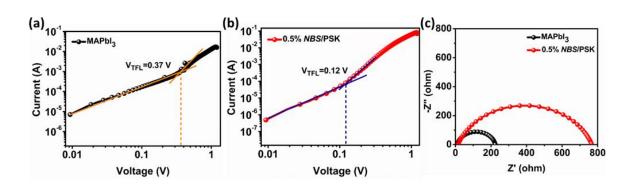


Figure 7.14: Current -voltage characteristics of the hole only devices (a) MAPbI $_3$  (b) with 0.5% NBS/PSK treatment, (c) Nyquist plots for the MAPbI $_3$  and 0.5% NBS treated PSCs measured with an applied voltage of 850 mV and under dark condition.

Where L represents the thickness of the perovskite  $\mathcal{E}_r$  and  $\mathcal{E}_0$  are the relative dielectric constant of MAPbI<sub>3</sub> and vacuum permittivity respectively, and e is the elementary charge. The trap-filled limit voltage ( $V_{\rm TFL}$ ) was found to be 0.37 V for MAPbI<sub>3</sub> and 0.12 V for 0.5% NBS treated PSC. The calculated defect densities ( $N_{\rm defects}$ ) are 8.05 x 10<sup>15</sup> cm<sup>-3</sup> and 2.61 x 10<sup>15</sup> cm<sup>-3</sup> for MAPbI<sub>3</sub> and 0.5% NBS/PSK treated PSCs. The lower defect density in the NBS treated device can be attributed to the improved crystallinity and favorable orientation of the perovskite grains upon NBS treatment.

The charge transport and the recombination of PSCs are mainly influenced by the resistance of the device. To understand the influence of *NBS* treatment on the charge dynamics of PSCs we performed the electrical impedance spectroscopy (EIS) measurements under dark conditions at an applied voltage of 850 mV and the fitted graphs are depicted. The equivalent circuit model of  $R_s$ + $R_{rec}$ /CPE includes the series resistance ( $R_s$ ), and the recombination resistance ( $R_{recom}$ ), while the constant phase element defining the carrier diffusion is represented as CPE.<sup>[35]</sup> The Nyquist plots (Figure 7.14

c) reveal the higher  $R_{\rm recom}$  based on 0.5% NBS treatment suggesting suppressed charge recombination at the perovskite/HTL interface, resulting in an enhanced  $V_{\rm OC}$  and  $J_{\rm SC}$ . The value for  $R_{\rm recom}$  for the MAPbI<sub>3</sub> and the 0.5% NBS treated PSCs are obtained as 213.6  $\Omega$  and 752.3  $\Omega$  respectively, which exemplifies an improved charge transfer behavior, with a lower surface defect for the NBS treated PSC.

# 7.2.6.2 Admittance spectroscopy measurements of with NBS treatment of $(MAPbBr_3)_{0.15}$ $(FAPbI_3)_{0.85}$

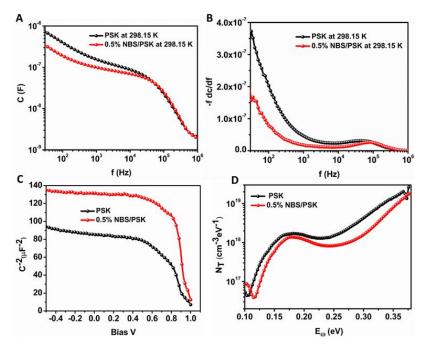


Figure 7.15: Admittance spectroscopy of pristine PSK and NBS treated devices, (a) Capacitance as a function of frequency at room temperature (298.15 K) for the pristine PSK and with 0.5% NBS, (b) plots showing the f×dC/df versus frequency at room temperature (c) Mott-Schottky plot for the pristine PSK and with 0.5% NBS/PSK and (d) trap density of states (NT) of the devices at 298.15 K.

We measured the capacitance-frequency (C-f) curve at room temperature (Figure 7.15 a) were noted. The plateau in the intermediate frequency (IF) range corresponds to the dielectric relaxation in the perovskites that can be described by the geometrical capacitance per unit area  $C_g = \epsilon \epsilon_0 / L$  ( $\epsilon$  and  $\epsilon_0$  refer to the dielectric constant and the permittivity of the vacuum, respectively, L is the layer thickness).

The geometrical capacitance is temperature independent. However, the capacitance behavior in the low frequency (LF) range shows dependency on temperature and ascribes to the interfacial properties of the device. The increment in the capacitance in the LF range at higher temperature signals higher charge accumulation at the interface, consequently lower charge extraction and higher capacitance build-up at the perovskite/HTL interface.<sup>[36]</sup> The capacitance build-up is lower for NBS treated devices, suggesting improved charge extraction(Figure 7.15 a). Upon NBS treatment, the trap carriers located at the interface gain sufficient energy and migrate from the interface to the respective charge selective layers, and the modified interface avoids charge accumulation.

The trap density  $(N_T)$  for the device was calculated using the following equations:

$$N_{T}(E_{\omega}) = \frac{V_{bi}}{qWk_{B}T} \left(-f\frac{dC}{df}\right)$$
 (1)

$$E_{\omega} = k_{\rm B} T \ln \left( \frac{v_{\rm o}}{f} \right) \tag{2}$$

where  $E\omega$  is the demarcation energy and f is the applied angular frequency. The attempt-to-escape frequency (ATEF,  $v_0$ ) was derived from (-fx dc/df) vs. frequency profile (Figure 7.15 b), as reported elsewhere.<sup>25,32</sup> We calculated

the build-in potential ( $V_{bi}$ ) and depletion layer width (W) from C<sup>-2</sup>-V plots (Figure 7.15 c) by performing Mott Schottky analysis.

According to the depletion, the width W is related to the capacitance by the equation

$$C=A\epsilon\epsilon_0/W$$

The density of fully ionized defect states N and build in potential  $V_{bi}$  is related to the capacitance C through the Mott Schottky relation:

$$\frac{1}{C^2} = \frac{2(V_{bi} - V)}{A^2 q \varepsilon \varepsilon_0 N} \tag{3}$$

Here A is the device active area and q is the elementary charge.  $\epsilon$  is dielectric constant of the perovskite which is taken as 32, the  $\epsilon_0$  is the permittivity of the vacuum, respectively

 $V_{bi}$  can be extracted from the intercept at the bias axis and the slope of the straight line gives the impurity of doping density N.

The width of the depletion junction is related to the capacitance through the relation:

$$W = \sqrt{\frac{2\epsilon\epsilon_0 V_{bi}}{qN}} \tag{4}$$

An improved build-in potential, of 1050 mV for the 0.5 % NBS treated was extracted at 10 kHz, while pristine PSK based PSC gave a value of 990 mV (Figure 7.15 c), this increment in  $V_{bi}$  resulted in higher  $V_{oc}$  for 0.5 % NBS treated device.

In a similar manner, with the increase in the build-in potential ( $V_{bi}$ ), the depletion width increases from 44 nm to 52 nm for the 0.5% NBS treated PSC. The depletion width increase will allow improve charge separation at the interface, which in turn will minimizes the recombination. The 0.5% NBS treated PSC (Figure 7.15 d) showed lower trap densities (1.384 ×  $10^{18}$  eV<sup>-1</sup>

cm<sup>-3</sup>) compared to pristine PSCs ( $1.724 \times 10^{18} \, \text{eV}^{-1} \, \text{cm}^{-3}$ ), implying that NBS treatment reduces the overall trap states located above the valence band of the perovskite and this improves the  $V_{oc}$ . The suppressed trap density corresponds to the efficient extraction of the photogenerated charge carrier and mitigating the interfacial charge recombination.

The defect energy distribution shows a broad band with a maximum peak at  $E_{\omega} = 0.181$  eV for pristine perovskites-based PSCs which shifts to lower energy (0.1799 eV) for 0.5% NBS treated PSCs. We ascribe this to the presence of shallow traps, and it is similar to the value of FAPbI<sub>3</sub> perovskites.<sup>33</sup>Additionally, typical density of deep traps (>0.25 eV) was also observed in lower frequency regions that shows reduction in NBS treated PSCs. These deep defects could be related to the origin of hysteresis and originated due to the polarization of the materials at the interface.<sup>34</sup>

#### 7.3 Conclusion

We investigated the halide exchange (I to Br) in perovskite via *NBS* treatment on the MAPbI<sub>3</sub> and (MAPbBr<sub>3</sub>)<sub>0.15</sub> (FAPbI<sub>3</sub>)<sub>0.85</sub>. The *NBS* solution in isopropyl alcohol generates HBr that further facilitates the bromide substitution in the perovskite post-annealing. The blue shift in the absorbance spectra and the crystallinity enhancement with the inclusion of bromide ions were more prominently ascribed by the XRD measurements on the treatment of NBS with MAPbI<sub>3</sub>. The employment of NBS reduces bulk and interfacial defects by refilling the grain boundaries and augmenting the crystal growth, beneficial for device application. In contrast molecular modulators currently used to mitigate such defects form poorly conductive aggregates at the perovskite interface with the charge collection layer,

impeding the extraction of photogenerated charge carriers. PM-IRRAS spectroscopy shows that NBS does not stay on the surface of the mixed perovskite- (MAPbBr<sub>3</sub>)<sub>0.15</sub> (FAPbI<sub>3</sub>)<sub>0.85</sub>. Instead, it undergoes a chemical reaction during the deposition process that results in the presence of bromide anions. Admittance and PL spectroscopy measurements support lower trap density and increase charge extraction. An optimal value of 0.5% NBS treatment showed an increment in the device efficiency value due to the reduction in charge recombination that improves the  $V_{\rm oc}$ . This reduced charge recombination was attributed to lower trap density near the valence band of the perovskite and gave high value of shunt resistance. Improved moisture and photostability with 0.5% NBS treated devices as compared to the pristine perovskite was noted, suggesting the use of N-haloimides for performance enhancement.

#### 7.4 References

- 1. J. Huang, Y. Yuan, Y. Shao and Y. Yan, *Nat. Rev. Mater.*, **2017**, *2*, 1-19.
- 2. A. Kojima, K. Teshima, Y. Shirai and T. Miyasaka, *J. Am. Chem. Soc*, **2009**, *131*, 6050-6051.
- 3. I. Repins, M. A. Contreras, B. Egaas, C. DeHart, J. Scharf, C. L. Perkins, B. To and R. Noufi, *Prog Photovolt.*, **2008**, *16*, 235-239.
- 4. F. Huang, M. Li, P. Siffalovic, G. Cao and J. Tian, *Energy Environ. Sci.*, **2019**, *12*, 518-549.
- 5. N. J. Jeon, J. H. Noh, W. S. Yang, Y. C. Kim, S. Ryu, J. Seo and S. I. Seok, *Nature*, **2015**, *517*, 476-480.
- 6. M. Cai, Y. Wu, H. Chen, X. Yang, Y. Qiang and L. Han, *Adv. Sci.*, **2017**, *4*, 1600269.
- 7. Y. Shao, Z. Xiao, C. Bi, Y. Yuan and J. Huang, *Nat. Commun.*, **2014**, *5*, 1-7.
- 8. B. Yang, O. Dyck, J. Poplawsky, J. Keum, A. Puretzky, S. Das, I. Ivanov, C. Rouleau, G. Duscher and D. Geohegan, *J. Am. Chem. Soc*, **2015**, *137*, 9210-9213.
- 9. L. K. Ono, Y. Qi and S. F. Liu, *Joule*, **2018**, *2*, 1961-1990.
- H. F. Zarick, N. Soetan, W. R. Erwin and R. Bardhan, *J. Mater. Chem. A.*,
   2018, 6, 5507-5537.
- 11. S. Wang, Y. Hua, M. Wang, F. Liu and L. Ding, *Mater. Chem. Front.*, **2019**, *3*, 1139-1142.
- 12. B. Zhang, F. Guo, J. Xue, L. Yang, Y. Zhao, M. Ge, Q. Cai, B. Liu, Z. Xie and D. Chen, *Sci. Rep.*, 2017, 7, 1-8.
- 13. S. Sadhu, T. Buffeteau, S. Sandrez, L. Hirsch and D. M. Bassani, *J. Am. Chem. Soc*, **2020**.

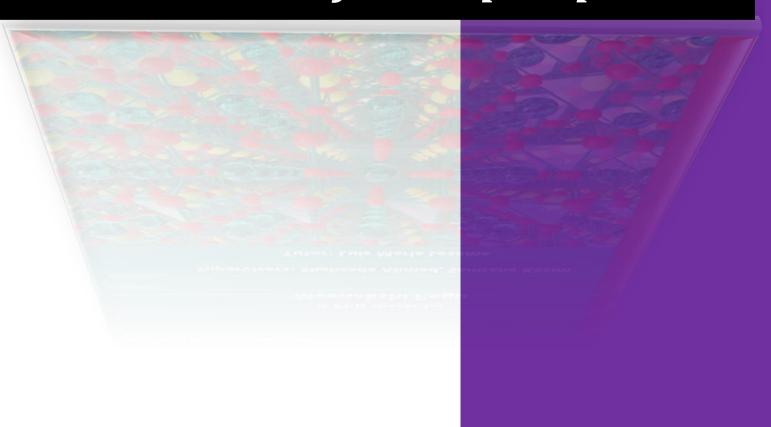
- 14. S. Mandal, D. Roy, C. K. De, S. Ghosh, M. Mandal, A. Das and P. K. Mandal, *Nanoscale Adv.*, **2019**, *1*, 3506-3513.
- 15. J. Xu, J. Yin, L. Xiao, B. Zhang, J. Yao and S. Dai, *Sol. Energy Mater Sol. Cells*, **2016**, *157*, 1026-1037.
- D. P. McMeekin, Z. Wang, W. Rehman, F. Pulvirenti, J. B. Patel, N. K. Noel,
   M. B. Johnston, S. R. Marder, L. M. Herz and H. J. Snaith, *Adv.Mater.*,
   2017. 29, 1607039.
- 17. J. Huang, M. Wang, L. Ding, Z. Yang and K. Zhang, *RSC Adv.*, **2016**, *6*, 55720-55725.
- 18. V. L. Pool, A. Gold-Parker, M. D. McGehee and M. F. Toney, *Chem. Mater.*, **2015**, *27*, 7240-7243.
- 19. L. Horner and E. Winkelmann, in *Newer methods of preparative Organic Chemistry*, Elsevier, 1964, pp. 151-198.
- 20. S. Paul and A. Samanta, *ACS Energy Lett.*, **2019**, *5*, 64-69.
- 21. N. Venkatasubramanian and V. Thiagarajan, *Can. J. Chem.*, **1969**, *47*, 694-697.
- 22. J. C. Fan, Z. C. Shang, J. Liang, X. H. Liu and Y. Liu, *J. Phys. Org. Chem.*, **2008**, *21*, 945-953.
- 23. C. Gao, Z. Hu, C. Yang, H. Xu, Y. Wang, H. Zhang, J. Zhang, Y. Zhu and J. Wang, *J. Alloys Compd.*, **2020**, *848*, 156247.
- 24. S. Pan, X. Yang, B. Cai, K. Yang, M. Ge, T. Zhang, H. Cui, L. Sun and W. Ji, *Sustain. Energy Fuels.*, **2021**, *5*, 2294-2300.
- 25. J.-M. Cha, J.-W. Lee, D.-Y. Son, H.-S. Kim, I.-H. Jang and N.-G. Park, *Nanoscale*, **2016**, *8*, 6341-6351.
- 26. M. Salado, M. Andresini, P. Huang, M. T. Khan, F. Ciriaco, S. Kazim and S. Ahmad, *Adv. Funct. Mater.*, **2020**, *2020*.

- 27. S. Sadhu, K. Aqueche, T. Buffeteau, J.-M. Vincent, L. Hirsch and D. M. Bassani, *Mater. Horiz.*, **2019**, *6*, 192-197.
- 28. E. Kucharska, J. Hanuza, A. Ciupa, M. Mączka and L. Macalik, *Vib. Spectrosc.*, **2014**, *75*, 45-50.
- 29. A. A. Bakulin, O. Selig, H. J. Bakker, Y. L. Rezus, C. Müller, T. Glaser, R. Lovrincic, Z. Sun, Z. Chen and A. Walsh, *J. Phys. Chem. Lett.*, **2015**, *6*, 3663-3669.
- 30. M. Pegu, S. Kazim, P. Huang, L. Lezama and S. Ahmad, *J. Mater. Chem. C*, **2021**.
- 31. R. Ruess, F. Benfer, F. Böcher, M. Stumpp and D. Schlettwein, *ChemPhysChem*, **2016**, *17*, 1505-1511.
- 32. O. Almora, C. Aranda, E. Mas-Marzá and G. Garcia-Belmonte, *Appl. Phys. Lett.*, **2016**, *109*, 173903.
- 33. J. Chen, L. Zuo, Y. Zhang, X. Lian, W. Fu, J. Yan, J. Li, G. Wu, C. Z. Li and H. Chen, *Adv. Energy Mater.*, **2018**, *8*, 1800438.
- 34. D. Prochowicz, P. Yadav, M. Saliba, M. Saski, S. M. Zakeeruddin, J. Lewinski and M. Gratzel, *ACS Appl. Mater. Interfaces*, **2017**, 9, 28418-28425.
- 35. X. Liu, J. He, P. Wang, Y. Liu, J. Xiao, Z. Ku, Y. Peng, F. Huang, Y. B. Cheng and J. Zhong, *ChemSusChem*, **2019**, *12*, 2385-2392.
- 36. R. A. Awni, Z. Song, C. Chen, C. Li, C. Wang, M. A. Razooqi, L. Chen, X. Wang, R. J. Ellingson and J. V. Li, *Joule*, **2020**, *4*, 644-657.

Chapter 8



### Conclusion and future perspective



#### Chapter 8. Conclusion and future perspective.

This thesis focuses on the work based on developing organic small molecules as hole-transporting materials (HTMs) and exploiting the large-size organic cation as an interface layer or doping to form a mixed-dimensional perovskite absorber in order to enhance the overall device performance and its long-term stability. The work was motivated by the advancement in the organic-inorganic halide perovskites using different charge selective layers and the excellent photovoltaic performances they exhibited within a decade. Hence, I have chosen to work on two different topics; firstly, exploiting organic semiconductors as the hole selective layers and secondly studying the interfacial engineering with the large organic cation on the surface of the perovskite layer.

### Chapter 8. Conclusion and future perspective.

#### **Content:**

8.1 Summary207-209
8.2 Future Outlook210

#### 8.1 Summary

In the second chapter, a small molecule tetra-indole (TTI) and its derivative MP-TTIF° comprised of fluorinated methoxy based diphenylamine as the substituents. The compounds were synthesized and studied as hole selective layers. TTI and MP-TTIF° gave a competitive performance with PCEs 15.83 % and 16.62%. The PCE was improved to 19.23% when TTI was used as passivating agent. The spectroscopic techniques such as UV-Vis, PL, XPS, EIS and surface studies such as XRD and SEM suggests that TTI helped in reducing the defects and additionally, the non-radiative recombination was found to reduce. Furthermore, the hydrophobic nature of TTI enhanced the stability of the device.

In the third chapter, I have introduced two novel TAT-based fluorinated small molecules MP-TF<sup>m</sup> and MP-TF<sup>o</sup>. The HTMs are synthesised through a simple and inexpensive synthetic route with good yield compared to widely used spiro-OMeTAD. The position of the fluorine (meta and ortho) atoms significantly showed adverse effect on the device performance. The meta-fluorinated TAT-based HTM showed more planar configuration as compared to the ortho-fluorinated counterpart. The dihedral angle was measured on the optimized structure calculated by DFT. The devices based on triazatruxene as HTMs showed promising mobility and electrical

#### Chapter 8. Conclusion and future perspective.

conductivity. The overall enhanced performance and improved stability of the PSCs due to the presence of the fluorine atoms as substituents was observed.

In the fourth chapter, three different metal-phthalocyanines (ZnPc) based dimers (ZnPc 1, ZnPc 2, ZnPc 3) as HTMs are discussed for the PSCs' performance and stability. Phthalocyanines are commonly known for their semi-conducting properties exhibiting outstanding chemical and thermal stability. The dimer ZnPc 3 showed PCE around of around 14.12% was obtained and showed long improved stability. PSCs based on the three dimers showed moisture stability under ambient atmospheric conditions.

The fifth chapter discusses the formation of mixed-dimensional perovskite by doping of 3-ammonium propionic acid iodide salt (3-APAI) into the MAPbI<sub>3</sub> precursor solution. We studied the formation of the mixed-dimensional perovskite through several spectroscopic techniques that have shown the interaction of 3APAI with the 3D perovskite layer. An array of measurements such as NMR, FTIR, XPS and XRD were conducted to study bonding interaction with the absorber layer. The overall PV performance was also recorded and the stability was measured by storing the devices in the dry environment.

#### Chapter 8. Conclusion and future perspective.

The sixth chapter showed that polarization-modulated infrared reflection-absorption spectroscopy (PM-IRRAS) can rapidly provide the necessary information on the interfacial layers formed by PEAI and FPEAI, which form parallel and perpendicularly oriented monolayers with substantial differences in the orientation with respect to the perovskite layer. We hypothesise that the more robust van der Waals interactions due to the higher electronegativity in FPEAI govern the orientation.

The seventh chapter reported the halide (I/Br) exchange behaviour upon surface treatment of *N*-Bromosuccinimide (*NBS*) on the perovskite layer. Halide exchange occurs after deposition and during the thermal annealing process through oxidation of the solvent (isopropyl alcohol) by *NBS*. *NBS* induces oxidation of secondary alcohols is expected to release HBr, which assists in the crystallisation process of the perovskite to offer large size grain, lowers the grain boundaries, and further decreases the trap density through passivating the defects.

#### 8.2 Future Outlook

We have demonstrated the synthesis and development of HTMs; which are the vital components of PSCs. The main features of HTMs were taken into account during the design and synthesis of HTMs. Additionally, the layered perovskite has evolved out incredibly in a very short span of time, which opens a wide area of research in the PV industry. The incorporation of layered perovskite absorbers into 3D hybrid perovskite forming multidimensional layered/3D perovskite adds on to a new approach to further improve the stability and performance of the devices. I hope that the works demonstrated in this thesis will contribute to the motivation of developing new organic semiconductors for perovskite solar cell application and further investigations of the layered hybrid perovskites can engrave its potential further as the future wide bandgap semiconductor for other optoelectronic applications. We believe that the development in this class of materials would accelerate and improve the pitfall of PSCs and lead to the future commercialization of PSCs in PV industries.

#### General materials and methods

The chemicals and solvents used in this thesis were purchased from commercial suppliers such as Tokyo Chemical Industry (TCI), Dyesol, Fischer Scientific, Sigma Aldrich, Acros Chemicals and employed as received without further purification unless noted. The moisture-sensitive reactions were carried out under nitrogen or argon atmosphere and under high vacuum with the standard Schlenk line. The reactions were monitored from time to time using thin-layer chromatography (TLC) on TLC Silica gel  $60 \, F_{254}$  aluminium sheets and visualized under UV light. The extraction of the crude product was carried out in a separating funnel using dichloromethane or ethyl acetate as the solvent and brine solution. The extracts were dried over  $Na_2SO_4$  and concentrated under reduced pressure using rotary vapour. The desired product was purified using flash chromatography using silica gel  $(230\text{-}400 \, \text{mesh})$  at varying solvent ratios.

#### Syntheses and characterization

The syntheses were carried out under the nitrogen atmosphere using the standard Schlenk lines.

**5,10,15,20-tetrahydrocycloocta**[**1,2-b:3,4-b':5,6-b":7,8-b"']tetraindole (TTI):** A solution of indoline-2-one (5g, 37.55 mmol) in POCl<sub>3</sub> (25 mL) was stirred and refluxed at 80°C for 8 hours. After cooling the mixture was slowly poured into ice water and stirred for 30 minutes. The mixture solution was slowly neutralized by adding KOH solution under continuous stirring. A dark green crude was obtained after extraction. The crude product was purified using silica gel column chromatography adding pure DCM to obtain TTI (16.27%) and TAT (18.1 %) as pale-yellow solids. <sup>1</sup>H NMR (500 MHz, DMSOd6):  $\delta$  ppm; 11.43 (s, 4H), 7.57 (d, J= 7.6, 4H), 7.41 (d, j=7.7, 4H), 7.07 (m, 8H); 13C (125 MHz, DMSOd6):  $\delta$  ppm; 137.75, 135.23, 127.81, 121.73, 120.02, 119.17, 111.80, 105.99.

5,10,15,20-tetrahexyl-5,10,15,20-tetrahydrocycloocta[1,2-b:3,4-

b':5,6-b":7,8-b"]tetraindole (3): To a solution of TTI (1.12 g, 1.1 mmol) in DMF, NaH (109 g, 4.5 mmol) was added and stirred at room temperature for 30 mins. 1-bromohexane (1 g, 6.6 mmol) was added dropwise to the mixture and the solution was refluxed for two hours under nitrogen. The cooled mixture was poured into water and extracted with dichloromethane. The organic phase was then dried over MgSO<sub>4</sub> and concentrated under reduced pressure. The product **2** was isolated with silica gel column chromatography at (0.05:9.5 ratio) DCM/Hexane mixture. Yield 62 % a pale-yellow solid.  $^{1}$ H NMR (500 MHz, CDCl<sub>3</sub>, ppm):  $\delta$  7.42-7.11 (16 H), 4.25-4.19 (m, 8 H), 1.58-1.45 (m, 4H), 1.34-1.28 (m, 4H), 0.92-0.89 (m, 4H), 0.64-0.4 (m, 32H).

#### 2,7,12,17-tetrabromo-5,10,15,20-tetrahexyl-5,10,15,20-

tetrahydrocycloocta[1,2-b:3,4-b':5,6-b":7,8-b"']tetraindole (4): To a solution of 3 (0.5 g. 0.63 mmol) in chloroform, *N*-bromosuccinimide (0.46 g, 2.6 mmol) in 3mL DMF was added dropwise at 0°C. The reaction mixture was stirred for 4 h, which was then washed with water and extracted with DCM. The organic phase was dried over MgSO<sub>4</sub> and the product was separated by silica gel column chromatography by (1:9) DCM/Hexane mixture. Yield 78 %, pale yellow solid.  $^{1}$ H NMR (500 MHz, CDCl<sub>3</sub>, ppm):  $\delta$  7.56 (s, 4H), 7.24-7.22 (m, 8H), 4.21-4.06 (m, 8H), 1.46-1.42 (m, 4H), 1.35-1.28 (m, 8H), 0.59 (m. 32H)

3-fluoro-4-methoxy-N-(4-methoxyphenyl)aniline ("F-DPA): To a two-neck round bottom flask, p-anisidine (3 g, 24.36 mmol), 4-bromo-3-fluoro-1-metoxybenzene (5.5g, 26.7 mmol), P(t-bu)<sub>3</sub>HBF<sub>4</sub> (212 mg, 0.73 mmol), NaOtBu (4.6g, 48.7 mmol) in anhydrous toluene (30 mL) were added and the mixture was purged under nitrogen for 15 mins. Pd<sub>2</sub>dba<sub>3</sub> (0.5 mmol) was added to the mixture and then purged again under nitrogen for 15 mins. After that the reaction mixture was stirred under reflux at 120°C for 12 hours. The crude was then quenched with water and extracted with ethyl acetate, and then dried with Na<sub>2</sub>SO<sub>4</sub>. The solvent was then removed under reduced pressure. The crude was purified by a silica gel column chromatography using ethyl acetate/hexane (9:1). Yield 76 %, yellow liquid. <sup>1</sup>H NMR (500 MHz, CDCl<sub>3</sub>, ppm):  $\delta$  7.73 (s, 1H), 7.01-6.97 (m, 3H), 6.86 (m, 2H), 6.71 (m, 2H), 3. 74-3.70 (s, 6H).

A similar procedure is followed for the synthesis of **2-fluoro-4-methoxy-N- (4-methoxyphenyl)aniline (°F-DPA).** 

Yield 73 %, dark yellow liquid.  $^{1}$ H NMR (500 MHz, CDCl<sub>3</sub>, ppm):  $\delta$  7.27 (s, 1H), 7.09 (t, 1H), 6.87 (dd, 1H), 6.80 (m, 4H), 6.68 (m, 1H), 3.72-3.68 (s, 6H)

5aE,10aE,15aE,20aE)-N<sup>2</sup>,N<sup>7</sup>,N<sup>12</sup>,N<sup>18</sup>-tetrakis(2-fluoro-4-methoxyphenyl)-5,10,15,20-tetrahexyl-N<sup>2</sup>,N<sup>7</sup>,N<sup>12</sup>,N<sup>18</sup>-tetrakis(4-methoxyphenyl)-5,10,15,20-tetrahydrocycloocta[1,2-b:3,4-b':5,6-b':7,8-b''']tetraindole-2,7,12,18-tetraamine:

To a two-neck round bottom flask, **4** (0.5 g, 0.45 mmol), °F-DPA (0.55 g, 2.24 mmol), P(t-bu) $_3$ HBF $_4$  (240 mg), NaO $^4$ Bu (0.34 g, 3.5 mmol) in anhydrous toluene (30 mL) were added and the mixture was purged under nitrogen for 15 mins. Pd $_2$ dba $_3$  (100 mg) was added to the mixture and then purged again under nitrogen for 15 mins. After that the reaction mixture was stirred under reflux at 120°C for 12 hours. The organic phase was dried over MgSO $_4$  and

the product was separated by silica gel column chromatography by DCM/Hexane mixture. Yield 41 %, light yellow solid.  $^1$ H NMR (500 MHz, DMSO-d6, ppm):  $\delta$  7.12-7.09 (8H), 6.97-6.68 (m, 8H), 6.75-6.68 (m, 18H), 6.61 (6H), 4.06-4.02 (m, 8H), 3.90-3.68 (24H), 1.26 (4H), 1.18 (8H), 0.58-0.47 (32H)

**10,15-dihydro-5H-diindolo[3,2-a:3',2'-c]carbazole (TAT):** A solution of indoline-2-one (5g, 37.55 mmol) in POCl<sub>3</sub> (25 mL) was stirred and refluxed at 80°C for 8 hours. After cooling, the mixture was slowly poured into ice water and stirred for 30 minutes. The mixture solution was slowly neutralized by adding NaOH solution under continuous stirring. A dark brown crude was obtained after extraction. The crude product was purified using silica gel column chromatography adding pure DCM to obtain TAT (Yield 18.1 %) as pale-yellow solids.  $^{1}$ H NMR (500 MHz, DMSO-d6, ppm):  $\delta$  11.87 (s, 3H), 8.68 (d, 3H), 7.73 (d, 3H), 7.39-7.33 (m, 6H).

#### 5,10,15-trihexyl-10,15-dihydro-5H-diindolo[3,2-a:3',2'-c]carbazole:

To a solution of **TAT** (1 g, 2.9 mmol) in DMF, NaH (200 mg, 10.2 mmol) was added and stirred at room temperature for 30 mins. 1-bromohexane (2.46 g, 11.6 mmol) was added dropwise to the mixture and the solution was refluxed for two hours under nitrogen. The cooled mixture was poured into water and extracted with dichloromethane. The organic phase was then dried over MgSO<sub>4</sub> and concentrated under reduced pressure. The product was isolated with silica gel column chromatography at (8:2 ratio) DCM/Hexane mixture. Yield 55 %, white solid.  $^1$ H NMR (500 MHz, CDCl<sub>3</sub>, ppm):  $\delta$  8.31 (d, 3H), 7.66 (d, 3H), 7.48 (t, 3H), 7.37 (t, 3H), 4.94 (m, 6H), 2.01 (m, 6H), 1.32-1.25 (m, 18H), 0.85-0.81 (9H).

#### 3,8,13-tribromo-5,10,15-trihexyl-10,15-dihydro-5H-diindolo[3,2-

a:3',2'-c]carbazole: To a solution of 5,10,15-trihexyl-10,15-dihydro-5H-diindolo[3,2-a:3',2'-c]carbazole (0.7 g, 1.16 mmol) in CHCl<sub>3</sub>, *N*-bromosuccinimide (0.64 g, 3.6 mmol) in 3mL DMF was added dropwise at 0°C. The reaction mixture was stirred for 4 h, which was then washed with water and extracted with DCM. The organic phase was dried over MgSO<sub>4</sub> and the product was separated by silica gel column chromatography by (1:9) DCM/Hexane mixture. Yield 63 %, light yellow solid.  $^{1}$ H NMR (500 MHz, DMSO-d6, ppm):  $\delta$  8.26-7.41 (m, 9H), 4.74-4.62 (m, 6H), 1.88 (m, 6H), 1.20-1.28 (m, 6H), 0.84-0.80 (9H)

N3,N8,N13-tris(3-fluoro-4-methoxyphenyl)-5,10,15-trihexyl-N3,N8,N13-tris(4-methoxyphenyl)-10,15-dihydro-5H-diindolo[3,2-a:3',2'-c]carbazole-3,8,13-triamine: To a two-neck round bottom flask, 3,8,13-tribromo-5,10,15-trihexyl-10,15-dihydro-5H-diindolo[3,2-a:3',2'-c]carbazole (0.5 g, 0.599 mmol), mF-DPA (0.59 g, 2.39 mmol), P(t-bu)<sub>3</sub>HBF<sub>4</sub> (180 mg), NaOtBu (0.34 g, 3.5 mmol) in anhydrous toluene (30 mL) were added and the mixture was purged under nitrogen for 15 mins. Pd<sub>2</sub>dba<sub>3</sub> (90 mg) was added to the mixture and then purged agin under nitrogen for 15 mins. After that the reaction mixture was stirred under reflux at 120°C for 12 hours. The cooled mixture was poured into water and extracted with dichloromethane. The organic phase was then dried over MgSO<sub>4</sub> and

concentrated under reduced pressure. The product was isolated with silica gel column chromatography at (8:2 ratio) DCM/Hexane mixture. Yield 68 %, pale yellow.  $^1$ H NMR (500 MHz, DMSO-d6, ppm):  $\delta$  8.34 (3H), 7.55-7.36 (15H), 6.93-6.64 (12H), 4.67-4.66 (6H), 3.42-3.27 (18H), 1.85 (6H), 1.06-0.99 (18H), 0.79-0.76 (9H).

A similar procedure is followed for the synthesis of N3,N8,N13-tris(2-fluoro-4-methoxyphenyl)-5,10,15-trihexyl-N3,N8,N13-tris(4-methoxyphenyl)-10,15-dihydro-5H-diindolo[3,2-a:3',2'-c]carbazole-3,8,13-triamine.

Yield 63 %, white solid.  $^1$ H NMR (500 MHz, CDCl<sub>3</sub>, ppm):  $\delta$  7.99 (3H), 7.24-7.04 (15H), 6.98-6.73 (12H), 4.81-4.32 (6H), 3.79-3.75 (18H), 1.75-1.66 (6H), 1.10-0.95 (18H), 0.67-0.66 (9H).

#### **Device Fabrication**

The fluorine-doped tin oxide (FTO) coated glass (TEC15, NSG 10, TEC 7) was used as substrate and was cleaned in sequence before use. Ultrasonication (2% Hellmanex water solution for 30 minutes) followed by rinsing with deionized water, acetone, and then isopropanol (IPA) was used and finally, the substrates were treated under UV-Ozone for 30 minutes for the removal of organic residue on the surface. TiO<sub>2</sub> compact layer was deposited on this substrate by spray pyrolysis at 500 °C using a precursor solution of titanium diisopropoxide bis(acetylacetonate) in anhydrous ethanol (1:19), and the substrates were annealed at 500 °C for further 30 minutes and left to cool down. The mesoporous TiO<sub>2</sub> layer was deposited on top of this through spin coating process (30 s at 4000 rpm), for this, a TiO<sub>2</sub> paste (Dyesol 30 NR-D) was diluted to 1:8 in ethanol. The TiO<sub>2</sub> coated substrates were annealed first at 125 °C, followed by 500 °C using a programmable ramp in four-step heating, and were finally maintained at 500°C for 30 min to acquire the anatase phase. On attaining room temperature, the substrates were treated under UV-Ozone for 30 minutes and transferred to an argon-filled glove box for perovskite layer deposition.

The precursor solution for preparing the MAPbI<sub>3</sub> was prepared by dissolving 1.2 M MAI: PbI<sub>2</sub> (1:1) in anhydrous DMSO solvent. The perovskite solutions

were spin-coated in a two-step sequence at 1000 and 4000 rpm for 10 s and 30 s, respectively. During the second step, 110  $\mu$ L of chlorobenzene was dripped as an antisolvent approach on the substrate 5s before the end of the spinning process. The perovskite coated substrates were annealed at 100 °C for one h in a glovebox.

For the mixed dimensional perovskite, 1.1 M solution of APAI: PbI<sub>2</sub> (2:1) was prepared. The resultant solution was then mixed with 1.2M solution of MAPbI<sub>3</sub> in different molar ratios (0%, 0.3%, 0.5%) to achieve the final 2D/3D (APA)<sub>x</sub>(MA)<sub>1-x</sub>PbI<sub>3</sub> solution. The perovskite solutions were spin-coated in a two-step sequence at 1000 and 4000 rpm for 10 s and 30 s, respectively. During the second step, 110  $\mu$ L of chlorobenzene was dripped as an antisolvent approach on the substrate 5s before the end of the spinning process. The perovskite coated substrates were annealed at 100 °C for one h in a glovebox.

The precursor solution for preparing the mixed perovskite  $(MAPbBr_3)_{0.15}(FAPbI_3)_{0.85}$  was prepared by dissolving FAI (1 M),  $PbI_2$  (1.2 M), MABr (0.2 M), and  $PbBr_2$  (0.2 M) in anhydrous DMF: DMSO 4:1 (v:v). The perovskite solution was spin-coated in a two-step sequence at 1000 and 6000 rpm for 10 and 30 s, respectively. During the second step, 110  $\mu$ L of chlorobenzene was dripped as an antisolvent approach on the substrate 5s

before the end of the spinning process. The perovskite-coated substrates were annealed at  $100\,^{\circ}\text{C}$  for 1 h in a glovebox.

On acquiring room temperature, the interfacial layers were deposited and annealed at 100 °C for 8 minutes. Once it acquires room temperature, Spiro-OMeTAD (70 mM) as hole selective layer was deposited by dissolving in chlorobenzene.

For the Spiro-OMeTAD and other HTMs were doped by adding bis-(trifluoromethylsulfonyl)imide lithium salt (Li-TFSI) and 4-*tert*-Butylpyridine (t-BP) in the molar ratio 0.5 and 3.3 respectively. 40  $\mu$ L of HTM solutions were spin-coated atop of the perovskite layer at 4000 rpm for 30 s, in an argon-filled glove box. The device fabrication was finished by evaporating an Au layer of 70 nm as a cathode under a low vacuum ( $10^{-6}$  torr). All solutions were prepared inside an argon-filled glove box with controlled moisture and oxygen conditions ( $O_2$  < 10 ppm,  $H_2O$  < 2 ppm).

#### **Device characterization**

The device photovoltaics parameters were measured utilizing current density–voltage (*J–V*) curves, registered with a Keithley 2400 source-meter under AM 1.5 G, 100 mW cm² illumination from a 450 W AAA solar simulator (ORIEL, 94023 A). NREL certified monocrystalline silicon solar cell was used for calibration. A black metal mask (0.1 cm²) was used over the square size active area (0.5 cm²) to reduce the influence of scattered light. The devices were measured at a scan rate: 100 mV s<sup>-1</sup>, pre-sweep delay: 10 s). The external quantum efficiency (EQE) measurements were carried out using a 150W Xenon lamp attached to with Bentham PVE300 motorized 1/4m monochromator as the light source.

#### **Thin-film Characterization**

For optical characterization, thin films were prepared on quartz substrate by spin coating of the precursors and materials in solution state. X-ray diffractograms were recorded using the D8 Advance diffractometer from Bruker (Bragg-Bretanto geometry, with an X-ray tube Cu K $\alpha$ ,  $\lambda$ =1.5406 angstrom). A scan of 5-10° was selected with an acquisition time of 1°/min. The absorption spectra were measured under a UV-Vis-IR

#### **Experimental Section**

spectrophotometer (Varian Cary 50 UV/Vis Spectrophotometer). Photoluminescence (PL) steady-state measurements were recorded with a spectrophotometer (Perkin Elmer Instrument LS55). XPS measurements were carried out on a SPECS system (Berlin, Germany) equipped with Phoibos 150 ID-DLD analyzer with monochromator Al K $\alpha$  radiation (1486.7 eV).

PM-IRRAS spectra of the mixed perovskites spin-coated onto gold substrates (15 × 20 mm), before and after different PEAI and FPEAI treatment (0.3 and 0.7%), were recorded on a Thermo Nicolet Nexus 670 FTIR spectrometer at a resolution of 4 cm<sup>-1</sup> during 4h acquisition time. All spectra were collected in a controlled dry environment (RH = 3%) protected from ambient light. Experiments were performed at an incidence angle of 75° using an external homemade goniometer reflection attachment and adding a ZnSe photoelastic modulator (PEM, Hinds Instruments, type III) after the polarizer. The ATR spectrum of the treated perovskites was recorded on the same FTIR spectrometer using a Silver-Gate (germanium crystal) ATR accessory (Specac). The ATR spectrum was obtained, at a resolution of 4 cm<sup>-1</sup>, by adding 500 scans. See Fig.2 for peak assignment of the vibrational modes of the mixed perovskite.

# <sup>1</sup>H/<sup>13</sup>C NMR Spectra:

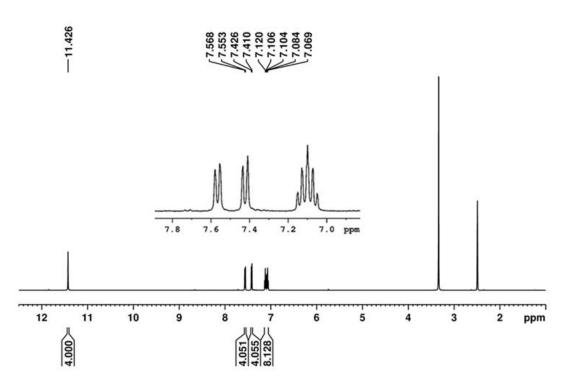


**Figure 1**: <sup>1</sup>H NMR of 5,10,15,20-tetrahydrocycloocta[1,2-b:3,4-b':5,6-b'':7,8-b''']tetraindole in DMSO-d6.

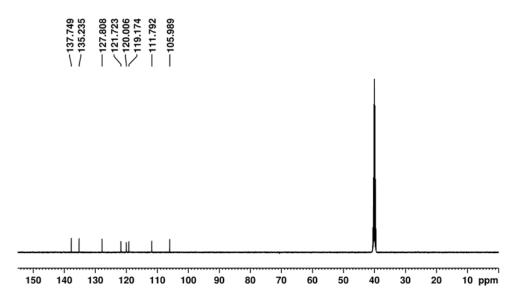


**Figure 2**:  $^{13}$ C NMR of 5,10,15,20-tetrahydrocycloocta[1,2-b:3,4-b':5,6-b'':7,8-b''']tetraindole in DMSO-d6.

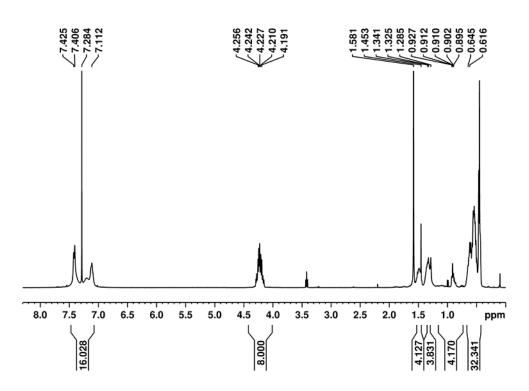


**Figure 3**: <sup>1</sup>H NMR 5,10,15,20-tetrahexyl-5,10,15,20-tetrahydrocycloocta[1,2-b:3,4-b':5,6-b'':7,8-b''']tetraindole.

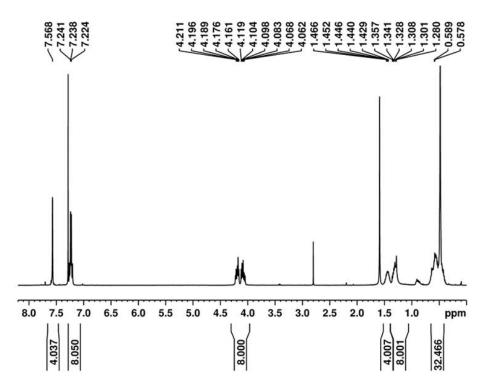


**Figure 4**: <sup>1</sup>H NMR of 2,7,12,17-tetrabromo-5,10,15,20-tetrahexyl-5,10,15,20-tetrahydrocycloocta[1,2-b:3,4-b':5,6-b'':7,8-b''']tetraindole.

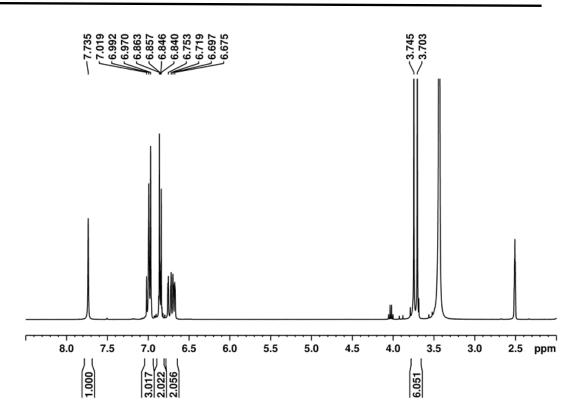


**Figure 5**: <sup>1</sup>H NMR of 3-fluoro-4-methoxy-N-(4-methoxyphenyl)aniline (mF-DPA).

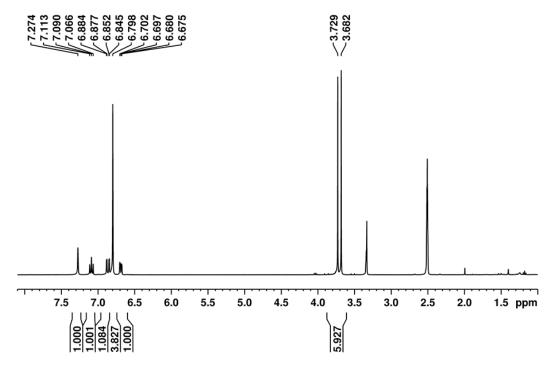


**Figure 6**: <sup>1</sup>H NMR of 2-fluoro-4-methoxy-N-(4-methoxyphenyl)aniline (oF-DPA).

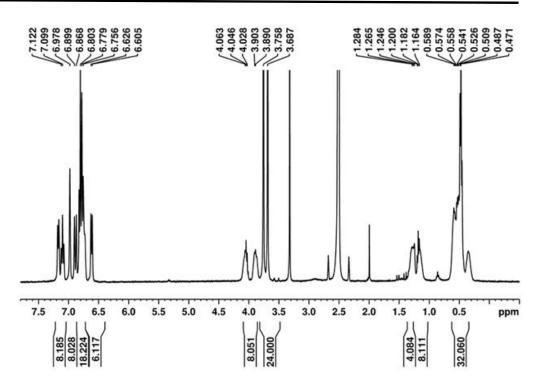


**Figure 7**:  $^{1}$ H NMR of 5aE,10aE,15aE,20aE)- $^{1}$ N $^{2}$ N $^{1}$ N $^{1}$ R-tetrakis(2-fluoro-4-methoxyphenyl)-5,10,15,20-tetrahexyl- $^{1}$ N $^{2}$ N $^{1}$ N $^{1}$ R-tetrakis(4-methoxyphenyl)-5,10,15,20-tetrahydrocycloocta[1,2-b:3,4-b':5,6-b'':7,8-b''']tetraindole-2,7,12,18-tetraamine.

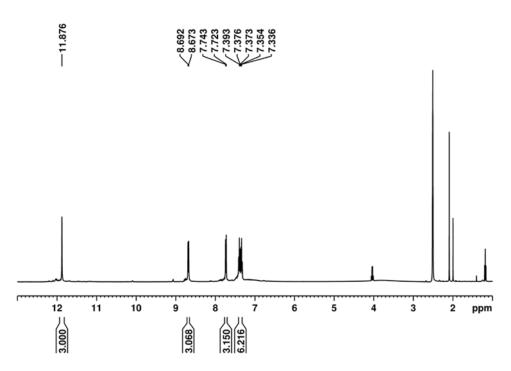


**Figure 8**: <sup>1</sup>H NMR of 10,15-dihydro-5H-diindolo[3,2-a:3',2'-c]carbazole.

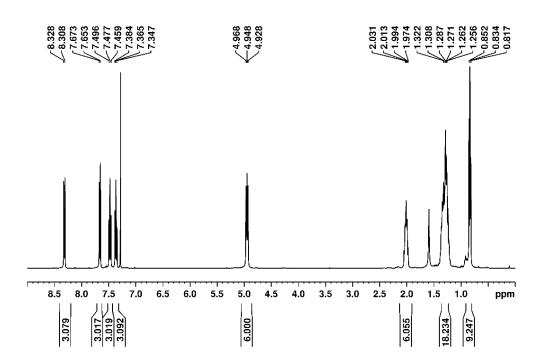
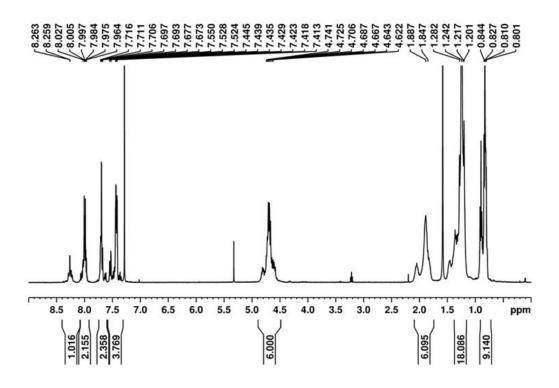


**Figure 9**: <sup>1</sup>H NMR of 5,10,15-trihexyl-10,15-dihydro-5H-diindolo[3,2-a:3',2'-c|carbazole.



# **Appendix**

**Figure 10**: <sup>1</sup>H NMR of 3,8,13-tribromo-5,10,15-trihexyl-10,15-dihydro-5H-diindolo[3,2-a:3',2'-c]carbazole.

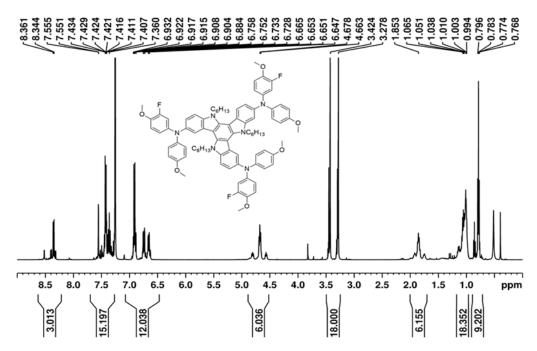
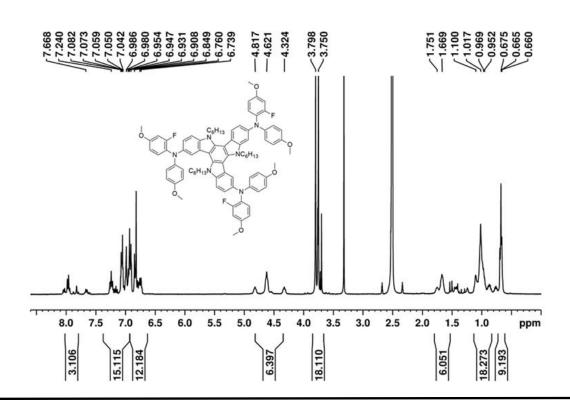


**Figure 11**: <sup>1</sup>H NMR of N3,N8,N13-tris(3-fluoro-4-methoxyphenyl)-5,10,15-trihexyl-N3,N8,N13-tris(4-methoxyphenyl)-10,15-dihydro-5H-diindolo[3,2-a:3',2'-c]carbazole-3,8,13-triamine.



# **Appendix**

**Figure 12**: <sup>1</sup>H NMR of N3,N8,N13-tris(2-fluoro-4-methoxyphenyl)-5,10,15-trihexyl-N3,N8,N13-tris(4-methoxyphenyl)-10,15-dihydro-5H-diindolo[3,2-a:3',2'-c]carbazole-3,8,13-triamine.

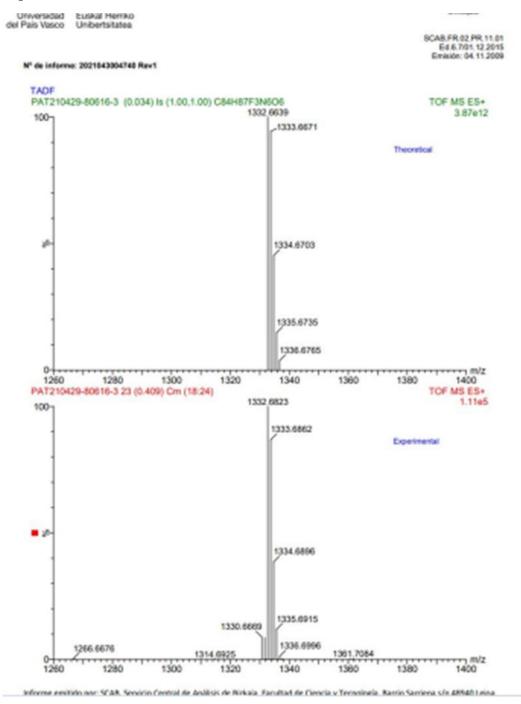


**Figure 13**: MALDI-TOF of N3,N8,N13-tris(3-fluoro-4-methoxyphenyl)-5,10,15-trihexyl-N3,N8,N13-tris(4-methoxyphenyl)-10,15-dihydro-5H-diindolo[3,2-a:3',2'-c]carbazole-3,8,13-triamine.

**MEENAKSHI PEGU** 

E-mail: meenakshi.pegu@bcmaterials .net, meenakshipegu.iitg@gmail.com

Mobile No: +34617753074

Nationality: India

**EDUCATION** 

PhD student in BCMaterials - Basque Center for Materials, Applications and

Nanostructures and University of Basque Country, October 2018- June 2022.

Final degree Project: Developing Hole Selective Layers and Implementing

Large-size Organic Cations for Perovskite Solar Cells.

Masters in Chemical Science, Indian Institute of technology, Guwahati, India.

Final degree Project: Developing of a new fluorescent chemosensor- 2-(4'-

Amino-2'-hydroxyphenyl)-1H-imidazo- [4,5-c]pyridine.

Bachelors in Chemistry, Dibrugarh University, India.

**PROJECT EXPERIENCE** 

1. Short Term Project: Summer Project at IIT Guwahati, India. Department of

Chemistry, IIT Guwahati, Assam, India, 781039

2. Long Term Project: "Design and Development of new functional

organic/organometallic molecules showing applications in material fields

(Thermally Activated Delayed Fluorescence (TADF) and Phosphorescence

Characteristics) mainly in optoelectronics and bio-imaging". Department of

238

Inorganic and Physical Chemistry, Indian Institute of Science (IISc), Bangalore, India, 560012

3. Short term scientific mission (STSM e-COST fellowship) for three months research stay June-August 2021: "Developing new small molecules as hole transporting materials and bulky organic 2D molecules for perovskite solar cells". Host Supervisor: Prof. Mohammad Khaja Nazeeruddin, GMF, EPFL, Sion, Valais 1950, Switzerland.

#### **PUBLICATIONS**

- 1. <u>Scientific article.</u> Meenakshi Pegu; Abolfazl Ghaderian; Shahzada Ahmad; Samrana Kazim. 2022. Reducing the Trap Density in MAPbI<sub>3</sub> Based Perovskite Solar Cells via Bromide Substitution. ChemplusChem, https://doi.org/10.1002/cplu.202200021
- 2. <u>Scientific article.</u> Meenakshi Pegu; Samrana Kazim; Thierry Buffeteau; Dario M Bassani; Shahzada Ahmad. 2021. Deciphering the Orientation of the Aromatic Spacer Cation in Bilayer Perovskite Solar Cells through Spectroscopic Techniques ACS Applied Materials & Interfaces. American Chemical Society. 13-40, pp.48219--48227.
- 3. <u>Scientific article.</u> Meenakshi Pegu; Samrana Kazim; Peng Huang; Luis Lezama; Shahzada Ahmad. 2021. Tetra-indole core as a dual agent: a hole selective layer that passivates defects in perovskite solar cells Journal of Materials Chemistry C. Royal Society of Chemistry. 9, pp.7074—7082.
- 4. <u>Scientific article</u>. Meenakshi Pegu; Samrana Kazim; Thierry Buffeteau; Dario M Bassani; Shahzada Ahmad. 2021. N-Bromosuccinimide as an Interfacial Alleviator for Br/I Exchange in Perovskite for Solar Cell

- Fabrication ACS Applied Energy Materials. American Chemical Society. 4-4, pp.3130—3140
- 5. **Book Chapter**. **Meenakshi Pegu**; Shahzada Ahmad; Samrana Kazim. (/3). 2021. Dopant-Free hole-transporting Materials for Perovskite Solar Cells: Materials, Processes, and Devices. Wiley-VCH GmbH. Chapter 10-331-367, pp.331-367. ISBN 9783527347155.
- 6. <u>Review article</u> Meenakshi Pegu; Muhammed PU Haris; Samrana Kazim;Shahzada Ahmad;. 2020. Understanding and harnessing the potential of layered perovskite-based absorbers for solar cells Emergent Materials. Springer International Publishing. pp.1-28.
- 7. <u>Scientific article</u>. Meenakshi Pegu; Laura Caliò; Mehrad Ahmadpour; Horst-Günter Rubahn; Samrana Kazim; Morten Madsen; Shahzada Ahmad. 2020. Dibenzo-tetraphenyl diindeno perylene as hole transport layer for high-bandgap perovskite solar cells Emergent Materials. Springer International Publishing. 3, pp.109-116
- 8. <u>Scientific article</u>. Yassine Raoui<sup>†</sup>; Meenakshi Pegu<sup>†</sup>; Samrana Kazim; Shahzada Ahmad. 2021. Interfacial modification of perovskite solar cells via Cs2CO3: Computational and experimental approach Solar Energy. Elsevier. 228, pp.700-705.
- 9. <u>Scientific article</u>. Naveen Harindu Hemasiri, Laura Caliò, <u>Meenakshi</u> Pegu, Samrana Kazim, Shahzada Ahmad. Molecular interface engineering via triazatruxene-based moieties/NiOx as hole selective bilayers in perovskite solar cells for reliability. **2022 Solar RRL**. Wiley-VCH GmbH
- 10. **Scientific article**. Shahzada Ahmad; Aysegul Uygun Oksuz; Samrana Kazim; et al; 2021. Predicting Perovskite Bandgap and Solar Cell Performance with Machine Learning Solar RRL. Wiley-VCH GmbH..

- 11. <u>Perspective</u>. Muhammed PU Haris; Samrana Kazim; <u>Meenakshi Pegu</u>; M Deepa; Shahzada Ahmad. 2021. Substance and shadow of formamidinium lead triiodide based solar cells Physical Chemistry Chemical Physics. Royal Society of Chemistry. 23-15, pp.9049--9060. 3.
- 12. <u>Scientific article</u>. Abolfazl Ghaderian; <u>Meenakshi Pegu</u>; Naveen Harindu Hemasiri; Peng Huang; Samrana Kazim; Shahzada Ahmad. 2021. Impact of Fluorine atoms on triphenylamine-based dopant free hole selective layer for perovskite solar cells Journal of Materials Chemistry C. Royal Society of Chemistry
- 13. <u>Scientific article</u>. Hassen Dhifaoui; <u>Meenakshi Pegu</u>; Walid Aloui; Abdelaziz Bouazizi; Samrana Kazim; Shahzada Ahmad. 2020. Tuning of MEH-PPV electro-optical properties by incorporation of benzylidene-malononitrile-based small organic molecules Emergent Materials. Springer International Publishing. 3-5, pp.687--692.
- 14. <u>Scientific article</u> Samir Kumar Sarkar; <u>Meenakshi Pegu</u>; Santosh Behera; Shiva Krishna; P. Thilagar. 2019. Aggregation-Induced and Polymorphism-Dependent ThermallyActivated Delayed Fluorescence (TADF) Characteristics of an Oligothiophene: Applications in Time-Dependent Live CellMulticolour Imaging Chemistry–An Asian Journal.
- 15. <u>Scientific article</u>. Santosh Behera; **Meenakshi Pegu**, G. Krishnamoorthy. 2018. Modulation of Twisted Intramolecular Charge Transfer Emission of 2-(4'-N,N-Dimethylaminophenyl)imidazopyridines in Aqueous Cucurbit[7]uril+ ChemistrySelect.

#### **CONFERENCES AND POSTERS**

- 1. MRS Fall virtual Conference 2020
- 2. Dyenamo Web Workshop ERC, 2020
- 3. Summer school on photovoltaics. Technical university of Denmark, 2020
- 4. Advances and Challenges in Perovskite solar cells. 2020
- 5. ACS Science Live: Advancing Energy, Storage, Capture and Conversion, 2021
- 6. HOPV Conference 2020
- 7. La Noche Europea de los Investigadores e Investigadoras de 2020
- 8. IRSEC 2020, 2021
- 9. Moscow Autumn Perovskite Photovoltaics International Conference 2020
- 10. Viper Conference 2021
- 11. Oral Seminar BC Materials 2020
- 12. Next generation Solar energy 2021
- 13. SP tech Conference 2021
- 14. Young Researchers Meet 2021, IISc Bangalore
- 15. Innovative Materials for Energy Workshop 2020
- 16. Poster presentation at Department of Physical and Inorganic Chemistry, Indian Institute of Science, Bangalore, 2018.